UNIVERSIDAD COMPLUTENSE DE MADRID
FACULTAD DE CIENCIAS QUÍMICAS

TESIS DOCTORAL

Cálculos DFT en el estudio de óxidos mixtos: estructura, propiedades y aplicaciones en la economía del hidrógeno

MEMORIA PARA OPTAR AL GRADO DE DOCTOR

PRESENTADA POR

Marianela Gómez Toledo

DIRIGIDA POR

María Elena Arroyo de Dompablo

Madrid

UNIVERSIDAD COMPLUTENSE DE MADRID

FACULTAD DE CIENCIAS QUÍMICAS

TESIS DOCTORAL

Cálculos DFT en el estudio de óxidos mixtos: estructura, propiedades y aplicaciones en la economía del hidrógeno

MEMORIA PARA OPTAR AL GRADO DE DOCTORA

PRESENTADA POR

Marianela Gómez Toledo

DIRECTORA

Maria Elena Arroyo de Dompablo

UNIVERSIDAD COMPLUTENSE DE MADRID

FACULTAD DE CIENCIAS QUÍMICAS

Doctorado en Química Avanzada

TESIS DOCTORAL

Cálculos DFT en el estudio de óxidos mixtos: estructura, propiedades y aplicaciones en la economía del hidrógeno

MEMORIA PARA OPTAR AL GRADO DE DOCTORA

PRESENTADA POR

Marianela Gómez Toledo

DIRECTORA

María Elena Arroyo de Dompablo

Madrid, 2025

Agradecimientos

Esta tesis ha sido mucho más que un trabajo de investigación. A lo largo del camino he contado con el apoyo, el ánimo y la generosidad de muchas personas que, de una forma u otra, han estado presentes y han hecho posible el haber llegado hasta aquí.

En primer lugar, quiero dar las gracias a las personas con las que he tenido el honor de colaborar durante el desarrollo de esta tesis. A la Doctora Laura Collado y al Doctor Víctor A. de la Peña O'Shea, de IMDEA Energía. Al Profesor Khalid Boulahya, y la Profesora Susana García Martín, de la Universidad Complutense; y a la Doctora Sara López Paz, de la Universidad de Copenhagen. Me gustaría también nombrar a D. Wilfredo More, del Instituto de Cerámica y Vidrio, y al Profesor Rodrigo González Prieto, de la Universidad Complutense, por ayudarme a completar las medidas de reflectancia difusa que han enriquecido el trabajo computacional.

Este trabajo de investigación no hubiera sido posible sin las instalaciones de MALTA Computing Centre (MCC). Me gustaría destacar a Jose Luis Casals Sainz, por toda la ayuda técnica prestada en estos años.

Por supuesto, no puedo más que agradecer a mi directora, la Profesora Elena Arroyo, haber depositado su confianza en mí. Elena, has sido una directora comprensiva y, a la vez, exigente cuando había que serlo, haciendo que mire con lupa todo lo que hago y que haya mejorado (o, al menos, intentado mejorar) día a día. Te lo agradezco de corazón. Estoy segura de que esta forma de trabajar tan minuciosa (casi artesana) que me has transmitido me va a acompañar siempre.

También quiero agradecer, de nuevo, a la Profesora Susana García Martín. Susana, muchas gracias por haberme confiado gran parte del estudio computacional que compone esta tesis. A lo largo de este proceso, no sólo he aprendido mucho científicamente hablando, sino que también he tenido la oportunidad de conocerte mejor a nivel personal, algo que valoro y me llevo conmigo como parte de esta etapa.

Quiero incluir también en estos agradecimientos a todas las personas que forman el Departamento de Química Inorgánica. En especial, debo nombrar al

Doctor Rafael Marín Gamero (a.k.a Rafa), que siempre ha estado dispuesto a echar una mano con cualquier cosa que necesitara, desde mover muebles a rellenar infinitos formularios, pasando por una conversación de lloradita, muchísimas gracias.

No creo que hubiera llegado hasta aquí de no ser por los grandes docentes que he tenido la suerte de encontrarme en mi camino académico. Quiero dar las gracias al Profesor Antonio Rey Gayo, que hizo que me enamorase de la Química Física. Antonio, gracias por enseñarme química y por tener siempre la puerta de tu despacho abierta (literal y figuradamente). Eres, sin duda, el mejor profesor que he tenido nunca. Por supuesto, quiero nombrar a la Profesora Ana Rubio Caparrós. Ana, cruzarme contigo en ese laboratorio de Química Física II cambió mi vida académica y eres un poco culpable de que esté escribiendo estas líneas. Me enseñaste (entre otras cosas) a hacer unas memorias decentes y a hablar en público, pero, sobre todo, me enseñase a confiar en mí, y nunca podré agradecértelo lo suficiente.

No quiero olvidarme de la gente que siempre ha estado dispuesta a contestar un mensaje, compartir un café, una comida, una cena o un viaje conmigo durante estos años. Primero, a (os pienso llamar doctoras porque ya lo sois) la Doctora Almudena Inchausti (o sea, la Mumu) y la Doctora Alessandra de Marcos (es decir, la Malessandra). Os quiero mucho (espero que imprimáis esto para tenerlo presente, porque no os lo digo lo suficiente). Gracias por todo. A Dawid (a veces Wavid o Deiwid), muchas gracias por las citas de heteros, los cafés, los audios interminables y las risas siendo MALAS. Te has convertido en uno de mis mejores amigos. A la gente que conocí hace 300 años y que siguen estando ahí: Paloma (Doctora Paloma García también, todo hay que decirlo) y Laura, gracias. A Pilar y Belén, gracias por ser las locas de los gatos conmigo. A la Doctora Carmen Martínez (me encanta hacer esto), gracias por las sesiones de llorería que acaban siendo una sesión de risas.

A mis amigos de toda la vida, Javi y Yeni que, aunque nos veamos una vez al año y sigan sin entender lo que hago, están siempre dispuestos a escucharme, gracias. A Pablo, al que conocí porque decidí ponerme en serio con el inglés y, míranos ahora, consiguiendo las cosas por las que nos quejábamos juntos. A Lorena (vamos, la Lore), gracias por las risas, los consejos y esa capacidad de bajar a cualquiera de las nubes. A Belén, que vivió conmigo cómo empecé esta

tesis, lloró conmigo viendo unas cuantas películas y (lo más importante) siempre está ahí para hacer el imbécil conmigo, muchas gracias. A Diana, que acaba de llegar, pero ha sido una amiga en modo intensivo y ha vivido el tramo final de esta aventura, gracias por la paciencia, los memes y las palabras bonitas.

También quiero dar unas gracias infinitas a mi familia, mis padres (Manuel y Marianela) y mi hermano (Manolo), pero también a mis abuelos (Felisa, Eladio, Faustino y Vicenta) y a mi tía Presen. Con esta tesis consigo el título académico más alto, pero no hubiera podido hacerlo si ellos no se hubieran quedado tantos días y tantas tardes conmigo cuando era una niña. Gracias por todo lo que habéis hecho por mí.

Por último, a mi compañera de vida. Adriana, creo que no me quedan cosas que decirte, pero quiero dejar escrito (una vez más) que lo que soy y lo que hago es gracias a que estás a mi lado (y a veces detrás, empujándome; o delante, tirando de mí). Siempre estás diciéndome que soy la mejor, pero debe quedar constancia de que yo sé que la mejor eres tú. Te quiero muchísimo.

El trabajo de investigación recogido en la presente tesis doctoral ha sido posible gracias a la Comunidad de Madrid y el contrato PEJ-2020-AI/IND-18065 del programa “Ayudas para la contratación de Ayudantes de Investigación y Técnicos de Laboratorio”; al Ministerio de Ciencia, Innovación y Universidades, y a la Agencia Estatal de Investigación y los proyectos ECSAWE (PID2022-139501OB-C22) y TED2021-130452B-C21.

Los cálculos realizados se han llevado a cabo, en su mayoría, en el MALTA Computing Centre (MCC).

Índice

Resumen

La creciente demanda energética y el impacto ambiental asociado al uso de combustibles fósiles han impulsado la búsqueda de fuentes de energía limpias y sostenibles. En este contexto, el hidrógeno se presenta como el vector energético del futuro, debido a su alta eficiencia de combustión, su abundancia y su baja huella ambiental. Esta tesis doctoral se centra en el estudio de materiales funcionales en el marco de la economía del hidrógeno. Concretamente, se investigan dos materiales: la familia $Sr_{2-x}Ba_xTa_2O_7$ ($0 \leq x \leq 1$), y su actividad como fotocatalizador para la generación de hidrógeno verde; y el sistema $YSr_2Cu_2FeO_{7+\delta}$ ($0 < \delta < 1$), derivado de YBaCuO, y su posible aplicación como electrodo de aire en celdas de combustible de óxido sólido (SOFC). Ambos óxidos mixtos presentan estructuras derivadas de la perovskita, lo que los hace candidatos atractivos para aplicaciones en el campo de la energía. La investigación recogida en esta tesis doctoral se sustenta en el estudio computacional de estos óxidos mixtos a través de cálculos mecano-cuánticos basados en la Teoría del Funcional de la Densidad, con el objetivo de establecer relaciones claras entre la estructura, la composición y las propiedades de los materiales estudiados.

Familia $Sr_{2-x}Ba_xTa_2O_7$

Se han investigado los óxidos mixtos pertenecientes a la familia $Sr_{2-x}Ba_xTa_2O_7$ ($0 \leq x \leq 1$) como fotocatalizadores para la generación de hidrógeno verde mediante la fotocatálisis del agua. Para ello, se han llevado a cabo cálculos DFT utilizando los funcionales PBE, SCAN y HSE06 para analizar el efecto de la sustitución de Sr por Ba en la estructura cristalina y las propiedades electrónicas de estos materiales. Se han explorado dos estructuras, una derivada del compuesto $Sr_2Ta_2O_7$ (Fases - $Ca_2Nb_2O_7$) y otra derivada de $BaSrTa_2O_7$ (Dion-Jacobson). Al analizar los cambios provocados dentro de los compuestos con idéntica estructura cristalina, los resultados indican que la incorporación de Ba no induce cambios significativos, pero sí afecta a la posición de las bandas de valencia y conducción, lo que puede influir en la actividad fotocatalítica. Además, se han sintetizado y caracterizado experimentalmente las fases $Sr_2Ta_2O_7$ y $BaSrTa_2O_7$, evaluándose su actividad fotocatalítica para la generación de hidrógeno a partir de irradiación UV. Se ha observado que la fase Dion-Jacobson $BaSrTa_2O_7$ presenta una mayor eficiencia en la producción de hidrógeno debido, probablemente, a una diferencia

clave observada entre la estructura cristalina de $BaSrTa_2O_7$ y la de $Sr_2Ta_2O_7$. Por otra parte, se ha validado la adecuación del funcional meta-GGA SCAN para estudiar óxidos de metales de transición d^0, por ser capaz de ofrecer resultados más cercanos a los experimentales que el funcional PBE, pero a un coste computacional más asequible que el funcional híbrido HSE06.

Sistema $YSr_2Cu_2FeO_{7+\delta}$

En esta tesis se ha realizado un estudio computacional del sistema $YSr_2Cu_2FeO_{7+\delta}$ ($0 < \delta < 1$), con el objetivo final de evaluar si este material presenta las propiedades adecuadas para actuar como electrodo de aire en celdas de combustible de óxido sólido (SOFC). En primer lugar, se ha estudiado el desempeño de distintos funcionales de intercambio-correlación, en particular PBE, PBE+*U*, SCAN y SCAN+*U*, en la descripción de los óxidos mixtos que componen esta familia. Los cálculos DFT revelaron que la elección del funcional y el valor del parámetro *U* influyen de manera significativa en la descripción de las propiedades estructurales, magnéticas y electrónicas del material. Para la metodología SCAN+*U*, se ha observado que la utilización de los valores adecuados de *U* para Cu y Fe, mejora la reproducción de las propiedades experimentales, como el band gap y los momentos magnéticos, en comparación con los resultados obtenidos mediante PBE+*U*. Estos resultados proporcionan una base sólida para futuras investigaciones en materiales complejos con múltiples metales de transición.

Por otro lado, se ha abordado el estudio de la movilidad del ion O^{2-} en el sistema $YSr_2Cu_2FeO_{7+\delta}$ mediante dinámica molecular *ab initio* (AIMD). Se ha simulado la difusión de iones óxido a diferentes temperaturas, utilizando modelos estructurales con diferentes contenidos de oxígeno (δ), obteniéndose parámetros con importancia para la aplicación buscada, como la energía de activación (Ea) o el coeficiente de difusión. Los resultados muestran que las vacantes de oxígeno desempeñan un papel crucial en el mecanismo de difusión.

En resumen, esta tesis doctoral ha demostrado el potencial de los óxidos mixtos con estructura derivada de la perovskita como materiales funcionales para tecnologías asociadas a la economía del hidrógeno. Se ha confirmado la actividad fotocatalítica de $BaSrTa_2O_7$, aportando una posible explicación a partir del análisis computacional llevado a cabo sobre la familia $Sr_{2-x}Ba_xTa_2O_7$ ($0 \leq x \leq 1$), y

se ha estudiado en profundidad el sistema $YSr_2Cu_2FeO_{7+\delta}$, centrando la atención en la elección del funcional adecuado y en la posible aplicación del material como cátodo en SOFC. Los resultados obtenidos son un punto de partida para futuras investigaciones computacionales en óxidos mixtos de complejidad similar a los analizados en este trabajo.

Abstract

The search for green and renewable energy sources has been accelerated owing to the increasing energy demand and the resulting climate impact. In this scenario, hydrogen emerges as a highly promising energy vector due to its high combustion efficiency, its outstanding abundance and its minimal environmental footprint. This doctoral thesis focuses on the study of functional materials within the hydrogen economy. Specifically, two materials are explored: the $Sr_{2-x}Ba_xTa_2O_7$ ($0 \leq x \leq 1$) family, and its photocatalytic activity for green hydrogen production; and the YBaCuO-derived $YSr_2Cu_2FeO_{7+\delta}$ ($0 < \delta < 1$) system, and its application as an air electrode in solid oxide fuel cells (SOFC). Both materials feature perovskite-derived structures that enhance their energy-related applications. The research herein presented has been carried out using Density Functional Theory (DFT) calculations to understand the relationship between structure, composition, and properties in the mixed oxides studied.

The $Sr_{2-x}Ba_xTa_2O_7$ ($0 \leq x \leq 1$) family

The $Sr_{2-x}Ba_xTa_2O_7$ ($0 \leq x \leq 1$) mixed oxides have been investigated as water electrolysis photocatalysts for green hydrogen production. To understand the impact of Ba for Sr substitution on the crystalline structure and electronic properties, DFT calculations using PBE, SCAN and HSE06 exchange-correlation functionals have been carried out.

Two different crystal structures have been studied: the $Sr_2Ta_2O_7$ (which is related to $Ca_2Nb_2O_7$ phases) and the $BaSrTa_2O_7$-derived (part of the Dion-Jacobson family). Results show that, when comparing materials with the same crystal structure, the Ba incorporation does not lead to significant changes in the overall electronic structure. However, it does affect the valence and conduction band edges, which could influence photocatalytic activity. Both $Sr_2Ta_2O_7$ and $BaSrTa_2O_7$ have been experimentally synthesized, assessing their photocatalytic activity for UV green hydrogen production. The Dion-Jacobson $BaSrTa_2O_7$ shows a high efficiency for hydrogen production. To find an explanation for this observation, its crystal structure has been carefully examined through computational analysis, revealing a key structural difference between $BaSrTa_2O_7$ and $Sr_2Ta_2O_7$. The suitability of the exchange-correlation functionals used in the DFT calculations has been assessed, concluding that SCAN provides the best accuracy-to-computational time ratio for d^0 transition metal oxides when compared to PBE and HSE06.

The $YSr_2Cu_2FeO_{7+\delta}$ ($0 < \delta < 1$) system

The $YSr_2Cu_2FeO_{7+\delta}$ ($0 < \delta < 1$) system has been computationally studied in this thesis to assess its properties for acting as a cathode material for SOFC. Firstly, the performance of various DFT methodologies has been analyzed, specifically PBE, PBE+*U*, SCAN and SCAN+*U* have been tested on describing these mixed oxides. DFT calculations revealed that the exchange-correlation functional and the *U* value significantly influence the description of the structural, electronic and magnetic properties. For the SCAN+*U* method, results show that using appropriate *U* values for Cu and Fe enhances the accuracy of predicted experimental properties, such as the band gap and magnetic moments, when compared to PBE+*U* results. These findings establish a robust basis for future research on complex materials containing multiple transition metals.

In addition, the mobility of the oxide ion in the $YSr_2Cu_2FeO_{7+\delta}$ system has been studied using *Ab initio* Molecular Dynamics (AIMD). Simulation of oxide ions diffusion at different temperatures has been conducted using structural models with different oxygen contents (δ), resulting in key parameters relevant to the intended applications, such as the activation energy (Ea) and the diffusion coefficient. The results show that oxygen vacancies play a crucial role in the diffusion mechanism.

In summary, this PhD thesis has illustrated the potential of mixed oxides with perovskite-derived structures as functional materials for technologies associated with the hydrogen economy. The photocatalytic activity of $BaSrTa_2O_7$ has been confirmed, with possible explanations supported by computational analysis of the $Sr_{2-x}Ba_xTa_2O_7$ ($0 \leq x \leq 1$) family. Furthermore, the $YSr_2Cu_2FeO_{7+\delta}$ ($0 < \delta < 1$) system was explored in detail, focusing on the selection of suitable functionals and the possible application of the material as a cathode in SOFC. The results obtained serve as a springboard for future computational investigations on mixed oxides of similar complexity to those analyzed in this work.

Lista de abreviaturas

AEL	Electrolizadores alcalinos *Alkaline Electroyzers*
AIMD	Dinámica molecular *ab initio* *Ab initio Molecular Dynamics*
ASR	Resistencia de polarización en superficie *Area Specific Resistance*
BC	Banda de conducción
BV	Banda de valencia
DFT	Teoría del funcional de la densidad *Density Functional Theory*
ESIT	Ecuación de Schrödinger independiente del tiempo
FF	Campos de fuerza *Force Fields*
GGA	Aproximación de gradiente generalizada *Generalized Gradient Approximation*
HF	Hartree-Fock
HOR	Reacción de oxidación de oxígeno *Hydrogen Oxidation Reaction*
HSE	Funcional híbrido Heyd-Scuseria-Ernzerhof
IR	Infrarrojo
LSC	$La_{1-x}Sr_xCoO_{3-\delta}$
LSCF	$La_{1-x}Sr_xCo_{1-y}Fe_yO_{3-\delta}$
LSM	$La_{1-x}Sr_xMnO_{3-\delta}$
MD	Dinámica molecular clásica *Classical Molecular Dynamics*
MIEC	Conductor iónico-electrónico mixto *Mixed ionic-electronic conductor*
MLFF	*Machine Learning Force Fields*

MM	Simulación multiescala *Multiscale Modeling*
MT	Metal de transición
OER	Reacción de evolución de oxígeno *Oxygen evolution reaction*
ORR	Reacción de reducción de oxígeno *Oxygen Reduction Reaction*
P2FUEL	De energía a gas de síntesis *power-to-synfuel*
P2G	De energía a gas *power-to-gas*
P2I	De energía a industria *power-to-industry*
P2M	De energía a movilidad *power-to-mobility*
P2P	De energía a energía *power-to-power*
PBCO	$PrBaCo_2O_{5+d}$
PBE	Funcional de Perdew, Burke y Ernzerhof
SBCO	$SmBaCo_2O_{5+d}$
SCAN	Fuertemente restringido y adecuadamente normalizado *Strongly Constrained and Appropriately Normed*
SOEC	Electrolizadores de óxido sólido *Solid Oxide Electrolyzers*
SOFC	Celda de combustible de óxido sólido *Solid Oxide Fuel Cell*
SQS	*Special Quasi-random Structures*
TEC	Coeficiente de expansión térmico *Thermal Expansion Coefficient*

TPB	Punto triple *Triple Phase Boundary*
UV	Ultravioleta
Vis	Visible
XES	Espectroscopía de emisión de rayos X *X-Ray emission spectroscopy*
YBCO	$YBa_2Cu_3O_{7-\delta}$
YSCFO	$YSr_2Cu_2FeO_{7+\delta}$

CAPÍTULO 1
Introducción

La generación de energía ha acompañado a la especie humana desde que las primeras civilizaciones descubrieran el fuego. Actualmente, la demanda de energía crece cada año, y se predice que aumente hasta en un 25% para el año 2040.[1] La mayor parte de la energía producida a nivel mundial proviene de la utilización de combustibles fósiles, lo que ha traído consigo un aumento de emisiones de gases de efecto invernadero, agravando el cambio climático y el calentamiento global.[2] En este escenario, en el que la aceleración de la búsqueda de fuentes de energía limpias y eficientes es de vital importancia, el hidrógeno emerge como uno de los protagonistas.[3]

El hidrógeno se presenta como el vector energético del futuro debido a que cuenta con numerosas ventajas frente a otros recursos energéticos. Entre dichas ventajas se encuentran su elevada abundancia, su baja huella ambiental —ya que, generalmente, su combustión sólo produce vapor de agua—, y su alta eficiencia de combustión (120-142 MJ/kg).[4, 5] En la **figura 1.1** se esquematiza la cadena de valor del hidrógeno, desde su producción hasta su almacenamiento y su uso en diversas aplicaciones. Se trata de un vector energético flexible, que permite integrar la electricidad renovable excedentaria para su producción, lo cual incrementa la participación de energías renovables en el sistema eléctrico. Por otro lado, al utilizarse como combustible, contribuye a la sustitución de fuentes de energía de origen fósil, abriendo nuevas rutas tecnológicas para la industria, la electrificación del transporte y la movilidad sostenible. Dentro de la cadena de valor del hidrógeno, atendiendo al sector dónde va a utilizarse este vector energético, pueden definirse cinco configuraciones de uso final: *power-to-gas* (P2G), *power-to-mobility* (P2M), *power-to-industry* (P2I), *power-to-synfuel* (P2FUEL) y *power-to-power* (P2P).[6]

El progreso hacia un sistema energético descarbonizado, flexible y eficiente se sustenta, entre otras, en tecnologías de producción de «hidrógeno verde» y su posterior uso como combustible en distintos sectores. Sin duda, los materiales desempeñan un papel fundamental en la producción, conversión y almacenamiento de energía. El desarrollo de tecnologías en el ámbito de la economía del hidrógeno hace necesario utilizar un amplio abanico de materiales que presenten las prestaciones adecuadas para cada aplicación específica. En este contexto, esta tesis doctoral se centra en el estudio de óxidos de metales de transición como materiales para la producción y el uso de hidrógeno. Concretamente, se estudia la familia $Sr_{2-x}Ba_xTa_2O_7$ ($0 \leq x \leq 1$) en el marco de la

producción de hidrógeno mediante fotocatálisis, y se investiga el sistema $YSr_2Cu_2FeO_{7+\delta}$ ($0 < \delta < 1$) para su potencial aplicación como electrodo de aire en pilas de combustible.

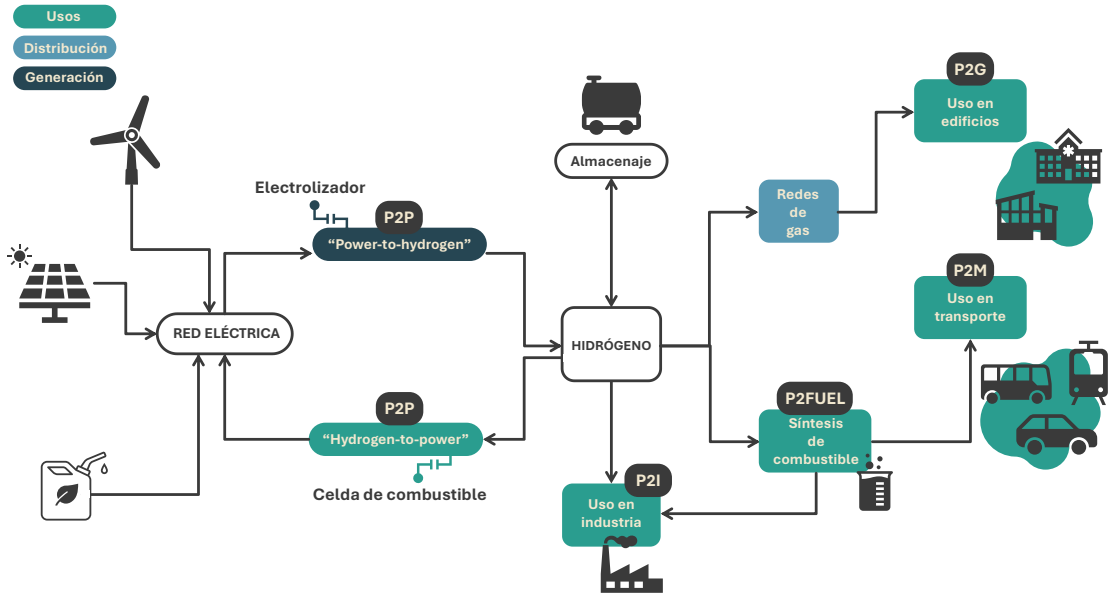

Figura 1.1: Esquema de la cadena de valor del hidrógeno. Algunos de los posibles usos del hidrógeno se representan en cuadros verdes, indicándose, en cada caso, la configuración de uso final (P2P, P2I, P2FUEL, P2M, P2G)

En esta tesis doctoral, se han empleado cálculos mecano-cuánticos con el objetivo de establecer una relación clara entre la estructura cristalina, la composición y las propiedades de $Sr_{2-x}Ba_xTa_2O_7$ ($0 \leq x \leq 1$) y $YSr_2Cu_2FeO_{7+\delta}$ ($0 < \delta < 1$). Por ello, aunque no se busca desarrollar nuevas metodologías computacionales, la sección 1.1. introduce brevemente el fundamento teórico sobre el que se sustentan los cálculos realizados. La estructura cristalina de los materiales estudiados puede describirse a partir de capas tipo perovskita. La sección 1.2. explora la estructura cristalina de estos compuestos y su relación con la perovskita cúbica ABO_3. Aunque ambos óxidos mixtos presentan cierta similitud estructural, sus propiedades difieren notablemente, lo que ha motivado su propuesta para distintas aplicaciones. Posteriormente, las secciones 1.3 y 1.4. abordan, respectivamente, las generalidades de los materiales fotocatalizadores y los electrodos de aire para SOFC. En cada una de ellas se presenta una revisión de los resultados experimentales y computacionales más relevantes para los materiales estudiados, $Sr_{2-x}Ba_xTa_2O_7$ (sección 1.3) y $YSr_2Cu_2FeO_{7+\delta}$ (sección 1.4).

1.1. Cálculos DFT en el estudio de materiales

Históricamente, el análisis y diseño de materiales se ha basado en el empleo de métodos experimentales de ensayo y error. Sin embargo, el desarrollo computacional que se ha dado en las últimas décadas ha propiciado el uso de nuevas tecnologías para este fin.[7, 8] Entre los objetivos fundamentales de esta tesis se encuentra la aplicación de metodologías de cálculo computacional para el estudio de sólidos inorgánicos.

Los métodos computacionales son especialmente útiles a la hora de examinar la relación estructura-composición-propiedades de los materiales. Como se esquematiza en la **figura 1.2**, la existencia de diferentes escalas de modelización permite obtener información que va desde la estructura electrónica del material estudiado, hasta la simulación de su posible aplicación en un dispositivo.[9] Además, existe la posibilidad de trabajar con modelos multiescala (*Multiscale Modeling*, MM), un enfoque que, en combinación con técnicas de *Machine Learning* es muy utilizado en el diseño de materiales.[10]

En la primera escala de modelización se trabaja a nivel atómico (núcleo y electrones), con modelos que dan acceso a información mecano-cuántica del material objeto de estudio. Los métodos para determinar la estructura electrónica de un sistema químico tienen como finalidad resolver la ecuación de Schrödinger independiente del tiempo (ESIT) (**ecuación 1**). Dicha ecuación relaciona la función de onda que describe el sistema (Ψ) con la energía de este (E).

$$\hat{H}\psi = E\psi \qquad (1)$$

$\hat{H}$ es el operador Hamiltoniano y E es el autovalor del operador, que representa la energía total del sistema. La resolución de la ESIT es factible para sistemas sencillos como el caso del átomo de hidrógeno. Sin embargo, la resolución de la ecuación se complica para sistemas con múltiples electrones. Para abordar este problema se han desarrollado diversos métodos como, por ejemplo, los métodos *ab initio* Hartree-Fock (HF) y post-Hartree-Fock. La Teoría del Funcional de la Densidad (DFT) nace, precisamente, como alternativa a HF.

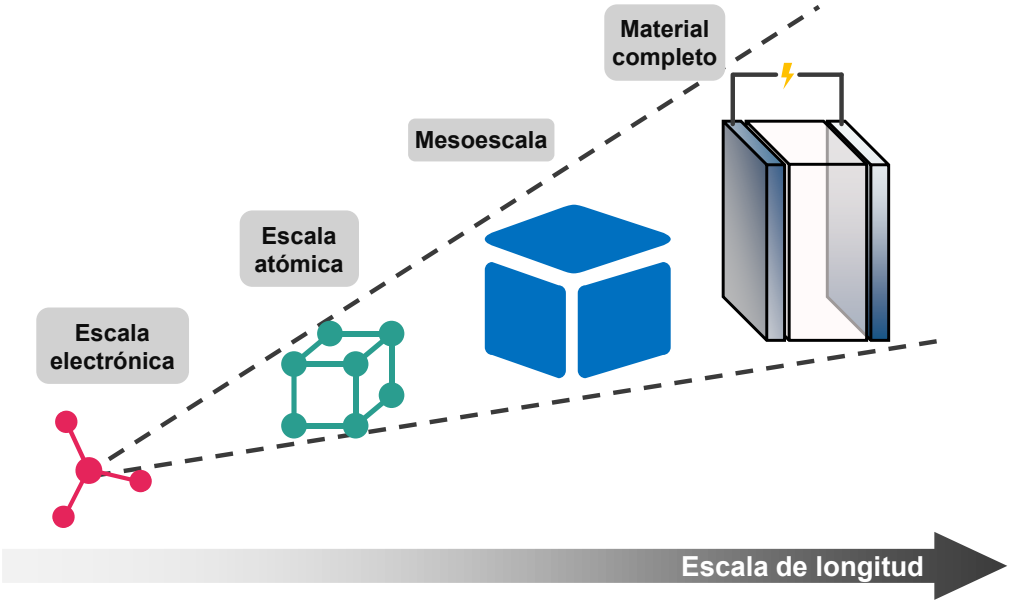

Figura 1.2: Representación esquemática de las diferentes escalas de simulación para el estudio de materiales.

La DFT fue desarrollada por Hohenberg, Khon y Sham[11, 12] en la década de 1960, bajo la premisa de que la energía del estado fundamental de un sistema, calculada a partir de la ESIT, es un funcional único de la densidad electrónica. A través de la utilización de un sistema ideal, Khon y Sham definieron una expresión (**ecuación 2**) para el Hamiltoniano en la que el tratamiento de las interacciones entre electrones queda recluido en un solo término. Este término —función de la densidad electrónica— es el llamado funcional de intercambio-correlación (*exchange-correlation functional*, XC).

$$\left(-\frac{\hbar^2}{2m}\nabla^2 + \hat{V} + \hat{V}_H + \hat{V}_{XC}\right)\varphi_i = \varepsilon_i\varphi_i \qquad (2)$$

Aunque no existe una expresión analítica para el funcional de intercambio correlación, hasta el momento se han formulado diferentes aproximaciones. La aproximación de gradiente generalizada (*Generalized Gradient Approximation*, GGA) tiene en cuenta tanto la densidad electrónica como su gradiente, y es una de las más utilizadas en el estudio de materiales a través de cálculos DFT.[13] Los funcionales GGA presentan una elevada precisión para el bajo coste computacional que lleva asociado su uso, siendo uno de los funcionales más conocidos el desarrollado por Perdew, Burke y Ernzerhof (PBE).[14] No obstante,

aunque los cálculos realizados utilizando funcionales como el PBE puedan ser adecuados para definir ciertos sistemas, están lejos de ser exactos.

En los cálculos realizados con funcionales GGA, la interacción de un electrón con su propia densidad (*self-interaction*) es una de las mayores fuentes de inexactitud. Una consecuencia de este error es la excesiva deslocalización electrónica, que da lugar a resultados equivocados cuando se estudian óxidos de metales de transición como el NiO[15] o el MnO_2.[16] Los funcionales GGA suelen dar una descripción de la estructura electrónica que no se corresponde con la realidad para materiales que presentan electrones *d* y *f* con una alta correlación. En otras palabras, los cálculos GGA predicen un comportamiento metálico en sistemas que son aislantes o semiconductores.[17-19]

Con el objetivo de mejorar la familia GGA, se añade un parámetro que tiene en cuenta la energía cinética, dando lugar a los funcionales meta-GGA. En 2015 Sun *et. al.* construyen un nuevo funcional meta-GGA: el SCAN[20] (*Strongly Constrained and Appropriately Normed*). El funcional SCAN satisface los 17 límites (*constraints*) que un funcional puede cumplir. Los 17 *constraints* podrían describirse como «condiciones» que pueden satisfacer los potenciales de intercambio y correlación utilizados en los funcionales. Si un funcional cumple estos «requisitos» dará, *a priori,* resultados más cercanos a la realidad; aunque esto no significa que dicho funcional sea válido para el estudio de cualquier material. El funcional SCAN ha demostrado ser más eficiente que el PBE en la predicción de la energía de formación de defectos en semiconductores,[21] en el estudio de superficies metálicas,[22] en la predicción de propiedades del estado fundamental de materiales magnéticos[23] y en la predicción de parámetros estructurales y del valor del band gap para óxidos de metales de transición con estructura tipo perovksita.[24] En esta tesis se utiliza el funcional SCAN para el estudio de todos los óxidos mixtos considerados.

A pesar de las mejoras asociadas al uso del funcional SCAN frente al PBE, en los meta-GGA sigue estando presente el error de auto interacción. Para solventar este problema, existen los funcionales híbridos, que incluyen una fracción de intercambio exacto obtenido a partir de métodos HF. La introducción de intercambio exacto mejora la descripción de los efectos de intercambio-correlación frente a los funcionales GGA y meta-GGA. Los funcionales híbridos dan como resultado valores de band gap más cercanos a los reales, aunque esta mejora en

la predicción de propiedades electrónicas conlleva un elevado coste computacional. En este trabajo se utiliza el funcional HSE06[25] para el análisis de la familia $Sr_{2-x}Ba_xTa_2O_7$. Los cálculos realizados con HSE06 son más lentos y consumen más recursos computacionales que aquellos realizados con SCAN o PBE.

La elección de la metodología DFT adecuada para explorar cada material es uno de los objetivos fundamentales de esta Tesis. Perdew y Schmidt definieron la escalera de Jacob (**figura 1.3**) para alcanzar la precisión química (*chemical accuracy*).[26, 27] Debe existir un método perfecto, válido para todos los sistemas, que resuelva la ecuación de Schrödinger sin utilizar ninguna aproximación. A partir de esta idea, cada peldaño de la escalera de Jacob estaría ocupado por una familia de funcionales que incluye más información física que el anterior.

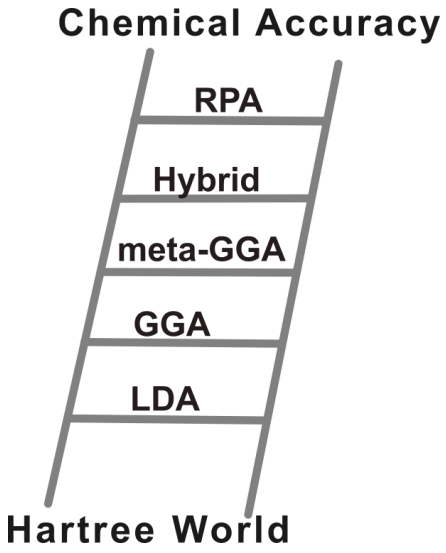

Figura 1.3: Escalera de Jacob de DFT. Adaptada de [27].

Existe otra metodología capaz de mejorar la predicción y descripción de sistemas altamente correlacionados. El método DFT+*U*, desarrollado en la década de 1990, incorpora un tratamiento explícito de las interacciones atómicas a través de un modelo de Hubbard.[28, 29] Esta metodología no va ligada a ningún funcional de intercambio-correlación, sino que puede añadirse a PBE (PBE+*U*) o SCAN (SCAN+*U*). El parámetro *U* de Hubbard permite el tratamiento independiente de los electrones *d* y *f*, separado de aquellos *s* y *p*. Este enfoque evita la excesiva deslocalización electrónica del método DFT. Tanto la metodología PBE+*U* como la SCAN+*U* se emplean en esta tesis doctoral. A pesar de que los resultados obtenidos pueden ser mejores frente a aquellos dados por los funcionales puros,

la elección del parámetro *U* complica el uso de esta metodología, especialmente en sistemas complejos como $YSr_2Cu_2FeO_{7+\delta}$ ($0 < \delta < 1$), en el que podría ser necesario introducir una corrección *U* diferente para cada metal de transición, y para cada valor de δ.

En esta tesis doctoral se aplican funcionales GGA (PBE), meta-GGA (SCAN), sus formas DFT+*U* (PBE+*U*, SCAN+*U*) y un funcional híbrido (HSE06) para el estudio de la familia $Sr_{2-x}Ba_xTa_2O_7$ (un único metal de transición (MT) d^0) y el sistema $YSr_2Cu_2FeO_{7+\delta}$ (dos MT d^n). Como se ha mencionado con anterioridad, ambos materiales presentan una estructura derivada de la pervoskita.

1.2. Perovskitas laminares

El término *Perovskita* engloba a una familia de materiales con fórmula general similar a o derivada de ABX_3. En la celda unidad de las perovskitas cúbicas ABX_3, tomando un cubo como referencia, el átomo A ocupa los 8 vértices del cubo, mientras que B se sitúa en el centro de este, y X ocupa el centro de las caras del cubo (véase la **figura 1.4**). Dentro de esta familia se encuentran los óxidos ABO_3 en los que B es un metal de transición y A es típicamente un catión de mayor tamaño, alcalino o alcalinotérreo.[30] La flexibilidad estructural y composicional de estos óxidos, así como la variedad de propiedades que presentan, los convierten en materiales candidatos para diversas aplicaciones en el campo de la energía.[31]

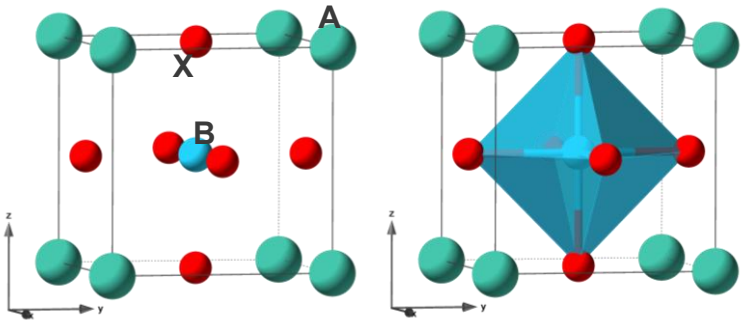

Figura 1.4: Celda unidad de una perovskita cúbica.

En general, las perovskitas presentan una amplia variedad estructural, siendo posible la sustitución de los cationes A o B, o la incorporación de varios cationes A y/o B dentro de la misma estructura. La organización de los cationes que componen la perovskita puede dar lugar a la formación de estructuras laminares, compuestas por capas tipo perovskita. Cuando existe un orden en los módulos o capas de perovskita, se forman fases homólogas. Estos compuestos en capas

pueden agruparse en diferentes familias (véase la **tabla 1.1**) en función de la orientación relativa de la capa de perovskita respecto al eje principal de una perovskita ideal.[32] Los materiales $Sr_{2-x}Ba_xTa_2O_7$ ($0 \leq x \leq 1$) estudiados en esta tesis, presentan tipos estructurales Dion-Jacobson y $Ca_2Nb_2O_7$ (**figura 1.5**).

Tabla 1.1: Clasificación de perovskitas en capas en función de la orientación de la capa de perovskita respecto al eje principal de una perovskita ideal y del desplazamiento respecto a las capas vecinas (adaptada de [32]).

Nombre	Fórmula	Orientación	Vector desplazamiento[a]
Ruddlesden – Popper	$A_{n+1}B_nO_{3n+1}$	$[100]_p$	$(a_p + b_p)/2$
Dion – Jacobson	$A'A_{n-1}B_nO_{3n+1}$	$[100]_p$	0 (Tipo I); a/2 (Tipo II); $(a_p + b_p)/2$ (Tipo III)
Aurivillius	$(Bi_2O_2)^{2+}(A_{n-1}B_nO_{3n+1})^{2-}$	$[100]_p$	$(a_p + b_p)/2$
Fases - $Ca_2Nb_2O_7$	$A_nB_nO_{3n+2}$	$[110]_p$	$(a_p + b_p)/2$

[a] a_p y b_p son los vectores de la celda unidad cúbica.

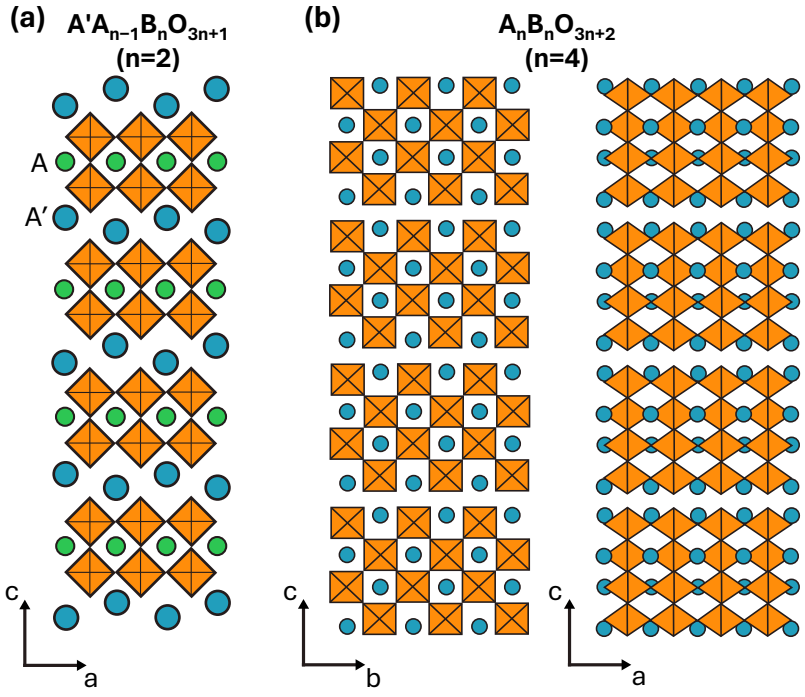

Figura 1.5: (a) Perovskita laminar perteneciente a la familia Dion-Jacobson de fórmula general $A'A_{n-1}B_nO_{3n+1}$ (n=2). Color: A' en azul, A en verde, B en naranja. (b) Perovskita laminar perteneciente a la familia Fases - $Ca_2Nb_2O_7$ de fórmula general $A_nB_nO_{3n+1}$ (n=4). Color: A en azul, B en naranja. Adaptada de [32].

Otro tipo de estructuras formadas por capas relacionadas con las perovskitas son aquellas derivadas de $YBa_2Cu_3O_{7-\delta}$ (YBCO) (**figura 1.6**). Este compuesto pertenece al grupo de cupratos superconductores, cuya estructura se puede definir a través del apilamiento vertical de tres bloques de perovskita cúbica deficientes en oxígeno. Y y Ba ocupan de forma alterna las posiciones A, mientras que las posiciones B están ocupadas por Cu. En estas estructuras se pueden distinguir dos tipos de iones Cu, el denominado Cu(1) que ocupa los llamados bloques de reserva de carga, y el Cu(2) que forma los bloques superconductores. La fase $YBa_2Cu_3O_7$ puede perder oxígeno, llegando hasta la composición $YBa_2Cu_3O_6$. Esta evolución va ligada al cambio de coordinación de los cationes Cu(1), que varía desde plano cuadrada ($YBa_2Cu_3O_7$) hasta una coordinación lineal ($YBa_2Cu_3O_6$).

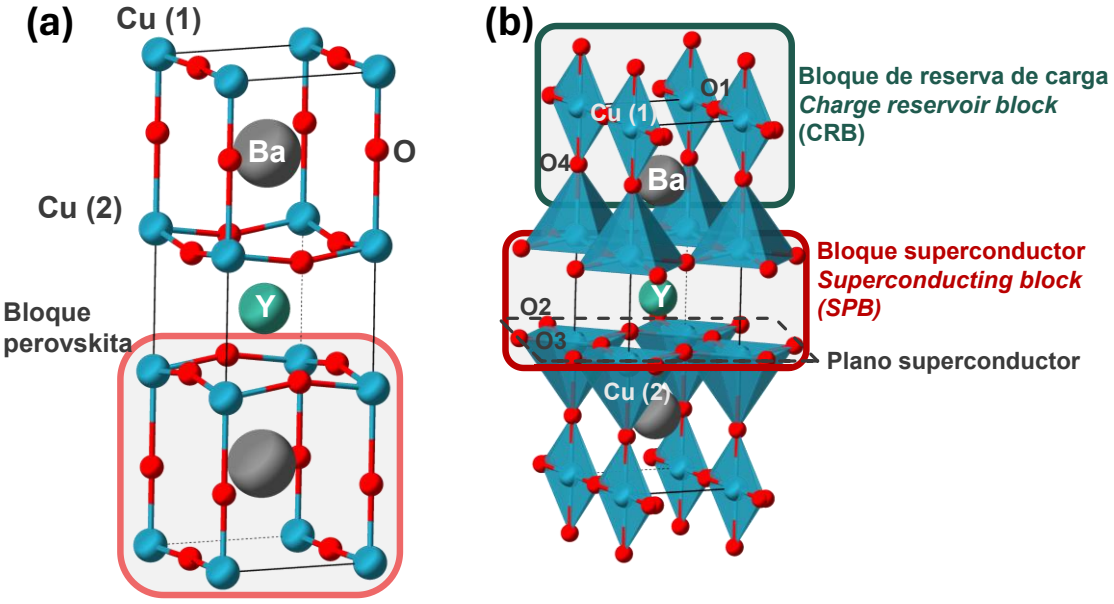

Figura 1.6: Celda ideal de $YBa_2Cu_3O_7$ sobre la que se indica: (a) el bloque de perovskita cúbica contenido en la celda unidad y (b) los bloques de reserva de carga y superconductor, así como los poliedros de coordinación de Cu(1) y Cu(2). También se indica el plano superconductor. Color: Cu en azul, Ba en gris, Y en verde y O en rojo. El bloque de reserva de carga aparece marcado en verde y el bloque superconductor en rojo.

Atendiendo a la estructura descrita, los cupratos derivados de YBCO presentan no-estequiometría de oxígeno. Esta condición, sumada a la posible sustitución de los cationes Y o Cu, resulta en la existencia de estructuras complejas con capas tipo perovskita en las que pueden existir varios metales de transición con estados de oxidación variables. Dentro de esta familia de cupratos superconductores se encuentra el sistema $YSr_2Cu_2FeO_{7+\delta}$ ($0 < \delta < 1$) (YSCFO).[33]

El óxido mixto YSCFO es uno de los materiales centrales de esta tesis doctoral. Por ello, en el **anexo I** se dedican unas palabas a la estructura electrónica de cupratos como $YBa_2Cu_3O_{7-\delta}$, en los que las propiedades electrónicas dependen del contenido en oxígeno.

En las siguientes secciones se recogen los antecedentes experimentales y computacionales para los dos óxidos mixtos con estructura derivada de la pervoskita que se han estudiado en la presente tesis doctoral.

1.3. Generación de H_2: Fotocatalizadores Ba-Sr-Ta-O

El hidrógeno es el elemento químico más abundante del universo. Debido a su alto valor ascensional, que hace imposible que exista aislado en la atmósfera terrestre, en la naturaleza se encuentra combinado con otros elementos químicos. Los métodos para la generación de hidrógeno molecular pueden clasificarse en dos grandes grupos encontrándose, por un lado, la producción a partir de combustibles fósiles y, por otro lado, la producción utilizando fuentes renovables (**figura 1.7**).[34] Actualmente, el 96% del hidrógeno producido a nivel mundial proviene de fuentes no renovables.[34, 35] Concretamente, las formas más comunes de producción de hidrógeno a partir de combustibles fósiles son el reformado de hidrocarburos y la pirolisis. Según la materia prima de partida, el hidrógeno producido utilizando combustibles fósiles se obtiene en un 47% a partir de gas natural, en un 27% a partir de carbón y en un 22% a partir de petróleo.[35]

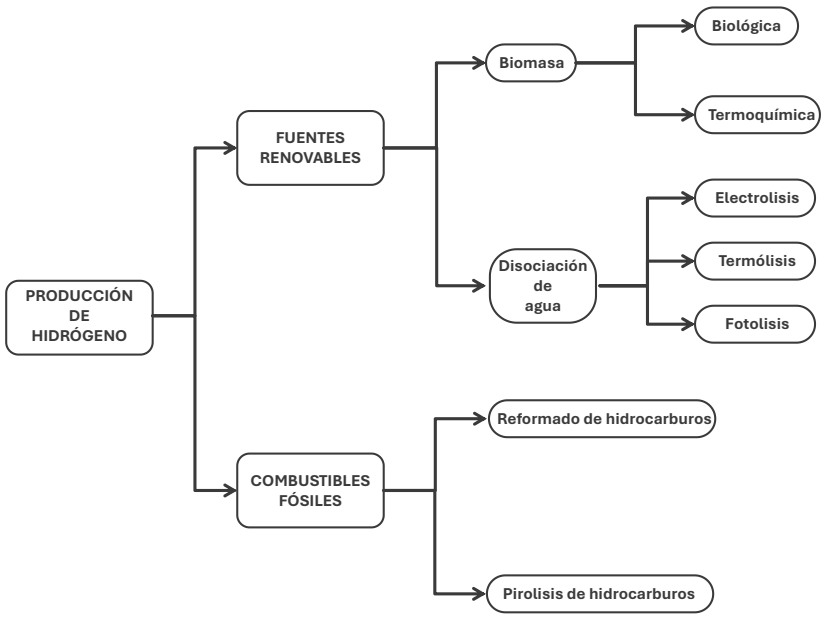

Figura 1.7: Métodos de producción de hidrógeno. Adaptada de [34].

El progreso hacia un sistema energético descarbonizado, flexible y eficiente se sustenta, entre otras, en tecnologías de producción de hidrógeno verde. El hidrógeno verde es aquel generado a partir de energías renovables.[36, 37] A pesar de que es posible obtener hidrógeno verde utilizando biomasa, la forma de producción más explorada es la disociación de la molécula de agua (*water splitting*). Entre las opciones disponibles para llevarla a cabo (**figura 1.7**), el método más utilizado emplea energía eléctrica (electrolisis). Sin embargo, pueden usarse otras fuentes de energía, como son la energía térmica (termólisis) o la energía fotónica (fotolisis).[38] En el caso de la fotolisis, se requiere la utilización de catalizadores eficientes en la región de emisión solar del espectro electromagnético, denominándose el proceso fotocatálisis.

La fotocatálisis es un fenómeno de superficie que tiene lugar en la interfase entre un material fotocatalizador y el electrolito que, en este caso, es agua. Los fotocatalizadores son materiales semiconductores que, al ser irradiados con luz solar, son capaces de absorber fotones, provocando la promoción de electrones desde la banda de valencia (BV) a la banda de conducción (BC). Este proceso también da lugar a la creación de huecos en la BV (**figura 1.8**).

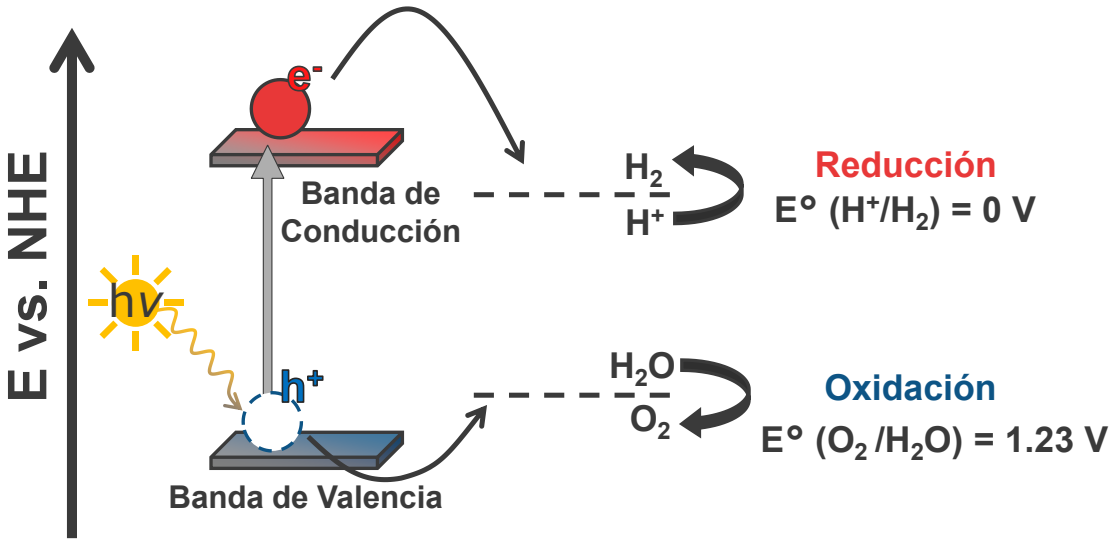

Figura 1.8: Esquema simplificado del proceso electrónico que tiene lugar durante la fotocatálisis de la disociación de la molécula de agua. Los huecos creados en la BV aparecen representados como h^+, mientras que los electrones promovidos a la BC aparecen como e^-.

Para que un material sea un buen fotocatalizador debe cumplir algunos requisitos fundamentales.[39, 40] Entre dichos requisitos se encuentran los siguientes:

1) El mínimo de la BC debe de estar por encima del potencial de reducción H^+/H_2, que equivale a 0 eV.
2) El máximo de la BV debe de encontrarse por debajo del potencial de la semirreacción de oxidación H_2O/O_2, que equivale a -1,23 eV.
3) La absorción de fotones procedentes de la luz solar tiene que ser efectiva. La luz solar está compuesta por un 7,2% de radiación ultravioleta (UV), un 45,6% de radiación infrarroja (IR) y un 47,2% de radiación visible (Vis). La energía de los fotones procedentes de la luz UV se encuentra entre 3,1 y 12 eV, mientras que la energía de la luz visible está entre los 1,6 y 3,1 eV. Lo ideal es que se absorban los fotones procedentes del visible, ya que la fracción de radiación UV es escasa, y la absorción de fotones en el IR es poco eficiente debido a su baja energía. Sin embargo, la mayoría de los fotocatalizadores absorben radiación UV-Vis.
4) Presentar alta estabilidad y resistencia a la corrosión.
5) Ser de bajo coste y tener una alta disponibilidad.

El proceso de disociación fotocatalítica directa de la molécula de agua puede descomponerse en distintos subprocesos que tienen lugar en diferentes escalas temporales. Estos procesos incluyen la absorción del fotón o fotones, la separación de la pareja electrón-hueco (excitón), o la difusión de los portadores de carga, entre otros.[41] Por todo esto, se debe destacar que la consecución de los requisitos mencionados no asegura que el material sea un buen fotocatalizador, puesto que aspectos como, por ejemplo, la naturaleza del band gap o la morfología del material también influyen directamente en la actividad catalítica.[42] No obstante, teniendo en cuenta los requisitos 1-3 mencionados anteriormente, y que la energía que absorberá el material fotocatalizador debe ser mayor o igual que el valor del band gap que presente, se puede definir que, para aprovechar al máximo la radiación visible, el band gap del material debería encontrarse entre 1,23 y 3,10 eV.

Existen diversos ejemplos de materiales fotocatalizadores utilizados en fotocatálisis directa que absorben la radiación UV.[42] Uno de los fotocatalizadores más estudiados —usado como material de referencia— es el TiO_2, un óxido de

metal de transición d^0, cuyo band gap es 3,2 eV. Debido a que, por su valor de band gap, sólo absorbe radiación UV, se han abordado numerosas estrategias para mejorar sus prestaciones.[39, 43, 44] Por otro lado, existen óxidos mixtos de titanio como el $SrTiO_3$ que han demostrado poseer una buena actividad fotocatalítica al combinarse con co-catalizadores metálicos.[45] El $SrTiO_3$ posee una estructura tipo perovskita ABO_3. De hecho, los óxidos de metales de transición d^0 con estructura tipo perovskita son una de las familias de materiales más estudiadas para la generación de hidrógeno a partir de agua.[46, 47] Teniendo en cuenta sus prometedoras prestaciones fotocatalíticas, en esta tesis se estudian los óxidos de tántalo $Sr_{2-x}Ba_xTa_2O_7$ ($0 \leq x \leq 1$), que presentan estructuras derivadas de la perovskita.

a. Antecedentes Experimentales en Ba-Sr-Ta-O

Se ha probado que algunos óxidos mixtos de tántalo, con estructura derivada de la perovskita, como $MTaO_3$ (M = Li, Na, K) o MTa_2O_6 (M= Sr, Ba, Sn, Ni, Mn, Co), poseen actividad fotocatalítica para la producción de hidrógeno a partir de agua.[39] Los valores de producción van desde 960 µmol g^{-1} h^{-1} de H_2 para el $SrTa_2O_6$, hasta 1980 µmol g^{-1} h^{-1} de H_2 en el caso de $NaTaO_3$.[48] Entre los óxidos mixtos de tántalo estudiados se encuentra $Sr_2Ta_2O_7$. Este compuesto posee una estructura laminar formada por capas tipo perovskita (véase $Ca_2Nb_2O_7$ en **tabla 1.1**)[49] y destaca por la posición de su BC, que favorece la reacción de evolución de hidrógeno (**figura 1.9**).[50] Debido al valor del band gap (4,6 eV), la actividad fotocatalítica ocurre en la región del UV. Se ha demostrado que este material puede fotocatalizar la electrolisis de agua, con valores de producción de H_2 de 52 µmol g^{-1} h^{-1} y 1000 µmol g^{-1} h^{-1}, en ausencia y presencia de NiO, respectivamente.[50] Se ha propuesto que la sustitución parcial de Sr por Ba, que da lugar a la familia $Sr_{2-x}Ba_xTa_2O_7$ ($0 \leq x \leq 0.3$), mejora la actividad fotocatalítica del material.[51]

Por otro lado, dentro de la familia Ba-Sr-Ta-O se ha sintetizado el compuesto $BaSrTa_2O_7$,[52] que cristaliza en una estructura en capas tipo perovskita perteneciente a la familia Dion-Jacobson (**figura 1.5a**). Sin embargo, aunque la estructura cristalina es conocida y, a pesar de su similitud con $Sr_2Ta_2O_7$, al comienzo de esta tesis doctoral, no se conocía información sobre la posible actividad fotocatalítica de $BaSrTa_2O_7$ para la producción de oxígeno a partir de agua.

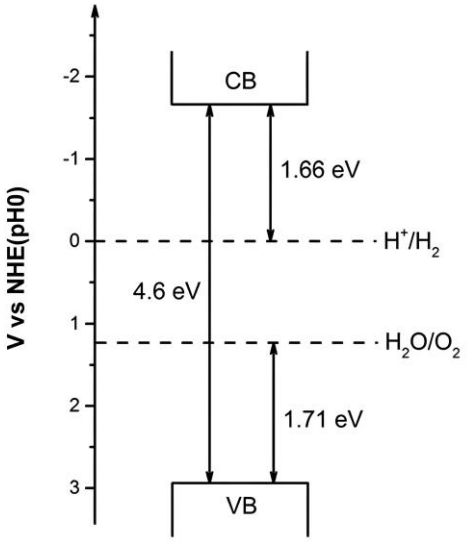

Figura 1.9: Posición de la BV y la BC de $Sr_2Ta_2O_7$ respecto a los potenciales redox del agua.[53]

b. DFT en el estudio de Ba-Sr-Ta-O

La utilidad de los cálculos DFT para el estudio de fotocatalizadores queda patente en el caso del TiO_2.[54] A través de la metodología DFT se ha estudiado, por ejemplo, cómo afecta la introducción de distintos MT a la posición de las bandas de valencia y de conducción de este óxido,[44] o por qué la introducción de Al y Cu mejora su actividad fotocatalítica.[55] Otro ejemplo de la utilización de cálculos DFT para el estudio de fotocatalizadores es el caso de $SrTiO_3$,[39] para el que se ha analizado a través de cálculos GGA y GGA+*U* el efecto que provoca la sustitución parcial de Ti con Co a la posición de la BV y la BC respecto a los potenciales redox del agua.[56]

En cuanto a la familia estudiada en este trabajo $Sr_{2-x}Ba_xTa_2O_7$, existen investigaciones computacionales que han explorado el uso de NiO como co-catalizador en $Sr_2Ta_2O_7$.[57] La metodología DFT también se ha empleado para investigar la actividad OER en superficies de $Sr_2Ta_2O_7$.[58] Además, se ha analizado el efecto que provoca la sustitución simultánea de Ta por V/Nb y de O por S en la estructura electrónica del material, demostrándose que el co-dopaje V-S y Nb-S permite mejorar la posición de las bandas de valencia y de conducción respecto al material puro $Sr_2Ta_2O_7$.[53] Con respecto a la estructura tipo Dion-Jacobson $BaSrTa_2O_7$,[52] hasta donde sabemos, no existen estudios computacionales centrados en esta fase.

1.4. Utilización de H_2: Electrodos de aire para SOFC basados en YBCO

Como se indica en la **figura 1.1**, el hidrógeno puede utilizarse en múltiples sectores, abarcando diferentes aplicaciones. Esta tesis se enmarca en la configuración P2P, donde el hidrógeno (idealmente verde) se utiliza en una celda de combustible para producir energía eléctrica y agua como único subproducto. La disposición P2P es, por lo tanto, cíclica, y la electricidad producida en la celda de combustible podría utilizarse de nuevo en la producción de H_2. Desde el punto de vista del almacenamiento de energía, este enfoque puede resultar especialmente útil, ya que en caso de que disminuya la producción de electricidad a partir de las fuentes renovables, la celda de combustible puede suplir dicha carencia de energía eléctrica, que se empleará en producir de nuevo H_2 a través de la electrolisis de agua.[59]

Las celdas de combustible transforman directamente la energía química en energía eléctrica. Existe una amplia variedad de celdas de combustible atendiendo, por ejemplo, al tipo de material o materiales por los que están formadas, al combustible utilizado o a su temperatura de operación.[60] Dentro de las celdas de combustible se incluyen las de óxido sólido (*Solid Oxide Fuel Cell*, SOFC), que operan a temperaturas que oscilan entre 650 y 1000°C. Las SOFC presentan varias ventajas sobre otro tipo de celdas, como su alta eficiencia de conversión.[61, 62] La **figura 1.10a** muestra un esquema del funcionamiento de una celda de combustible de óxido sólido, en la que la reacción de reducción del oxígeno (*Oxygen Reduction Reaction*, ORR) tiene lugar en el cátodo o electrodo de aire, y la reacción de oxidación del hidrógeno (*Hydrogen Oxidation Reaction*, HOR) se produce en el ánodo. En este tipo de celdas, el electrolito debe permitir la movilidad de iones óxido desde el cátodo o electrodo de aire hasta el ánodo, mientras bloquea el paso de electrones.

Para que en el electrodo de aire o cátodo se produzca la reacción ORR es fundamental que el material utilizado presente las propiedades conductoras adecuadas. De acuerdo con la **figura 1.10b**, existen diferentes procesos involucrados en la reacción de reducción de oxígeno, como son la adsorción y posterior disociación del O_2, y el transporte del oxígeno adsorbido hasta la interfase cátodo/electrolito.[63] La reacción entre el O_2 y los electrones transferidos al cátodo ocurre en las regiones conocidas como puntos triples de fase (*Triple*

Phase Boundary, TPB), donde coexisten físicamente y están en contacto activo el O_2, el material del cátodo y el electrolito, permitiendo la transferencia de carga y la electrocatálisis.

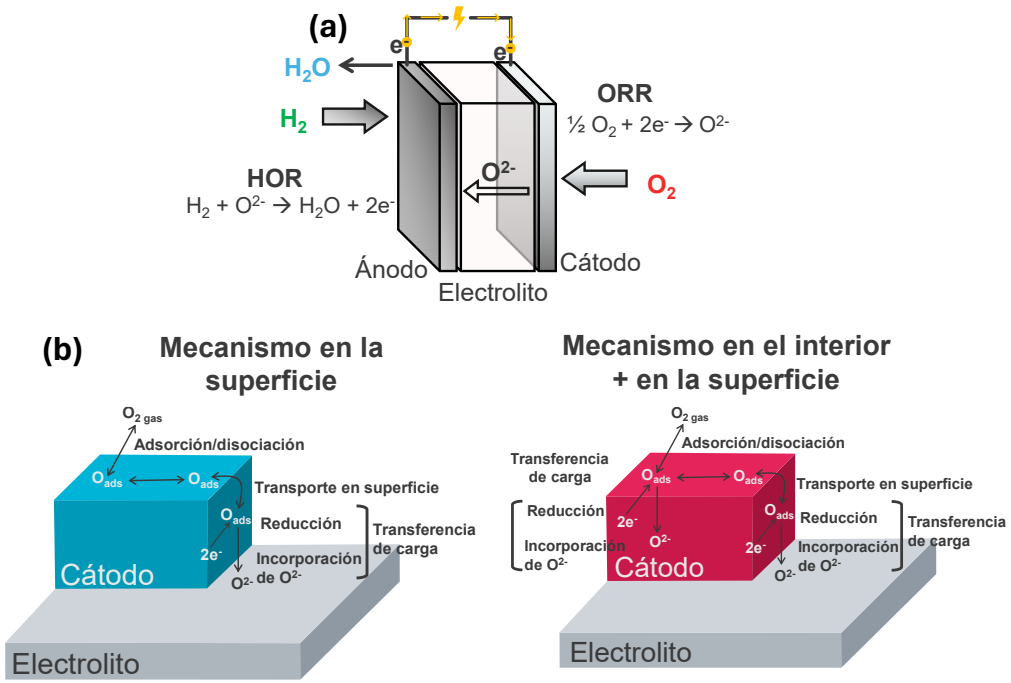

Figura 1.10: (a) Esquema de una celda de combustible de óxido sólido. (b) Esquema de los pasos de reacción que se producen durante la ORR, mostrando los posibles caminos para un material de electrodo que presenta solamente conductividad eléctrica (azul), frente a un material de electrodo que presenta conductividad mixta (rojo). Adaptada de [63].

Si el material utilizado en este electrodo presenta una alta conductividad iónica, el transporte de oxígeno no ocurrirá únicamente en la superficie del material, sino que podrá producirse a través de su interior (*bulk*), acelerando así la cinética de la reacción. Por lo tanto, es deseable que el material empleado en el cátodo presente alta conductividad electrónica y alta conductividad iónica (*Mixed ionic-electronic conductivity*, MIEC). Además, el material debe ser estable a la temperatura de operación de la celda y no reaccionar con sus otros componentes. Otro aspecto que debe considerarse es que el material utilizado como electrodo de aire posea un valor del coeficiente de expansión térmico (*Thermal Expansion Coefficient*, TEC) similar al resto de los componentes del dispositivo.

a. Antecedentes Experimentales en YSCFO

Uno de los materiales más utilizados típicamente como electrodo de aire en SOFC es la perovskita $La_{1-x}Sr_xMnO_{3-\delta}$ (LSM), que ha sido considerada durante

mucho tiempo material de referencia, ya que, entre otras particularidades, presenta una elevada conductividad electrónica y es estable en las condiciones de operación de las SOFC.[64, 65, 66] Por ello, un punto de partida para el diseño de nuevos materiales que puedan actuar como electrodo de aire en las celdas de combustible de óxido sólido comienza con la búsqueda de compuestos que compartan propiedades estructurales, composicionales y/o electrónicas con el LSM.[62, 66, 67] Este es el caso de óxidos como $La_{1-x}Sr_xCoO_{3-\delta}$ (LSC) o $La_{1-x}Sr_xCo_{1-y}Fe_yO_{3-\delta}$ (LSCF).[64] Los óxidos basados en cobalto presentan una elevada actividad catalítica, pero también muestran importantes desventajas, como valores TEC incompatibles con los de electrolitos típicos.[68] Este hecho, sumado a la baja disponibilidad del Co, ha dirigido la atención de la investigación hacia óxidos formados por metales de transición más abundantes. Los compuestos derivados de YBCO cumplen con esta premisa.[69]

El sistema $YSr_2Cu_2FeO_{7+\delta}$ ($0 < \delta < 1$)[70-72] se ha estudiado como potencial electrodo de aire en pilas de combustible de óxido sólido.[33, 73] Este sistema se deriva del YBCO a través del dopaje con Sr en la posición A, sustituyendo parcialmente el Y, y con Fe en la posición B, sustituyendo parcialmente los cationes Cu. La estructura de los dos extremos ideales del sistema se representa en la **figura 1.11**. Los iones Fe presentes en los planos $FeO_{1+\delta}$ pueden variar su coordinación, pasando de octaedros en el extremo ideal $YSr_2Cu_2FeO_8$ a tetraedros en la fase reducida $YSr_2Cu_2FeO_7$. Es importante mencionar que el Fe presenta una preferencia por ocupar las posiciones Cu(1) (mostrado para YBCO en la **figura 1.6**), aunque se ha reportado la existencia de *antisite* en varias fases del sistema,[71, 72, 74-76] si bien el grado de desorden es menor a menores contenidos de oxígeno.[33, 73]

Como ocurre en otros cupratos, las complejas propiedades electrónicas y magnéticas del YSCFO están íntimamente ligadas al contenido en oxígeno y este, a su vez, a las condiciones de síntesis. Las fases con alto contenido en oxígeno como $YSr_2Cu_2FeO_{7.85}$ —con estados de oxidación formales Fe^{4+} y Cu^{3+}/ Cu^{2+}—, presentan un comportamiento metálico y superconductor (T_c = 70 K).[77] Para estos materiales, se ha observado que la existencia de superconductividad depende en gran medida del procedimiento de síntesis y de la distribución de los cationes de Fe y Cu.[70]. Las fases de bajo contenido en oxígeno (como $YSr_2Cu_2FeO_{7.11}$[71]) son aislantes, habiéndose descrito durante el desarrollo de esta tesis doctoral propiedades magnéticas de la fase $YSr_2Cu_2FeO_{7.08}$.[78]

A composiciones intermedias, López-Paz *et. al.* reportaron, a partir de medidas de conductividad, que la fase $YSr_2Cu_2FeO_{7.56}$ es un conductor tipo *p*, produciéndose en el sistema YSCFO una disminución de los huecos al aumentar la temperatura,[73] una observación que coincide con la realizada previamente por Sansom y colaboradores en un compuesto de contenido de oxígeno similar ($YSr_2Cu_2FeO_{7.42}$).[33] Un mayor contenido en oxígeno en los planos $FeO_{1+\delta}$ significa un mayor número de huecos en la banda formada por los estados Cu-Fe 3*d* y O 2*p*.[77, 79]

Además de las propiedades electrónicas, la conductividad iónica del sistema $YSr_2Cu_2FeO_{7+\delta}$ es vital para su aplicación como cátodo en SOFC. Para los compuestos de contenidos de oxígeno intermedios, los átomos de Fe pueden adoptar coordinación octaédrica, de pirámide de base cuadrada y/o tetraédrica. Se ha propuesto que la presencia de vacantes en la red aniónica facilita la difusión de iones óxido dentro de la estructura.[30]

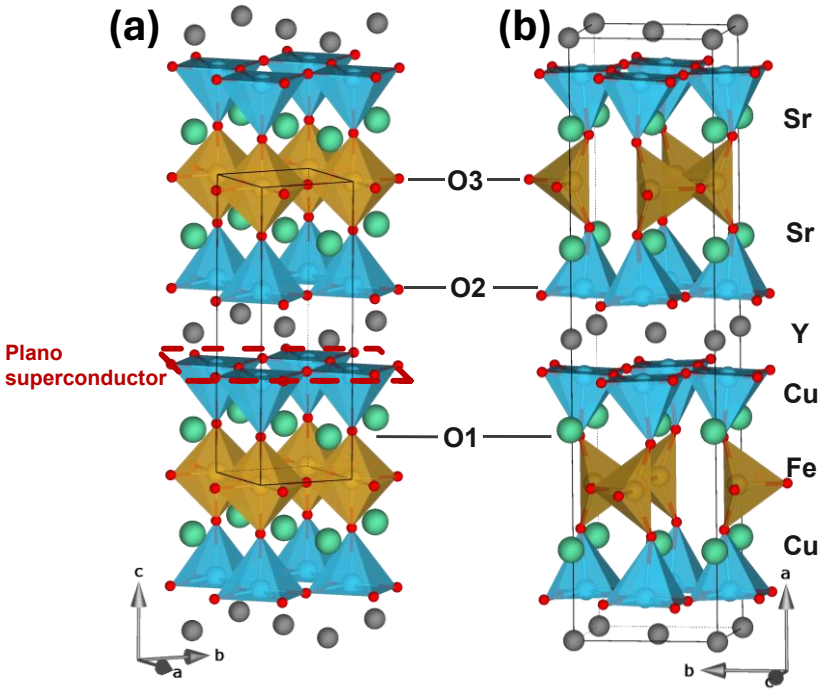

Figura 1.11: Estructura de las fases ideales (a) $YSr_2Cu_2FeO_8$ y (b) $YSr_2Cu_2FeO_7$ pertenecientes al sistema $YSr_2Cu_2FeO_{7+\delta}$ ($0 < \delta < 1$). Se indican los tres tipos de oxígenos presentes en la estructura y el plano superconductor. Color: Sr en verde, Y en gris, Cu en azul, Fe en marrón y O en rojo.

Con respecto a las posibles aplicaciones de $YSr_2Cu_2FeO_{7+\delta}$, sólo se han estudiado los términos $\delta = 0{,}42$[33] y 0,56.[73] Sansom *et. al.* descartan este material debido a la histéresis observada al evaluar la variación de la conductividad con la

presión parcial de oxígeno.[33] Más recientemente, el trabajo desarrollado por López-Paz *et. al.*[73], subraya el interés del material. En la **figura 1.12** se muestran medidas de resistencia de polarización en superficie (*Area Specific Resistance*, ASR) en celdas simétricas $YSr_2Cu_2FeO_{7+\delta}$: CGO | CGO | $YSr_2Cu_2FeO_{7+\delta}$: CGO, que han resultado en valores de ASR de 0.20 Ω cm² y 0.08 Ω cm² a 923 y 973 K, respectivamente.[73]

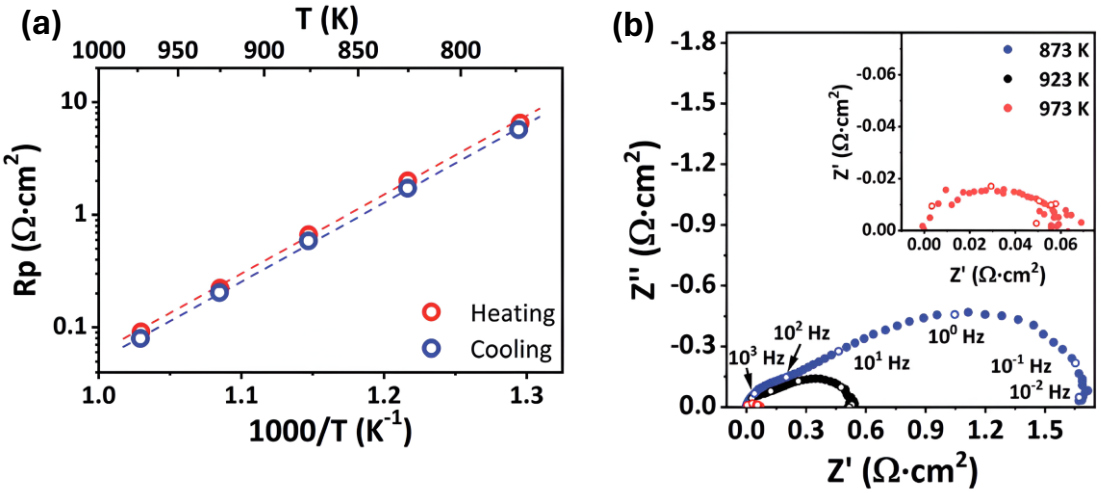

Figura 1.12: (a) Valores de resistencia a la polarización del electrodo frente a la inversa de la temperatura medidos en celdas simétricas $YSr_2Cu_2FeO_{7+\delta}$:CGO | CGO | $YSr_2Cu_2FeO_{7+\delta}$:CGO. (b) Diagramas de impedancia de celdas simétricas a 873 K (azul), 923 K (negro) y 973 K (rojo).[73]

b. DFT en el estudio de YSFCO

La búsqueda de materiales que puedan integrarse en dispositivos como las SOFC se ha visto multiplicada en los últimos años.[61, 66] En este contexto, se ha demostrado que las propiedades MIEC son fundamentales para que un material actúe de forma eficiente como electrodo de aire en una celda de combustible de óxido sólido. Esta conductividad mixta puede modularse con el fin de mejorar las prestaciones de los materiales, cuya estructura es comúnmente derivada de la perovskita.

Los cálculos DFT pueden acelerar el diseño de nuevos electrodos de arie para SOFC, ya que esta metodología permite comprender los principios estructurales, electrónicos y composicionales que están detrás de la conductividad electrónica e iónica de los materiales. Sin embargo, en comparación con el número de trabajos experimentales, los estudios computacionales resultan escasos.[61] Como se discutirá a lo largo de esta tesis doctoral, la alta complejidad electrónica derivada de la existencia de varios MT con configuraciones d^n, así como la existencia de no-

estequiometría de oxígeno, complican el uso de la metodología DFT para el estudio de estos materiales. Teniendo en cuenta que estas particularidades son, precisamente, las que provocan que presente buenas propiedades MIEC, surge la obligatoriedad de utilizar varias metodologías combinadas para lograr una compresión de estos sistemas. Un ejemplo de la combinación de varias metodologías es la investigación llevada a cabo por Muñoz-García y colaboradores. En este estudio, se analizó a través de cálculos PBE+*U* la estructura electrónica, la energía de formación de vacantes y la difusión de oxígeno en las familias $La_{1-x}Sr_xMO_3$ (M = Cr, Mn, Fe, Co) y $Sr_2Fe_{2-x}Mo_xO_6$.[80] La difusión del ion óxido a través de la estructura del material se estudió a través de dinámica molecular clásica (*Classical Molecular Dynamics*, MD). La combinación de DFT y MD también se ha empleado para el estudio del sistema $Sm_{0.75}A_{0.25}Co_{1-x}Mn_xO_{2.88}$ (A = Ca, Sr; x = 0.125, 0.25).[81]

Los cálculos MD permiten simular el movimiento de partículas dentro de un sistema a lo largo del tiempo. La posición de las partículas se calcula a partir de la resolución de las ecuaciones de Newton, mientras que las fuerzas de interacción dentro del sistema se calculan a través de métodos que reciben el nombre de campos de fuerza (*force fields*, FF). No obstante, si se quiere tener en cuenta la estructura electrónica calculada, es necesario recurrir a la dinámica molecular *ab initio* (*Ab initio Molecular Dynamics*, AIMD). La AIMD combina el cálculo DFT de la estructura electrónica del sistema y el cálculo del movimiento de partículas de la dinámica molecular. Esta técnica es más cara computacionalmente que la MD clásica, por lo que se debe trabajar con sistemas con menor número de átomos a tiempos de simulación más cortos. La metodología AIMD se ha utilizado para estudiar algunos materiales empleados como cátodos en SOFC, como los óxidos $PrBaCo_2O_{5+d}$ (PBCO) y $SmBaCo_2O_{5+d}$ (SBCO).[82] En esta tesis se utilizará para estudiar el sistema $YSr_2Cu_2FeO_{7+\delta}$ ($0 < \delta < 1$).

Debe señalarse que la aplicación de cálculos DFT en el estudio de compuestos que contengan metales con electrones *d* y *f* altamente correlacionados no es trivial. Dado que la estructura electrónica tiene una importancia muy significativa en las propiedades de los materiales con capacidad para catalizar reacciones como la ORR, la elección de la metodología adecuada es esencial para predecir y entender las propiedades de los materiales. Como se ha comentado, existen casos de éxito para el meta-GGA SCAN en la descripción o predicción de propiedades de varios óxidos de metales de transición.[83-86] Por otra parte, la

metodología SCAN+*U* también se ha utilizado en el análisis de algunos materiales con potencial aplicabilidad en la generación de energías renovables.[87-92] Sin embargo, ninguno de los ejemplos mencionados para el funcional SCAN incluye óxidos complejos con más de un metal de transición. Esta ausencia en la literatura motivó la investigación del óxido complejo $YSr_2Cu_2FeO_{7+\delta}$ en el marco de esta tesis doctoral.

Por otra parte, recientemente, la predicción de la actividad de óxidos de metales de transición para catalizar OER y ORR se ha visto mejorada por el uso de descriptores electrónicos.[93, 94] Estos descriptores son parámetros numéricos, extraídos directamente de la estructura electrónica calculada para el material, que muestran correlación con propiedades de interés para la catálisis. Uno de los más utilizados es el centro de banda O 2*p*, para el que se ha demostrado una relación lineal con la resistencia específica de superficie (ASR),[95] o la energía de formación de vacantes.[93] Se ha demostrado también que el centro de banda O 2*p* presenta correlación con el coeficiente superficial de intercambio de oxígeno para varios compuestos con aplicabilidad como cátodo en SOFC (**figura 1.13**).[96] Según estos estudios, el centro de banda O 2*p* —definido como el centroide de la densidad de estados parcial calculada para el oxígeno— permite predecir si una perovskita ABO_3 será buen catalizador incluso antes de sintetizarlo. Este hecho ejemplifica el potencial de los cálculos DFT para el diseño de materiales que puedan ser utilizados como electrodos en dispositivos como las SOFC. No obstante, la mayoría de los estudios mencionados se han realizado para perovskitas con un solo metal de transición. Por ello, es necesario realizar estudios centrados en el uso del centro de banda O 2*p* como descriptor electrónico para perovskitas más complejas, o para óxidos con otras estructuras cristalinas.

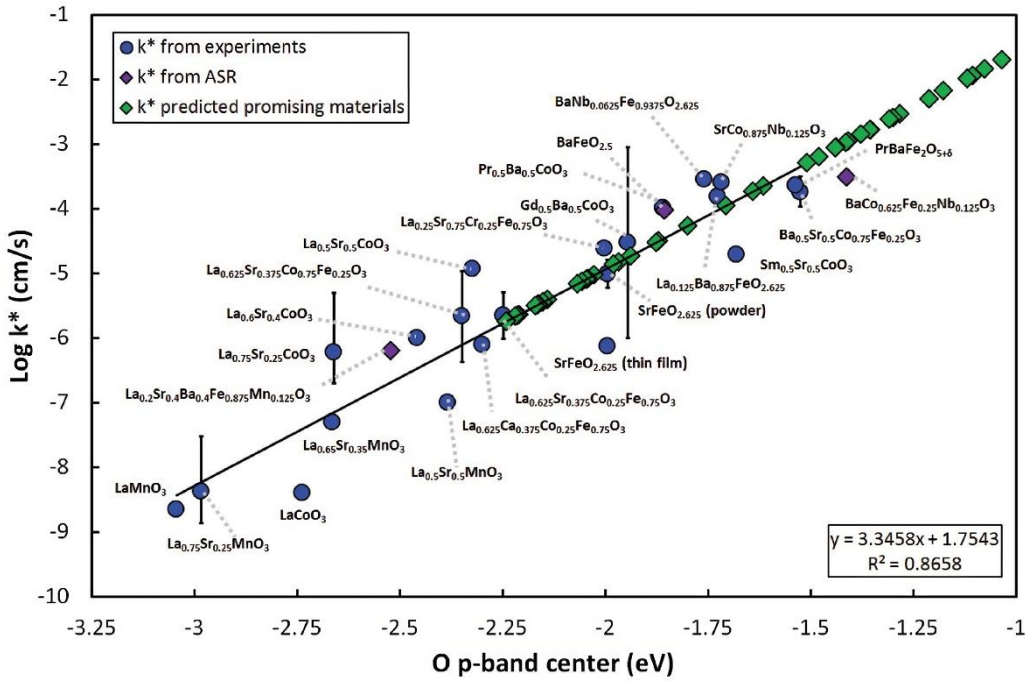

Figura 1.13: Correlación entre el centro de banda O 2*p* — relativo al nivel de Fermi y calculado con PBE+*U*— para óxidos de metales de transición con aplicabilidad como electrodo de aire en SOFC y el coeficiente superficial de intercambio de oxígeno.[96]

Con respecto al sistema $YSr_2Cu_2FeO_{7+\delta}$ ($0 < \delta < 1$), a pesar de que se han llevado a cabo diversos trabajos experimentales que estudian distintas fases del sistema, hasta la fecha de inicio de esta tesis doctoral no existían estudios computacionales.

1.5. Referencias

(1) Ahmad, T.; Zhang, D. A critical review of comparative global historical energy consumption and future demand: The story told so far. *Energy Reports* **2020**, *6*, 1973-1991. DOI: 10.1016/j.egyr.2020.07.020.

(2) Wang, J.; Azam, W. Natural resource scarcity, fossil fuel energy consumption, and total greenhouse gas emissions in top emitting countries. *Geoscience Frontiers* **2024**, *15* (2). DOI: 10.1016/j.gsf.2023.101757.

(3) Hosseini, S. E. Hydrogen fuel, a game changer for the world's energy scenario. *International Journal of Green Energy* **2023**, *21* (6), 1366-1382. DOI: 10.1080/15435075.2023.2244050.

(4) *Heat Values of Various Fuels*. World Nuclear Association, 2020. https://world-nuclear.org/information-library/facts-and-figures/heat-values-of-various-fuels (accessed 2024 06/08/2024).

(5) Evro, S.; Oni, B. A.; Tomomewo, O. S. Carbon neutrality and hydrogen energy systems. *International Journal of Hydrogen Energy* **2024**, *78*, 1449-1467. DOI: 10.1016/j.ijhydene.2024.06.407.

(6) Vidas, L.; Castro, R. Recent developments on hydrogen production technologies: State-of-the-art review with a focus on green-electrolysis. *Applied Sciences* **2021**, *11* (23). DOI: 10.3390/app112311363.

(7) Tao, Q.; Xu, P.; Li, M.; Lu, W. Machine learning for perovskite materials design and discovery. *npj Computational Materials* **2021**, *7* (1). DOI: 10.1038/s41524-021-00495-8.

(8) Liao, X.; Lu, R.; Xia, L.; Liu, Q.; Wang, H.; Zhao, K.; Wang, Z.; Zhao, Y. Density functional theory for electrocatalysis. *Energy & Environmental Materials* **2021**, *5* (1), 157-185. DOI: 10.1002/eem2.12204.

(9) Li, Z.; Zhang, H.; Xu, H.; Xuan, J. Advancing the multiscale understanding on solid oxide electrolysis cells via modelling approaches: A review. *Renewable and Sustainable Energy Reviews* **2021**, *141*. DOI: 10.1016/j.rser.2021.110863.

(10) Bishara, D.; Xie, Y.; Liu, W. K.; Li, S. A state-of-the-art review on machine learning-based multiscale modeling, simulation, homogenization and design of materials. *Archives of Computational Methods in Engineering* **2022**, *30* (1), 191-222. DOI: 10.1007/s11831-022-09795-8.

(11) Hohenberg, P.; Kohn, W. Inhomogeneous electron gas. *Physical Review* **1964**, *136* (3B), B864-B871. DOI: 10.1103/PhysRev.136.B864.

(12) Kohn, W.; Sham, L. J. Self-consistent equations including exchange and correlation effects. *Physical Review* **1965**, *140* (4A), A1133-A1138. DOI: 10.1103/PhysRev.140.A1133.

(13) Marzari, N.; Ferretti, A.; Wolverton, C. Electronic-structure methods for materials design. *Nat Mater* **2021**, *20* (6), 736-749. DOI: 10.1038/s41563-021-01013-3.

(14) Perdew, J. P.; Chevary, J. A.; Vosko, S. H.; Jackson, K. A.; Pederson, M. R.; Singh, D. J.; Fiolhais, C. Atoms, molecules, solids, and surfaces: Applications of the generalized gradient approximation for exchange and correlation. *Phys Rev B Condens Matter* **1992**, *46* (11), 6671-6687. DOI: 10.1103/physrevb.46.6671.

(15) Rohrbach, A.; Hafner, J.; Kresse, G. Molecular adsorption on the surface of strongly correlated transition-metal oxides: A case study for CO/NiO(100). *Physical Review B* **2004**, *69* (7). DOI: 10.1103/PhysRevB.69.075413.

(16) Kitchaev, D. A.; Peng, H.; Liu, Y.; Sun, J.; Perdew, J. P.; Ceder, G. Energetics ofMnO2polymorphs in density functional theory. *Physical Review B* **2016**, *93* (4). DOI: 10.1103/PhysRevB.93.045132.

(17) Sham, L. J.; Schlüter, M. Density-functional theory of the energy gap. *Physical Review Letters* **1983**, *51* (20), 1888-1891. DOI: 10.1103/PhysRevLett.51.1888.

(18) Mori-Sanchez, P.; Cohen, A. J.; Yang, W. Many-electron self-interaction error in approximate density functionals. *J Chem Phys* **2006**, *125* (20), 201102. DOI: 10.1063/1.2403848.

(19) Mori-Sanchez, P.; Cohen, A. J.; Yang, W. Localization and delocalization errors in density functional theory and implications for band-gap prediction. *Phys Rev Lett* **2008**, *100* (14), 146401. DOI: 10.1103/PhysRevLett.100.146401.

(20) Sun, J.; Ruzsinszky, A.; Perdew, J. P. Strongly constrained and appropriately normed semilocal density functional. *Phys Rev Lett* **2015**, *115* (3), 036402. DOI: 10.1103/PhysRevLett.115.036402.

(21) Sun, J.; Remsing, R. C.; Zhang, Y.; Sun, Z.; Ruzsinszky, A.; Peng, H.; Yang, Z.; Paul, A.; Waghmare, U.; Wu, X.; et al. Accurate first-principles structures and energies of diversely bonded systems from an efficient density functional. *Nat Chem* **2016**, *8* (9), 831-836. DOI: 10.1038/nchem.2535.

(22) Patra, A.; Bates, J. E.; Sun, J.; Perdew, J. P. Properties of real metallic surfaces: Effects of density functional semilocality and van der Waals nonlocality. *Proc Natl Acad Sci U S A* **2017**, *114* (44), E9188-E9196. DOI: 10.1073/pnas.1713320114.

(23) Sokolovskiy, V.; Baigutlin, D.; Miroshkina, O.; Buchelnikov, V. Meta-GGA SCAN functional in the prediction of ground state properties of magnetic materials: Review of the current state. *Metals* **2023**, *13* (4). DOI: 10.3390/met13040728.

(24) Paul, A.; Sun, J.; Perdew, J. P.; Waghmare, U. V. Accuracy of first-principles interatomic interactions and predictions of ferroelectric phase transitions in

perovskite oxides: Energy functional and effective Hamiltonian. *Physical Review B* **2017**, *95* (5). DOI: 10.1103/PhysRevB.95.054111.

(25) Heyd, J.; Scuseria, G. E.; Ernzerhof, M. Hybrid functionals based on a screened Coulomb potential. *The Journal of Chemical Physics* **2003**, *118*. DOI: 10.1063/1.1564060.

(26) Perdew, J. P. Jacob's ladder of density functional approximations for the exchange-correlation energy. In AIP Conference Proceedings, 2001.

(27) Perdew, J. P. Climbing the ladder of density functional approximations. *MRS Bulletin* **2013**, *38* (9), 743-750. DOI: 10.1557/mrs.2013.178.

(28) Anisimov, V. I.; Aryasetiawan, F.; Lichtenstein, A. I. First-principles calculations of the electronic structure and spectra of strongly correlated systems: The LDA+*U* method. *Journal of Physics: Condensed Matter* **1997**, *9* (4), 767-808. DOI: 10.1088/0953-8984/9/4/002.

(29) Anisimov, V. V.; Zaanen, J.; Andersen, O. K. Band theory and Mott insulators: Hubbard U instead of Stoner I. *Phys Rev B Condens Matter* **1991**, *44* (3), 943-954. DOI: 10.1103/physrevb.44.943 From NLM PubMed-not-MEDLINE.

(30) Woodward, P. M.; Karen, P.; Evans, J. S. O.; Vogt, T. *Solid State Materials Chemistry*; Cambridge University Press, 2021. DOI: 10.1017/9781139025348.

(31) Monama, G. R.; Ramohlola, K. E.; Iwuoha, E. I.; Modibane, K. D. Progress on perovskite materials for energy application. *Results in Chemistry* **2022**, *4*. DOI: 10.1016/j.rechem.2022.100321.

(32) Tilley, R. J. D. *Perovskites Structure-Property Relationships*; John Wiley & Sons, Ltd, 2016.

(33) Sansom, J. E. H.; Kendrick, E.; Rudge-Pickard, H. A.; Islam, M. S.; Wright, A. J.; Slater, P. R. Synthesis and characterisation of the perovskite-related cuprate phases $YSr_2Cu_2MO_{7+y}$(M = Co, Fe) for potential use as solid oxide fuel cell cathode materials. *Journal of Materials Chemistry* **2005**, *15* (23). DOI: 10.1039/b502641e.

(34) Nikolaidis, P.; Poullikkas, A. A comparative overview of hydrogen production processes. *Renewable and Sustainable Energy Reviews* **2017**, *67*, 597-611. DOI: 10.1016/j.rser.2016.09.044.

(35) Dragassi, M.-C.; Royon, L.; Redolfi, M.; Ammar, S. Hydrogen storage as a key energy vector for car transportation: A tutorial Review. *Hydrogen* **2023**, *4* (4), 831-861. DOI: 10.3390/hydrogen4040051.

(36) Zainal, B. S.; Ker, P. J.; Mohamed, H.; Ong, H. C.; Fattah, I. M. R.; Rahman, S. M. A.; Nghiem, L. D.; Mahlia, T. M. I. Recent advancement and assessment of green hydrogen production technologies. *Renewable and Sustainable Energy Reviews* **2024**, *189*. DOI: 10.1016/j.rser.2023.113941.

(37) Megía, P. J.; Vizcaíno, A. J.; Calles, J. A.; Carrero, A. Hydrogen production technologies: From fossil fuels toward renewable sources. A mini review. *Energy & Fuels* **2021**, *35* (20), 16403-16415. DOI: 10.1021/acs.energyfuels.1c02501.

(38) Gupta, A.; Likozar, B.; Jana, R.; Chanu, W. C.; Singh, M. K. A review of hydrogen production processes by photocatalytic water splitting – From atomistic catalysis design to optimal reactor engineering. *International Journal of Hydrogen Energy* **2022**, *47* (78), 33282-33307. DOI: 10.1016/j.ijhydene.2022.07.210.

(39) Osterloh, F. E. Inorganic Materials as Catalysts for Photochemical Splitting of Water. *Chem. Matter.* **2008**, *20*, 35-54. DOI: 10.1021/cm7024203.

(40) Wang, Z.; Li, C.; Domen, K. Recent developments in heterogeneous photocatalysts for solar-driven overall water splitting. *Chem Soc Rev* **2019**, *48* (7), 2109-2125. DOI: 10.1039/c8cs00542g.

(41) Takanabe, K. Photocatalytic Water Splitting: Quantitative Approaches toward Photocatalyst by Design. *ACS Catalysis* **2017**, *7* (11), 8006-8022. DOI: 10.1021/acscatal.7b02662.

(42) Villa, K.; Galán-Mascarós, J. R.; López, N.; Palomares, E. Photocatalytic water splitting: advantages and challenges. *Sustainable Energy & Fuels* **2021**, *5* (18), 4560-4569. DOI: 10.1039/d1se00808k.

(43) Ijaz, M.; Zafar, M. Titanium dioxide nanostructures as efficient photocatalyst: Progress, challenges and perspective. *International Journal of Energy Research* **2020**, *45* (3), 3569-3589. DOI: 10.1002/er.6079.

(44) Yan, H.; Wang, X.; Yao, M.; Yao, X. Band structure design of semiconductors for enhanced photocatalytic activity: The case of TiO_2. *Progress in Natural Science: Materials International* **2013**, *23* (4), 402-407. DOI: 10.1016/j.pnsc.2013.06.002.

(45) Sakata, Y.; Miyoshi, Y.; Maeda, T.; Ishikiriyama, K.; Yamazaki, Y.; Imamura, H.; Ham, Y.; Hisatomi, T.; Kubota, J.; Yamakata, A.; et al. Photocatalytic property of metal ion added $SrTiO_3$ to Overall H_2O splitting. *Applied Catalysis A: General* **2016**, *521*, 227-232. DOI: 10.1016/j.apcata.2015.12.013.

(46) Sun, K.; Li, Z.; Cao, Y.; Wang, F.; Qyyum, M. A.; Han, N. Recent advancements in perovskite electrocatalysts for clean energy-related applications: Hydrogen production, oxygen electrocatalysis, and nitrogen reduction. *International Journal of Hydrogen Energy* **2024**, *52*, 1104-1126. DOI: 10.1016/j.ijhydene.2023.07.009.

(47) Zhang, G.; Liu, G.; Wang, L.; Irvine, J. T. Inorganic perovskite photocatalysts for solar energy utilization. *Chem Soc Rev* **2016**, *45* (21), 5951-5984. DOI: 10.1039/c5cs00769k.

(48) Kato, H.; Asakura, K.; Kudo, A. Highly efficient water splitting into H_2 and O_2 over Lanthanum-doped $NaTaO_3$ photocatalysts with high crystallinity and surface nanostructure. *J. Am. Chem. Soc* **2003**, *125*, 3082-3089. DOI: 10.1021/ja027751g

(49) Ishizawa, N.; Marumo, F. Compounds with Perovskite-Type Slabs. II. The Crystal Structure of Sr2Ta20. *Acta Cryst. B* **1976**, *132*. DOI: 10.1107/S0567740876008261.

(50) Kudo, A.; Kato, H.; Nakagawa, S. Water Splitting into H_2 and O_2 on New $Sr_2M_2O_7$ (M = Nb and Ta) Photocatalysts with Layered Perovskite Structures: Factors Affecting the Photocatalytic Activity. *J. Phys. Chem. B* **2000**, *104*.

(51) Kim, K. Y.; Eun , T. H.; Lee, S.-S.; Chon, U. Photocatalytic activities and structural changes of barium-doped strontium tantalate. *Resources Processing* **2009**, *56*, 138–144. DOI: 10.4144/rpsj.56.138.

(52) Le Berre, F.; Crosnier-Lopez, M.-P.; Fourquet, J.-L. Cationic ordering in the new layered perovskite $BaSrTa_2O_7$. *Solid State Sciences* **2004**, *6* (1), 53-59. DOI: 10.1016/j.solidstatesciences.2003.10.008.

(53) Peng, Y.; Ma, Z.; Hu, J.; Wu, K. A first-principles study of anionic (S) and cationic (V/Nb) doped $Sr_2Ta_2O_7$ for visible light photocatalysis. *RSC Advances* **2017**, *7* (65), 40922-40928. DOI: 10.1039/c7ra07113b.

(54) Eidsvag, H.; Bentouba, S.; Vajeeston, P.; Yohi, S.; Velauthapillai, D. TiO_2 as a photocatalyst for water splitting-An experimental and theoretical review. *Molecules* **2021**, *26* (6). DOI: 10.3390/molecules26061687.

(55) Farzaneh, A.; Javidani, M.; Esrafili, M. D.; Mermer, O. Optical and photocatalytic characteristics of Al and Cu doped TiO_2: Experimental assessments and DFT calculations. *Journal of Physics and Chemistry of Solids* **2022**, *161*. DOI: 10.1016/j.jpcs.2021.110404.

(56) Lamhani, M.; Chchiyai, Z.; Elomrani, A.; Manoun, B.; Hasnaoui, A. Enhanced photocatalytic water splitting of $SrTiO_3$ perovskite through cobalt doping: experimental and theoretical DFT understanding. *Inorg Chem* **2023**, *62* (33), 13405-13418. DOI: 10.1021/acs.inorgchem.3c01758.

(57) Zhang, Y.; Yuan, Y.; Cai, J.; Dong, H.; Zhou, X. Theoretical studies on layered perovskite photocatalysts $Sr_2M_2O_7$ (M = Nb and Ta) modified by NiO cocatalysts. *The Journal of Physical Chemistry C* **2022**, *127* (1), 319-327. DOI: 10.1021/acs.jpcc.2c07959.

(58) Bouri, M.; Niederhauser, N.; Künzli, B.; Amsler, M.; Aschauer, U. Oxygen Evolution Reaction Activity of $Sr_2Ta_2O_7$ and $Sr_2Nb_2O_7$ Surfaces. *The Journal of Physical Chemistry C* **2022**, *126* (15), 6556-6563. DOI: 10.1021/acs.jpcc.2c00649.

(59) Song, P.; Sui, Y.; Shan, T.; Hou, J.; Wang, X. Assessment of hydrogen supply solutions for hydrogen fueling station: A Shanghai case study. *International Journal of Hydrogen Energy* **2020**, *45* (58), 32884-32898. DOI: 10.1016/j.ijhydene.2020.09.117.

(60) Traversa, A. B. S. E. Solid oxide fuel cells (SOFCs): a review of an environmentally clean and efficient source of energy. *Renewable and Sustainable Energy Reviews* **2002**, *6*, 433-455. DOI: 10.1016/S1364-0321(02)00014-X.

(61) Ndubuisi, A.; Abouali, S.; Singh, K.; Thangadurai, V. Recent advances, practical challenges, and perspectives of intermediate temperature solid oxide fuel cell cathodes. *Journal of Materials Chemistry A* **2022**, *10* (5), 2196-2227. DOI: 10.1039/d1ta08475e.

(62) Tarutin, A. P.; Filonova, E. A.; Ricote, S.; Medvedev, D. A.; Shao, Z. Chemical design of oxygen electrodes for solid oxide electrochemical cells: A guide. *Sustainable Energy Technologies and Assessments* **2023**, *57*. DOI: 10.1016/j.seta.2023.103185.

(63) Yang, G.; Jung, W.; Ahn, S.-J.; Lee, D. Controlling the oxygen electrocatalysis on perovskite and layered oxide thin films for solid oxide fuel cell cathodes. *Applied Sciences* **2019**, *9* (5). DOI: 10.3390/app9051030.

(64) Richter, J.; Holtappels, P.; Graule, T.; Nakamura, T.; Gauckler, L. J. Materials design for perovskite SOFC cathodes. *Monatshefte für Chemie - Chemical Monthly* **2009**, *140* (9), 985-999. DOI: 10.1007/s00706-009-0153-3.

(65) Jiang, S. P. A comparison of O_2 reduction reactions on porous (La,Sr)MnO_3 and (La,Sr)(Co,Fe)O_3 electrodes. *Solid State Ionics* **2002**, *146*, 1-22. DOI: 10.1016/S0167-2738(01)00997-3.

(66) Hu, S.; Li, J.; Zeng, Y.; Pu, J.; Chi, B. A mini review of the recent progress of electrode materials for low-temperature solid oxide fuel cells. *Phys Chem Chem Phys* **2023**, *25* (8), 5926-5941. DOI: 10.1039/d2cp05133h.

(67) Hussain, S.; Yangping, L. Review of solid oxide fuel cell materials: cathode, anode, and electrolyte. *Energy Transitions* **2020**, *4* (2), 113-126. DOI: 10.1007/s41825-020-00029-8.

(68) Wang, F.; Zhou, Q.; He, T.; Li, G.; Ding, H. Novel $SrCo_{1-y}Nb_yO_{3-\delta}$ cathodes for intermediate-temperature solid oxide fuel cells. *Journal of Power Sources* **2010**, *195* (12), 3772-3778. DOI: 10.1016/j.jpowsour.2009.12.081.

(69) Li, K.; Niemczyk, A.; Świerczek, K.; Stępień, A.; Naumovich, Y.; Dąbrowa, J.; Zajusz, M.; Zheng, K.; Dabrowski, B. Co-free triple perovskite $La_{1.5}Ba_{1.5}Cu_3O_{7\pm\delta}$ as a promising air electrode material for solid oxide fuel cells. *Journal of Power Sources* **2022**, *532*. DOI: 10.1016/j.jpowsour.2022.231371.

(70) Mochiku, T.; Mihara, Y.; Hata, Y.; Kamisawa, S.; Furuyama, M.; Suzuki, J.-i.; Kadowaki, K.; Metoki, N.; Fujii, H.; Hirata, K. Crystal Structure of Magnetic Superconductor $FeSr_2YCu_2O_{6+\delta}$. *Journal of the Physical Society of Japan* **2002**, *71* (3), 790-796. DOI: 10.1143/jpsj.71.790.

(71) Mochiku, T.; Nakano, Y.; Oikawa, K.; Kamiyama, T.; Fujii, H.; Hata, Y.; Suzuki, J.; Kakeya, I.; Kadowaki, K.; Hirata, K. Atomic ordering in $FeSr_2LnCu_2O_{6+\delta}$ system (Ln=Nd, Y and Er). *Physica C: Superconductivity* **2003**, *400* (1-2), 43-52. DOI: 10.1016/s0921-4534(03)01322-4.

(72) Wuernisha, T.; Mochiku, T.; Hata, Y.; Hoshikawa, A.; Fujii, H.; Yasuoka, H.; Kitazawa, H. Cation disorder and superconductivity in the Fe-based copper oxide

$FeSr_2Y_{1-x}Nd_xCu_2O_{6+\delta}$. *Physica C: Superconductivity* **2008**, *468* (15-20), 1195-1197. DOI: 10.1016/j.physc.2008.05.030.

(73) López-Paz, S. A.; Marín-Gamero, R.; Martínez de Irujo-Labalde, X.; Sánchez-Marcos, J.; Perez-Coll, D.; Alario y Franco, M. Á.; García-Martín, S. YBaCuO-type perovskites as potential air electrodes for SOFCs. The case of $YSr_2Cu_2FeO_{7+\delta}$. *Journal of Materials Chemistry A* **2021**, *9* (13), 8554-8560. DOI: 10.1039/d1ta00111f.

(74) Slater, P. R.; Greaves, C. Synthesis and structural characterisation of $YSr_2Cu_{3-x}M_xO_{7\pm x}$ (M=Fe, Ti, Al, Co, Ga, Pb; OS<x< l), and de non-existence of the parent phase $YSr_2Cu_3O_7$. *Physica C* **1991**, *180*, 299-309.

(75) Pissas, M.; Kallias, G.; Simopoulos, A.; Niarchos, D.; Kostikas, A. Mossbauer and crystal-structure study of $YSr_2Cu_2FeO_y$ isomorphic with $YBa_2(Cu_{1-x}Fe_x)_3O_y$. *Phys Rev B Condens Matter* **1992**, *46* (21), 14119-14125. DOI: 10.1103/physrevb.46.14119 From NLM PubMed-not-MEDLINE.

(76) Kumar, S.; Dogra, A.; Husain, M.; Kishan, H.; Awana, V. P. S. Comparative study of $MSr_2RECu_2O_{7+\delta}$ compounds with M=Al, Nb, Fe, Ru, Ga and Co and RE=Eu, Y. *Journal of Alloys and Compounds* **2010**, *493* (1-2), 352-357. DOI: 10.1016/j.jallcom.2009.12.101.

(77) Lopez-Paz, S. A.; Martinez de Irujo-Labalde, X.; Sanchez-Marcos, J.; Ritter, C.; Moran, E.; Alario-Franco, M. A. Soft Magnetic Switching in a $FeSr_2YCu_2O_{7.85}$ Superconductor with Unusually High Iron Valence. *Inorg Chem* **2019**, *58* (19), 12809-12814. DOI: 10.1021/acs.inorgchem.9b01770.

(78) López-Paz, S. A.; Sari, D. P.; Sánchez-Marcos, J.; Liborio, L.; Sturniolo, S.; Ritter, C.; Hillier, A. D.; Alario-Franco, M. A. Triple mgnetic sacking in an Iron-cntaining cuprate with Cu–Fe–Cu magnetic blocks. *Chemistry of Materials* **2024**, *36* (17), 8199-8207. DOI: 10.1021/acs.chemmater.4c00588.

(79) López-Paz, S. A.; Sari, D. P.; Hillier, A. D.; Alario-Franco, M. A. Coexistence of magnetism and superconductivity in the iron containing $FeSr_2YCu_2O_{7.57}$ cuprate as studied by μSR. *AIP Advances* **2021**, *11* (1). DOI: 10.1063/9.0000093.

(80) Munoz-Garcia, A. B.; Ritzmann, A. M.; Pavone, M.; Keith, J. A.; Carter, E. A. Oxygen transport in perovskite-type solid oxide fuel cell materials: Insights from quantum mechanics. *Acc Chem Res* **2014**, *47* (11), 3340-3348. DOI: 10.1021/ar4003174.

(81) Olsson, E.; Cottom, J.; Aparicio-Angles, X.; de Leeuw, N. H. Combined density functional theory and molecular dynamics study of $Sm_{0.75}A_{0.25}Co_{1-x}Mn_xO_{2.88}$ (A = Ca, Sr; x = 0.125, 0.25) cathode material for next generation solid oxide fuel cell. *Phys Chem Chem Phys* **2020**, *22* (2), 692-699. DOI: 10.1039/c9cp04892h.

(82) Woo, S. H.; Yang, H. J.; Kim, Y. Investigation of the effect of off-stoichiometric composition on oxygen transport in layered perovskite materials for SOFC cathode. *Materials Letters* **2024**, *361*. DOI: 10.1016/j.matlet.2024.136114.

(83) Hinuma, Y.; Hayashi, H.; Kumagai, Y.; Tanaka, I.; Oba, F. Comparison of approximations in density functional theory calculations: Energetics and structure of binary oxides. *Physical Review B* **2017**, *96* (9). DOI: 10.1103/PhysRevB.96.094102.

(84) Furness, J. W.; Zhang, Y.; Lane, C.; Buda, I. G.; Barbiellini, B.; Markiewicz, R. S.; Bansil, A.; Sun, J. An accurate first-principles treatment of doping-dependent electronic structure of high-temperature cuprate superconductors. *Communications Physics* **2018**, *1* (1). DOI: 10.1038/s42005-018-0009-4.

(85) Varignon, J.; Bibes, M.; Zunger, A. Mott gapping in 3*d* ABO_3 perovskites without Mott-Hubbard interelectronic repulsion energy *U*. *Physical Review B* **2019**, *100* (3). DOI: 10.1103/PhysRevB.100.035119.

(86) Iglesias, L.; Bibes, M.; Varignon, J. First-principles study of electron and hole doping effects in perovskite nickelates. *Physical Review B* **2021**, *104* (3). DOI: 10.1103/PhysRevB.104.035123.

(87) Wexler, R. B.; Gautam, G. S.; Stechel, E. B.; Carter, E. A. Factors governing oxygen vacancy formation in oxide perovskites. *J Am Chem Soc* **2021**, *143* (33), 13212-13227. DOI: 10.1021/jacs.1c05570.

(88) Kaczkowski, J.; Pugaczowa-Michalska, M.; Plowas-Korus, I. Comparative density functional studies of pristine and doped bismuth ferrite polymorphs by GGA+*U* and meta-GGA SCAN+*U*. *Phys Chem Chem Phys* **2021**, *23* (14), 8571-8584. DOI: 10.1039/d0cp06157c.

(89) Zeng, Y.; Hu, Q.; Pan, M.; Zhang, K.; Grasso, S.; Hu, C.; Feng, Q. Investigation of double perovskites Sr_2SmNbO_6 and X_2CoNbO_6 (X=Sr,Ba) with SCAN functional and plus *U* correction. *Advanced Powder Materials* **2022**, *1* (2). DOI: 10.1016/j.apmate.2021.11.006.

(90) Verma, M.; Pentcheva, R. Metal-insulator transition and robust thermoelectricity via strain-tuned interplay between structural and electronic properties in $(SrVO_3)/(SrTiO_3)(001)$ superlattices. *Physical Review Research* **2022**, *4* (3). DOI: 10.1103/PhysRevResearch.4.033013.

(91) Long, O. Y.; Sai Gautam, G.; Carter, E. A. Evaluating optimal *U* for 3*d* transition-metal oxides within the SCAN+*U* framework. *Physical Review Materials* **2020**, *4* (4). DOI: 10.1103/PhysRevMaterials.4.045401.

(92) Sai Gautam, G.; Carter, E. A. Evaluating transition metal oxides within DFT-SCAN and SCAN+*U* frameworks for solar thermochemical applications. *Physical Review Materials* **2018**, *2* (9). DOI: 10.1103/PhysRevMaterials.2.095401.

(93) Giordano, L.; Akkiraju, K.; Jacobs, R.; Vivona, D.; Morgan, D.; Shao-Horn, Y. Electronic structure-based descriptors for oxide properties and functions. *Acc Chem Res* **2022**, *55* (3), 298-308. DOI: 10.1021/acs.accounts.1c00509.

(94) Hwang, J.; Rao, R. R.; Giordano, L.; Katayama, Y.; Yang, Y.; Shao-Horn, Y. Perovskites in catalysis and electrocatalysis. *Science* **2017**, *358*, 751-756. DOI: 10.1126/science.aam7092.

(95) Lee, Y.-L.; Kleis, J.; Rossmeisl, J.; Shao-Horn, Y.; Morgan, D. Prediction of solid oxide fuel cell cathode activity with first-principles descriptors. *Energy & Environmental Science* **2011**, *4* (10). DOI: 10.1039/c1ee02032c.

(96) Jacobs, R.; Mayeshiba, T.; Booske, J.; Morgan, D. Material discovery and design principles for stable, high activity perovskite cathodes for solid oxide fuel cells. *Advanced Energy Materials* **2018**, *8* (11). DOI: 10.1002/aenm.201702708.

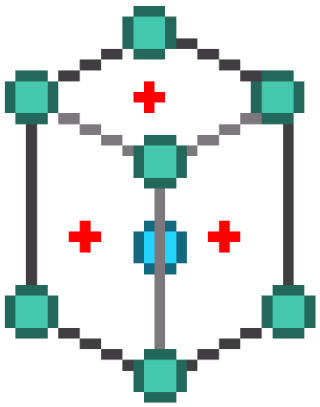

CAPÍTULO 2
Objetivos

La producción de hidrógeno verde y su utilización como combustible son dos de los retos que se deben afrontar para conseguir la plena descarbonización del sistema energético, y para facilitar la integración efectiva de las tecnologías renovables en dicho sector. Las tecnologías involucradas requieren avances científicos encaminados a optimizar las prestaciones de los materiales utilizados. Esta tesis doctoral se enmarca en el desarrollo de nuevos materiales para la generación y utilización de hidrógeno verde. Atendiendo a la aplicación de los materiales se diferencian dos ámbitos de estudio: la producción de hidrógeno verde mediante fotocatálisis de agua, y la utilización de hidrógeno como combustible en SOFC. Para el estudio de ambos tipos de materiales se ha utilizado la metodología DFT, con el **objetivo final** de entender la relación estructura-composición-propiedades y, a partir de este entendimiento, mejorar las propiedades de los materiales estudiados. Adicionalmente, se pueden establecer los siguientes **objetivos específicos**:

Objetivo 1

El primer objetivo específico es el diseño de perovskitas en capas basadas en tántalo para generación de H_2 verde mediante fotocatálisis del agua.

Para cumplir este objetivo, en el capítulo 3 de esta tesis se explora la familia Ba-Sr-Ta-O, analizando a través de cálculos computacionales distintas composiciones dentro de los materiales $Sr_{2-x}Ba_xTa_2O_7$ ($0 \leq x \leq 1$). Se estudia la influencia de la estructura cristalina y la composición de las fases en sus propiedades electrónicas. Además, se sintetizan y caracterizan los compuestos $Sr_2Ta_2O_7$ y $BaSrTa_2O_7$, para posteriormente demostrar su actividad fotocatalítica.

Objetivo 2

El segundo objetivo específico de la presente tesis doctoral es estudiar perovskitas laminares con estructura derivada de YBCO, para evaluar algunas de sus propiedades de cara a su potencial aplicación como electrodo de aire en pilas de combustible. Concretamente, se desea conocer qué efecto tiene la relación estructura-composición en las propiedades de estos materiales para llevar a cabo la ORR en celdas de combustible. La consecución de este objetivo puede dar lugar, a largo plazo, al diseño de nuevos electrodos de aire.

Con este objetivo, en los capítulos 4, 5 y 6 de esta tesis doctoral se explora en profundidad el sistema $YSr_2Cu_2FeO_{7+\delta}$ ($0 < \delta < 1$), propuesto por algunos autores como electrodo de aire o cátodo en celdas de combustible de óxido sólido. El estudio computacional de este sistema con una estructura electrónica altamente compleja hace necesario definir los objetivos específicos de índole computacional que se mencionan a continuación.

Objetivo 3

Gran parte del trabajo realizado está enfocado en la evaluación de distintos funcionales de intercambio-correlación para el estudio de óxidos de metales de transición que pueden presentar alta correlación electrónica. En concreto, se pretende comprar la capacidad del funcional SCAN para reproducir aspectos estructurales y electrónicos con el método PBE+*U*, utilizado en las últimas décadas.

Con este objetivo, en el capítulo 4 se afronta el reto que supone la elección del funcional adecuado para la descripción del sistema YSCFO. Para ello, ha sido necesario realizar un estudio experimental paralelo, que incluye la síntesis de la fase $YSr_2Cu_2FeO_{7.08,}$ así como la caracterización de las fases $YSr_2Cu_2FeO_{7.85}$ y $YSr_2Cu_2FeO_{7.08}$. La combinación de los cálculos DFT con información experimental ha permitido validar algunos resultados teóricos. Este estudio es un punto de partida para desarrollar un nuevo enfoque a la hora de explorar óxidos mixtos que presentan más de un metal de transición.

Objetivo 4

Este objetivo, complementario al anterior, plantea el análisis del desempeño del funcional SCAN+*U* en la descripción de óxidos mixtos que poseen dos metales de transición y que pueden presentar alta localización electrónica.

En el capítulo 5 se investiga en profundidad el efecto del valor del parámetro *U* en el método SCAN+*U* sobre la estructura cristalina, el momento magnético, y el comportamiento electrónico del material $YSr_2Cu_2FeO_{7+\delta}$. La evaluación de la influencia del valor del parámetro *U* —aplicado sobre Cu y Fe— en las propiedades mencionadas, ofrece información clave para futuros estudios que apliquen SCAN+*U* sobre sistemas de complejidad similar.

Objetivo 5

Como último objetivo específico, se pretende utilizar Dinámica Molecular ab initio para simular la difusión de iones óxido en perovskitas complejas a temperaturas finitas.

Para cumplir este objetivo, se ha estudiado la conductividad iónica del sistema $YSr_2Cu_2FeO_{7+\delta}$, incluyendo fases «virtuales» que no han sido sintetizadas. Los resultados más relevantes se presentan en el capítulo 6. El análisis realizado en este capítulo sirve como punto de partida para comprender el transporte iónico en estos materiales y predecir su aplicabilidad como electrodo de aire en SOFC.

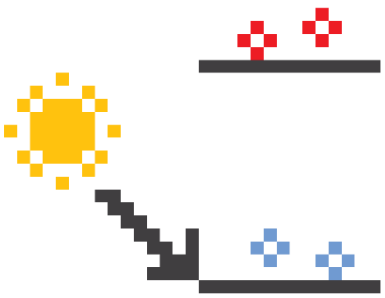

CAPÍTULO 3

Upgrading photocatalytic hydrogen evolution in Ba–Sr–Ta–O perovskite-type layered structures

International Journal of Hydrogen Energy 63 (2024) 1003–1012

Contents lists available at ScienceDirect

International Journal of Hydrogen Energy

journal homepage: www.elsevier.com/locate/he

Upgrading photocatalytic hydrogen evolution in Ba–Sr–Ta–O perovskite-type layered structures

Marianela Gómez-Toledo [a], Khalid Boulahya [a], Laura Collado [b], Víctor A. de la Peña O'Shea [b], M. Elena Arroyo-de Dompablo [a,*]

[a] Departamento de Química Inorgánica, Universidad Complutense de Madrid, 28040 Madrid, Spain
[b] Photoactivated Processes Unit, IMDEA Energy Institute, Parque Tecnológico de Móstoles, Avda. Ramón de la Sagra 3, 28935, Móstoles, Madrid, Spain

ARTICLE INFO

Handling editor: Umit Demirci

Keywords:
Photocatalyst
Hydrogen production
Layered perovskites
Mixed oxides
$Sr_2Ta_2O_7$
$BaSrTa_2O_7$

ABSTRACT

Photocatalytic hydrogen evolution from water is investigated in Ba–Sr–Ta–O layered compounds possessing two different crystal structures: $Sr_2Ta_2O_7$ (S.G. *Cmcm*, a (110) type layered pervoskite), and $BaSrTa_2O_7$ (S.G. *Immm*, a (100) type layered perovskite). High purity samples of $BaSrTa_2O_7$ and $Sr_2Ta_2O_7$ are successfully prepared by solid state reaction. Hydrogen production under UV irradiation is 26% larger in $BaSrTa_2O_7$ (15.2 mmol g^{-1}) than in $Sr_2Ta_2O_7$ (11.4 mmol g^{-1}). The band gaps determined by diffuse reflectance spectroscopy (DRS) are 4 eV and 4.6 eV for $BaSrTa_2O_7$ and $Sr_2Ta_2O_7$, respectively. Density Functional Theory (DFT) calculations provide insights into the crystal and electronic structures of $Sr_2Ta_2O_7$, $BaSrTa_2O_7$, and their derived series $Sr_{2-x}Ba_xTa_2O_7$ ($0 \leq x \leq 1$). It is found that independently of the Sr/Ba content, the $BaSrTa_2O_7$-derived series show a ~0.6 eV lower band gap and a wider conduction band than the $Sr_2Ta_2O_7$-derived series. DFT results indicate that the enhanced hydrogen production of $BaSrTa_2O_7$ is related to particular features of its crystal structure which favor Ta–Ta interactions.

1. Introduction

Strategies to decrease fossil fuel dependence and the development of energy production from renewable sources have been explored in the last decades. In this scenario, green hydrogen is called to play a significant role in low-carbon future: counterbalancing electricity as a zero-carbon energy carrier that can be easily stored and transported, and enabling a reliable, publicly accepted, sustainable and competitive energy system [1,2]. The design of materials able to absorb sunlight and photocatalyze the water dissociation reaction is key for green hydrogen production [3]. Photocatalysts should have a suitable electronic structure [4] in terms of the band gap energy and the position of the band-edges. For UV–visible light absorption, the band gap must be larger than 1.7 eV, the bottom of the conduction band (CB) should be more negative than the reduction potential of water (H_2O/H_2, 0 eV), while the top of the valence band (VB) should lie above the water oxidation potential (H_2O/O_2, 1.23 eV). The mentioned characteristics can be tuned by varying the crystal structure and/or composition of the catalyst, and thereby its electronic structure.

In the last years, a wide range of semiconducting materials have been developed for photocatalytic applications under UV illumination. Metal oxide photocatalysts can be typically classified depending on the electronic configuration of the metal into d^0, d^{10} and f^0 [5]. One of the most investigated d^0 photocatalysts is TiO_2 [6] (band gap of 3.2 eV), which is widely used as a benchmark for energy and environmental applications. On the other hand, titanates such as $SrTiO_3$ —which exhibits the ABO_3 perovskite structure— have turned out to function well in the UV region when combined with metal ions co-catalysts [7]. Another well-known class of d^0-semiconductors displaying photocatalytic activity in the UV region are the tantalates, such as $MTaO_3$ (M = Li, Na, K) or MTa_2O_6 (M = Sr, Ba, Sn, Ni, Mn, Co), whose hydrogen evolution performance is summarized in Table S1 [5]. Generally, these materials present perovskite-related structures. Perovskite compounds are very promising functional materials since they are structurally stable, possess flexible structures-compositions for easy tuning and are cost-effective.

Lately, layered compounds based on perovskite-type blocks have been investigated for their photocatalytic properties [8,9]. Electronically, d^0 layered perovskites show conduction band edges that are well

* Corresponding author.
E-mail address: mearroyo@ucm.es (M.E. Arroyo-de Dompablo).

https://doi.org/10.1016/j.ijhydene.2024.02.346
Received 23 November 2023; Received in revised form 24 January 2024; Accepted 27 February 2024
Available online 23 March 2024

above the electrochemical potential of H_2O/H_2 (0 eV). Layered compounds built of perovskite blocks can be grouped attending to the perovskite-slab orientation relative to the principal axis of an ideal cubic perovskite in (100) —which include Ruddlesden-Popper ($A'_2A_{n-1}B_nO_{3n+1}$), Dion Jacobson ($A'[A_{n-1}B_nO_{3n+1}]$), and Aurivillius ($(Bi_2O_2)^{2+}(A_{n-1}B_nO_{3n+1})^{2-}$) families — (110), and (111) types [10] (see Figure S1). The mixed oxide $Sr_2Ta_2O_7$ [11], which can be classified as (110) layered perovskite type, has been found to be active for photocatalytic hydrogen evolution under UV radiation (see Table 1). Samples prepared by solid state reactions exhibited hydrogen evolution rates of 52 μmol $g^{-1}h^{-1}$ and 1000 μmol $g^{-1}h^{-1}$,in the absence or presence of NiO co-catalyst, respectively [12]. $Sr_2Ta_2O_7$ presents a wide band gap (4.6 eV), which hinders visible light absorption. Nevertheless, its high CB position makes the compound attractive for further studies [12]. In this regard, computational studies at the Density Functional Theory (DFT) level have focus on chemical doping of the oxide ions and transition metal (TM) at the B-site [13,14]. As for compositional variations affecting the A-site, an experimental study claims that the partial Ba substitution for Sr in $Sr_{2-x}Ba_xTa_2O_7$ ($0 \leq x \leq 0.3$) leads to an improved photocatalytic activity for water dissociation into hydrogen [15].

The photocatalytic activity for water splitting attained in $Sr_2Ta_2O_7$ makes appealing the investigation of other perovskite-type layered tantalates. In the Ba–Sr–Ta–O system, Le Berre et al. reported the $BaSrTa_2O_7$ perovskite-type (100) layered compound [16]. To the best of our knowledge, the electronic structure as well as the photocatalytic activity of $BaSrTa_2O_7$ remain unknown. Although both, $Sr_2Ta_2O_7$ and $BaSrTa_2O_7$, show perovskite-type slab structures, as described below, there are some crystallographic differences —e.g., relative orientation

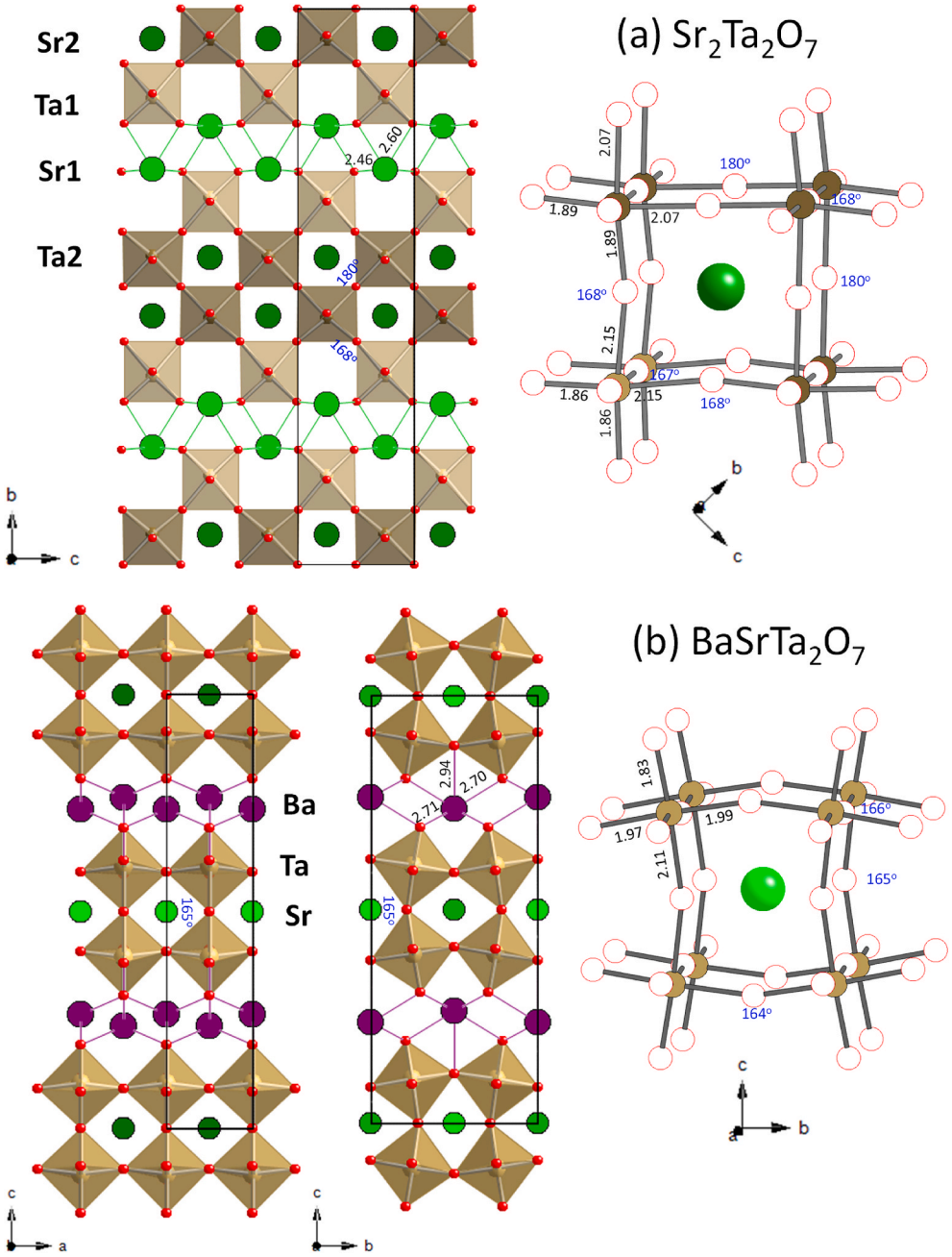

Fig. 1. Representation of the crystal structures of (a) $Sr_2Ta_2O_7$ (S.G. *Cmcm)* [11] and (b) $BaSrTa_2O_7$ (S.G. *Immm*) [16]. The centers of eight [TaO_6] octahedra form a distorted cube which corresponds to the unit cell of the perovskite. Selected bond distances (Å) are in black and O–Ta–O angles (°) in blue. Color code: Ta in brown, Sr1 in light green, Sr2 in dark green, Ba in pruple and O in red/white.

respective to the cubic perovskite axis, number of perovskite units in the layers, octahedral rotation, and coordination of cations in the interlayer space — that might cause variations in band gap and/or band-edges positions, which could end up in a distinct photocatalytic activity in water-splitting reactions.

The present work combines experimental and computational techniques to complete previous research on $Sr_2Ta_2O_7$ and, as a novelty, to investigate $BaSrTa_2O_7$. We will demonstrate that both $Sr_2Ta_2O_7$ and $BaSrTa_2O_7$ are active towards UV-driven photocatalytic hydrogen production, also finding an improved performance in $BaSrT_2O_7$ compared to $Sr_2Ta_2O_7$. Computational simulations via DFT are used to disclose the features in the electronic structures of $Sr_2Ta_2O_7$ and $BaSrTa_2O_7$ (band gap and band-edge energy) that might cause their different hydrogen production rates. To assess the role of chemical composition and structure in the catalytic properties, additional DFT work is performed to investigate the substituted $Sr_{2-x}Ba_xTa_2O_7$ ($0 \leq x \leq 1$) compounds derived from the crystal structures of $Sr_2Ta_2O_7$ ((110) layered perovskite) and $BaSrTa_2O_7$ ((100) layered perovskite).

The crystal structures of $Sr_2Ta_2O_7$ and $BaSrTa_2O_7$

$Sr_2Ta_2O_7$ crystalizes in a layered structure formed by perovskite slabs stacked along the *b* axis (see Fig. 1a and Figure S1). The perovskite-type layers are composed of sharing vertexes octahedral units [TaO_6], with the layer widths corresponding to twice the face diagonal of a cubic perovskite. It is worth noting that Ta is displaced from the centre of the octahedra (see Figure S2). A sift of $a/2$ exists between adjacent layers. It is significant to remark that some bond-length distinctions exist between Ta near the inter-layer zone (Ta1) and Ta inside the perovskite blocks (Ta2). Conversely, Sr presents two different coordination environments, Sr1 is located near the boundaries of the perovskite layer with C.N. = 6, while Sr2 is placed inside the perovskite blocks with C.N. = 12. Both Sr^{2+} ions occupy the 4*c* site of the *Cmcm* space group (S.G.).

The crystal structure of $BaSrTa_2O_7$ derives from the Dion-Jacobson family of general formula A'[$A_{n-1}B_nO_{3n+1}$], with n = 2 and B = Ta, being A = Sr and A' = Ba [16]. The layers are formed by corner-sharing [TaO_6] octahedral units, which are stacked along the *c* axis (Fig. 1b and Figure S1). Adjacent layers are shifted by $(a+b)/2$, with Ba located in the interlayer space (4*j* site of *Immm* S.G.). The [TaO_6] octahedral units are slightly rotated along the *a* axis, which results in C.N. = 7 for the interlayer Ba cations. In addition, the Ta–O octahedra is distorted, being the Ta atom out of the centre of the octahedra (Figure S2). The Sr1 and Sr2 cations located inside the pervoskite layers (2*b* and 2*c* sites of *Immm* S.G.) display a distorted polyhedra with 12 coordination number.

2. Methodology

2.1. Experimental

$Sr_2Ta_2O_7$ and $BaSrTa_2O_7$ powders were synthesized by solid state reactions, using stoichiometric mixtures of the starting reactants $SrCO_3$, $BaCO_3$ and Ta_2O_5 of purity >99.95%. The mixtures of reactants were pre-treated at 900 °C for carbonates decomposition. For $Sr_2Ta_2O_7$, the pelletized mixture was then calcined at 1400 °C during 20 h. Similarly to the procedure reported by Le Berre et al. [16], the synthesis of $BaSrTa_2O_7$ required two consecutive treatments of 96 h at 1400 °C with a grinding and re-pelletizing in between.

X-Ray powder diffraction (PXRD) patterns were acquired on a Bruker D8 Advance A25 diffractometer in a Debye-Scherrer configuration equipped with a Cu Kα1 radiation source (λ = 1.5418 Å) and Johansson monochromator. Rietveld refinements were carried out with the Fullprof Suite program [17].

Ultraviolet–visible diffuse reflectance spectra (UV–vis DRS) were obtained by using a PerkinElmer Lambda950 UV/VIS spectrometer equipped with an external 150 mm integrating sphere over the range 2500 - 250 nm with data interval of 1 nm. The obtained data were converted from reflectance to absorbance using the Kubelka-Munk theory [18] and Tauc method [19].

Photocatalytic experiments were conducted in a slurry photoreactor with an effective volume of 130 mL. For each experiment, 0.025 g of photocatalyst were added to a H_2O/Methanol (9:1) v/v aqueous solution. The reaction temperature (20 °C) was measured with a thermocouple situated on the photoreactor wall. The suspension was magnetically stirred, and an argon flow (60 mL/min) was used to remove the air (verified by GC) under darkness and then irradiated by a 150 W medium-pressure Hg UV lamp. H_2 evolution was monitored every 3.8 min by means of an Agilent micro-GC equipped with two channels with a molecular sieve and a PPQ column, respectively. Pt was employed as co-catalyst, the metal was photo-deposited in-situ using $H_2PtCl_6{\cdot}6H_2O$ to obtain a nominal loading of 0.5 wt% Pt.

2.2. Computational

The DFT calculations have been performed using the VASP (Vienna Ab-initio Simulation Package) software, developed at the Universität Wien [20]. For the description of the interaction between core electrons and nuclei, the Projector Augmented Wave (PAW) method [21] has been used, precisely $4s^24p^65s^2$ for Sr, $5p^66s^25d^3$ for Ta, $5s^25p^66s^2$ for Ba and $2s^22p^4$ for O have been treated as valence electrons. The strongly constrained and appropriately normed (SCAN) [22] *meta*-GGA exchange-correlation (XC) functional have been employed to investigate $Sr_2Ta_2O_7$, $BaSrTa_2O_7$, and the related $Sr_{2-x}Ba_xTa_2O_7$ ($0 \leq x < 1$). In addition, calculations using the GGA-PBE and the Heyd–Scuseria–Ernzerhof (HSE) [23], a hybrid XC-functional, have been carried out for $Sr_2Ta_2O_7$ and $BaSrTa_2O_7$. Specifically, the HSE06 functional has been employed, setting the range separation parameter (HFSCREEN) to 0.2 $Å^{-1}$. The sampling of the first Brillouin zone was performed under the Monkhorts-Pack scheme, using a 6 x 2 x 6, and a 6 x 4 x 2 *k*-point mesh for $Sr_2Ta_2O_7$ and $BaSrTa_2O_7$ structures, respectively. A Gaussian smearing parameter of 0.05 eV was used, and the energy cut-off was set at 600 eV throughout all calculations. In addition, the tolerance threshold to achieve self-consistency in total energy was set at 1E-4 eV. The structural relaxations were performed over cell shape, cell volume, and atomic positions. The tetrahedron method with Blöch corrections [24] was employed for all the density of states (DOS) calculations. Additionally, Bader charge analysis [25] was carried out on the charge density files, employing the python library pymatgen [26].

Crystallographic models. To simulate the crystal structure of the known compounds $Sr_2Ta_2O_7$ [11] and $BaSrTa_2O_7$ [16], the initial atomic positions were taken from the Inorganic Crystal Structure Database (ICSD codes 601 and 99953, respectively). The compound $Sr_2Ta_2O_7$ undergoes a paraelectric-to-ferroelectric phase transition on cooling (at 166 K), which is accompained by a change in the S.G. from *Cmcm* to *Cmc2* [27]. In this work we have considered the centrosymetric structure stable at room temperature (S.G. *Cmcm*).

To assess the role of chemical composition, two series of hypothetical $Sr_{2-x}Ba_xTa_2O_7$ compounds have been considered possessing i) the crystal structure of $Sr_2Ta_2O_7$, denoted as perovskite-block or PB-compounds

Table 1
Summary of the calculated models in $Sr_{2-x}Ba_xTa_2O_7$ from experimentally known $Sr_2Ta_2O_7$ (ICSD code 601) and $BaSrTa_2O_7$ (ICSD code 99953) structures.

x in $Sr_{2-x}Ba_xTa_2O_7$	Site 1 (Interlayer) C.N. = 6 (PB), 7 (DJ)	Site 2 (Perovskite slab) C.N. = 12	Code
0 (ICSD 601)	100% Sr	100% Sr	PB-0
0.25	75% Sr 25% Ba	100% Sr	PB6-025
0.25	100 % Sr	75% Sr 25% Ba	PB12-025
0.5	50% Ba 50% Sr	100% Sr	PB6-05
0.5	100 % Sr	50% Ba 50% Sr	PB12-05
1	100% Ba	100% Sr	PB6-1
1	100% Sr	100% Ba	PB12-1
1 (ICSD 99953)	100% Ba	100 % Sr	DJ-1
1	100 % Sr	100 % Ba	DJ-1exch
0	100% Sr	100% Sr	DJ-0

and ii) the crystal structure of $BaSrTa_2O_7$, denoted as Dion-Jacobson or simply DJ-compounds. Table 1 list the investigated models of PB and DJ-$Sr_{2-x}Ba_xTa_2O_7$. In the $Sr_2Ta_2O_7$ there are two different sites for Sr (Fig. 1), and therefore Ba substitution for Sr may occur in whichever site. Models denoted as PB-6 and PB-12 refer, respectively, to substitution on the interlayer Sr1 cations (C.N = 6) and on the perovskite slab Sr2 cations (C.N = 12). Three different compositions are studied in each PB model: x = 0.25, x = 0.5 and x = 1. For the DJ-$Sr_{2-x}Ba_xTa_2O_7$ compounds, in addition to the reported $BaSrTa_2O_7$, we have considered a model where Ba and Sr crystallographic positions are interchanged (denoted as DJ-1exch), and the hypothetical x = 0 term, DJ-derived $Sr_2Ta_2O_7$, denoted DJ-0.

2.2.1. CB and VB edges positions

As stated in the introduction section, the energy position of the CB and VB edges relative to water redox potentials is vital when studying the driving force of photocatalytic materials. However, the determination of the band-edge position is not trivial from first principles calculations. Some authors have suggested exhaustive calculation methods [28,29], which require high computational costs. A good approximation is to use an empirical expression to determine the position of the band edges relative to the water redox potentials [30,31]. This expression allows to calculate the centre of the band gap in a semiconductor through the difference between the normal hydrogen electrode (NHE) potential and the vacuum, and the electronegativity of the neutral atoms in the Mulliken scale [32]. Equation (1) shows the expression in Ref. [30] particularized for the present case of Sr_{2-x} $Ba_xTa_2O_7$:

$$E_{CB/VB} = E_0 + \left(\chi_{Sr}^{(2-x)}\, \chi_{Ba}^{x}\, \chi_{Ta}^{2}\, \chi_{O}^{7}\right)^{1/N} \pm E_g/2 \quad (1)$$

where E_0 is the energy difference between NHE potential and the vacuum and is equal to −4.5 eV, χ is the electronegativity of the neutral atoms, and N is the number of total atoms. Hence, adding or subtracting half of the band gap to the E_0 and electronegativity terms summation, gives the valence band maximum (VBM) and the conduction band minimum (CBM) positions in the NHE scale, respectively.

3. Results

3.1. Experimental

Structural characterization. Fig. 2 shows the PXRD patterns of the synthesized $Sr_2Ta_2O_7$ and $BaSrTa_2O_7$. The refined lattice parameters confirmed both samples to be apparently single phases by PXRD. The corresponding patterns can be fully indexed to an orthorhombic unit cell. For $Sr_2Ta_2O_7$ (S.G. *Cmcm*), the refined lattice parameters are a = 3.94413(21) Å, b = 27.1799(152) Å, c = 5.68834(34) Å and V = 609.45 Å,^{3} in good agreement with previous works [11] (see Table 2). For $BaSrTa_2O_7$ (S.G. *Immm*), the refined values are a = 3.9848(23) Å, b = 7.82165(45) Å, c = 20.11667(101)1 Å and V = 631.54 Å^3, which are close to those reported by Le Berre et al. [16] (see Table 2). Using the

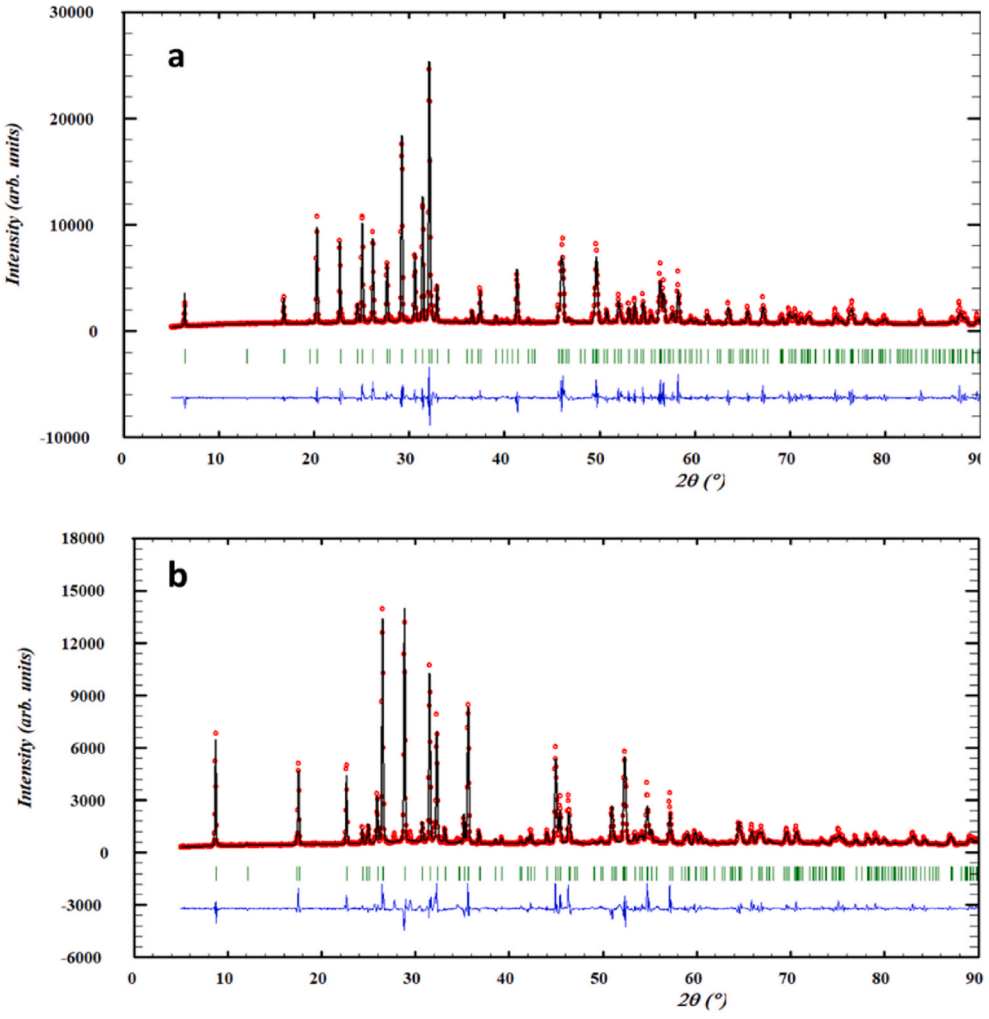

Fig. 2. Experimental (red points), calculated (solid black line) and associated difference (blue line at bottom) PXRD patterns for (a) $Sr_2Ta_2O_7$ and (b) $SrBaTa_2O_7$. The vertical bars (green) indicate the positions of the Bragg peaks.

Table 2
Calculated unit cell parameters (Å), unit cell volume (Å^3), and bond-lengths (Å), for $Sr_2Ta_2O_7$ and $BaSrTa_2O_7$ compared to the experimental data [11,16] (ICSD 601 and 99953, respectively). The relative error is given (%).

$Sr_2Ta_2O_7$	Experimental	Calculated				$BaSrTa_2O_7$	Experimental	Calculated			
		SCAN	error	HSE06	error			SCAN	error	HSE06	error
a	3.937(6)	3.9537	0.4	3.9528	0.4	*a*	3.99372(5)	3.987	0.8	3.9879	0.1
b	27.198(6)	27.1894	0.03	27.3614	0.6	*b*	7.8428(1)	7.8293	0.7	7.8304	0.2
c	5.692(7)	5.6951	0.04	5.6996	0.1	*c*	20.1609(3)	20.2897	1.9	20.3765	1.1
Volume	609.5	612.22	0.4	616.44	0.1	Volume	631.48	633.35	0.3	636.29	0.8
Sr1–O	2.47(1) x 4	2.480 x 4	0.4	2.489 x 4	0.1	Sr1–O	2.72(3) x 4	2.733 x 4	0.5	2.730 x 4	0.4
Sr1–O	2.60(1) x 2	2.575 x 2	1.0	2.571 x 2	0.1	Sr1–O	2.63(3) x 4	2.603 x 4	1	2.600 x 4	1.1
Sr1–O	3.27(1) x 2	3.313 x 2	1.3	3.358 x 2	0.3	Sr1–O	3.10(3) x 4	3.029 x 4	2.3	3.030 x 4	2.3
Sr2–O	2.71 (1)x 4	2.719 x 4	0.3	2.713 x 4	0.0	Sr2–O	2.65(2) x 4	2.569 x 4	3.1	2.565 x 4	3.2
Sr2–O	2.827(3) x 4	2.837 x 4	0.4	2.843 x 4	0.1	Sr2–O	2.69(3) x 4	2.695 x 4	0.2	2.694 x 4	0.1
Sr2–O	2.850(4) x 2	2.852 x 2	0.1	2.855 x 2	0.02	Sr2–O	2.98(3) x 4	3.000 x 4	0.7	3.004 x 4	0.8
Sr2–O	2.70(3)	2.629	2.6	2.62	0.3	Ba–O	2.705(3) x 2	2.713 x 2	0.3	2.724 x 2	0.7
Sr2–O	2.74(3)	2.743	0.1	2.756	0.6	Ba–O	2.713(2) x 4	2.712 x 4	0.04	2.721 x 4	0.3
Ta1–O	1.87(1) x 2	1.855 x 2	0.8	1.860 x 2	0.1	Ba–O	2.94(1)	3.038	3.3	3.054	3.9
Ta1–O	1.979 (4)x 2	1.997 x 2	0.9	1.995 x 2	0.1	Ta–O	2.011(3) x 2	2.005 x 2	0.3	2.005 x 2	0.3
Ta1–O	2.16(1) x 2	2.157 x 2	0.1	2.153 x 2	0.03	Ta–O	1.977(9)	1.999	1.1	1.999	1.1
Ta2–O	1.89(1) x 2	1.855 x 2	1.9	1.902 x 2	0.1	Ta–O	1.976(6)	1.981	0.3	1.982	0.3
Ta2–O	1.980(4) x 2	1.989 x 2	0.5	1.988 x 2	0.04	Ta–O	2.113(6)	2.111	0.1	2.108	0.2
Ta2–O	2.070(1) x 2	2.071 x 2	0.04	2.069 x 2	0.005	Ta–O	1.830(3)	1.856	1.4	1.858	1.5
mean Ta–O	1.992	1.987	0.2	1.995	0.4	mean Ta–O	1.986	1.993	0.3	1.993	0.3

above results, the structural models proposed for the two materials under study were checked using the Fullprof software. The fit of the PXRD data to the models, confirms its validity to describe the average structures of both compounds. Nevertheless, a small amount (around 1%) of $Ba_3SrTa_2O_9$ phase was detected in the refinement of $BaSrTa_2O_7$.

DRS analysis. Fig. 3 shows the Tauc plots for $Sr_2Ta_2O_7$ and $BaSrTa_2O_7$. Both materials are insulators with band gaps falling within the UV region, and in line with the band gap values reported for tantalates [5,33]. The direct band gap of $Sr_2Ta_2O_7$ (4.6 eV in Fig. 3a) agrees with reported value in literature (4.6 eV) [12]. Remarkably, the band gap of $BaSrTa_2O_7$ is 0.5–0.6 eV narrower than the band gap of $Sr_2Ta_2O_7$, independently of the considered nature of the transition (direct or indirect).

Photocatalytic hydrogen production. The photocatalytic activity of $Sr_2Ta_2O_7$ and $BaSrTa_2O_7$ was investigated for UV-driven hydrogen production in the presence of Pt co-catalyst (0.5 wt% Pt). As shown in Fig. 4, both samples were active for hydrogen evolution reaching cumulative productions in the range of mmol. In particular, $Sr_2Ta_2O_7$ reached 11.4 mmol g^{-1} after 6h of UV illumination, while the performance of $BaSrTa_2O_7$ increased by 26% and reached 15.2 mmol g^{-1}. Likewise, the H_2 production rate of $BaSrTa_2O_7$ was higher than that of $Sr_2Ta_2O_7$ (2.9 mmol g^{-1} h^{-1} and 2.0 mmol g^{-1} h^{-1}, respectively). Based on our results, the enhanced hydrogen evolution performance of $BaSrTa_2O_7$ is tentatively ascribed to its lower band gap energy and its wider CB. This assumption is further evaluated below by DFT calculations.

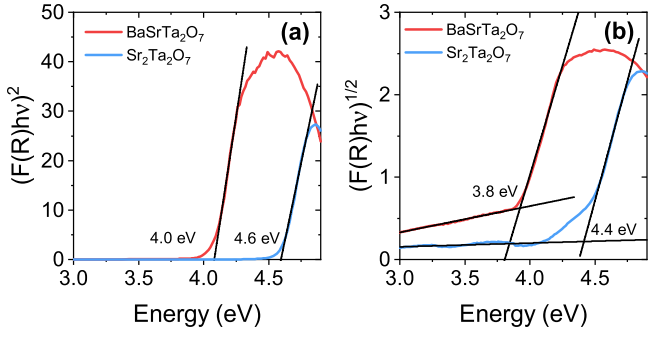

Fig. 3. Tauc plot from DRS UV/visible measurements of synthesized $Sr_2Ta_2O_7$ and $BaSrTa_2O_7$ considering (a) a direct and (b) an indirect allowed electronic transition.

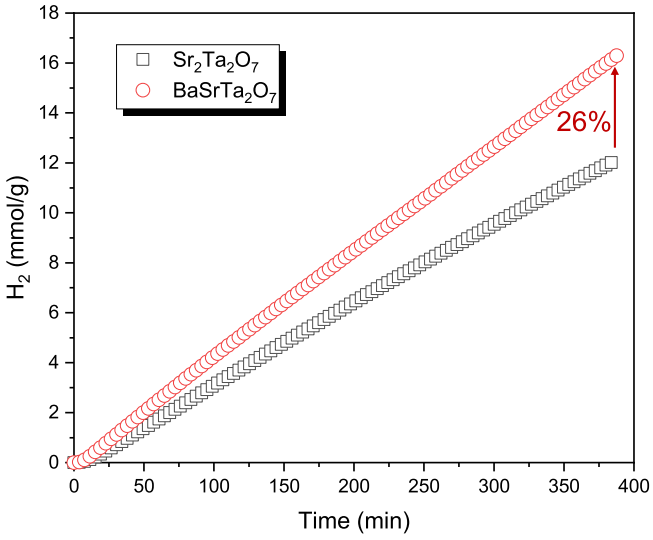

Fig. 4. Cumulative UV-driven hydrogen production of $Sr_2Ta_2O_7$ and $BaSrTa_2O_7$ using Pt (0.5 wt%) as co-catalyst.

Interestingly, the photocatalytic activities reported in this work surpass those reported in literature for Ta-based oxides (Table S1) and in particular for $Sr_2Ta_2O_7$, further improving these values for the Dion-Jacobson compound $BaSrTa_2O_7$.

3.2. Computational

3.2.1. $Sr_2Ta_2O_7$ and $BaSrTa_2O_7$

For all the tested functionals (SCAN, HSE06 and PBE) the calculated cell parameters, as well as the interatomic distances, are in good agreement with the experimental values (Table 2 and Table S2 for PBE). The major deviation (3.3% SCAN, 3.9 HSE06 and 4.4 % PBE) is observed for the Ba–O distance related to the interlayer space of $BaSrTa_2O_7$ (see Fig. 1a).

Fig. 5 exhibits the calculated density of states (DOS) within the SCAN and HSE06 functionals for $Sr_2Ta_2O_7$ and $BaSrTa_2O_7$. The partial density of Ta and O are represented in blue and red lines, respectively. Following the general scheme of the perovskite band structure (Figure S3), the

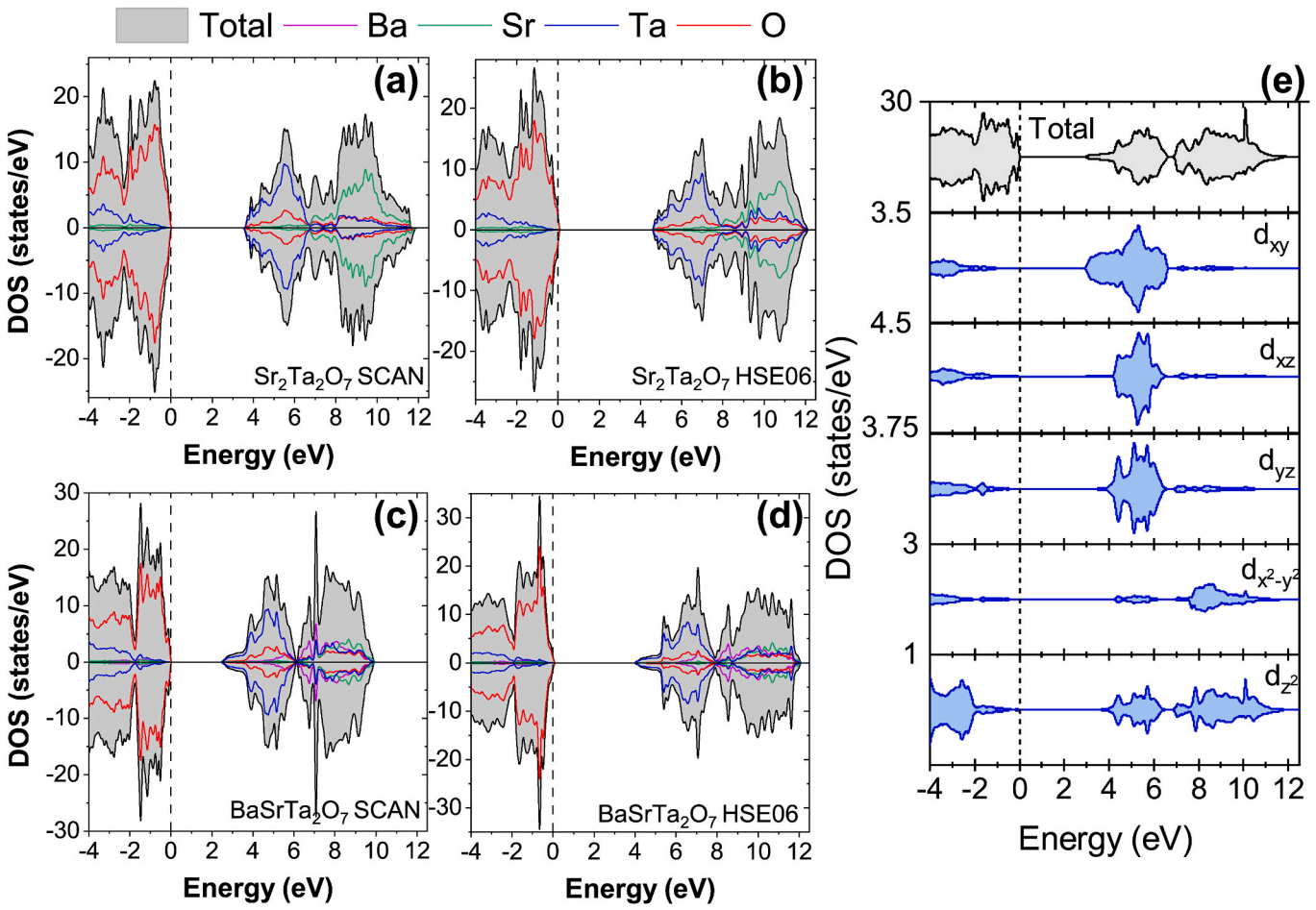

Fig. 5. Calculated DOS for $Sr_2Ta_2O_7$ using the (a) SCAN and the (b) HSE06 functionals, and for $BaSrTa_2O_7$ using the (c) SCAN, and the (d) HSE06 functionals. The black lines denote the total DOS, with the partial contributions of atoms shown in blue (Ta), green (Sr), pink (Ba) and red (O). The zero of the energy has been set at the Fermi level. DOS units refer to the calculated cell. Panel (e) displays the orbital projected density of states of $BaSrTa_2O_7$ from SCAN calculation, indicating the contribution of each Ta-5*d* orbital to the conduction band.

overlapping between Ta 5*d*-orbitals and O-2*p* orbitals form the bonding Π-O(2*p*)-Ta(t_{2g}) and σ-O(2*p*)-Ta(e_g) bands, with major contribution of O-2*p* states, and the corresponding antibonding bands with major contribution of Ta-5*d* states. The band gap opens within the occupied Π-band and the unoccupied Π*-band. A clear picture emerges in $Sr_2Ta_2O_7$ and $BaSrTa_2O_7$: the top of VB is mainly formed by O-2*p* states, while the bottom of CB is constructed mostly by Ta-5*d* empty states. Nevertheless, overlapping between Ta and O occurs in both bands, which is a demonstration of Ta–O covalence. The calculated effective Bader charges (Table S3) support the strong covalent character of the Ta–O bonding. Importantly, $BaSrTa_2O_7$ presents a wider CB that $Sr_2Ta_2O_7$. In particular, the bottom of the CB of $BaSrTa_2O_7$ shows a widening arising from the Ta-5d_{xy} orbital (Fig. 5e). As discussed below, this is linked to particular crystal structural features of $BaSrTa_2O_7$ which are not present in $Sr_2Ta_2O_7$. It should be noted that Ba/Sr states barely contribute to the valence band, with the corresponding empty n*s* and n*p* states placed at high energies above the Fermi level (8 eV). This is indicative of the ionic interaction between the Ta–O perovskite layers and the inter/intralayer alkaline-earth ions.

Table 3 compares the calculated band gap values to the experimental ones. The same trends in dependency on the XC functional for band gap accuracy hold for both $Sr_2Ta_2O_7$ and $BaSrTa_2O_7$. The hybrid functional-HSE06 yields band gaps in excellent agreement with the experimental values (4.58 eV and 3.95 eV, for $Sr_2Ta_2O_7$ and $BaSrTa_2O_7$, respectively), although at the expense of a high computational cost [34,35]. The calculated values using the SCAN functional underestimate the experimental ones in 1 eV. Unsurprisingly, the underestimation within the PBE is as large as 1.5 eV. Noteworthy, the results show that independently of the XC-functional –SCAN, HSE06, PBE–, the calculated band gaps of $Sr_2Ta_2O_7$ and $BaSrTa_2O_7$ differ in about 0.6 eV. In this sense, all the tested functionals correctly reproduce the band gap difference between the two compounds extracted from the UV–vis DRS measurements.

Table 3
Calculated band gap values for $Sr_2Ta_2O_7$ and $BaSrTa_2O_7$ oxides. Experimental data (this work) are given for comparison. The difference between the two compounds is given as $Sr_2Ta_2O_7$ minus $BaSrTa_2O_7$ values.

Compound	Experimental (eV)		Calculated (eV)			
	Direct	Indirect	PBE	PBE-other works	SCAN	HSE06
$Sr_2Ta_2O_7$	4.6	4.4	3.07	2.91 [36], 2.88 [14], 2.93 [13]	3.57	4.58
$BaSrTa_2O_7$	4.0	3.8	2.56	2.19 [36]	3	3.95
Difference	0.6	0.6	0.51	0.72 [36]	0.57	0.63

3.2.2. Substituted $Sr_{2-x}Ba_xTa_2O_7$ compounds

$BaSrTa_2O_7$ and $Sr_2Ta_2O_7$ differ not only in composition, but also in crystal structure. A DFT investigation of $Sr_{2-x}Ba_xTa_2O_7$ compounds allows to elucidate the role of the Ba/Sr content and of the structure in the electronic structure. The results for $Sr_2Ta_2O_7$ and $BaSrTa_2O_7$ demonstrate that the SCAN functional correctly reproduces the lattice parameters and the interatomic distances of the experimental structures, and it is suitable to extract qualitative trends from electronic structure calculations. Indeed, recent works demonstrate the suitability and reliability of the SCAN functional to investigate transition metal oxides at a moderate computational cost, even in complex oxides with the electronic structure dominated by strong electron correlation [37,38]. Consequently, the DFT study of the substituted $Sr_{2-x}Ba_xTa_2O_7$ series of compounds –with either the PB or the DJ structure-has been performed using the SCAN functional.

The relative thermodynamic stability of the hypothetical PB and DJ-$Sr_{2-x}Ba_xTa_2O_7$ compounds towards the existing compounds PB-$Sr_2Ta_2O_7$ and DJ-$BaSrTa_2O_7$ can be evaluated considering the energy of the reaction:

$$(1 - x)\ Sr_2Ta_2O_7 + x\ BaSrTa_2O_7 \rightarrow Sr_{2-x}Ba_xTa_2O_7 \quad (2)$$

The calculated energy of reaction (2) is positive for all the modelled $Sr_{2-x}Ba_xTa_2O_7$ compounds (Figure S4), indicating their poor stability and trend to decompose into the experimentally know compounds. This is in line with the unsuccessful attempts to prepare PB-$Sr_{2-x}Ba_xTa_2O_7$ with $x > 0.3$ [15]. Nevertheless, the analysis of the calculated crystal and electronic structures of PB and DJ-$Sr_{2-x}Ba_xTa_2O_7$ compounds is relevant to understand the relation between chemical composition, crystallographic structure, and catalytic properties.

In $Sr_{2-x}Ba_xTa_2O_7$ ($0 \leq x \leq 1$) compounds, a greater Ba content produces larger lattice parameters and cell volume (Figures S5 and S7), consistently with its larger ionic radii (ionic radii for C.N. = 12: 1.44 Å for Sr^{2+}, and 1.61 Å for Ba^{2+} [39]). All the investigated $Sr_{2-x}Ba_xTa_2O_7$ compounds present minor structural distortions compared to the parent structures (DJ or PB) (**see S.I.**). Regarding the electronic structure of PB-DJ-$Sr_{2-x}Ba_xTa_2O_7$, the calculated DOS indicate that the electronic structures of the parent compounds (DJ-$BaSrTa_2O_7$ and PB-$Sr_2Ta_2O_7$) do not suffer significant changes when distinct x values are considered (see Figures S10-S11). Indeed, for each structural type, the DOS features are maintained at every studied composition, with only subtle variations in the calculated band gap. Noteworthy, the bottom of the CB is clearly different in the PB-series than in the DJ-series, with the widening arising from $5d_{xy}$ states dominating in the latter.

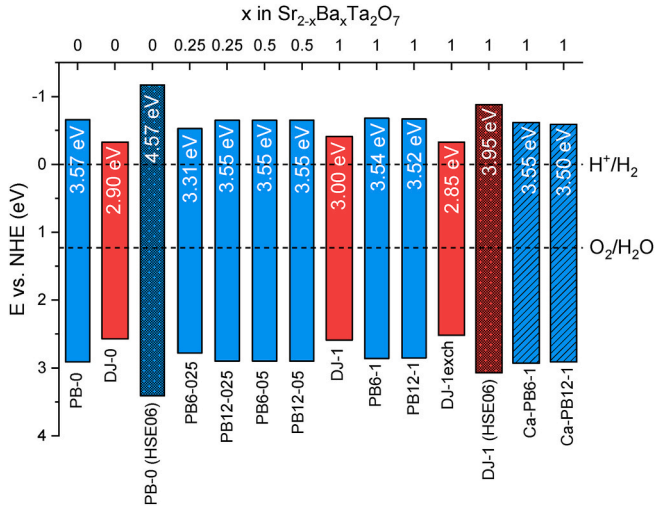

Fig. 6. Valence and conduction band-edges in the NHE scale extracted from DFT calculations of $Sr_{2-x}Ba_xTa_2O_7$ compounds, and $Sr_{2-x}Ca_xTa_2O_7$ compounds (taken from Ref. [40]). The value of the calculated band gap is also shown. Electrochemical redox potentials for water are drawn as dashed lines. Blue and red bars correspond to the PB and DJ series, respectively.

Along with band gap value, band-edges energy is vital for a semiconductor to show photocatalytic activity. Fig. 6 shows the VB and CB edges in the NHE scale, and the calculated band gap of the different structures and compositions studied for the $Sr_{2-x}A_xTa_2O_7$ compounds (A = Ba and Ca [40]), within the PB structure (in blue) and the DJ structure (in red). The calculated values for band edge positions indicate that all the modelled compounds fulfil the requirement of the positions of CB and VB edges relative to the electrochemical water redox potentials. The CBM is more negative than the H^+/H_2 potential, and the VBM is more positive than O_2/H_2O potential in all cases. As inferred from Fig. 6, the DJ series yields SCAN-band gaps values around 3 eV, whilst the band gap of the PB series is around 3.5 eV.

4. Discussion

The determined band gaps of the PB-$Sr_2Ta_2O_7$ (4.6 eV) and DJ-$BaSrTa_2O_7$ (4 eV) samples have shown a ~0.6 eV difference, which is well reproduced by DFT calculations. In addition, DFT calculations disclose a notorious difference in the width and the shape of the bottom of the CB of these compounds. In $BaSrTa_2O_7$, the wider conduction band and narrower band gap is likely to produce an enhancement of the photocatalytic activity, which is indeed confirmed by a 26% increase in hydrogen production of DJ-$BaSrTa_2O_7$ compared to PB-$Sr_2Ta_2O_7$. In an attempt to rationalize the observed photocatalytic performance of PB-$Sr_2Ta_2O_7$ and DJ-$BaSrTa_2O_7$, this section discusses the relation between electronic structure, crystal structure and chemical composition.

DFT calculations for $Sr_{2-x}Ba_xTa_2O_7$ compounds reveal that the Ba/Ca content does not induce significant crystallographic or electronic structure modifications (band gaps, and band-edges/shape). Given the Coulomb type interaction between the [TaO_6] octahedral and the alkaline earth-cations in the perovskite blocks and in interlayer space, the nature of the alkaline-earth (Ca, Ba or Sr) has a minor impact on the band gap. Therefore, for a given structural type (PB or DJ), the band gap variation with the Ba/Sr content (x value) is in the order of 0.2 eV. This is similar to the calculated band gap (PBE) variation encountered in the layered $MCa_2Ta_3O_{10}$ (M = alkaline cation), composed of a triple perovskite $MCaTa_3O_{10}$ slab [41]: 2.17 eV (Li), 2.18 eV (K) and 2.20 eV (Rb) [36].

Ruling out a prominent role of Ba/Sr in the electronic structure of $Sr_{2-x}Ba_xTa_2O_7$, the focus is on the crystal structure. As a matter of fact, the major differences in the electronic structure are observed between DJ-derived ((100) type layered-perovskite) and PB-derived ((110) type layered-perovskite) compounds. DFT calculations uncover that for a given structural type (PB or DJ), and independently on the Ba/Sr content, the band gap values, band-edge positions and bands shape are nearly the same. The crystallographic differences between PB and DJ structures include the number of perovskite units in the layers, octahedral tilting, and coordination of cations in the interlayer space. The structural factors affecting the modification of the electronic structure are not easy to evaluate since they are highly correlated.

The electronic structure of cubic ABO_3 perovskites is formed essentially by 180° TM – O – TM interaction of octahedral site cations (see Figure S3). Therefore, in d^0 perovskites, the band gap is determined by the energy difference between the bonding and anti-bonding interactions between the TM-n*d* and O-2*p*, which are extremely connected to the TM – O – TM angles. The tilting of the TM octahedra is a well-recognized key factor in the electronic structure of perovskite oxides [33,42,43]. Octahedra tilting, and hence the deviation of the TM – O – TM angle from 180°, worsens the TM – O overlapping, leading to narrower bands and an increment of the band gap width [33] (see Table S10). Nonetheless, the effect observed in the tittle perovskite-type layered compounds is the opposite. As seen in Fig. 1 and in the **SI**, the distortion of Ta–O–Ta angles is lower in PB-compounds (wider band gap) than in DJ-compounds (narrower band gap).

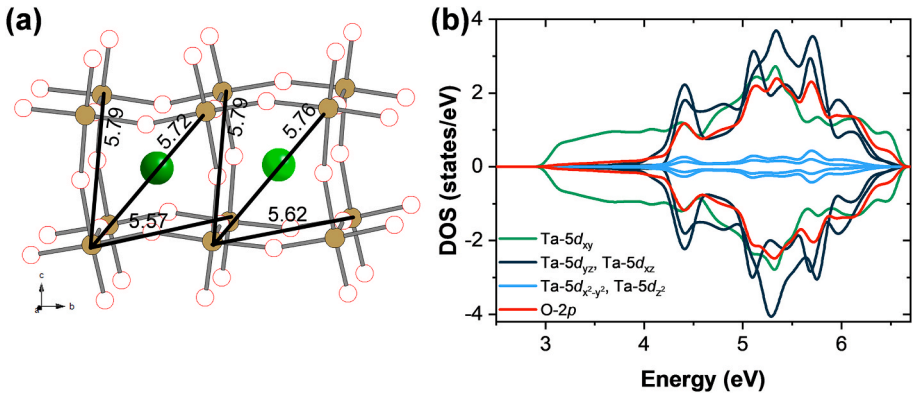

Fig. 7. (a) Snapshot of the DJ-$BaSrTa_2O_7$ crystal structure, showing the eight octahedra that form the unit cell of the perovskite for Sr1 (light green) and Sr2 (dark green). The Ta–Ta distances at the diagonals of the perovskite unit cell are indicated in black. Color code: Sr1 in light green, Sr2 in dark green, O in red and Ta in brown. (b) Orbital projected DOS for DJ-compounds, with the Fermi level set as the zero of energy. At the bottom of the conduction band the mayor contribution is of Ta-5d_{xy} states with almost no contribution of O-2p states (TM-TM band). Color code: Ta-5d_{xy} in green, Ta-5d_{yz} and Ta-5d_{xz} in dark blue, Ta-5d^2_{xy} and Ta-5d^2_z in light blue and O in red.

The calculated DOS indicate that in DJ compounds the widening of the conduction band and narrowing of the band gap is related to Ta-d_{xy} orbitals (Fig. 5). This suggests direct Ta–Ta interactions through the overlapping of the Ta-d_{xy} orbitals across the face diagonal of the cubic structure. Indeed, in $BaSrTa_2O_4$ the Ta–Ta distances along the [110] diagonal are much shorter than in the [011] and [101] diagonals (Fig. 7a). As can be observed in Fig. 7b, the distinct Ta–Ta distances break down the t_{2g} orbitals degeneracy, bringing the 5d_{xy} orbital to the bottom of the conduction band. While Ta–Ta distances seem to be key in the electronic structure, they are interrelated with the bending of Ta–O–Ta angles and the off-centred of Ta ions in the octahedra.

The connectivity of Ta octahedra is another likely cause of slight variations in the CB width, affecting the band gap value, as previously observed by Eng et al. in layered d^0 perovskites [42]. In $Sr_2Ta_2O_7$, Ta1 (i.e., the one near the interlayer zone), only shares 4 vertices with neighbour octahedral, while Ta2 shares its 6 corners. Meanwhile, in $BaSrTa_2O_7$ all Ta are connected by 5 vertices; this open active site could facilitate the reagent adsorption and activation. It is plausible that the different connectivity could play a role in the electronic structure of these compounds.

In summary, the enhanced photocatalytic activity for hydrogen evolution reaction of $BaSrTa_2O_7$ is likely rooted in peculiarities of its electronic structure, a topic that has been previously well studied for perovskite compounds [33,42,43]. From a careful analysis of the crystal structure features, determining the electronic structure of $Sr_2Ta_2O_7$ and $BaSrTa_2O_7$, the most remarkable finding is the shorter Ta–Ta distance in $BaSrTa_2O_7$, which promotes the 5d_{xy} orbital overlapping, causing the band widening and band gap narrowing.

It should be remarked that the present computational study has addressed the very fundamental requirements of the materials to catalyse water splitting (band gap, band-edge energy, and shape) that are amenable to basic DFT investigations. As highlighted by Morales-García et al., the detailed description of photocatalyzed processes from calculations should take into account the localization of the regions where electrons and holes are placed, the determination of the lifetime of the photogenerated species, as well as the usage of strategies capable of exploring reaction mechanism on the exited-state [44]. Therefore, the research herein exposed is a starting point to further study the performance of $BaSrTa_2O_7$ and related DJ-perovskites as photocatalysts.

5. Conclusions

This work demonstrates for the first time the photocatalytic hydrogen evolution activity of the perovskite-type layered $BaSrTa_2O_7$ (a Dion-Jacobson (100)-type layered perovskite, S.G. *Immm*). This material exceeds the activity reported for most tantalates. The $BaSrTa_2O_7$ hydrogen production is 26% higher than that of $Sr_2Ta_2O_7$ (S.G. *Cmcm,* a (110)-type layered perovskite). While both materials are perovskites-type layered compounds based on Ta, their measured band gap energies differ in a substantial value of 0.6 eV. DFT calculations allowed a comprehensive analysis of the crystal and electronic structures of $Sr_2Ta_2O_7$ and $BaSrTa_2O_7$, and related $Sr_{2-x}Ba_xTa_2O_7$ compounds. It is found that the major differences in the electronic structure between $BaSrTa_2O_7$-derived and $Sr_2Ta_2O_7$-derived compounds obey their distinct crystal structures. Among the structural factors controlling the electronic structure, the shorter Ta–Ta distance in the diagonal of the perovskite unit-cell of $BaSrTa_2O_7$ enhances the Ta–Ta t_{2g} orbital overlapping, promoting the widening of the bottom of the conduction band and a band gap narrowing.

Although certainly many other factors control the hydrogen production, tuning the electronic structure of DJ-$BaSrTa_2O_7$ by compositional modifications is a successful approach to enhance its photocatalytic activity. This work demonstrates the minor impact of the alkaline-earth nature and content in the electronic structure of $BaSrTa_2O_7$. Hence, a plausible strategy is the substitution of Ta with other transition metals favouring TM–TM interactions that might lead to better photocatalytic performance for hydrogen evolution.

Some words must be devoted to computational methodologies. The HSE06 and SCAN functionals correctly reproduce the experimental unit cell parameters and bond lengths, as well as the measured band gap difference between $Sr_2Ta_2O_7$ and $BaSrTa_2O_7$. The hybrid HSE06 XC-functional provides band gap values extremely close to the experimentally known in metal transition oxides (errors in this work are below 0.1 eV). However, in terms of computational time, the utilization of hybrid XC-functionals is extremely costly, and in some cases prohibited. In line with recent advances in the development of *meta*-GGA functionals, the present results validate the utilization of the SCAN functional to investigate the crystal and electronic structures of transition metal oxides and extract band gap trends.

Author contributions

Marianela Gómez-Toledo: Investigation, Methodology, Software, Data curation, Validation, Formal analysis, Visualization, Writing – Original Draft. **Khalid Boulahya**: Supervision, Investigation, Resources, Writing – Review & Editing. **Laura Collado**: Investigation, Validation, Visualization, Writing – Review & Editing. **Víctor A. de la Peña O'Shea**: Project Administration, Funding acquisition, Writing – Review & Editing. **Elena Arroyo-de Dompablo**: Conceptualization, Supervision, Funding acquisition, Project Administration, Writing – Original Draft.

Declaration of competing interest

The authors declare that they have no known competing financial interests or personal relationships that could have appeared to influence the work reported in this paper.

Acknowledgments

UCM authors thank funding from MCIN/AEI/10.13039/501100011033 ERDF A way of making Europe - EU across the project ECSAWE (PID2022-139501OB-C22) and from Universidad Complutense de Madrid (FEI-EU-22-01- 4129585). MGT thanks Comunidad de Madrid for contract (PEJ-2020-AI/IND-18065) of the program "Ayudas para la contratación de Ayudantes de Investigación y Técnicos de Laboratorio". IMDEA authors acknowledge ARMONIA (PID2020–1191 25RJ-I00) and the strategic research lines project SOL-Future (PLE C2021-0079069) funded by MICIU/AEI/10.13039/501100011033 and NextGenerationEU/PRTR. Additional funding was received from TED2021-130173B–C41. The authors acknowledge Wilfredo More and ICV-CISC for DRS measurements, as well as MALTA-Consolider and I2Basque for access to computational facilities.

Appendix A. Supplementary data

Supplementary data to this article can be found online at https://doi.org/10.1016/j.ijhydene.2024.02.346.

References

[1] Abdalla AM, Hossain S, Nisfindy OB, Azad AT, Dawood M, Azad AK. Hydrogen production, storage, transportation and key challenges with applications: a review. Energy Convers Manag 2018;165:602–27. https://doi.org/10.1016/j.enconman.2018.03.088.

[2] Megía PJ, Vizcaíno AJ, Calles JA, Carrero A. Hydrogen production Technologies: from fossil fuels toward renewable sources. A Mini review. Energy & Fuels 2021; 35:16403–15. https://doi.org/10.1021/acs.energyfuels.1c02501.

[3] Ishaq H, Dincer I, Crawford C. A review on hydrogen production and utilization: challenges and opportunities. Int J Hydrogen Energy 2022;47:26238–64. https://doi.org/10.1016/j.ijhydene.2021.11.149.

[4] Wang Z, Li C, Domen K. Recent developments in heterogeneous photocatalysts for solar-driven overall water splitting. Chem Soc Rev 2019;48:2109–25. https://doi.org/10.1039/c8cs00542g.

[5] Osterloh FE. Inorganic materials as catalysts for photochemical splitting of water. Chem Mater 2008;20:35–54. https://doi.org/10.1021/cm7024203.

[6] Yan H, Wang X, Yao M, Yao X. Band structure design of semiconductors for enhanced photocatalytic activity: the case of TiO_2. Prog Nat Sci: Mater Int 2013;23: 402–7. https://doi.org/10.1016/j.pnsc.2013.06.002.

[7] Sakata Y, Miyoshi Y, Maeda T, Ishikiriyama K, Yamazaki Y, Imamura H, et al. Photocatalytic property of metal ion added $SrTiO_3$ to Overall H_2O splitting. Appl Catal Gen 2016;521:227–32. https://doi.org/10.1016/j.apcata.2015.12.013.

[8] Hu Y, Mao L, Guan X, Tucker KA, Xie H, Wu X, et al. Layered perovskite oxides and their derivative nanosheets adopting different modification strategies towards better photocatalytic performance of water splitting. Renew Sustain Energy Rev 2020;119. https://doi.org/10.1016/j.rser.2019.109527.

[9] Brito AS, Bouquet V, Demange V, Cheviré F, Guilloux-Viry M, Marinho TD, et al. Theoretical-experimental evaluation of the photocatalytic activity of $KCa_2Ta_{3-x}Nb_xO_{10}$. Mater Lett 2019;253:392–5. https://doi.org/10.1016/j.matlet.2019.07.006.

[10] Zhang G, Liu G, Wang L, Irvine JT. Inorganic perovskite photocatalysts for solar energy utilization. Chem Soc Rev 2016;45:5951–84. https://doi.org/10.1039/c5cs00769k.

[11] Ishizawa N, Marumo F, Kawamura T, Kimura M. Compounds with perovskite-type slabs. II. The crystal structure of $Sr_2Ta_2O_7$. Acta Crystallogr B 1976;32:2564. https://doi.org/10.1107/S0567740876008261.

[12] Kudo A, Kato H, Nakagawa S. Water splitting into H_2 and O_2 on new $Sr_2M_2O_7$ (M = Nb and Ta) photocatalysts with layered perovskite structures: factors affecting the photocatalytic activity. J Phys Chem B 2000;104:571–5. https://doi.org/10.1021/jp9919056.

[13] Liu P, Nisar J, Ahuja R, Pathak B. Layered perovskite $Sr_2Ta_2O_7$ for visible light photocatalysis: a first principles study. J Phys Chem C 2013;117:5043–50. https://doi.org/10.1021/jp310945e.

[14] Peng Y, Ma Z, Hu J, Wu K. A first-principles study of anionic (S) and cationic (V/Nb) doped $Sr_2Ta_2O_7$ for visible light photocatalysis. RSC Adv 2017;7:40922–8. https://doi.org/10.1039/c7ra07113b.

[15] Kim KY, Eun TH, Lee S-S, Chon U. Photocatalytic activities and structural changes of barium-doped strontium tantalate. Resour Process 2009;56:138–44. https://doi.org/10.4144/rpsj.56.138.

[16] Le Berre F, Crosnier-Lopez M-P, Fourquet J-L. Cationic ordering in the new layered perovskite $BaSrTa_2O_7$. Solid State Sci 2004;6:53–9. https://doi.org/10.1016/j.solidstatesciences.2003.10.008.

[17] Rodriguez-Carvajal J. Recent advances in magnetic structure determination neutron powder diffraction. Physica B 1993;192:55–69. https://doi.org/10.1016/0921-4526(93)90108-I.

[18] Kubelka P, Munk FA. Contribution to the optics of pigments. Z Technol Phys 1931; 12:593–9.

[19] Tauc J, Grigorovic R, Vancu A. Optical properties and electronic structure of Amorphous Germanium. Phys Status Solidi 1966;15:627. https://doi.org/10.1002/pssb.19660150224.

[20] Kresse G, Joubert D. From ultrasoft pseudopotentials to the projector augmented-wave method. Phys Rev B 1999;59:1758. https://doi.org/10.1103/PhysRevB.59.1758.

[21] Blochl PE. Projector augmented-wave method. Phys Rev B Condens Matter 1994; 50:17953–79. https://doi.org/10.1103/physrevb.50.17953.

[22] Sun J, Ruzsinszky A, Perdew JP. Strongly constrained and appropriately normed Semilocal density functional. Phys Rev Lett 2015;115:036402. https://doi.org/10.1103/PhysRevLett.115.036402.

[23] Heyd J, Scuseria GE, Ernzerhof M. Hybrid functionals based on a screened Coulomb potential. J Chem Phys 2003;118:8207. https://doi.org/10.1063/1.1564060.

[24] Blochl PE, Jepsen O, Andersen OK. Improved tetrahedron method for Brillouin-zone integrations. Phys Rev B Condens Matter 1994;49:16223–33. https://doi.org/10.1103/physrevb.49.16223.

[25] Bader RFW. Atoms in Molecules: a Quantum theory. Oxford, U.K: Oxford University Press; 1990.

[26] Ong SP, Richards WD, Jain A, Hautier G, Kocher M, Cholia S, et al. Python Materials Genomics (pymatgen): a robust, open-source python library for materials analysis. Comput Mater Sci 2013;68:314–9. https://doi.org/10.1016/j.commatsci.2012.10.028.

[27] Ishizawa N, Marumo F, Iwai S. Compounds with perovskite-type slabs. IV. Ferroelectric phase transitions in $Sr_2(Ta_{1-x}Nb_x)_2O_7$ ($x \sim 0.12$) and $Sr_2Ta_2O_7$. Acta Crystallogr B 1980;37:26–31. https://doi.org/10.1107/S0567740881002124.

[28] Moses PG, Miao M, Yan Q, Van de Walle CG. Hybrid functional investigations of band gaps and band alignments for AlN, GaN, InN, and InGaN. J Chem Phys 2011; 134:084703. https://doi.org/10.1063/1.3548872.

[29] Wu Y, Chan MKY, Ceder G. Prediction of semiconductor band edge positions in aqueous environments from first principles. Phys Rev B 2011;83. https://doi.org/10.1103/PhysRevB.83.235301.

[30] Castelli IE, Landis DD, Thygesen KS, Dahl S, Chorkendorff I, Jaramillo TF, et al. New cubic perovskites for one- and two-photon water splitting using the computational materials repository. Energy Environ Sci 2012;5. https://doi.org/10.1039/c2ee22341d.

[31] Castelli IE, Olsen T, Datta S, Landis DD, Dahl S, Thygesen KS, et al. Computational screening of perovskite metal oxides for optimal solar light capture. Energy Environ Sci 2012;5:5814–9. https://doi.org/10.1039/c1ee02717d.

[32] Boeyens JCA. The periodic electronegativity table. Z Naturforsch 2008;63: 199–209. https://doi.org/10.1515/znb-2008-0214.

[33] Kato H, Kudo A. Water splitting into H_2 and O_2 on alkali tantalate photocatalysts $ATaO_3$ (A = Li, Na, and K). J Phys Chem B 2001;105:4285–92. https://doi.org/10.1021/jp004386b.

[34] Bilc DI, Orlando R, Shaltaf R, Rignanese GM, Íñiguez J, Ghosez P. Hybrid exchange-correlation functional for accurate prediction of the electronic and structural properties of ferroelectric oxides. Phys Rev B 2008;77. https://doi.org/10.1103/PhysRevB.77.165107.

[35] Viñes F, Lamiel-García O, Ko KC, Lee JY, Illas F. Systematic study of the effect of HSE functional internal parameters on the electronic structure and band gap of a representative set of metal oxides. J Comput Chem 2017;30:781–9. https://doi.org/10.1002/jcc.24744.

[36] Jain A, Ong SP, Hautier G, Chen W, Richards WD, Dacek S, et al. Commentary: the Materials Project: a materials genome approach to accelerating materials innovation. Apl Mater 2013;1. https://doi.org/10.1063/1.4812323.

[37] Sai Gautam G, Carter EA. Evaluating transition metal oxides within DFT-SCAN and SCAN+*U* frameworks for solar thermochemical applications. Phys Rev Mater 2018; 2:095401. https://doi.org/10.1103/PhysRevMaterials.2.095401.

[38] Gómez-Toledo M, López-Paz SA, García-Martín S, Arroyo-de Dompablo ME. Metal-to-Insulating transition in the perovskite system $YSr_2Cu_2FeO_{(8-\delta)}$ ($0 < \delta < 1$) modeled by DFT methods. Inorg Chem 2023;62:3445–56. https://doi.org/10.1021/acs.inorgchem.2c03475.

[39] Shannon RD. Revised effective ionic radii and systematic studies of interatomie distances in halides and chaleogenides. Acta Crystallogr 1976;A32:751–67. https://doi.org/10.1107/S0567739476001551.

[40] Gómez-Toledo M, Boulahya K, Arroyo-de Dompablo ME. First principles study on the features of $Ca_xSr_{2-x}Ta_2O_7$ (x = 0, 1) as a photocatalytic material. Engineering Proceedings 2022:31. https://doi.org/10.3390/asec2022-13794.

[41] Toda K, Teranishi T, Ye Z-G, Sato M, Hinatsu Y. Structural chemistry of new ion-exchangeable tantalates with layered perovskite structure: new dion–jacobson phase $MCa_2Ta_3O_{10}$ (M = alkali metal) and ruddlesden–popper phase $Na_2Ca_2Ta_3O_{10}$. Mater Res Bull 1999;34:971–82. https://doi.org/10.1016/S0025-5408(99)00084-7.

[42] Eng HW, Barnes PW, Auer BM, Woodward PM. Investigations of the electronic structure of d^0 transition metal oxides belonging to the perovskite family. J Solid State Chem 2003;175:94–109. https://doi.org/10.1016/s0022-4596(03)00289-5.

[43] Bouafia H, Hiadsi S, Abidri B, Akriche A, Ghalouci L, Sahli B. Structural, elastic, electronic and thermodynamic properties of $KTaO_3$ and $NaTaO_3$: Ab initio investigations. Comput Mater Sci 2013;75:1–8. https://doi.org/10.1016/j.commatsci.2013.03.030.

[44] Morales-Garcia A, Vines F, Sousa C, Illas F. Toward a Rigorous Theoretical description of photocatalysis using Realistic models. J Phys Chem Lett 2023;14: 3712–20. https://doi.org/10.1021/acs.jpclett.3c00359.

Supporting Information

Upgrading photocatalytic hydrogen evolution in Ba-Sr-Ta-O perovskite-type layered structures

Marianela Gómez-Toledo[1], Khalid Boulahya[1], Laura Collado[2], Víctor A. de la Peña O'Shea[2] and M. Elena Arroyo-de Dompablo[1,*]

[1]Departamento de Química Inorgánica, Universidad Complutense de Madrid, 28040 Madrid, Spain

[2] Photoactivated Processes Unit, IMDEA Energy Institute, Parque Tecnológico de Móstoles, Avda. Ramón de la Sagra 3, 28935 Móstoles, Madrid, Spain

* Correspondence: mearroyo@ucm.es

Table S1. Selected Ta-oxides reported as UV-photocatalyst for the water splitting reaction. For more details see [1] and references therein.

Oxide	**Cocatalyst**	**Maximum H_2 production rate reported**
Ta_2O_5	NiO_x	1150 μmol g^{-1} h^{-1} [2]
$Rb_4Nb_6O_{17}$	NiO	936 μmol g^{-1} h^{-1} [3]
$NaTaO_3$	NiO	1980 μmol g^{-1} h^{-1} [4]
$La_{1/3}TaO_3$	NiO	70 μmol g^{-1} h^{-1} [5]
$KTa_{0.2}Ti_{0.8}O_{1.1}$	NiO	1000 μmol g^{-1} h^{-1} [6]
$SrTa_2O_6$	NiO	960 μmol g^{-1} h^{-1} [7]
$NiTa_2O_6$		11 μmol g^{-1} h^{-1} [2]
$Ca_2Ta_2O_7$	NiO	340 μmol g^{-1} h^{-1} [8]
Bi_2LaTaO_7		41.8 μmol g^{-1} h^{-1} [9]
$Sr_2Ta_2O_7$	NiO	1000 μmol g^{-1} h^{-1} [10]
$Sr_2Ta_2O_7$		52 µmol g^{-1} h^{-1} [10]
$Sr_2Ta_2O_7$ $BaSr_2Ta_2O_7$	Pt	2000 µmol·g^{-1}·h^{-1} (this work) 2900 µmol·g^{-1}·h^{-1} (this work)
$KBa_2Ta_3O_{10}$	NiO	150 μmol g^{-1} h^{-1} [11]
$Sr_4Ta_2O_9$, $M_5Ta_4O_{15}$ (M=Sr, Ba)	NiO	64 μmol g^{-1} h^{-1} ($Sr_4Ta_2O_9$) [12] 2388 μmol g^{-1} h^{-1} ($Sr_5Ta_4O_{15}$) [12] 2080 µmol g^{-1} h^{-1} ($Ba_5Ta_4O_{15}$) [13]
$K_3Ta_3Si_2O_{13}$	NiO	368 μmol g^{-1} h^{-1} [14]
La_3TaO_7		328 μmol g^{-1} h^{-1} [15]
$LaTaO_4$	NiO	578 μmol g^{-1} h^{-1} [16]

1. $Sr_2Ta_2O_7$ and $BaSrTa_2O_7$

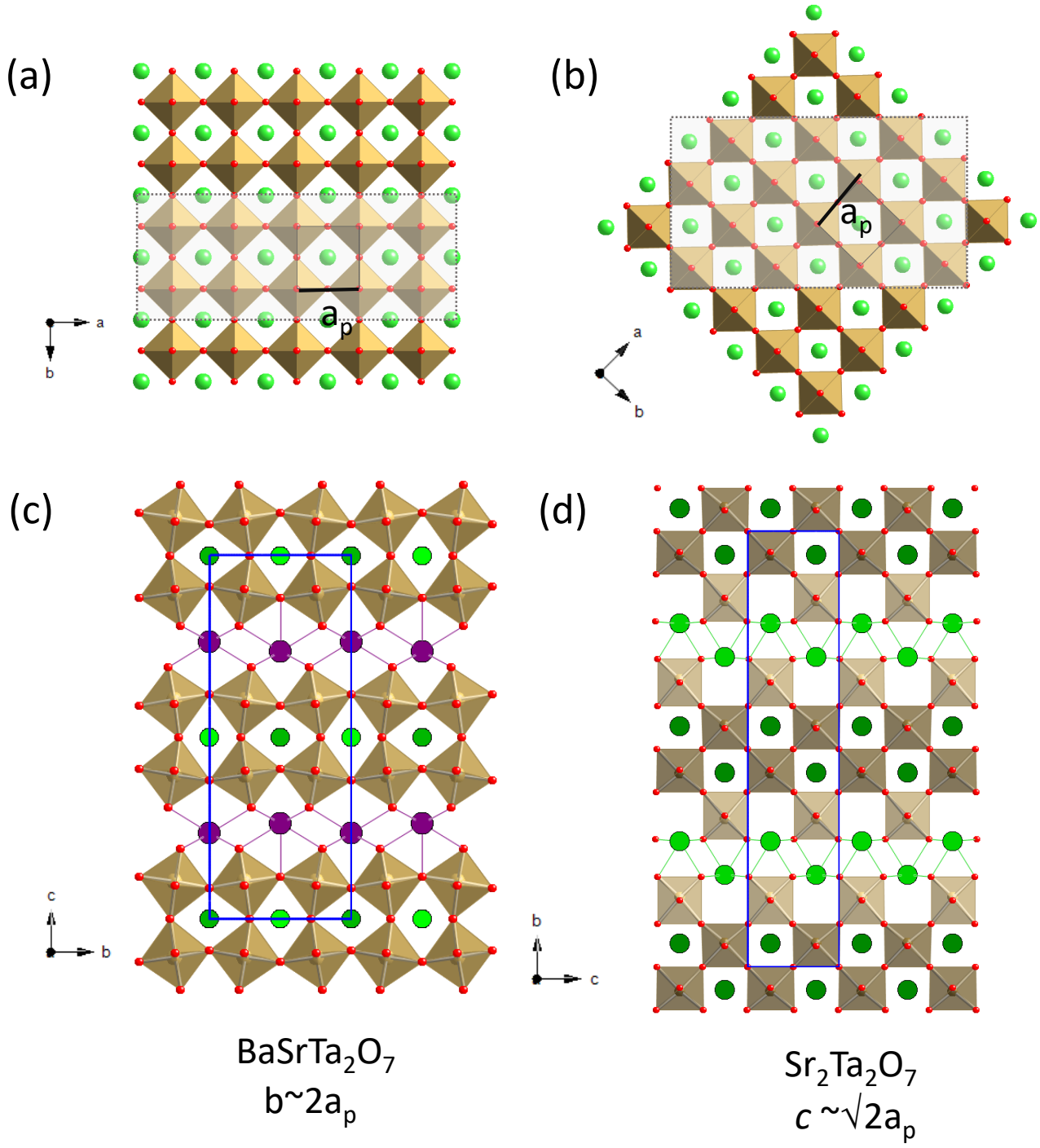

Figure S1. (a) (100) and (b) (110) slabs relative to the principal axis of an ideal cubic perovskite structure and the resulting layered perovskites of (c) $BaSrTa_2O_7$ and (d) $Sr_2Ta_2O_7$. Color code: Ta in brown, Sr in green, Ba in purple and O in red.

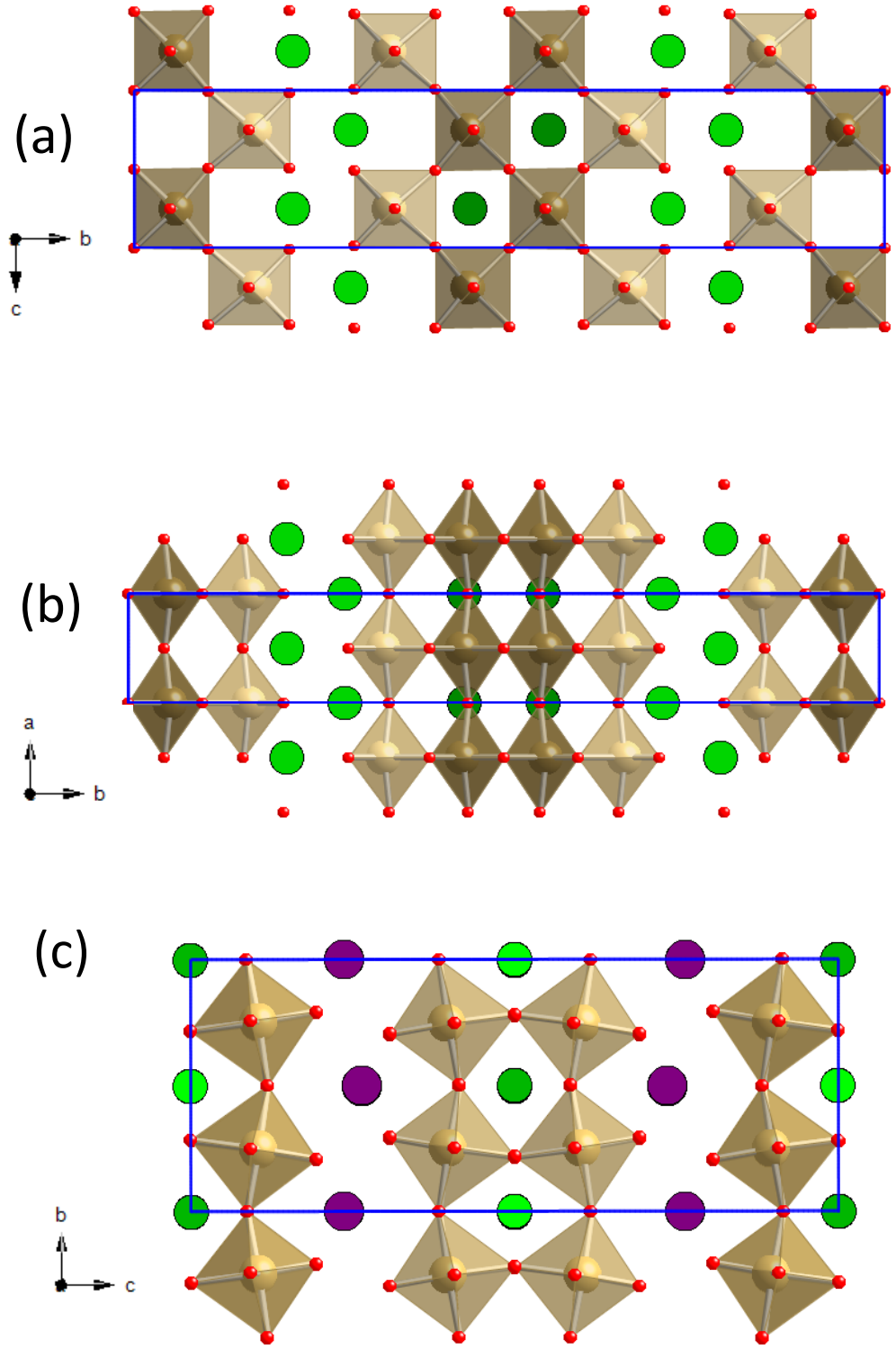

Figure S2. The crystal structure of $Sr_2Ta_2O_7$ viewed (a) along the *a* (b) along *c*, and (c) the structure of $BaSrTa_2O_7$ viewed along *a*. Note the displacements of the Ta atoms from the centers of their respective octahedra in the perovskite slabs. Color code: Ta in brown, Sr in green, Ba in purple and O in red.

Table S2: Calculated unit cell parameters (Å), unit cell volume (Å^3), and bond-lengths (Å) for $Sr_2Ta_2O_7$ and $BaSrTa_2O_7$ obtained within GGA-PBE XC-functional.

$Sr_2Ta_2O_7$	Experimental	Calculated		$BaSrTa_2O_7$	Experimental	Calculated	
		GGA	error			GGA	error
a	3.9376	3.9893	1.3	*a*	3.993725	4.0261	0.8
b	27.1986	27.6043	1.5	*b*	7.84281	7.9000	0.7
c	5.6927	5.7473	1.0	*c*	20.16093	20.5429	1.9
Volume	609.5	632.9	3.8	Volume	631.48	653.4	3.5
Sr1-O	2.47 x 4	2.508 x 4	1.5	Sr1–O	2.72 x 4	2.756	1.3
Sr1-O	2.60 x 2	2.590 x 2	0.4	Sr1–O	2.63 x 4	2.621	0.3
Sr1-O	3.27 x 2	3.385 x 2	3.5	Sr1–O	3.10 x 4	3.062	1.2
Sr2-O	2.71 x 4	2.739 x 4	1.1	Sr2–O	2.65 x 4	2.588	2.3
Sr2-O	2.827 x 4	2.870 x 4	1.5	Sr2–O	2.69 x 4	2.721	1.2
Sr2-O	2.850 x 2	2.879 x 2	1.0	Sr2–O	2.98 x 4	3.035	1.8
Sr2-O	2.7	2.645	2.0	Ba–O	2.705 x 2	2.748 x 2	1.6
Sr2-O	2.74	2.784	1.6	Ba–O	2.713 x 4	2.741	1.0
Ta1-O	1.87 x 2	1.882 x 2	0.6	Ba–O	2.94	3.070	4.4
Ta1-O	1.979 x 2	2.014 x 2	1.8	Ta–O	2.011 x 2	2.024 x 2	0.6
Ta1-O	2.16 x 2	2.169 x 2	0.4	Ta–O	1.977	2.018	2.1
Ta2-O	1.89 x 2	1.922 x 2	1.7	Ta–O	1.976	2.000	1.2
Ta2-O	1.980 x 2	2.006 x 2	1.3	Ta–O	2.113	2.172	2.8
Ta2-O	2.070 x 2	2.086 x 2	0.8	Ta–O	1.83	1.880	2.7
mean Ta-	1.992	2.013	1.1	mean Ta-	1.986	2.020	1.7

Table S3. Calculated local effective Bader charges (Q) for $Sr_2Ta_2O_7$ and $BaSrTa_2O_7$ oxides.

PB-$Sr_2Ta_2O_7$			DJ-$BaSrTa_2O_7$		
	SCAN	HSE06		SCAN	HSE06
Q (Sr1)	1.67	1.68	Q (Ba)	1.65	1.67
Q (Sr2)	1.63	1.64	Q (Sr)	1.62	1.64
Q (Ta1)	2.83	2.93	Q (Ta)	2.87	2.96
Q (Ta2)	2.88	2.96	Q (O1)	-1.29	-1.32
Q (O1)	-1.26	-1.30	Q (O2)	-1.31	-1.33
Q (O2)	-1.28	-1.30	Q (O3)	-1.27	-1.30
Q (O3)	-1.30	-1.33	Q (O4)	-1.37	-1.40
Q (O4)	-1.36	-1.38	Q (O5)	-1.25	-1.28

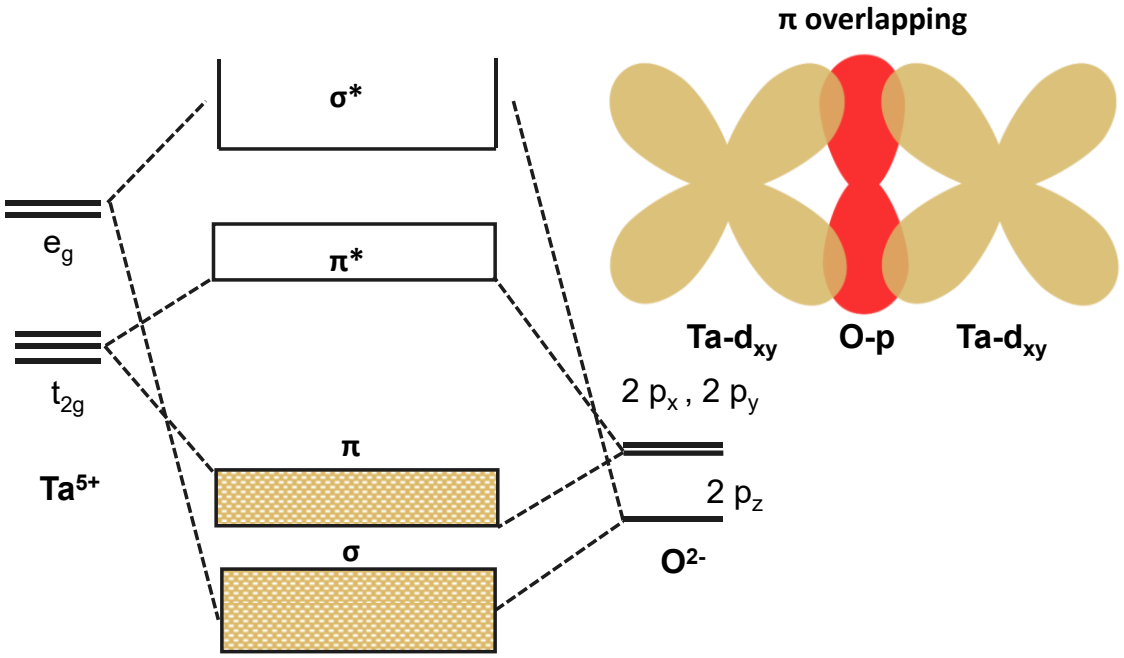

Figure S3. Schematic band structure of a cubic pervoskite (left)**.** The overlapping TM *d*-orbitals and O-2*p* orbitals form the bonding Π-O(2*p*)-TM(t_{2g}) and the σ-O(2*p*)-TM(e_g) bands, with major contribution of O-2*p* states, and the corresponding antibonding bands with major contribution of TM-*d* states. For TM being Ta, the band gap opens within the occupied Π-O(2*p*)-Ta(t_{2g}) band and the unoccupied band Π*-O(2*p*)-Ta(t_{2g}). The right panel shows the ideal π-type ovelapping between Ta-5d_{xy} and O-2*p* orbitals in a cubic pervoskite (Ta-O-Ta angle 180°). In the perpendicular directions the d_{yx} and d_{zy} orbitals overlap in an identical manner. Adapted from [17].

2. Substituted $Sr_{2-x}Ba_xTa_2O_7$

2.1. Relative stability

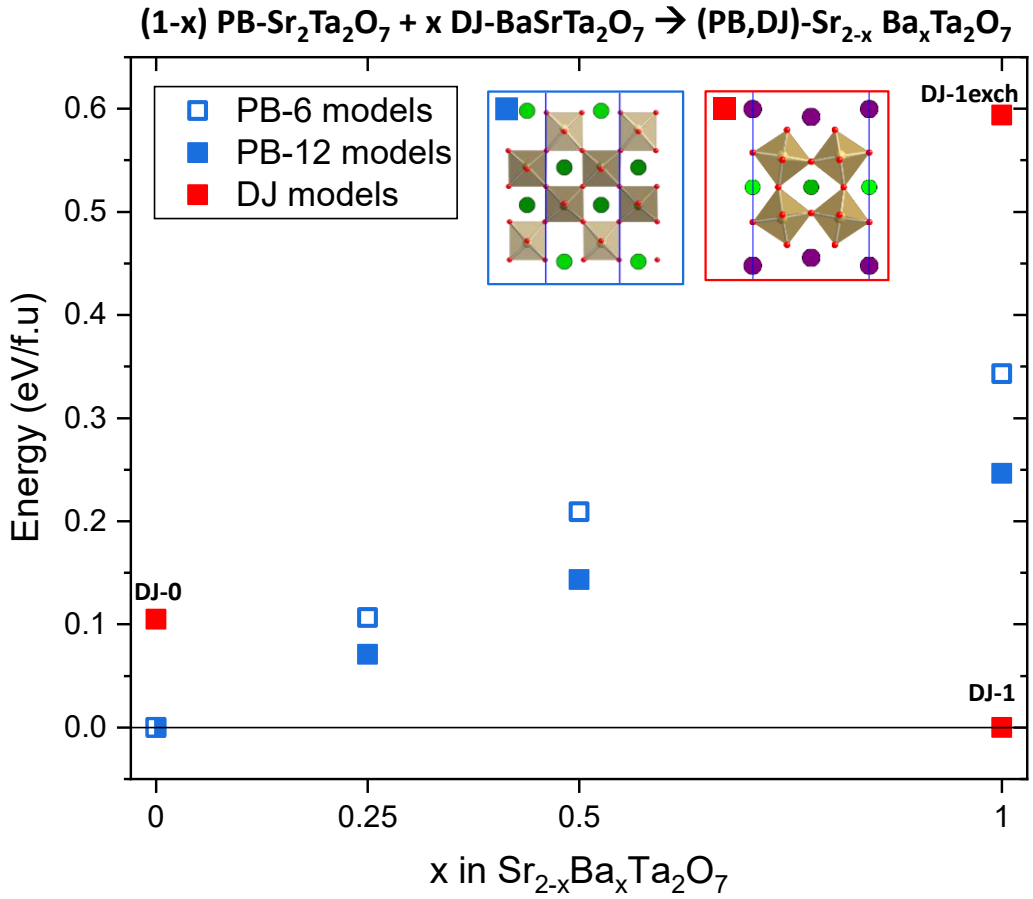

Figure S4: Calculated relative energy per formula unit for the modelled $Sr_{2-x}Ba_xTa_2O_7$ ($0 \leq x \leq 1$) compounds according to equation (2) in the main text. PB-$Sr_{2-x}Ba_xTa_2O_7$ are shown in blue, and DJ-$Sr_{2-x}Ba_xTa_2O_7$ in red. The model's names are shown as indicated in the main text (**Table 1**).

DFT calculations offer information about the relative stability of the modelled $Sr_{2-x}Ba_xTa_2O_7$ ($0 \leq x \leq 1$) compounds with different crystal structures (**Figure S4**, PB in blue and DJ in red). It is worth mentioning that for x=0 and x=1 the most stable structures agree with the experimentally observed: for x = 1 the Dion-Jacobson $BaSrTa_2O_7$ and, contrariwise, for x = 0, the PB-$Sr_2Ta_2O_7$. For x=0, the DJ-0 is 0.1 eV/f.u. less stable than the experimentally observed PB-structure. For x =1, the DJ-1 is much more stable than any of the other tested hypothetical models (0.25 and 0.35 eV/f.u.). The DJ-1exch, with Ba inside the perovskite slab and Sr in the interlayer site, is particularly unstable (0.6 eV/f.u.). Within the PB structure the models with Ba inside the perovskite slab site (PB12 models) are more stable than those with Ba in the interlayer site (PB6 models), with the energy difference between

PB6 and PB12 models becoming larger with the increasing of Ba content. In addition, the introduction of Ba increases the instability for both PB6 and PB12 models respective to the end members. As a bottom line, site preference is opposite in the PB and DJ structures; the largest cation (Ba^{2+}) preferably occupy the inside-slabs site in former and the interlayer site in the later.

2.2. Details on the Crystal Structure of the PB compounds

Table S4: Calculated (SCAN) unit cell parameters for the modelled $Sr_{2-x}Ba_xTa_2O_7$ ($0.25 < x < 1$) compounds with $Sr_2Ta_2O_7$ (PB-0) crystal structure.

$Sr_{2-x}Ba_xTa_2O_7$	PB6 models			PB12 models		
	x = 0.25	**x = 0.5**	**x = 1**	**x = 0.25**	**x = 0.5**	**x = 1**
a (Å)	3.9660	3.9794	4.0046	3.9613	3.9710	3.9885
b(Å)	27.1845	27.1869	27.2012	27.2664	27.3198	27.4250
c (Å)	5.7336	5.7669	5.8352	5.7146	5.7317	5.7693
V ($Å^3$)	61.81	62.39	63.56	61.72	62.18	63.11

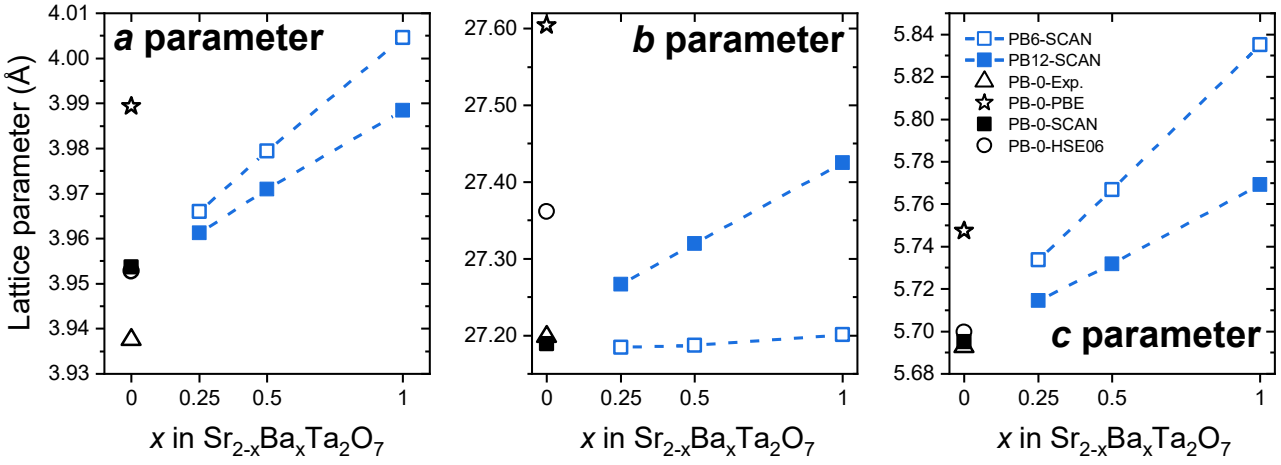

Figure S5. Calculated lattice parameters (SCAN) for PB-$Sr_{2-x}Ba_xTa_2O_7$ compounds, with the PB6 models shown as blue hollow symbols and the PB12 models denoted by blue filled symbols. The experimental and calculated SCAN, PBE and HSE06 values for parent PB-0 are given for comparison. The dashed lines are a guide for the eye. The lattice parameters increase linearly with the Ba content following Vegard´s law. There are, however, some differences depending on whether Ba occupies the interlayer site (PB6 models) or is positioned inside the perovskite slab (PB12 models).

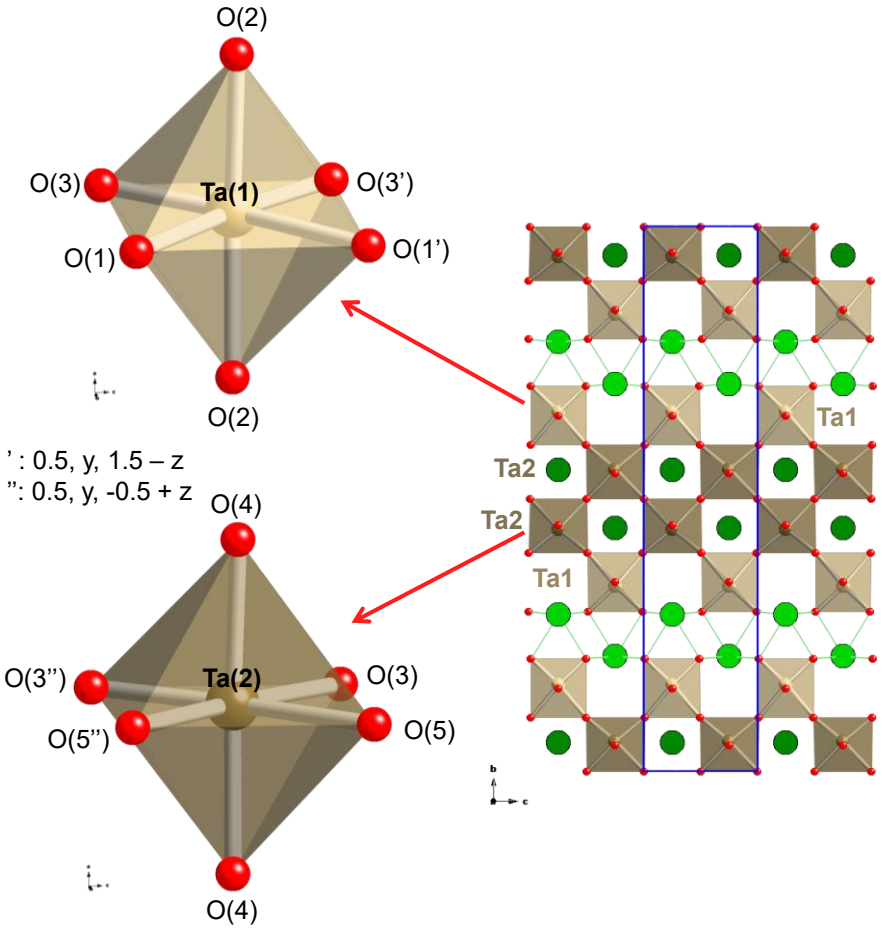

Figure S6. Ta coordination environnements in PB-$Sr_2Ta_2O_7$.

Table S5: Calculated (SCAN) bond angles (°) in selected PB-$Sr_{2-x}Ba_xTa_2O_7$ compounds

Angle	$Sr_2Ta_2O_7$ (PB-0)	PB6-1	PB12-1
O(2) - Ta(1) - O(1)	95.555 x 4	95.938 x 4	94.742 x 4
O(2) - Ta(1) - O(3)	83.735 x 4	83.583 x 4	84.697 x 4
O(1) - Ta(1) - O(3)	93.111 x 2	92.352 x 2	91.504 x 2
O(1) - Ta(1) - O(1')	94.120	92.256	95.047
O(3) - Ta(1) - O(3')	79.659	83.040	81.944
O(4) - Ta(2) - O(3)	93.947 x 4	93.850 x 4	93.451 x 4
O(4) - Ta(2) - O(5)	85.487 x 4	85.646 x 4	85.060 x 4
O(3) - Ta(2) - O(5)	86.018 x 2	84.787 x 2	87.538 x 2
O(3) - Ta(2) - O(3'')	101.106	101.632	99.711
O(5) - Ta(2) - O(5'')	86.857	88.794	85.214

2.3. Details on the Crystal Structure of the DJ compounds

Table S6. Calculated (SCAN) unit cell parameters for the modelled $Sr_{2-x}Ba_xTa_2O_7$ ($0 \leq x \leq 1$) compounds with $BaSrTa_2O_7$ (DJ-1) crystal structure.

$Sr_{2-x}Ba_xTa_2O_7$	Model DJ-0	Model DJ-1exch	$BaSrTa_2O_7$ (DJ-1)
	x = 0	x = 1	x = 1
a (Å)	3.9721	4.0020	3.987
b(Å)	7.7529	7.8678	7.8293
c(Å)	19.5456	19.8073	20.2897
V (Å^3)	60.19	62.37	63.33

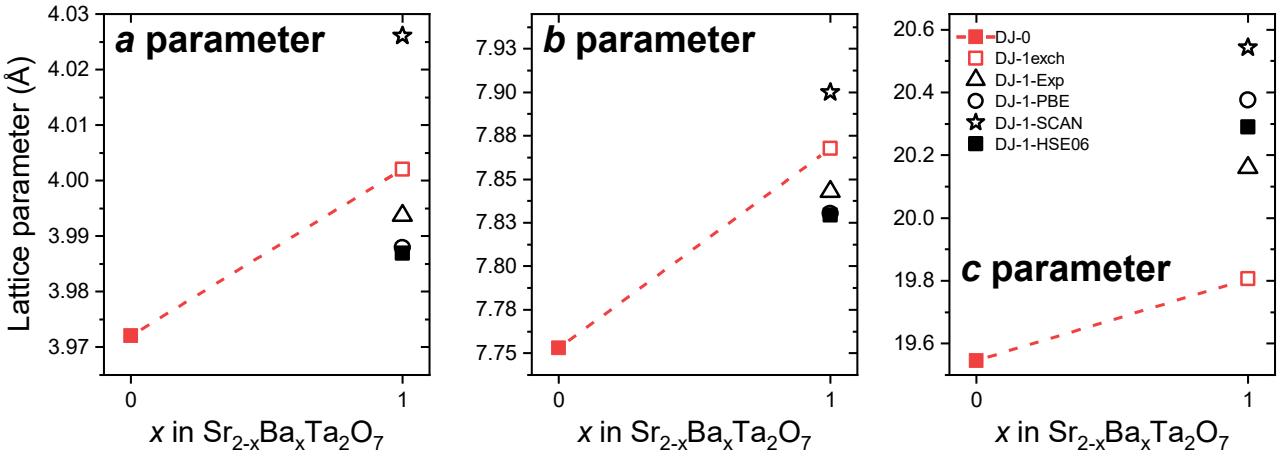

Figure S7. Calculated lattice parameters (SCAN) for compositional modifications in $BaSrTa_2O_7$, (DJ-1) where the DJ-0 phase is shown as red filled symbol, and the DJ-1exch is shown as hollow symbol. The experimental and calculated PBE and HSE06 values for parent DJ-$BaSrTa_2O_7$ are given. The dashed lines are a guide for the eye. For these DJ-$Sr_{2-x}Ba_xTa_2O_7$ compounds, unsurprisingly, at x=1, placing Ba in the perovskite layer and Sr in the interlayer space (DJ-1exch) causes the contraction of the *c* axis, and a slight expansion in *a* and *c* lattice parameters.

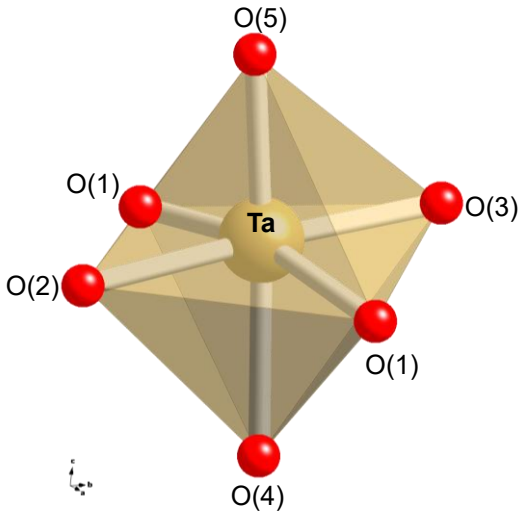

Figure S8. Ta coordination in DJ- $Sr_{2-x}Ba_xTa_2O_7$ compounds.

Table S7: Calculated (SCAN) bond angles (°) in the modelled DJ-$Sr_{2-x}Ba_xTa_2O_7$ compounds.

Angle	$BaSrTa_2O_7$ (DJ-1)	DJ-1exch	DJ-0
O(1)–Ta–O(1)	167.994	170.411	167.514
O(4)–Ta–O(5)	177.325	172.952	176.126
O(2)–Ta–O(3)	171.931	172.535	172.537
O(1)–Ta–O(2)	88.269	89.141	88.272
O(1)–Ta–O(3)	90.908	90.240	90.936
O(1)–Ta–O(4)	84.114	85.214	83.849
O(1)–Ta–O(5)	95.824	94.715	96.064
O(2)–Ta–O(4)	84.539	83.068	83.743
O(2)–Ta–O(5)	92.786	89.884	92.383
O(3)–Ta–O(4)	87.393	89.467	88.794
O(3)–Ta–O(5)	95.282	97.581	95.081

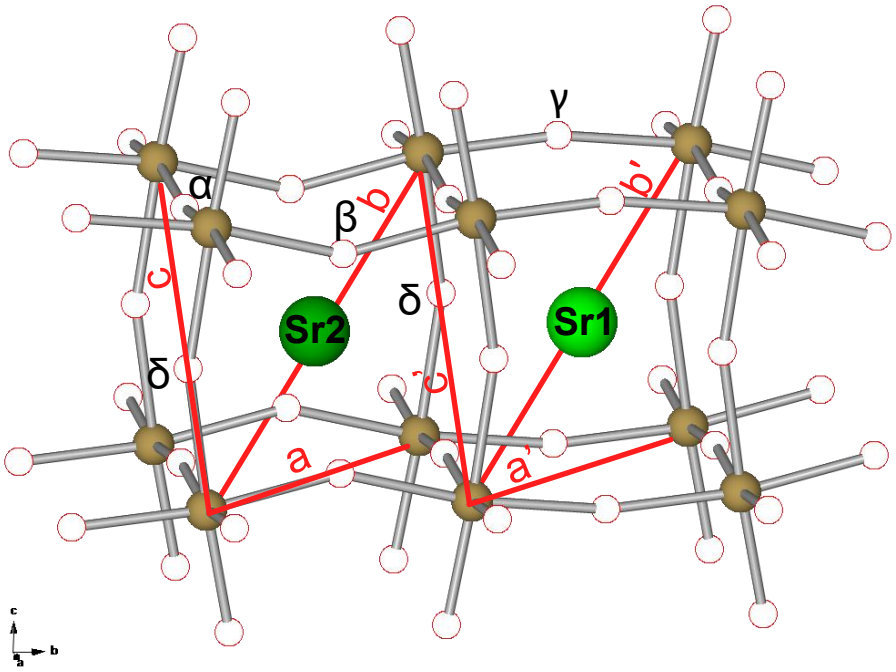

Figure S9. Snapshot of the DJ-$Sr_{2-x}BaTa_2O_7$ crystal structure, showing the eight octahedra that form the unit cell of the perovskites for Sr1 and Sr2. Relevant Ta-Ta distances and Ta-O-Ta angles are indicated in red. Sr1 is shown in light green and Sr2 in dark green.

Table S8. Ta-O-Ta angles depicted in Figure S9 for the DJ-$Sr_{2-x}BaTa_2O_7$ compounds.

Angle	$BaSrTa_2O_7$ (exp)	$BaSrTa_2O_7$ (DJ-1)	DJ-1exch	DJ-0
α	166.57	167.99	170.41	167.51
δ	165.46	163.74	171.88	161.60
β	158.90	152.82	158.11	149.08
γ	164.17	168.96	172.94	164.00

Table S9. Ta-Ta distances depicted in Figure S9 for the DJ-$Sr_{2-x}BaTa_2O_7$ compounds.

Sr	d Ta-Ta	$BaSrTa_2O_7$ (exp)	$BaSrTa_2O_7$ (DJ-1)	DJ-1exch	DJ-0
1	a’	5.62	5.61	5.65	5.59
	b’	7.01	6.99	7.15	6.99
	c’	5.79	5.78	5.94	5.78
2	a	5.57	5.56	5.59	5.52
	b	6.97	6.96	7.10	6.93
	c	5.79	5.78	5.94	5.78

2.4. Electronic Structure of PB and DJ compounds

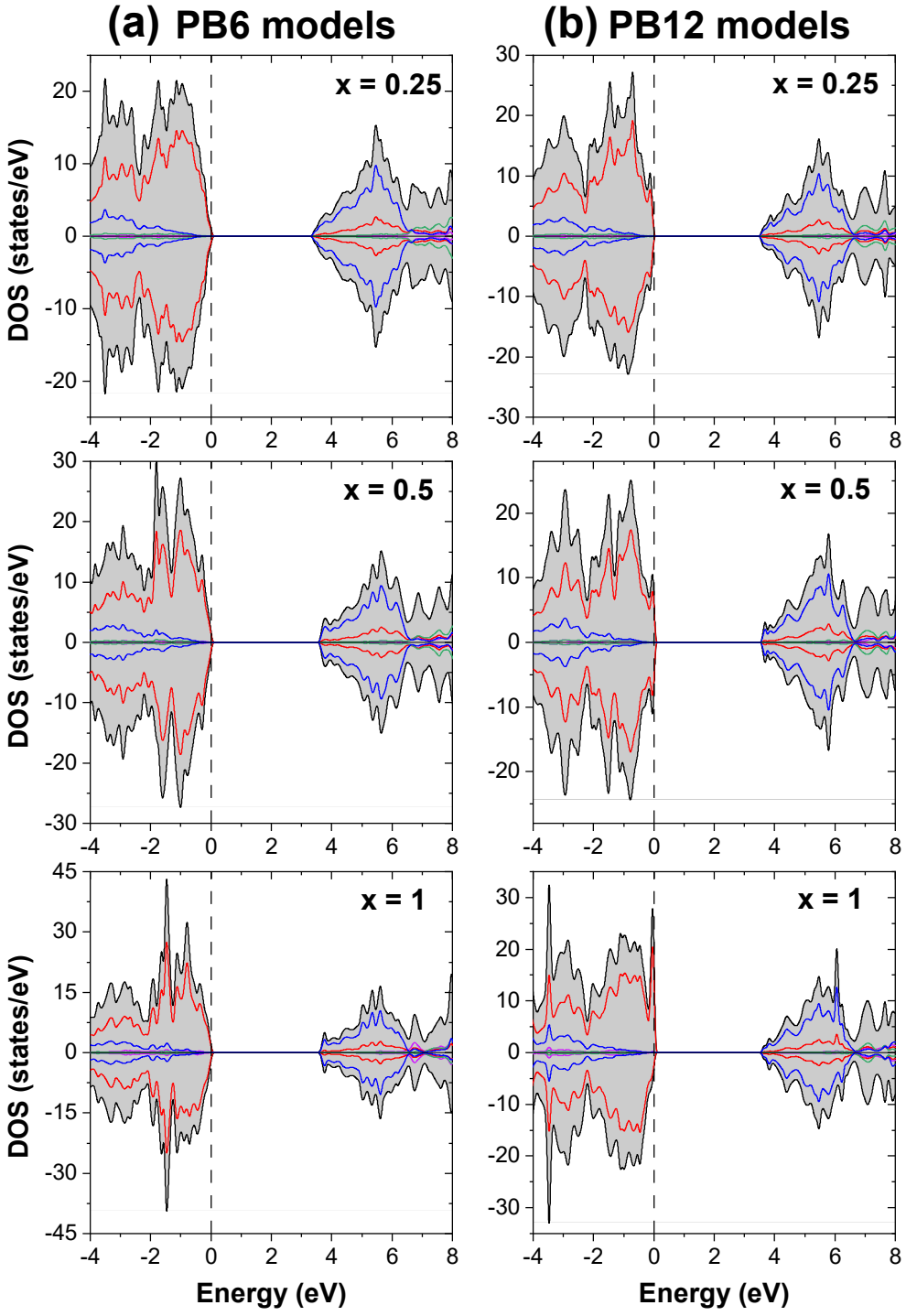

Figure S10. Calculated (SCAN) PDOS for PB-$Sr_{2-x}Ba_xTa_2O_7$ models (a) PB6 and (b) PB12. The Fermi level is set as the zero of energy. Ta contribution is shown in blue, Sr in green, Ba in pink and O in red. DOS units refers to the calculated cell.

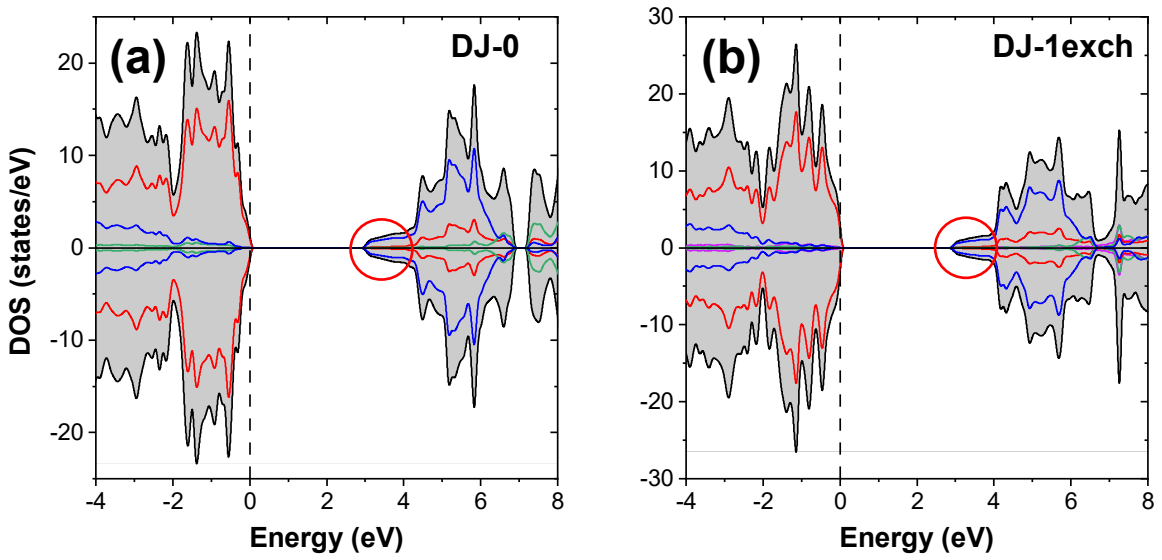

Figure S11. Calculated (SCAN) PDOS for DJ-$Sr_{2-x}Ba_xTa_2O_7$ models (a) DJ-0 and (b) DJ-1exch. The Fermi level is set as the zero of energy. Ta contribution is shown in blue, Sr in green, Ba in pink and O in red. DOS units refer to the calculated cell. Red circle indicates the widening of the conduction band arising from Ta-5d_{xy} states (see main text).

Table S10. Experimental and calculated band gap values for some perovskite-type AMO_3 and $AA´M_2O_6$ compounds.

Material	B - O – B Angle	Experimental band gap (eV)	Calculated band gap (eV)
$NaTaO_3$	163° [a]	4.0 [a]	3.69 [c]
$KTaO_3$	180° [a]	3.6 [a]	3.40 [c]
$CaTiO_3$	156° [18]	3.8; 4.38[d]	2.31[b]; 2.45[d]
$SrTiO_3$	180°[19]	3.25 [20]	1.86[b]; 3.06 [21]
$BaTiO_3$	180° [22]	3.20[e]	2.62[b]; 1.20[e]
Ca_2ScTaO_6	148°	-	4.11[f], 3.73[b]
Sr_2ScTaO_6	160°	-	3.78[f], 3.42[b]
Ba_2ScTaO_6	180°	-	3.35 [f], 3.02[b]

[a]reference[23]; [b]reference [24] ; [c] reference [25]; [d] reference [26]; [e] reference [27], [f] reference [28]

References

[1] Osterloh FE. Inorganic materials as catalysts for photochemical splitting of water. Chem Mater. 2008; 20: 35-54. DOI: 10.1021/cm7024203.

[2] Kato H, Kudo A. New tantalate photocatalysts for water decomposition into H_2 and O_2 Chemical Physics Letters. 1998; 295: 487-92. DOI: 10.1016/S0009-2614(98)01001-X.

[3] Sayama K, Arakawa H, Domen K. Photocatalytic water splitting on nickel intercalated $A_4Ta_xNb_{6-x}O_{17}$ (A = K, Rb). Catalysis Today. 1996; 28: 175-82. DOI: 10.1016/0920-5861(95)00224-3.

[4] Kato H, Asakura K, Kudo A. Highly Efficient Water Splitting into H_2 and O_2 over Lanthanum-Doped $NaTaO_3$ Photocatalysts with High Crystallinity and Surface Nanostructure. Journal of the American Chemical Society. 2003; 125: 3082-9. DOI: 10.1021/ja027751g.

[5] Shimizu K-i, Itoh S, Hatamachi T, Kodama T, Sato M, Toda K. Photocatalytic Water Splitting on Ni-Intercalated Ruddlesden−Popper Tantalate $H_2La_{2/3}Ta_2O_7$. Chemistry of Materials. 2005; 17: 5161-6. DOI: 10.1021/cm050982c.

[6] Mitsui C, Nishiguchi H, Fukamachi K, Ishihara T, Takita Y. Photocatalytic Decomposition of Pure Water over NiO Supported on $KTa(M)O_3$ (M = Ti^{4+}, Hf^{4+}, Zr^{4+}) Perovskite Oxide. Chemistry Letters. 1999; 28: 1327-8. DOI: 10.1246/cl.1999.1327.

[7] Kato H, Kudo A. Photocatalytic Decomposition of Pure Water into H_2 and O_2 over $SrTa_2O_6$ Prepared by a Flux Method. Chemistry Letters. 1999; 28: 1207-8. DOI: 10.1246/cl.1999.1207.

[8] Ikeda S, Fubuki M, Takahara YK, Matsumura M. Photocatalytic activity of hydrothermally synthesized tantalate pyrochlores for overall water splitting. Applied Catalysis A: General. 2006; 300: 186-90. DOI: 10.1016/j.apcata.2005.11.007.

[9] Luan J-F, Hao X-P, Zheng S-R, Luan G-Y, Wu X-S. Structural, photophysical and photocatalytic properties of Bi_2MTaO_7 (M = La and Y). Journal of Materials Science. 2006; 41: 8001-12. DOI: 10.1007/s10853-006-0869-y.

[10] Kudo A, Kato H, Nakagawa S. Water splitting into H_2 and O_2 on new $Sr_2M_2O_7$ (M = Nb and Ta) photocatalysts with layered perovskite structures: Factors affecting the photocatalytic activity. J Phys Chem B. 2000; 104: 571-5. DOI: 10.1021/jp9919056.

[11] G. Kim H, W. Hwang D, Kim J, G. Kim Y, S. Lee J. Highly donor-doped (110) layered perovskite materials as novel photocatalysts for overall water splitting. Chemical Communications. 1999: 1077-8. DOI: 10.1039/A902892G.

[12] Yoshioka K, Petrykin V, Kakihana M, Kato H, Kudo A. The relationship between photocatalytic activity and crystal structure in strontium tantalates. Journal of Catalysis. 2005; 232: 102-7. DOI: 10.1016/j.jcat.2005.02.021.

[13] Otsuka H, Kim K, Kouzu A, Takimoto I, Fujimori H, Sakata Y, et al. Photocatalytic Performance of $Ba_5Ta_4O_{15}$ to Decomposition of H_2O into H_2 and O_2. Chemistry Letters. 2005; 34: 822-3. DOI: 10.1246/cl.2005.822.

[14] Kudo A, Kato H. Photocatalytic Decomposition of Water into H_2 and O_2 over Novel Photocatalyst $K_3Ta_3Si_2O_{13}$ with Pillared Structure Consisting of Three TaO_6 Chains. Chemistry Letters. 1997; 26: 867-8. DOI: 10.1246/cl.1997.867.

[15] Abe R, Higashi M, Sayama K, Abe Y, Sugihara H. Photocatalytic Activity of R_3MO_7 and $R_2Ti_2O_7$ (R = Y, Gd, La; M = Nb, Ta) for Water Splitting into H_2 and O_2. The Journal of Physical Chemistry B. 2006; 110: 2219-26. DOI: 10.1021/jp0552933.

[16] Machida M, Murakami S, Kijima T, Matsushima S, Arai M. Photocatalytic Property and Electronic Structure of Lanthanide Tantalates, $LnTaO_4$ (Ln = La, Ce, Pr, Nd, and Sm). The Journal of Physical Chemistry B. 2001; 105: 3289-94. DOI: 10.1021/jp004297z.

[17] Atkins P, Overton T, Rourke J, Weller M, Armstrong F, Hagerman M. Shrivers & Atkins' Inorganic Chemistry. 5th ed. Great Britain: University Press; 2010.

[18] Sasaki S, Prewitt CT, Bass JD, Schulze WA. Orthorhombic Perovskite $CaTiO_3$ and $CdTiO_3$: Structure and Space Group. Acta Crystallographica C. 1987; 43: 1668-74. DOI: 10.1107/s0108270187090620.

[19] Abramov YA, Tsirelson VG, Zavodnik VE, Ivanov SA, Brown ID. The chemical bond and atomic displacements in $SrTiO_3$ from X-ray diffraction analysis. Acta Crystallographica B. 1995; 51: 942-51. DOI: 10.1107/S0108768195003752.

[20] Benthem KV, Elsässer C, French RH. Bulk electronic structure of $SrTiO_3$:Experiment and theory. 2001; 90. DOI: doi.org/10.1063/1.1415766.

[21] Adewale A, Abdullah C. First principles enhanced electronic band structure of $SrTiO_3$ using DFT+*U* method. International Journal of Nanoelectronics and Materials. 2019; 12: 11-8. DOI.

[22] Buttner RH, Maslen EN. Structural parameters and electron difference density in $BaTiO_3$. Acta Crystallographica B. 1992; 48: 764-9. DOI: 10.1107/S010876819200510X.

[23] Kato H, Kudo A. Water Splitting into H_2 and O_2 on Alkali Tantalate Photocatalysts $ATaO_3$ (A = Li, Na, and K). J Phys Chem B. 2001; 105: 4285-92. DOI: 10.1021/jp004386b.

[24] Jain A, Ong SP, Hautier G, Chen W, Richards WD, Dacek S, et al. Commentary: The Materials Project: A materials genome approach to accelerating materials innovation. APL Materials. 2013; 1. DOI: 10.1063/1.4812323.

[25] Bouafia H, Hiadsi S, Abidri B, Akriche A, Ghalouci L, Sahli B. Structural, elastic, electronic and thermodynamic properties of $KTaO_3$ and $NaTaO_3$: Ab initio investigations. Computational Materials Science. 2013; 75: 1-8. DOI: 10.1016/j.commatsci.2013.03.030.

[26] Krause A, Weber WM, Pohl D, Rellinghaus B, Kersch A, Mikolajick T. Investigation of band gap and permittivity of the perovskite $CaTiO_3$ in ultrathin layers. Journal of Physics D: Applied Physics. 2015; 48. DOI: 10.1088/0022-3727/48/41/415304.

[27] Zhang Zi-Ying Yd-l, Shao Jian-Xin, Liu Yun-Hu, Jing Qun. Electronic Structures and Optical Properties of $BaTiO_3$. Acta Physico-Chimica Sinica. 2009; 25: 1731-6. DOI: 10.3866/PKU.WHXB20090819.

[28] Eng HW, Barnes PW, Auer BM, Woodward PM. Investigations of the electronic structure of d^0 transition metal oxides belonging to the perovskite family. Journal of Solid State Chemistry. 2003; 175: 94-109. DOI: 10.1016/s0022-4596(03)00289-5.

CAPÍTULO 4

Metal-to-Insulating Transition in the Perovskite System $YSr_2Cu_2FeO_{8-\delta}$ ($0 < \delta < 1$) Modeled by DFT Methods

Inorganic Chemistry

pubs.acs.org/IC

Article

Metal-to-Insulating Transition in the Perovskite System $YSr_2Cu_2FeO_{8-\delta}$ ($0 < \delta < 1$) Modeled by DFT Methods

Marianela Gómez-Toledo, Sara A. López-Paz, Susana García-Martín, and M. Elena Arroyo-de Dompablo*

Cite This: *Inorg. Chem.* 2023, 62, 3445−3456

Read Online

ACCESS | Metrics & More | Article Recommendations | Supporting Information

ABSTRACT: Progress in the design of functional perovskite oxides relies on advances in density functional theory (DFT) methods to efficiently and effectively model complex systems composed of several transition-metal ions. This work reports the application of DFT methods to investigate the electronic structure of the $YSr_2Cu_2FeO_{8-\delta}$ ($0 < \delta < 1$) family in which the insulating, metal, or superconducting behaviors and even anion conductivity can be tuned by modifying the oxygen content. In particular, we assess the performance of the generalized gradient approximation (GGA), its Hubbard-*U* correction (GGA + *U*), and the strongly constrained and appropriately normed (SCAN) to model the metallic (idealized $YSr_2Cu_2FeO_8$) and insulating (idealized $YSr_2Cu_2FeO_7$) phases of the system. The analysis of the DFT results is supported by DC resistivity measurements that denote the metal character of the synthesized $YSr_2Cu_2FeO_{7.86}$ and the semiconducting character of $YSr_2Cu_2FeO_{7.08}$ prepared under reducing conditions. In addition, the band gap of $YSr_2Cu_2FeO_{7.08}$, in the range of 0.73−1.2 eV, has been extracted from diffuse reflectance spectroscopy (DRS). While the three methodologies (GGA, GGA + *U*, SCAN) permit the reproduction of the crystal structures of the synthetized oxides (determined here in the case of $YSr_2Cu_2FeO_{7.08}$ by neutron powder diffraction (NPD)), the SCAN emerges as the only one capable to predict the basic electronic and magnetic properties across the $YSr_2Cu_2FeO_{8-\delta}$ ($0 < \delta < 1$) series. The picture that emerges for the metal ($\delta = 0$) to insulating ($\delta = 1$) transition is the one in which oxygen vacancies contribute electrons to the filling of the Cu/Fe-3$d_{x^2-y^2}$ states of the conduction band. These results validate the SCAN functional for future DFT investigations of complex functional oxides that combine several transition metals.

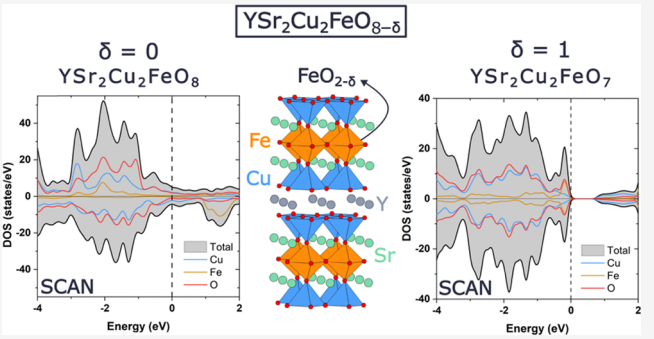

1. INTRODUCTION

Perovskite-type oxides (ABO_3 and related materials) exhibit a broad range of functional properties that derive in multiple and relevant applications.[1] To better understand the properties and optimize the applications of these oxides, a profound knowledge of their crystal and electronic-structure relationships is compulsory. Nowadays, electronic-structure calculations based on density functional theory (DFT) are extensively applied to successfully predict and design materials with particular properties. Since the development of DFT by Holenberg, Kohn, and Sham,[2,3] a great deal of improvement on exchange-correlation (XC) functionals has been reported, such as the widely used generalized gradient approximation (GGA) developed in the late 1980s.[4,5] The GGA functionals have offered some acceptable results in the modeling of perovskite oxides based on d^0 transition metals (TM).[6−9] However, the overestimation of electron delocalization and metallic character is a known failure of DFT methods for systems with localized and strongly interacting *d*-electrons and *f*-electrons.[10−13] In the 1990s, the DFT + *U* method introduced an explicit treatment of electron correlation with a Hubbard-like model for a subset of states in the system.[10,14] Vast literature demonstrates the suitability of the DFT + *U* approach to investigate TM oxides with strong Coulomb correlations. More recently, the strongly constrained and appropriately normed (SCAN) meta-GGA functional[15] has shown good performance to model the basic physical properties and phenomena associated to correlated oxides.[16,17] For instance, investigations on perovskite-related oxides using meta-GGA functionals (and particularly SCAN) have accurately described the transition from the insulating to the metallic character of La_2CuO_4 by substitution of La by Sr in the superconducting system;[18] the layered ordering stabiliza-

Received: September 30, 2022
Published: February 14, 2023

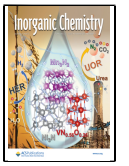

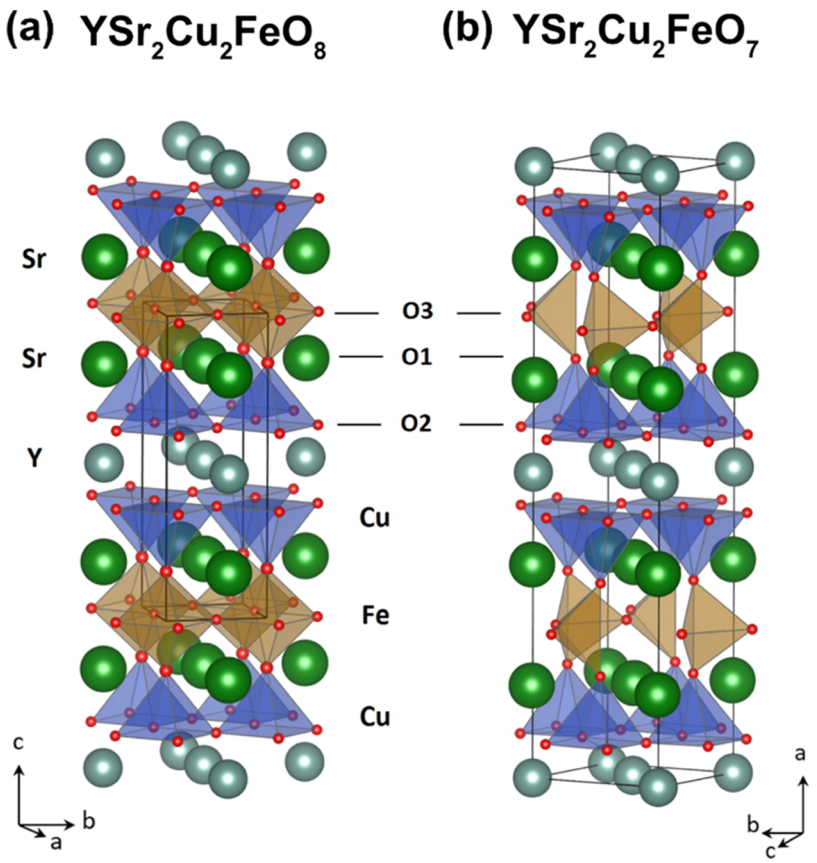

Figure 1. Crystal structure representations of (a) idealized stoichiometric oxide $YSr_2Cu_2FeO_8$ ($a_p \times a_p \times 3a_p$ unit cell, S.G. *P*4/*mmm*) and (b) idealized stoichiometric oxide $YSr_2Cu_2FeO_7$ ($6a_p \times \sqrt{2}a_p \times \sqrt{2}a_p$ unit cell, S.G. *Ima*2).

tion of the Bi_2MFeO_6 perovskites (M = Al, Ga, In) induced by the Fe−magnetic interactions;[19] the effect of the hole and electron doping in the electronic structure of $Sm_{1-x}M_xNiO_3$ (M = Ca, Ce);[20] and have predicted the structural cubic-symmetry breaking, band-gap existence, and magnetic behavior in ABO_3 perovskites with B = 3*d*-TM.[21]

Despite the substantial progress in the computational investigation of perovskites, the scenario complicates when different TM ions occupy the B positions, even if this occurs in an ordered manner. Hence, assessing the performance of DFT methodologies and, specifically, of the recently developed SCAN functional at a basic property-level prediction—crystal, electronic, and magnetic structures—is a prerequisite to further investigating the particular properties of complex perovskite oxides. In the present work, we focus on the $YSr_2Cu_2FeO_{8-\delta}$ ($0 < \delta < 1$) family derived from the so-called "YBaCuO" superconducting cuprates.[22,23] Figure 1a,b displays the graphic representation of the crystal structure of the idealized stoichiometric endmembers $YSr_2Cu_2FeO_8$ and $YSr_2Cu_2FeO_7$ (δ = 0 and 1, respectively). The structures consist of an alternation of $FeO_{2-\delta}$/SrO/CuO_2/Y/CuO_2/SrO layers along the *c*-axis or *a*-axis (space group (S.G.) *P*4/*mmm* and S.G. *Ima*2 settings, respectively). The idealized $YSr_2Cu_2FeO_8$, with [FeO_6] octahedral units in the Fe layers, presents a tetragonal (S.G. *P*4/*mmm*) crystal structure with $a_p \times a_p \times 3a_p$ unit cell dimensions (a_p refers to the lattice parameter of the cubic perovskite structure).[24] Lowering the oxygen content ($\delta > 0$) creates vacancies in the O3 positions of the $FeO_{2-\delta}$ layer (Figure 1) so that in the $YSr_2Cu_2FeO_{8-\delta}$ family, the Fe atoms may adopt octahedral, tetrahedral, and/or square pyramid coordination.[23−27] In combination with the Y and Sr ordering, there is layered ordering of the coordination polyhedra (octahedra O, square pyramid SP, and tetrahedra T) around the Fe and Cu atoms in the manner O/SP/SP/O in the idealized $YSr_2Cu_2FeO_8$ and like T/SP/SP/T in the idealized $YSr_2Cu_2FeO_7$. In addition, in the idealized $YSr_2Cu_2FeO_7$, the different orientation of the tetrahedral coordination polyhedra of the Fe atoms leads to a sixfold superstructure ($6a_p \times \sqrt{2}a_p \times \sqrt{2}a_p$ within the *Ima*2 space group).[23,28]

$YSr_2Cu_2FeO_{8-\delta}$ ($0 < \delta < 1$) compounds show a non-stoichiometric anion sublattice resulting from the interplay between different oxidation states of Fe and Cu atoms.[22,23,29] Oxides of the system, with different oxygen content and properties, have already been reported. The highly oxidized term $YSr_2Cu_2FeO_{7.85}$ obtained experimentally in ozone flow, with Fe in the unusual 4+ formal oxidation state and mixed Cu^{3+} and Cu^{2+} valences, is a metallic oxide with a superconducting transition at T_c = 70 K.[24] The compound presents magnetic ordering arising from the ferromagnetic (FR) interactions below T_N = 110 K between Fe^{4+} cations with parallel in-plane spins in the $FeO_{2-\delta}$ layers coupled with a soft character of the antiferromagnetic (AFM) interactions between layers.[24] The low oxygen content terms $YSr_2Cu_2FeO_{7.08}$,[27] $YSr_2Cu_2FeO_{7.11}$,[28] and $YSr_2Cu_2FeO_{7.04}$,[26] prepared under reducing conditions, are insulators with mainly Fe^{3+} and Cu^{2+}. In between those extremes, air-synthesized $YSr_2Cu_2FeO_{7.56}$, mixed valence Fe^{3+}/Fe^{4+} and Cu^{2+}/Cu^{3+} oxide, exhibits an interesting electrochemical behavior associated with catalytic activity in the oxygen reduction

https://doi.org/10.1021/acs.inorgchem.2c03475
Inorg. Chem. 2023, 62, 3445−3456

reaction (ORR), being a potential air electrode for solid oxide fuel cells (SOFCs).[26,27]

Modeling the evolution of the electronic structure of $YSr_2Cu_2FeO_{8-\delta}$ from the metallic phase ($\delta \sim 0$) to the insulating one ($\delta \sim 1$), which is to say, the metal-to-insulating transition as a function of the oxygen content, constitutes a challenge for DFT methods, apart from the relevance of tuning the electronic properties of these materials to manage particular applications. Indeed, few computational works deal with the two facts that are found in $YSr_2Cu_2FeO_{8-\delta}$ oxides: first, the combination of two transition-metal ions in the B positions of the crystal structure, and second, the occurrence of oxygen nonstoichiometry. Both aspects highly condition the electronic properties of the materials.

We here report DFT calculations for the idealized stoichiometric compounds $YSr_2Cu_2FeO_8$ and $YSr_2Cu_2FeO_7$ as representatives of the experimentally obtained $YSr_2Cu_2FeO_{7.85}$ and $YSr_2Cu_2FeO_{7.08}$. The calculations have been performed within the GGA-Perdew, Burke, and Ernzerhof (PBE) functional (hereafter denoted as simply GGA), its Hubbard correction PBE + U (denoted as GGA + U), and the meta-GGA-SCAN functional (denoted as SCAN). We demonstrate that the three methodologies fairly reproduce the crystal structures. However, the prediction of the electrical and magnetic properties depends on the functional used for the calculation. While the metallic behavior and magnetic features of the $YSr_2Cu_2FeO_8$ phase are well described with the GGA and SCAN functionals, the SCAN and GGA + U offer the best approaches to investigate the $YSr_2Cu_2FeO_7$ compound. We also support the electronic-structure calculations with resistivity experiments that confirm the metal-to-insulating transition in the $YSr_2Cu_2FeO_{8-\delta}$ ($0 < \delta < 1$) system. In addition, the optical band gap of $YSr_2Cu_2FeO_{7.08}$ has been determined from diffuse reflectance spectroscopy (DRS).

2. METHODOLOGY

2.1. Experimental Section. Our previous works cover the synthesis and structural characterization of several $YSr_2Cu_2FeO_{8-\delta}$ oxides.[24,27,30] In this work, polycrystalline $YSr_2Cu_2FeO_{8-\delta}$ (δ = 0.15 and 0.92) compounds have been prepared by the conventional ceramic method in air. The intimate mixtures of Fe_2O_3 (Aldrich 99.99%), CuO (Aldrich 99.9999%), previously decarbonated Y_2O_3 (Aldrich 99.9%), and previously dehydrated $SrCO_3$ (Aldrich 99.9%) in the stoichiometric relations were subjected to an initial treatment at 1173 K for 12 h in air. The resulting powders were ground in an agate mortar, pelletized, and subjected to several treatments at 1253 K in air, for 72 h, with intermediate grindings. The air-prepared sample was heated at 1023 K for 24 h in N_2 flow to obtain $YSr_2Cu_2FeO_{7.08}$ oxide and the N_2 prepared compound was oxidized in ozone at 473 K to obtain $YSr_2Cu_2FeO_{7.85}$.

The crystal structure of the $YSr_2Cu_2FeO_{7.08}$ compound at room temperature (RT) was determined by neutron powder diffraction (NPD) using the high-resolution D2B instrument at the ILL (Grenoble, France) with a wavelength of λ = 1.594 Å. Rietveld refinements were performed following the Fullprof software.[31]

DC electrical resistivity measurements of sintered pellets of $YSr_2Cu_2FeO_{7.85}$ and $YSr_2Cu_2FeO_{7.08}$ have been performed in the temperature region $5 < T < 300$ K using a Quantum Design PPMS device. Four-probe electrical contacts were made using conductive mixed silver paste and gold wires. The resistivity was measured in sweep mode with a heating rate of 2 K/min.

DRS measurements have been carried out to determine the optical band gap in $YSr_2Cu_2FeO_{7.08}$. The experiments have been performed in a Cary 5G spectrophotometer with an external integrating sphere. The measurement range was 300−3300 nm and the data interval was 1 nm. As stated by Kubelka and Munk,[32] diffuse reflectance spectra can be transformed into absorption spectra through the Kubelka−Munk function ($F(R_\infty)$, eq 1)

$$F(R_\infty) = \frac{K}{S} = \frac{(1 - R_\infty)^2}{2R_\infty} \quad (1)$$

where R_∞ is the absolute reflectance of an infinitely thick specimen and K and S are the absorption and scattering coefficients, respectively. $F(R_\infty)$ is proportional to the extinction coefficient (α), which can be expressed by eq 2, according to the Tauc method[33]

$$(\alpha h\nu)^{1/\gamma} = A(h\nu - E_g) \quad (2)$$

where h is the Plank constant, ν is the photon frequency, E_g is the band-gap energy, and A is a constant. The γ factor considers the nature of the electronic transition, being equal to 1/2 for allowed direct and 2 for allowed indirect transition.

Replacing α with $F(R_\infty)$ results in the following expression (eq 3)

$$F(R_\infty)(h\nu)^{1/\gamma} = A(h\nu - E_g) \quad (3)$$

The band gap can thus be extracted from diffuse reflectance spectra transformed according to eq 3. Linear fitting of the Tauc plot followed by extrapolating to the x-axis intersection gives the band-gap value.

2.2. Computational Section. Calculations for the idealized stoichiometric endmembers of the $YSr_2Cu_2FeO_{8-\delta}$ family, $YSr_2Cu_2FeO_8$ and $YSr_2Cu_2FeO_7$, have been performed using the ab initio total-energy and molecular dynamics program Vienna *ab initio* simulation package (VASP) developed at the Universität Wien.[34,35] The interaction of core electrons with the nuclei is described by the projector augmented wave (PAW) method[36] with $2s^2 2p^4$ of O, $3s^2 3p^6 3d^7 4s^1$ of Fe, $3p^6 3d^{10} 4p^1$ of Cu, $4s^2 4p^6 5s^2$ of Sr, and $4s^2 4p^6 4d^1 5s^2$ of Y treated as valence electrons. For the GGA approximation, we selected the exchange and correlation functional form developed by Perdew, Burke, and Ernzerhof (PBE).[37] On the other hand, for the meta-GGA approximation, the strongly constrained and appropriately normed (SCAN)[15] functional was used. In all cases, the energy cut off for the plane wave basis set was kept fixed at a constant value of 600 eV throughout the calculations. The integration in the Brillouin zone is done on appropriate sets of k-points determined by the Monkhorst−Pack scheme. The k-point meshes were set at 2 × 8 × 8 for $YSr_2Cu_2FeO_7$ and 10 × 10 × 4 for $YSr_2Cu_2FeO_8$, using a Gaussian smearing parameter of 0.05 eV. For the density of states (DOS) calculations, the tetrahedron method with Blöchl corrections[38] was used. Self-consistency was achieved with a tolerance in total energy of 1×10^{-4} eV for geometry optimization and 1×10^{-6} eV for DOS calculations.

A local Hubbard-U (GGA + U) was added to Fe and Cu atoms following the simplified rotationally invariant framework developed by Dudarev et al.[39] Typically, U is formulated as U_{eff}

https://doi.org/10.1021/acs.inorgchem.2c03475
Inorg. Chem. 2023, 62, 3445−3456

Table 1. Atomic Positions and Cell Parameters Obtained from the Rietveld Refinement of the NPD Data for $YSr_2Cu_2FeO_{7.08}$[a]

atom	site	x	y	z	Biso (Å)	occ.
Y	4a	0	0	0	0.20(4)	1
Sr	8h	0	0.34911(7)	0.0067(8)	0.68(4)	1
Fe1/Cu1	8i	0.0440(8)	0.25	0.5584(5)	1.0(7)	0.426(7)/0.074(7)
Cu2/Fe2	8h	0	0.42610(8)	0.5000(5)	0.28(3)	0.85(1)/0.15(1)
O1	8h	0	0.3257(1)	0.4739(7)	1.30(5)	1
O2a	8g	0.25	0.0630(1)	0.25	0.39(2)	1
O2b	8g	0.25	−0.0649(1)	0.25	0.39(2)	1
O3	8i	0.390(1)	0.25	0.616(1)	2.1(1)	0.574(3)

[a]S.G. *Imma* (no. 74); a = 5.4053(1) Å, b = 22.9136(5) Å, c = 5.4577(1) Å, V = 675.98(2) Å^3, δ = 0.92; R_p = 3.62%; R_{wp} = 4.66%; χ^2 = 4.22.

= $U - J$, where U is the onsite Coulomb term and J the exchange term. In this work, this effective parameter is simply referred to as U. The J value was fixed to 1 eV. An effective U value of 4 eV was used for the d orbitals of Cu and Fe, that were found appropriate in previous GGA + U investigations.[13,40−42] The local magnetic moments are taken from the difference between the projected electron density of up and down spins onto 1 Å radius sphere. Bader charge analysis[43] was performed on the charge density files[44] using the pymatgen package.[45]

In the present work, we have performed calculations using the idealized stoichiometric compositions $YSr_2Cu_2FeO_7$ and $YSr_2Cu_2FeO_8$ and perfect Cu/Fe ordering within the crystal structures. The crystallographic model of $YSr_2Cu_2FeO_8$ oxide has been constructed taking the initial positions from $YSr_2Cu_2FeO_{7.86}$ (ICSD file 11514),[24] considering a ferromagnetic 2 × 2 × 1 superstructure of the tetragonal $a_p \times a_p \times 3a_p$ unit cell shown in Figure 1a (that is, $Y_4Sr_8Cu_8Fe_4O_{32}$ composition). For $YSr_2Cu_2FeO_7$ oxide, the $6a_p \times \sqrt{2}a_p \times \sqrt{2}a_p$ (S.G. *Ima*2) unit cell has been used for the calculations ($Y_4Sr_8Cu_8Fe_4O_{28}$), corresponding to an ideal arrangement of the tetrahedral chains (Figure 1b). The initial cell parameters and atomic positions of $YSr_2Cu_2FeO_7$ were taken from the ICSD record of isostructural $YSr_2Cu_2GaO_7$.[46] Although the magnetic structure of $YSr_2Cu_2FeO_{8-\delta}$ phases with high δ values ($\delta \sim 1$) has not yet been experimentally determined, magnetic interactions associated to Fe^{3+} and Cu^{2+} cations are expected, and, as explained below, different magnetic structures have been considered.

3. RESULTS AND DISCUSSION

3.1. Experimental Section. The crystal structure and superconducting behavior of the compound with the highest oxygen content, $YSr_2Cu_2FeO_{7.86}$, has previously been reported.[24] In this work, the crystal structure of $YSr_2Cu_2FeO_{7.08}$ is refined by NPD. Table 1 lists the results of the Rietveld refinement of the NPD pattern of $YSr_2Cu_2FeO_{7.08}$ (Figure 2). The refined occupation factors of 8i and 8h crystallographic positions reveal certain disorder (antisite location) of the Fe and Cu atoms. Note that consistently with the oxygen content (δ = 0.92 in $YSr_2Cu_2FeO_{8-\delta}$), there is an occupation of 0.574 for O3 in 8i positions. In the idealized term δ = 1 ($YSr_2Cu_2FeO_7$) where only tetrahedral-Fe is present, the fractional occupancy of O3 is of 0.5. Importantly, the results indicate that corrugation of the [FeO_4] tetrahedral units and their relative orientation along the stacking direction originate an additional superstructure with a diagonal orthorhombic unit cell of dimensions $\sqrt{2}a_p \times 6a_p \times \sqrt{2}a_p$ in the *Imma* space group (note the change of S.G. setting as described in Table 2). Therefore, the refined crystal structure of $YSr_2Cu_2FeO_{7.08}$ is

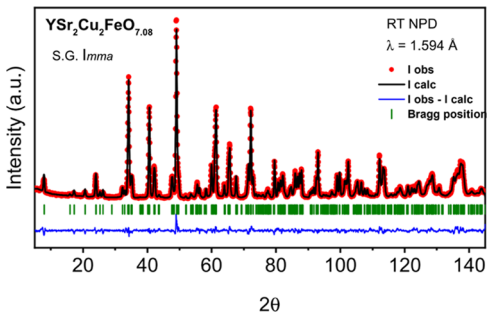

Figure 2. Rietveld refinement of the room temperature (RT) NPD pattern of $YSr_2Cu_2FeO_{7.08}$.

in close agreement with the one reported by Mochiku et al. (ICSD file 151653) for the $YSr_2Cu_2FeO_{7.11}$ compound.[28] The crystallographic model with the *Imma* space group accounts for the presence of two types of tetrahedral chains in the Fe layers, which are left- and right-hand rotated. In this sense, the crystal structure of $YSr_2Cu_2FeO_{7.08}$ can be considered as a disordered version of the model crystal structure of the stoichiometric $YSr_2Cu_2GaO_7$ determined by Roth et al. (ICSD file 71263, used for the DFT calculations)[46] in which the presence of a single chain orientation is well captured within the *Ima*2 space group, as it is represented in Figure 1b.

The variation of the resistivity with the temperature of $YSr_2Cu_2FeO_{7.86}$ shows the expected superconducting/metallic transition at T_c = 70 K (Figure 3a).[24] Above the T_c, the increase of the electrical resistance with temperature reflects the metallic character (inset in Figure 3a). On the contrary, $YSr_2Cu_2FeO_{7.08}$ oxide presents a semiconducting/insulating transition near 200 K (Figure 3b). The logarithmic plot of resistance (inset in Figure 3b) shows an activated behavior in the 200−300 K temperature range, with an activation energy (E_a) of 0.147(4) eV.

The optical band gap of the $YSr_2Cu_2FeO_{7.08}$ phase has been extracted from DRS measurements. The Tauc plot and Kubelka−Munk analysis offer an approximate estimation of optical band gap.[32,33,47] However, if the nature of the electronic transition is not well known (as in the present case), the γ parameter (eq 2) value becomes an important source of uncertainty. For $YSr_2Cu_2FeO_{7.08}$, considering a direct allowed electronic transition, from the Tauc plot we derive a band-gap value of 1.2 eV, while a band gap of 0.73 eV results if an indirect electronic transition is considered (Figure 3c). Methods such as photoluminescence (PL)[48] and X-ray photoelectron spectroscopy (XPS)[49] that offer an accurate band-gap determination are out of the scope of this paper. Given the above, this work considers the interval 1.2−0.73 eV

https://doi.org/10.1021/acs.inorgchem.2c03475
Inorg. Chem. 2023, 62, 3445−3456

Table 2. Calculated Unit Cell Parameters (Å), Unit Cell Volume (Å^3), Volume per Atom (Å^3), and Selected Bond Lengths (Å) for $YSr_2Cu_2FeO_7$ and $YSr_2Cu_2FeO_8$ Idealized Oxides[a]

$YSr_2FeCu_2O_8$	experimental $YSr_2FeCu_2O_{7.85}$	GGA	GGA + U	SCAN	$YSr_2FeCu_2O_7$	experimental[b] $YSr_2FeCu_2O_{7.08}$	C-AF GGA	C-AF GGA + U	C-AF SCAN
a, b	3.8145(3)	3.8252	3.8315	3.7861	a	22.9136(5)[b]	23.1337	23.1424	22.8529
c	11.327(7)	11.3803	11.5457	11.2755	b	5.4577(1)[b]	5.5007	5.5069	5.4411
V	164.81(1)	166.52	169.50	161.62	c	5.4053(1)[b]	5.4241	5.4265	5.3744
V per atom	11.77	11.89	12.10	11.54	V	675.98(2)	690.13	691.63	668.22
d Fe−O3	1.9072(2)	1.9126	1.9157	1.8930	V per atom	13.00	13.27	13.30	12.85
d Fe−O1	1.843(4)	1.8550	1.8813	1.8417	mean d Fe−O	1.8732	1.8754	1.9014	1.8732
d Fe−O1/d Fe−O3	0.9663	0.9699	0.9820	0.9729	Fe−O3−Fe	124.6°	126.0°	122.9°	124.5°
d Cu−O2	1.9244(4)	1.9355	1.9473	1.9147	d Cu−O2	1.933(2)/1.934(2)	1.9365/1.9456	1.9413/1.9507	1.9267/1.9338
d Cu−O1	2.117(4)	2.1134	2.1197	2.0812	d Cu−O1	2.302(4)	2.4327	2.3883	2.3449
d Cu−O1/d Cu−O2	1.1000	1.0919	1.0885	1.0870	d Cu−O1/d Cu−O2	1.1906	1.2533	1.2273	1.2148
d Cu−Cu	3.407(4)	3.4435	3.5439	3.4297	d Cu−Cu	3.384(4)	3.2837	3.3506	3.3095
d Cu−Fe	3.960(3)	3.9684	4.0009	3.9229	d Cu−Fe	4.056(2)	4.1639	4.1337	4.0815

[a]The experimental data of $YSr_2Cu_2FeO_{7.86}$ (ICSD—11514) and $YSr_2Cu_2FeO_{7.08}$ (this work) are included for comparison. For the GGA + U method, a value of U = 4 eV is used for both Cu and Fe. [b]Lattice parameters given in the setting for the S.G. *Imma*. The unit cell metrics corresponding with the S.G. *Ima2* (Table 1) is a (*Imma*) < > c (*Ima2*); b (*Imma*) < > a (*Ima2*); and c (*Imma*) < > b (*Ima2*).

to compare the band gap of $YSr_2Cu_2FeO_{7.08}$ with the DFT-calculated band gap.

3.2. DFT Investigation of $YSr_2Cu_2FeO_{8-\delta}$. *3.2.1. Metallic $YSr_2Cu_2FeO_8$ Phase.* Regardless of the constraints in comparing the experimental data of $YSr_2Cu_2FeO_{7.85}$ (δ = 0.15) and the idealized model $YSr_2Cu_2FeO_8$ (δ = 0), all of the utilized DFT methodologies reproduce the experimental lattice parameters and bond distances (Table 2), with small deviations ranging from a maximum of 4% (GGA + U) to a minimum of 0.2% (SCAN). The compression of the Fe octahedra (d Fe−O1/d Fe−O3 < 1) and the elongation of the Cu-square pyramid (d Cu−O1/d Cu−O2 > 1) along the c-axis are also well captured. There are, however, some subtle differences in the predicting capabilities of the four DFT methodologies. Both the GGA and GGA + U methods tend to produce larger lattice parameters, bonding distances (see for instance Fe−O1), and cell volume than the SCAN functional. For the $YSr_2Cu_2FeO_{8-\delta}$ family, both a and c lattice parameters decrease with increasing oxygen content,[23] and hence the idealized stoichiometric compound $YSr_2Cu_2FeO_8$ should have a lower volume than the synthesized $YSr_2Cu_2FeO_{7.85}$. In this respect, the SCAN functional offers superior performance in predicting such volume reduction.

The calculated magnetic moments and effective Bader charges (Table 3) differ among the different methodologies due to the distinct description of the transition-metal−oxygen bonding. The effective charge of all ions increases from the GGA to the GGA + U, as expected, due to the decreasing covalency of the Fe−O and Cu−O chemical bonds when correlation effects are taken into account. The poor electron localization in the GGA and SCAN approximations yields low magnetic moments on the transition-metal ions (0−0.2 and 2.7−3.0 μ_B per Cu and Fe atom, respectively). Treating the correlation effects results in higher electron localization and larger calculated magnetic moments for Cu atoms (0.5 μ_B) and Fe atoms (3.4 μ_B). Neutron diffraction results and Mössbauer spectra of $YSr_2Cu_2FeO_{7.85}$ yielded a magnetic moment μ_0 (Fe) = 1.7−2 μ_B per Fe atom that the authors attributed to Fe^{4+} ion in low-spin configuration ($t_{2g}^4e_g^0$).[24] No magnetic moment was detected for $Cu^{3+/2+}$ ions. In this regard, although quantitative comparison of magnetic moments with experiments is complicated due to the observed Cu/Fe antisite mixing[24,S0] and differences in the oxygen content, the GGA, and SCAN methodologies offer a more appropriate description than the GGA + U.

The three DFT approximations predict the metallic behavior of the $YSr_2Cu_2FeO_8$ oxide (see calculated DOS in Figure 4). Compared to the GGA method, the introduction of the U term produces a downshift of the occupied Cu/Fe-3d states. The U parameter keeps the 3d orbitals of Fe ions atomic-like, diminishing their hybridization with the 2p orbitals of the oxygen ions (less covalent Fe−O bonding). Although the Fe down-spin states are partially occupied under all approximations, the occupancy is the lowest for the GGA + U methodology, therefore resulting in the larger magnetic moment of 3.4 μ_B per Fe atom, which is close to that expected for a high-spin Fe^{4+} configuration ($t_{2g}^3e_g^1$), and deviates from the experimental observations.

3.2.2. Insulating $YSr_2Cu_2FeO_7$ Phase. Figure 5a−c shows the magnetic structures considered to model the idealized $YSr_2Cu_2FeO_7$ oxide. In the A-type structure, there are FM Cu/Fe in-plane interactions, while the planes order antiferromagnetically along the a-axis (tetragonal c-axis in $YSr_2Cu_2FeO_8$). In

https://doi.org/10.1021/acs.inorgchem.2c03475
Inorg. Chem. 2023, 62, 3445−3456

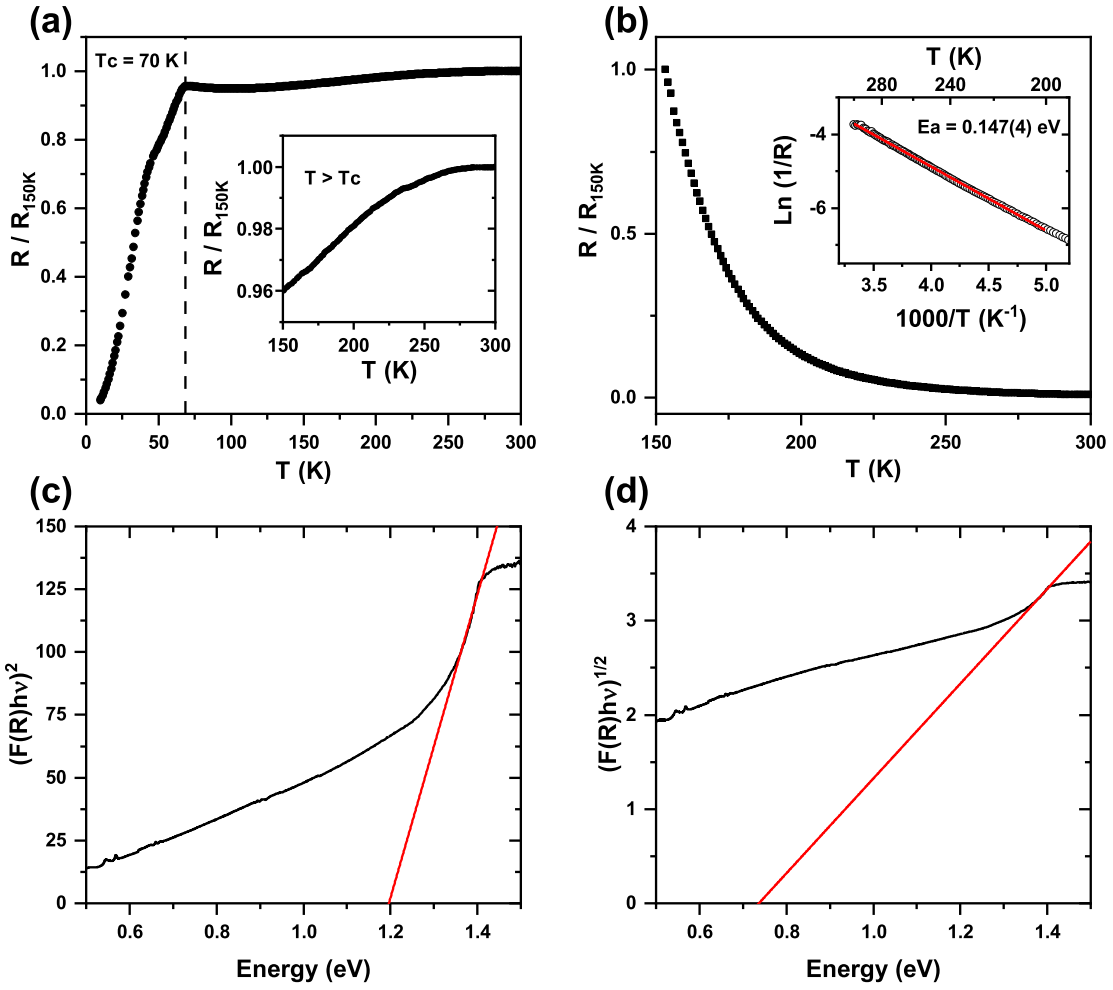

Figure 3. Normalized DC resistance for (a) $YSr_2Cu_2FeO_{7.85}$ and (b) $YSr_2Cu_2FeO_{7.08}$ oxides. The Arrhenius plot used for the determination of the activation energy (E_a) is also shown in panel (b) as an inset. Tauc plot for $YSr_2Cu_2FeO_{7.08}$ oxide considering direct (c) and indirect (d) allowed electronic transitions.

Table 3. Calculated Local Magnetic Moments μ (in μ_B per Atom) and Effective Bader Charges (Q) for Idealized $YSr_2Cu_2FeO_7$ and $YSr_2Cu_2FeO_8$ Oxides[a]

	$YSr_2Cu_2FeO_8$			C-AFM $YSr_2Cu_2FeO_7$			
	GGA	GGA + U	SCAN		GGA	GGA + U	SCAN
Q (Fe)	1.796	1.881	1.930	Q (Fe)	1.481	1.643	1.628
Q (Cu)	1.073	1.090	1.157	Q (Cu)	0.942	1.010	1.081
Q (O1)	−1.158	−1.187	−1.228	Q (O1)	−1.267	−1.324	−1.347
Q (O2)	−1.187	−1.192	−1.232	Q (O2)	−1.235	−1.260	−1.310
Q (O3)	−1.125	−1.175	−1.175	Q (O3)	−1.210	−1.297	−1.300
μ (Fe)	2.7	3.4	3.0	μ (Fe)	3.6	4.1	3.9
μ (Cu)	0.0	0.5	0.2	μ (Cu)	0.0	0.5	0.5
μ (O1)	0.1	0.0	0.1	μ (O1)	0.2	0.2	0.2
μ (O2)	0.0	0.1	0.0	μ (O2)	0.0	0.0	0.0
μ (O3)	0.2	0.1	0.1	μ (O3)	0.0	0.0	0.0

[a]Within the GGA + U method, a value of U = 4 eV is used for both Cu and Fe.

the C-type, for each magnetic site, an in-plane AFM configuration between nearest-neighbor spins exits, while a FM configuration is set between the Fe and Cu planes. However, the sign reverses across the Y-layers due to the AFM direct exchange between Cu^{2+} cations at the face-confronted pyramids. Within each (CuO_2−SrO−FeO−SrO−CuO_2) block, a C-type magnetic ordering is thus defined since the Cu/Fe magnetic moments can be grouped as chains along the a-axis (tetragonal c-axis in $YSr_2Cu_2FeO_8$). The G-type presents the same AFM in-plane magnetic ordering of the C-type, but with AFM interactions between the Cu and Fe planes.

The four magnetic states tested to model $YSr_2Cu_2FeO_7$ follow the energetic ordering: FM ∼ A-AFM ≫ G-AFM ∼ C-AFM (Table 4). The large stabilization of the G and C-AFM types (about 0.4 eV/fu respective to the FM configuration) denotes strong in-plane Cu/Fe AFM interactions. On the

https://doi.org/10.1021/acs.inorgchem.2c03475
Inorg. Chem. 2023, 62, 3445−3456

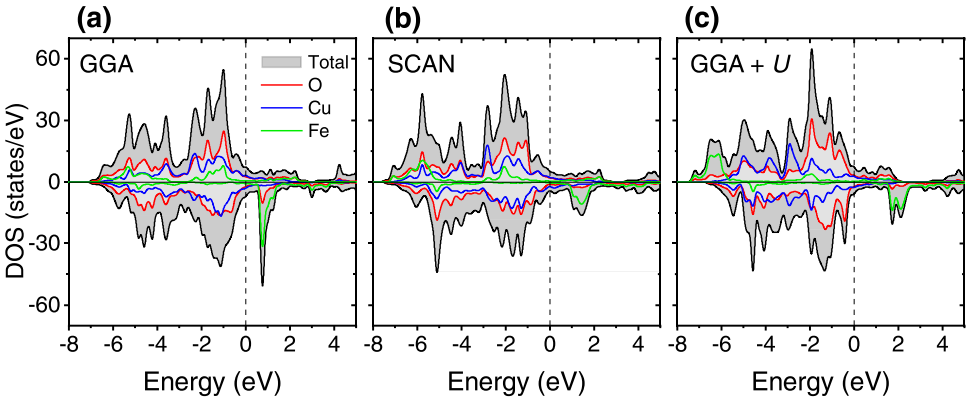

Figure 4. Calculated total and atom-projected density of states for $YSr_2Cu_2FeO_8$: (a) GGA functional, (b) SCAN functional, and (c) GGA + U method. The Fermi level is set as the zero of energy. Up-spin (or majority) and down-spin (or minority) contributions are shown in the upper and lower parts of the panels, respectively. Color code: total DOS in gray, Cu contribution in blue, Fe contribution in green, and O contribution in red. DOS units refer to the calculated cell.

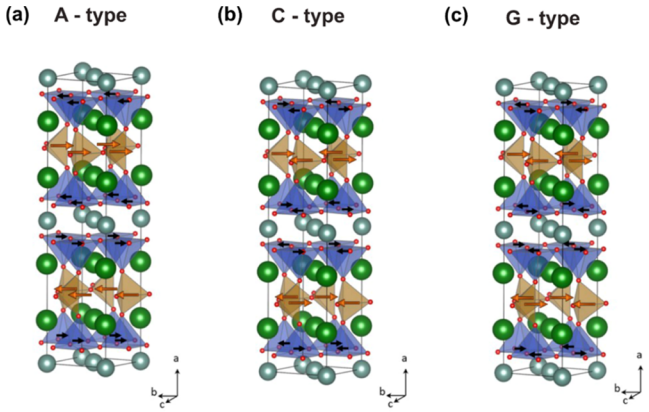

Figure 5. (a–c) Magnetic structures (C, G, A) used to simulate $YSr_2Cu_2FeO_7$ (S.G. *Ima*2). Arrows indicate the spin orientation of the Fe and Cu atoms within the magnetic structure. Color code: Fe atoms in brown, Cu atoms in blue, Sr atoms in green, Y atoms in gray, and O atoms in red.

Table 4. Calculated Total-Energy Differences for Magnetic Configurations (Figure 5a–c) in $YSr_2Cu_2FeO_7$ (in eV/fu)[a]

type	GGA	GGA + U	SCAN
A-AFM	0.020	0.020	−0.075
C-AFM	−0.248	−0.424	−0.414
G-AFM	−0.228	−0.375	−0.408

[a]The FM ordering is set as the zero of energy.

other hand, the small energy difference between G and C-AFM types, and between A-AFM and FM types, (5 meV/fu) suggests weak interplane magnetic interactions. The GGA, GGA + U, and SCAN methodologies predict the C-AFM to be the ground state, which has therefore been chosen to investigate the crystal and electronic structures of $YSr_2Cu_2FeO_7$.

Independently on the utilized functional, the optimization of the crystal structure of the idealized $YSr_2Cu_2FeO_7$ oxide results in lattice parameters in reasonable agreement with the experimental values of $YSr_2Cu_2FeO_{7.08}$ with errors below 2.1% (Table 2 and Figure S1). The GGA and GGA + U tend to overestimate the lattice parameters and TM–O distances, while the SCAN functional underestimates them. For the Fe environment, all of the approximations give a satisfactory description of the average bond distances (errors below 0.7%), and even of the corrugation of the [FeO] layers, the SCAN results being the closest to the experimental values. However, the Cu–O square pyramidal environment is more elongated than the one experimentally observed (d axial/d equatorial, d Cu–O1/d Cu–O2 in Table 2). Since the hybridization of the Cu-apical oxygen plays a significant role in the electronic structure of YBCO-related oxides,[51] it is worth noting that the deviations in the Cu–O1 bond lengths are of 5.5% (GGA), 3.6% (GGA + U), and 1.7% (SCAN). According to the major deviation in the Cu–O1 bond distance, the GGA fails to reproduce the semiconducting behavior of $YSr_2Cu_2FeO_{7.08}$ (calculated DOS in Figure 6a) in clear disagreement with the experimental observations (Figure 3b).

While the GGA incorrectly predicts the metallic behavior for the ground state of idealized $YSr_2Cu_2FeO_7$, a band gap of 0.85 eV opens in the GGA + U (U-Cu and U-Fe = 4 eV), and noteworthy, a near band gap of 0.63 eV is obtained using the SCAN functional (Figure 6). Compared to the $YSr_2Cu_2FeO_8$ phase, in both SCAN and GGA + U, the effective charge of the TMs decreases (Table 3), and the TM–O distances increase (Table 2), in agreement with the lower formal oxidation states of Fe^{3+} and Cu^{2+} in $YSr_2Cu_2FeO_7$. The effective charge on oxygen ions increases, approaching the oxide ion O^{2-}. SCAN and GGA + U methods predict nearly the same calculated magnetic moments for TM ions: μ(Cu) = 0.5 μ_B per atom and μ(Fe) ∼ 4 μ_B per atom. The magnetic moment of the Cu ions is in good agreement with the experimental values reported in similar Cu^{2+} compounds.[52,53] The magnetic moment on Fe ions suggests a high-spin Fe^{3+} configuration ($e^2t_2^3$, magnetic moment of the free ion μ_0 = 5.0 μ_B). It is worth to note that magnetic moment values between 3 and 4 μ_B per atom have been experimentally observed in other complex Fe^{3+}-tetrahedral oxides.[54,55] On the other hand, the Fe–O and Cu–O covalencies bring an appreciable spin moment of ∼0.2 μ_B in the shared O1 site. As observed in the atom-projected density of states (Figure 6c), the U term shifts the TM-3d states to lower energies; yet, there is a good hybridization of TM-3d to O-2p states (see band at −6 eV). In summary, for the insulating compound, SCAN offers very similar results to the GGA + U in terms of band-gap and magnetic moments, although there are clear differences in the shape and nature of the states at the Fermi level. To further analyze the appropriateness of the SCAN vs. the GGA + U method, in a

https://doi.org/10.1021/acs.inorgchem.2c03475
Inorg. Chem. 2023, 62, 3445–3456

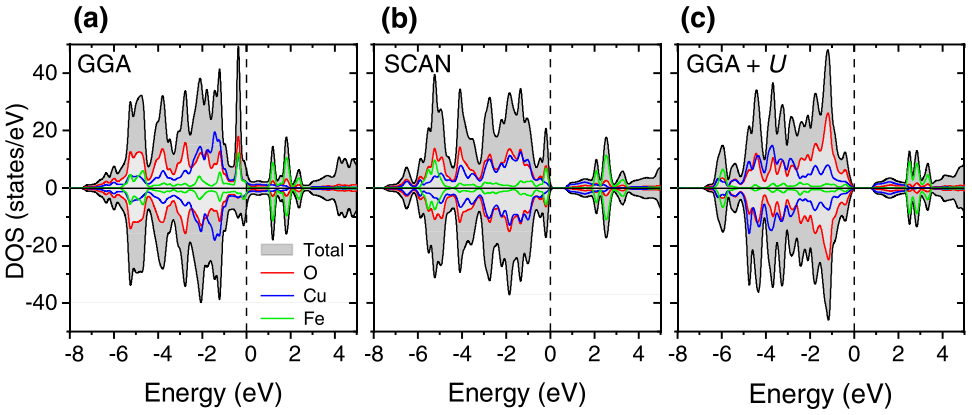

Figure 6. Calculated total and atom-projected density of states (DOS) for the ground-state C-magnetic structure of the idealized $YSr_2Cu_2FeO_7$: (a) GGA functional, (b) SCAN functional, and (c) GGA + *U* method. The Fermi level is set as the zero of energy. Up-spin (or majority) and down-spin (or minority) contributions are shown. Color code: total black, Cu contribution in blue, Fe contribution in green, and O contribution in red. DOS units refer to the calculated cell.

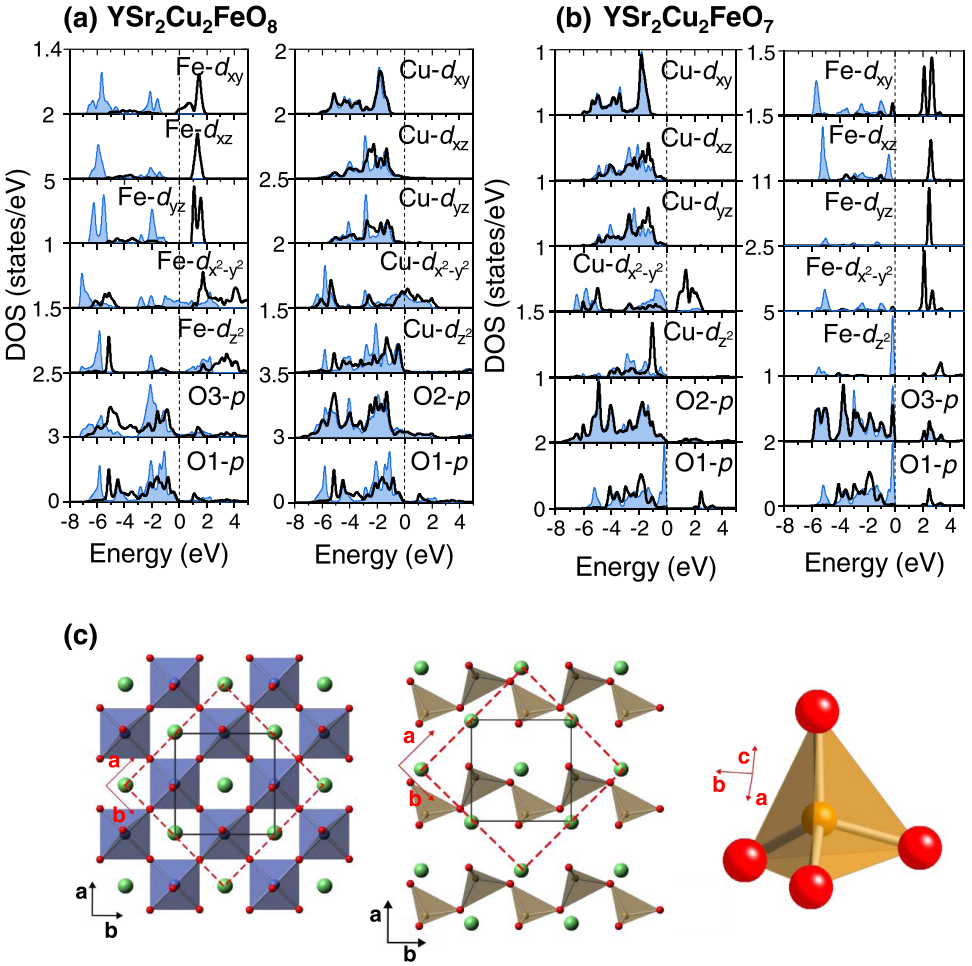

Figure 7. Orbital-projected density of states within the SCAN functional for (a) idealized $YSr_2Cu_2FeO_8$ showing the Fe-3*d*, O3-2*p* and O1-2*p* and Cu-3*d*, O2-2*p*, and O1-2*p* orbitals, and (b) idealized $YSr_2Cu_2FeO_7$ showing the Cu-3*d*, O2-2*p* and O1-2*p* and Fe-3*d*, O3-2*p*, and O1-2*p* orbital contribution. Color code: up-spin (or majority) in blue and down-spin (or minority) in black. (c) Crystallographic cell used for the orbital-projected DOS of $YSr_2Cu_2FeO_7$ (in red) and its relation to the to the crystal setting in the *Ima*2 S.G. (in black).

first approximation, the calculated DOS could be qualitatively compared with experimental photoelectron spectroscopy (PES). It is however important to point out that such comparison neglects the excitation aspects, which can be taken into account by quasi-particle calculations in the GW approach.[56]

For the sake of completeness, the relation between the electronic properties and the magnetic structure of $YSr_2Cu_2FeO_7$ is analyzed within the SCAN and GGA + *U*

https://doi.org/10.1021/acs.inorgchem.2c03475
Inorg. Chem. 2023, 62, 3445−3456

methods (Figure S2). Once more, both DFT approximations yield the same results in terms of the insulating/metallic behavior. The calculated DOS for the G magnetic structure, with in-plane Cu/Fe AFR interactions, corresponds to an insulating compound with the same band gap of the C-magnetic structure (0.63 eV in SCAN, 0.85 eV in GGA+ U). The FR and A magnetic structures, with in-plane Cu/Fe FR interactions, generate metallic properties. These results reveal that, for the idealized $YSr_2Cu_2FeO_7$, the insulating character couples to the in-plane AFM Cu/Fe ordering.

3.2.3. On the Metal-to-Insulating Transition in the $YSr_2Cu_2FeO_{8-\delta}$ ($0 < \delta < 1$) Family. The above results highlight that the SCAN functional reproduces the metal and the insulating character of $YSr_2Cu_2FeO_8$ and $YSr_2Cu_2FeO_7$ compounds, respectively. The orbital-projected DOS (Figure 7) adds more insights into the comprehensive interpretation of the chemical bonding and the evolution of the electronic properties as a function of the δ value. Starting with the metallic $YSr_2Cu_2FeO_8$, in the Fe octahedra, the hybridization of O3(2p)−Fe($3d_{x^2-y^2}$) and O1(2p)−Fe($3d_{z^2}$) produces the lower energy band σ-O(p)−Fe(e_g) and the upper energy band σ*-O(p)−Fe(e_g). As observed in Figure 7a, the occupation of the bonding sigma band occurs in both spin channels, with the Fermi level crossing the $3d_{x^2-y^2}$ majority spin orbital. The Π O(2p)−Fe($3t_{2g}$) bands are fully occupied in the up-spin channel, but also show some occupancy in the down-spin channel. As deduced from the calculated magnetic moments, the 3d-Fe orbitals filling does not correspond to either LS-Fe^{4+} ($t_{2g}^4e_g^0$) or HS-Fe^{4+} ($t_{2g}^3e_g^1$), but to an itinerant character where every 3d orbital contributes to the magnetic moment, in agreement with the metallic properties of the oxide. For the Cu-3d states, the crystal field splitting of the Cu−O square pyramidal environment lifts the degeneracy of the Cu-e_g orbitals to the lower-lying $3d_{z^2}$ and higher-lying $3d_{x^2-y^2}$ orbitals. The strong hybridization O2(2p)−Cu($3d_{x^2-y^2}$) produces a wide band that is partially filled in both spin channels, yielding a low net spin of 0.3 μ_B. The Fermi level lies in the band constructed mainly from the Cu-$3d_{x^2-y^2}$ and O2-2p orbitals and in a minor extent in the band constructed from Fe-$3d_{x^2-y^2}$ and O3-2p orbitals. Therefore, these bands have the largest implication in the electronic properties of the $YSr_2Cu_2FeO_{8-\delta}$ family.

Upon vacancies incorporation in $YSr_2Cu_2FeO_8$ (Figure 7a) to form $YSr_2Cu_2FeO_7$ (Figure 7b), according to the Fermi-level displacement, electron filling occurs in the Cu-$3d_{x^2-y^2}$ derived band. Since in $YSr_2Cu_2FeO_7$ the Cu ions have the nominal valence of 2+, and hence a nominal d^9 state, there are fully occupied t_{2g} orbitals and d_{z^2} orbitals, while the $d_{x^2-y^2}$ orbital remains half-filled yielding a low net spin of 0.5 μ_B. The energy gap opens between the occupied and the unoccupied Cu-$3d_{x^2-y^2}$ orbitals. On the other hand, the analysis of the Fe-3d states upon electron doping of $YSr_2Cu_2FeO_8$ is more complicated, since the coordination around the Fe atoms changes from octahedral in $YSr_2Cu_2FeO_8$ to tetrahedral in $YSr_2Cu_2FeO_7$. According to crystal field theory, in the tetrahedral field, the Fe-3d orbitals split into two manifolds, a lower one with two levels and an upper one with three levels (these would be of e and t_2 character respectively, if the local symmetry were perfectly tetrahedral). This is not observed in Figure 7b due to the orientation of the Fe tetrahedra relative to the crystallographic cell axes utilized for the orbital-projected DOS (Figure 7c). Nevertheless, for all of the Fe-3d states, the up-spin channel is fully occupied and the down-spin channel is almost empty, the energy separation between up and down-spin channels being rather large. This electron density localization leads to the aforementioned high-spin Fe^{3+} configuration.

In summary, the results of the SCAN methodology indicate that in the $YSr_2Cu_2FeO_{8-\delta}$ family, the lowering of the oxygen content drives the metal-to-insulating transition by electron doping. A reduction in the oxygen content (higher δ value) results in a decrease in the nominal valence of Cu/Fe ions, and hence in the filling of the Cu/Fe-$3d_{x^2-y^2}$ states. This picture is fully consistent with the well-documented importance of filling control in the electronic structure of high T_c cuprates, a typical example being the insulating to metal transition in $La_{2-x}Sr_xCuO_4$ induced by hole doping ($x = 0$ metallic).[18,57]

Remarkably, the SCAN functional offers a feasible interpretation of the metal-to-insulating transition in the $YSr_2Cu_2FeO_{8-\delta}$ family, when looking at the idealized compounds with $\delta = 0$ and 1. However, in addition to distinct oxygen contents (δ values), the synthesized compounds $YSr_2Cu_2FeO_{7.86}$ ($\delta = 0.14$) and $YSr_2Cu_2FeO_{7.08}$ ($\delta = 0.92$) show antisite disorder, with a Cu/Fe mixing close to 15% (see Table 1 and ref 24). As noted by different authors,[22−24,58,59] the mutual substitution of Cu and Fe depends on the annealing history/oxygen content. The simulation of the random distribution of the antisite defects that occurs in the real materials requires the utilization of the special quasi-random structures (SQS) approach,[60] which is out of the scope of this work. The antisite disorder could perturb the AFM in-plane ordering that, as discussed above, is critically linked to the insulating behavior of the investigated compounds with the lowest oxygen contents ($\delta \sim 0$). It is foreseeable that the concentration and location of both oxygen vacancies and antisite defects drastically influence the magnetic and electronic properties of the $YSr_2Cu_2FeO_{8-\delta}$ family. This is in agreement with the observed dependence between the property and the synthetic history of the materials.

4. CONCLUSIONS

The precise modeling of the ground-state properties in complex oxides that contain more than one type of TM ions remains challenging, especially with the irruption of correlated oxides as functional materials. In this work, we have examined the capabilities of different DFT methodologies (GGA, GGA + U, SCAN) to model the crystal structure and the electronic and magnetic properties of $YSr_2Cu_2FeO_{8-\delta}$ compounds in which the oxygen content in the $FeO_{2-\delta}$ layers drives the average oxidation states of both Fe and Cu cations, thereby determining the electrical properties. We have found that the SCAN and GGA methodologies are valid to simulate the metallic properties of the oxide with the highest oxygen content of the family ($\delta = 0$, idealized-$YSr_2Cu_2FeO_8$) and the itinerant character of its bonding electrons. Introducing the U term (GGA + U) results in excessive electron localization and large magnetic moments that deviate from the experimental observations, therefore discarding this methodology for property prediction in the metallic phases of the $YSr_2Cu_2FeO_{8-\delta}$ system. Contrariwise, the insulating character of the compound with the lowest oxygen content ($\delta = 1$, idealized-$YSr_2Cu_2FeO_7$) is well captured when electron correlations are treated by the U parameter using the GGA + U approximation. Importantly, the results point out that the SCAN functional also offers a good platform to investigate these insulating compounds. These results render the SCAN

https://doi.org/10.1021/acs.inorgchem.2c03475
Inorg. Chem. 2023, 62, 3445−3456

functional as the only one well suited, among the utilized methodologies, to investigate the basic electronic properties across the $YSr_2Cu_2FeO_{8-\delta}$ series. It should be noted that, together with the lack of an adjustable U parameter, other benefits of the SCAN functional are the affordable computational cost and the transferability of results among different works. Yet, a severe limiting factor for the DFT investigation of the $YSr_2Cu_2FeO_{8-\delta}$ family resides in the need of complex crystallographic models to take into account the antisite Cu/Fe disorder and the fractional occupancies of the O3 site that occur in the synthesized materials.

■ ASSOCIATED CONTENT

Supporting Information

The Supporting Information is available free of charge at https://pubs.acs.org/doi/10.1021/acs.inorgchem.2c03475.

Calculated lattice parameters and density of states for the A-AFM, G-AFM, and FM magnetic structures of $YSr_2Cu_2FeO_7$ (PDF)

■ AUTHOR INFORMATION

Corresponding Author

M. Elena Arroyo-de Dompablo − *Departamento de Química Inorgánica, Universidad Complutense de Madrid, 28040 Madrid, Spain;* orcid.org/0000-0001-5249-3562; Email: e.arroyo@quim.ucm.es

Authors

Marianela Gómez-Toledo − *Departamento de Química Inorgánica, Universidad Complutense de Madrid, 28040 Madrid, Spain;* orcid.org/0000-0001-5594-4146

Sara A. López-Paz − *Departamento de Química Inorgánica, Universidad Complutense de Madrid, 28040 Madrid, Spain; Department of Quantum Matter Physics, University of Geneva, CH-1211 Geneva, Switzerland*

Susana García-Martín − *Departamento de Química Inorgánica, Universidad Complutense de Madrid, 28040 Madrid, Spain;* orcid.org/0000-0003-0729-4892

Complete contact information is available at: https://pubs.acs.org/10.1021/acs.inorgchem.2c03475

Author Contributions

M.G.-T. performed the DFT calculations including the data preparation/analysis, tables, and graphical representations. She performed the spectroscopy measurements, interpretation, and graphics, and she also contributed in writing the original draft of the manuscript. S.A.L.-P. conducted the experimental research comprising the synthesis and structural and electrical characterization of the materials. S.G.-M. led the experimental project administration. M.E.A.-d.D. directed the computational investigation, led the computational project administration, and wrote the draft of the manuscript. All authors contributed in the discussion and writing of the final version of the manuscript. All authors have given approval to the final version of the manuscript.

Notes

The authors declare no competing financial interest.

■ ACKNOWLEDGMENTS

The authors thank MCIN/AEI/10.13039/501100011033 and "NextGenerationEU"/PRTR for funding the Projects PID2019-106662RB-C44 and TED2021-130452B-C21. M.E.A.-d.D. and M.G.-T. acknowledge funding for computational research and spectroscopy measurements from Universidad Complutense de Madrid (FEI-EU-22-01-4129585). M.G.-T. thanks Comunidad de Madrid for contract (PEJ-2020-AI/IND-18065) of the program "Ayudas para la contratación de Ayudantes de Investigación y Técnicos de Laboratorio". The authors acknowledge Dr. Clemens Ritter for the neutron diffraction measurements and the ILL for beam time allocation in the D2B instrument under the experiment code 5-23-705. Data are available from ILL at DOI: 10.5291/ILL-DATA.5-23-705. The authors are grateful to R. González-Prieto for his assistance in the Reflectance Diffuse Spectroscopy measurements.

■ REFERENCES

(1) Irvine, J.; Rupp, J. L. M.; Liu, G.; Xu, X.; Haile, S.; Qian, X.; Snyder, A.; Freer, R.; Ekren, D.; Skinner, S.; Celikbilek, O.; Chen, S.; Tao, S.; Shin, T. H.; O'Hayre, R.; Huang, J.; Duan, C.; Papac, M.; Li, S.; Celorrio, V.; Russell, A.; Hayden, B.; Nolan, H.; Huang, X.; Wang, G.; Metcalfe, I.; Neagu, D.; Martin, S. G. Roadmap on inorganic perovskites for energy applications. *J. Phys.: Energy* **2021**, *3*, No. 031502.

(2) Hohenberg, P.; Kohn, W. Inhomogeneous electron gas. *Phys. Rev. B: Condens. Matter Mater. Phys.* **1964**, *136*, B864−B871.

(3) Kohn, W.; Sham, L. J. Self-consistent equations including exchange and correlation effects. *Phys. Rev.* **1965**, *140*, A1133.

(4) Perdew, J. P. Generalized gradient approximations for exchange and correlation - a look backward and forward. *Phys. B* **1991**, *172*, 1−6.

(5) Perdew, J. P.; Yue, W. Accurate and simple density functional for the electronic exchange energy - Generalized Gradient Approximation. *Phys. Rev. B: Condens. Matter Mater. Phys.* **1986**, *33*, 8800−8802.

(6) Piskunov, S.; Heifets, E.; Eglitis, R. I.; Borstel, G. Bulk properties and electronic structure of $SrTiO_3$, $BaTiO_3$, $PbTiO_3$ perovskites: an ab initio HF/DFT study. *Comput. Mater. Sci.* **2004**, *29*, 165−178.

(7) Eng, H. W.; Barnes, P. W.; Auer, B. M.; Woodward, P. M. Investigations of the electronic structure of d^0 transition metal oxides belonging to the perovskite family. *J. Solid State Chem.* **2003**, *175*, 94−109.

(8) Oja, R.; Tyunina, M.; Yao, L.; Pinomaa, T.; Kocourek, T.; Dejneka, A.; Stupakov, O.; Jelinek, M.; Trepakov, V.; van Dijken, S.; Nieminen, R. M. d^0 Ferromagnetic Interface between Nonmagnetic Perovskites. *Phys. Rev. Lett.* **2012**, *109*, No. 127207.

(9) Bilc, D. I.; Orlando, R.; Shaltaf, R.; Rignanese, G. M.; Iniguez, J.; Ghosez, P. Hybrid exchange-correlation functional for accurate prediction of the electronic and structural properties of ferroelectric oxides. *Phys. Rev. B: Condens. Matter Mater. Phys.* **2008**, *77*, No. 165107.

(10) Anisimov, V. I.; Zaanen, J.; Andersen, O. K. Band Theory and Mott Insulators - Hubbard-U Instead of Stoner-I. *Phys. Rev. B: Condens. Matter Mater. Phys.* **1991**, *44*, 943−954.

(11) Zhou, F.; Marianetti, C. A.; Cococcioni, M.; Morgan, D.; Ceder, G. Phase separation in Li_xFePO_4 induced by correlation effects. *Phys. Rev. B: Condens. Matter Mater. Phys.* **2004**, *69*, No. 201101.

(12) Ganduglia-Pirovano, M. V.; Hofmann, A.; Sauer, J. Oxygen vacancies in transition metal and rare earth oxides: Current state of understanding and remaining challenges. *Surf. Sci. Rep.* **2007**, *62*, 219.

(13) Wang, L.; Maxisch, T.; Ceder, G. Oxidation energies of transition metal oxides within the GGA+U framework. *Phys. Rev. B: Condens. Matter Mater. Phys.* **2006**, *73*, No. 195107.

(14) Anisimov, V. I.; Aryasetiawan, F.; Lichtenstein, A. I. First-principles calculations of the electronic structure and spectra of strongly correlated systems: The LDA+U method. *J. Phys.: Condens. Matter* **1997**, *9*, 767−808.

(15) Sun, J.; Ruzsinszky, A.; Perdew, J. P. Strongly Constrained and Appropriately Normed Semilocal Density Functional. *Phys. Rev. Lett.* **2015**, *115*, No. 036402.
(16) Hinuma, Y.; Hayashi, H.; Kumagai, Y.; Tanaka, I.; Oba, F. Comparison of approximations in density functional theory calculations: Energetics and structure of binary oxides. *Phys. Rev. B: Condens. Matter Mater. Phys.* **2017**, *96*, No. 094102.
(17) Kitchaev, D. A.; Peng, H.; Liu, Y.; Sun, J.; Perdew, J. P.; Ceder, G. Energetics of MnO_2 polymorphs in density functional theory. *Phys. Rev. B: Condens. Matter Mater. Phys.* **2016**, *93*, No. 045132.
(18) Furness, J. W.; Zhang, Y.; Lane, C.; Buda, I. G.; Barbiellini, B.; Markiewicz, R. S.; Bansil, A.; Sun, J. An accurate first-principles treatment of doping-dependent electronic structure of high-temperature cuprate superconductors. *Commun. Phys.* **2018**, *1*, No. 11.
(19) Kaczkowski, J.; Pugaczowa-Michalska, M.; Płowaś-Korus, I. Isovalent cation ordering in Bi-based double perovskites: A density functional analysis. *J. Magn. Magn. Mater.* **2022**, *548*, No. 168984.
(20) Iglesias, L.; Bibes, M.; Varignon, J. First-principles study of electron and hole doping effects in perovskite nickelates. *Phys. Rev. B: Condens. Matter Mater. Phys.* **2021**, *104*, No. 035123.
(21) Varignon, J.; Bibes, M.; Zunger, A. Mott gapping in 3d ABO_3 perovskites without Mott-Hubbard interelectronic repulsion energy *U*. *Phys. Rev. B: Condens. Matter Mater. Phys.* **2019**, *100*, No. 035119.
(22) Shimoyama, J.; Otzschi, K.; Hinouchi, T.; Kishio, K. Discovery of superconductivity in Fe-based cuprates. *Phys. C* **2000**, *341*−*348*, 563−564.
(23) Mochiku, T.; Nakano, Y.; Hoshikawa, A.; Sato, S.; Oikawa, K.; Ishigaki, T.; Kamiyama, T.; Kadowaki, K.; Hirata, K. Superstructure in $Sr_2YCu_2FeO_{6+\delta}$. *Phys. C* **2004**, *412*−*414*, 115−119.
(24) López-Paz, S. A.; Martinez de Irujo-Labalde, X.; Sanchez-Marcos, J.; Ritter, C.; Moran, E.; Alario-Franco, M. A. Soft Magnetic Switching in a $FeSr_2YCu_2O_{7.85}$ Superconductor with Unusually High Iron Valence. *Inorg. Chem.* **2019**, *58*, 12809−12814.
(25) Mochiku, T.; Hata, Y.; Yamaguchi, K.; Tsuchiya, Y.; Hoshikawa, A.; Iwase, K.; Sulistyanintyas, D.; Ishigaki, T.; Yasuoka, H.; Hirata, K. Annealing effect on structure and superconductivity in $FeSr_2YCu_2O_{6+\delta}$ magnetic superconductor. *Phys. Procedia* **2012**, *45*, 73−76.
(26) Sansom, J. E. H.; Kendrick, E.; Rudge-Pickard, H. A.; Islam, M. S.; Wright, A. J.; Slater, P. R. Synthesis and characterisation of the perovskite- related cuprate phases $YSr_2Cu_2MO_{7+y}$ (M = Co, Fe) for potential use as solid oxide fuel cell cathode materials. *J. Mater. Chem.* **2005**, *15*, 2321−2327.
(27) López-Paz, S. A.; Marin-Gamero, R.; Martinez de Irujo-Labalde, X.; Sanchez-Marcos, J.; Perez-Coll, D.; Franco, M. A. A. Y.; Garcia-Martin, S. YBaCuO-type perovskites as potential air electrodes for SOFCs. The case of $YSr_2Cu_2FeO_{7+\delta}$. *J. Mater. Chem. A* **2021**, *9*, 8554−8560.
(28) Mochiku, T.; Nakano, Y.; Oikawa, K.; Kamiyama, T.; Fujii, H.; Hata, Y.; Suzuki, I.; Kakeya, I.; Kadowaki, K.; Hirata, K. Atomic ordering in $FeSr_2LnCu_2O_{6+\delta}$ system (Ln = Nd, Y and Er). *Phys. C* **2003**, *400*, 43−52.
(29) Pissas, M.; Kallias, G.; Moraitakis, E.; Niarchos, D.; Simopoulos, A. Site occupancy of Fe in the oxygen-saturated $YSr_2Cu_{3-x}Fe_xO_y$ compound for x=0.25 up to 1. *Phys. C* **1994**, *234*, 127−136.
(30) Lopez-Paz, S. A.; Sari, D. P.; Hillier, A. D.; Alario-Franco, M. A. Coexistence of magnetism and superconductivity in the iron containing $FeSr_2YCu_2O_{7.57}$ cuprate as studied by μ-SR. *AIP Adv.* **2021**, *11*, No. 015011.
(31) Rodriguez-Carvajal, J. Recent advances in magnetic structure determination by neutron powder diffraction. *Physica B* **1993**, *192*, 55−69.
(32) Kubelka, P.; Munk, F. A. Contribution to the Optics of Pigments. *Z. Technol. Phys.* **1931**, *12*, 593−599.
(33) Tauc, J.; Grigorovici, R.; Vancu, A. Optical Properties And Electronic Structure of Amorphous Germanium. *Phys. Status Solidi B* **1966**, *15*, 627−637.
(34) Kresse, G.; Furthmuller, J. Efficient iterative schemes for ab initio total-energy calculations using a plane-wave basis set. *Phys. Rev. B* **1996**, *54*, 11169.
(35) Kresse, G.; Joubert, D. From ultrasoft pseudopotentials to the projector augmented-wave method. *Phys. Rev. B* **1999**, *59*, 1758.
(36) Blöchl, P. E. Projector augmented-wave method. *Phys. Rev. B* **1994**, *50*, 17953.
(37) Perdew, J. P.; Burke, K.; Ernzerhof, M. Generalized gradient approximation made simple. *Phys. Rev. Lett.* **1996**, *77*, 3865−3868.
(38) Blöchl, P. E.; Jepsen, O.; Andersen, O. K. Improved tetrahedron method for Brillouin-zone integrations. *Phys. Rev. B: Condens. Matter Mater. Phys.* **1994**, *49*, 16223−16233.
(39) Dudarev, S. L.; Botton, G. A.; Savrasov, S. Y.; Szotek, Z.; Temmerman, W. M.; Sutton, A. P. Electronic structure and elastic properties of strongly correlated metal oxides from first principles: LSDA+*U*, SIC-LSDA and EELS study of UO_2 and NiO. *Phys. Status Solidi A* **1998**, *166*, 429−443.
(40) Arroyo y de Dompablo, M. E.; Lee, Y.-L.; Morgan, D. First Principles Investigation of Oxygen Vacancies in Columbite MNb_2O_6 (NI = Mn, Fe, Co, Ni, Cu). *Chem. Mater.* **2010**, *22*, 906−913.
(41) Ritzmann, A. M.; Dieterich, J. M.; Carter, E. A. Density functional theory plus *U* analysis of the electronic structure and defect chemistry of LSCF ($La_{0.5}Sr_{0.5}Co_{0.25}Fe_{0.75}O_{3-\delta}$). *Phys. Chem. Chem. Phys.* **2016**, *18*, 12260−12269.
(42) Jain, A.; Shyue Ping, O.; Hautier, G.; Chen, W.; Richards, W. D.; Dacek, S.; Cholia, S.; Gunter, D.; Skinner, D.; Ceder, G.; Persson, K. A. Commentary: The Materials Project: A materials genome approach to accelerating materials innovation. *APL Mater.* **2013**, *1*, No. 011002.
(43) Bader, R. F. W. *Atoms in Molecules: A Quantum Theory*; Oxford University Press: Oxford, U.K., 1990.
(44) Henkelman, G.; Arnaldsson, A.; Jónsson, H. A fast and robust algorithm for Bader decomposition of charge density. *Comput. Mater. Sci.* **2006**, *36*, 354−360.
(45) Ong, S. P.; Richards, W. D.; Jain, A.; Hautier, G.; Kocher, M.; Cholia, S.; Gunter, D.; Chevrier, V. L.; Persson, K. A.; Ceder, G. Python Materials Genomics (pymatgen): A robust, open-source python library for materials analysis. *Comput. Mater. Sci.* **2013**, *68*, 314−319.
(46) Roth, G.; Adelmann, P.; Heger, G.; Knitter, R.; Wolf, T. The crystal-structure of $RESr_2GaCu_2O_7$. *J. Phys. I* **1991**, *1*, 721−741.
(47) Dolgonos, A.; Mason, T. O.; Poeppelmeier, K. R. Direct optical band gap measurement in polycrystalline semiconductors: A critical look at the Tauc method. *J. Solid State Chem.* **2016**, *240*, 43−48.
(48) Wu, J.; Walukiewicz, W.; Yu, K. M.; Ager, J. W.; Haller, E. E.; Lu, H.; Schaff, W. J.; Saito, Y.; Nanishi, Y. Unusual properties of the fundamental band gap of InN. *Appl. Phys. Lett.* **2002**, *80*, 3967−3969.
(49) Kobayashi, H.; Mori, T.; Namba, K.; Nakato, Y. New method for determination of energy distribution of surface states in the semiconductor band-gap: XPS measurements under biases. *Solid State Commun.* **1994**, *92*, 249−254.
(50) Pissas, M.; Kallias, G.; Simopoulos, A.; Niarchos, D.; Sonntag, R. Neutron diffraction study of the deoxygenated $YSr_2Cu_{3-x}Fe_xO_{6+y}$ (x = 0.8 and 1) compound. *Phys. B* **1998**, *253*, 1−9.
(51) Ohta, Y.; Tohyama, T.; Maekawa, S. Transition-temperature in copper-oxide superconductors correlated with energy-level of apical oxygen. *Phys. C* **1990**, *166*, 385−387.
(52) Tranquada, J. M.; Moudden, A. H.; Goldman, A. I.; Zolliker, P.; Cox, D. E.; Shirane, G.; Sinha, S. K.; Vaknin, D.; Johnston, D. C.; Alvarez, M. S.; Jacobson, A. J.; Lewandowski, J. T.; Newsam, J. M. Antiferromagnetism in $YBa_2Cu_3O_{6+x}$. *Phys. Rev. B: Condens. Matter Mater. Phys.* **1988**, *38*, 2477−2485.
(53) Tranquada, J. M.; Cox, D. E.; Kunnmann, W.; Moudden, H.; Shirane, G.; Suenaga, M.; Zolliker, P.; Vaknin, D.; Sinha, S. K.; Alvarez, M. S.; Jacobson, A. J.; Johnston, D. C. Neutron-diffraction determination of antiferromagnetic structure of Cu ions in $YBa_2Cu_3O_{6+x}$ with x = 0.0 and 0.15. *Phys. Rev. Lett.* **1988**, *60*, 156−159.

https://doi.org/10.1021/acs.inorgchem.2c03475
Inorg. Chem. 2023, 62, 3445−3456

(54) De Irujo-Labalde, X. M.; Amador, U.; Ritter, C.; Goto, M.; Patino, M. A.; Shimakawa, Y.; Garcia-Martin, S. 3D to 2D Magnetic Ordering of Fe3+ Oxides Induced by Their Layered Perovskite Structure. *Inorg. Chem.* **2021**, *60*, 8027−8034.
(55) Martínez de Irujo-Labalde, X.; Goto, M.; Urones-Garrote, E.; Amador, U.; Ritter, C.; Patino, M. E. A.; Koedtruad, A.; Tan, Z.; Shimakawa, Y.; Garcia-Martin, S. Multiferroism induced by spontaneous structural ordering in antiferromagnetic iron perovskites. *Chem. Mater.* **2019**, *31*, 5993−6000.
(56) Jiang, H.; Gomez-Abal, R. I.; Rinke, P.; Scheffler, M. First-principles modeling of localized *d* states with the GW @ LDA + *U* approach. *Phys. Rev. B* **2010**, *82*, No. 045108.
(57) Imada, M.; Fujimori, A.; Tokura, Y. Metal-insulator transitions. *Rev. Mod. Phys.* **1998**, *70*, 1039−1263.
(58) Fujii, H.; Mihara, Y.; Mochiku, T.; Hata, Y.; Kadowaki, K. Order, disorder and superconductivity in $FeSr_2YCu_2O_{6+\delta}$. *Phys. C* **2004**, *415*, 85−93.
(59) Hata, Y.; Mihara, Y.; Mochiku, T.; Suzuki, J.; Kakeya, I.; Kadowaki, K.; Kita, E.; Yasuoka, H. Redistribution of Fe ion and superconductivity of $FeSr_2YCu_2O_{6+y}$ system. *Phys. C* **2004**, *417*, 17−24.
(60) Zunger, A.; Wei, S. H.; Ferreira, L. G.; Bernard, J. E. Special quasirandom structures. *Phys. Rev. Lett.* **1990**, *65*, 353−356.

https://doi.org/10.1021/acs.inorgchem.2c03475
Inorg. Chem. 2023, 62, 3445−3456

Supporting Information

Metal to insulating transition in the perovskite system $YSr_2Cu_2FeO_{8-\delta}$ ($0 < \delta < 1$) modeled by DFT methods

Marianela Gómez-Toledo[1], Sara A. López-Paz[1, 2], Susana García-Martín[1] and M. Elena Arroyo-de Dompablo[1]*

1. Departamento de Química Inorgánica, Universidad Complutense de Madrid, 28040 Madrid, Spain.

2. Department of Quantum Matter Physics, University of Geneva, CH-1211, Geneva, Switzerland

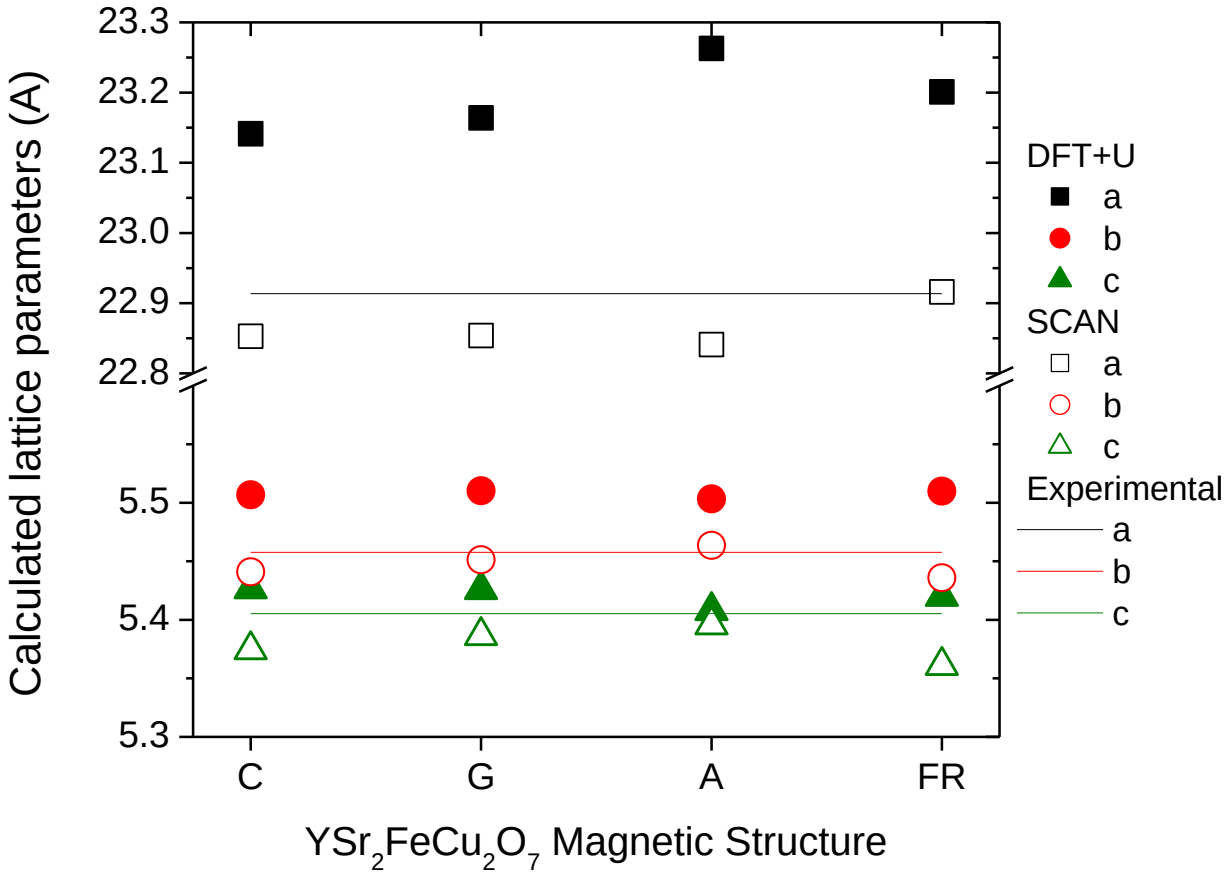

Figure S1. Calculated lattice parameters for the idealized $YSr_2Cu_2FeO_7$ in the C, G, A and FR magnetic structures (S.G. *I*ma2). The experimental data of $YSr_2Cu_2FeO_{7.08}$ (Table I in main text) are included for comparison.

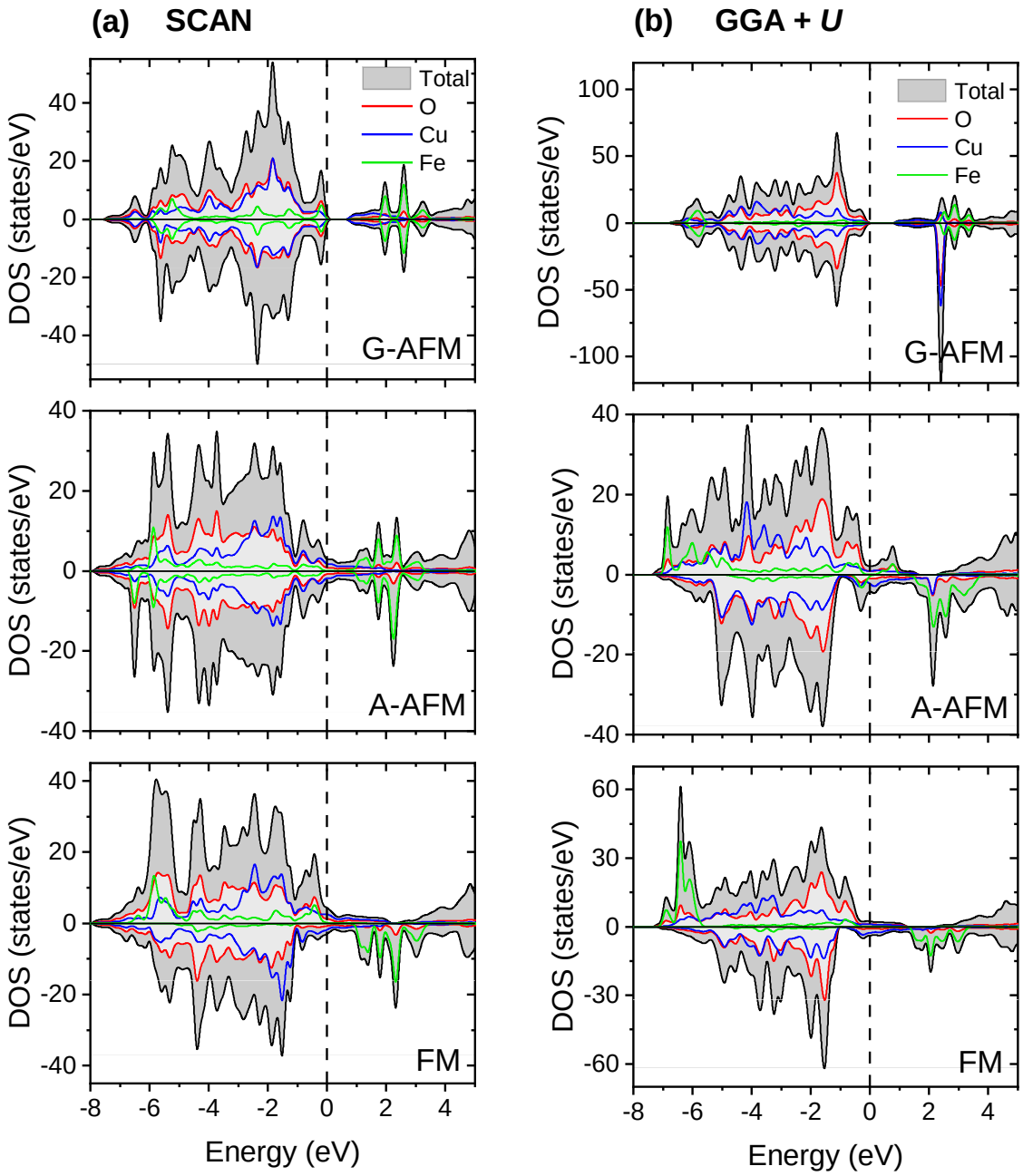

Figure S2. Calculated total and atom-projected density of states for idealized $YSr_2Cu_2FeO_7$ in the G, A and FR magnetic structures. (a) SCAN functional and (b) GGA+*U* method. The Fermi level is set as the zero of energy. Up spin (or majority) and down spin (or minority) contributions are shown. Color code: total grey, Cu contribution in blue, Fe contribution in green, O contribution in red. DOS units refer to the calculated cell.

CAPÍTULO 5

The SCAN+*U* method in the investigation of complex transition metal oxides: a case study on $YSr_2Cu_2FeO_{7+\delta}$ (δ = 0, 1)

PCCP

PAPER

View Article Online
View Journal | View Issue

Cite this: *Phys. Chem. Chem. Phys.*, 2024, **26**, 17255

The SCAN+*U* method in the investigation of complex transition metal oxides: a case study on $YSr_2Cu_2FeO_{7+\delta}$ (δ = 0, 1)

Marianela Gómez-Toledo and Elena M. Arroyo-de Dompablo *

Received 28th February 2024,
Accepted 27th May 2024

DOI: 10.1039/d4cp00874j

rsc.li/pccp

Assessment of DFT methods is essential to sustain reliability in the computational investigation of complex transition metal oxides. This work evaluates the performance of the strongly constrained and appropriately normed (SCAN) functional and its extended Hubbard-*U* methodology (SCAN+*U*) to model the $YSr_2Cu_2FeO_{7+\delta}$ ($0 < \delta < 1$) perovskite-based system. The influence of the individual U_{Cu} and U_{Fe} Hubbard parameters ($0 < U < 4$ eV) on the calculated electronic, magnetic and crystal structures of the end members δ = 1 (metallic) and δ = 0 (insulating) is analyzed. The introduction of the *U*-correction terms enhances the reproduction of the crystal structures, with a U_{Cu} value of 1 eV improving the band gap accuracy for the $YSr_2Cu_2FeO_7$ phase, while maintaining the metallic characteristics of $YSr_2Cu_2FeO_8$. At a fixed U_{Cu} value, the results are almost insensitive to the U_{Fe} value used in the calculations. The findings emphasize that for oxides containing several TM ions, the optimal U_{TM} values may differ from those of the simple TM oxides.

Introduction

Transition metal (TM) oxides are one of the most interesting classes of solids, exhibiting excellent properties and applications in a wide variety of fields. Methods based on density functional theory (DFT) play a central role in designing advanced functional oxides. They enable the identification of promising materials through property prediction and facilitate the understanding of the underlying structure–composition–property relationships. A current challenge is selecting a DFT methodology capable of modelling complex TM oxides with strongly interacting d-electrons. The GGA + *U* method has been extensively used in the last few decades; to the GGA exchange–correlation functional, a TM-specific Hubbard *U* parameter is added describing the on-site Coulomb interaction between localized electrons. However, progress in the modelling of correlated TM oxides requires testing and evaluating advanced exchange–correlation functionals.

The recently developed strongly constrained and appropriately normed (SCAN) meta-GGA functional[1] has demonstrated a superior performance in reproducing the fundamental physical properties and phenomena associated with correlated oxides.[2–8] Furthermore, studies have shown that incorporating the SCAN functional into the DFT+*U* framework (SCAN+*U*) can enhance the accuracy in reproducing certain physical properties of transition metal oxides.[9–13] For example, Carter and coworkers demonstrated that the introduction of the Hubbard term improves the reproduction of the ground-state properties of binary 3d TM oxides, being critical for the prediction of the most stable polymorphs of Mn_2O_3 and Fe_3O_4.[9,10] The SCAN+*U* method has also been used to evaluate the formation energy of anion vacancies, which are highly involved in properties related to energy applications, of ABO_3 perovskites with various A and B (TM) elements and diverse electronic structures.[11] For $BiFeO_3$ polymorphs, the effect of Fe-site doping on the phase stability, as well as on the structural and ferroelectric properties, has been assessed.[12] For oxides containing two TM ions, double Nb-perovskites (Sr_2SmNbO_6, Sr_2CoNbO_6 and Ba_2CoNbO_6) have been investigated,[14] although the authors dropped the treatment of correlation in Nb to simplify the analysis.

Assessing the performance of the SCAN+*U* method in modelling complex transition metal oxides represents a crucial step forward in the predictive design of functional oxides, especially defying for oxides containing different TM ions. This study focuses on the SCAN+*U* method in the investigation of complex oxides $YSr_2Cu_2FeO_{7+\delta}$, for which the SCAN functional correctly captures the metal-to-insulating transition as a function of the oxygen content.[8] The perovskite-related crystal structure of the $YSr_2Cu_2FeO_{7+\delta}$ system (Fig. 1) can be referred to the YBaCuO-type structure with the replacement of one layer of Cu atoms with Fe.[15,16] The $YSr_2Cu_2FeO_8$ (δ = 1) idealized compound, with $[FeO_6]$ octahedral units in the FeO_2 layers (Fig. 1a), is a metallic

Departamento de Química Inorgánica, Universidad Complutense de Madrid, 28040 Madrid, Spain. E-mail: e.arroyo@quim.ucm.es

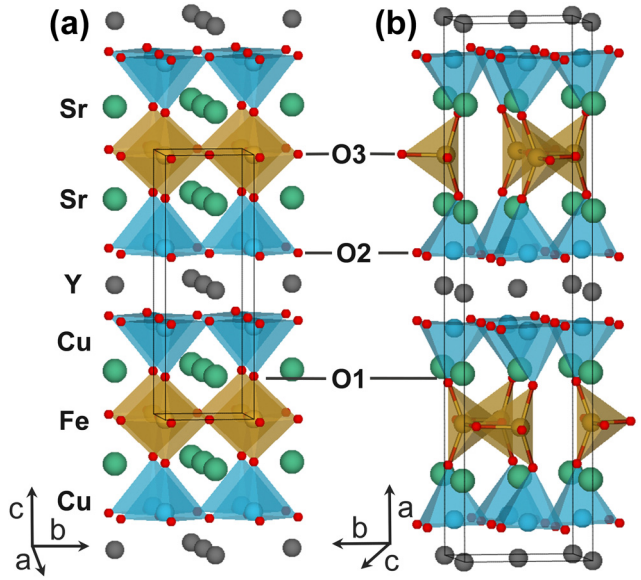

Fig. 1 Crystal structures of the idealized models of $YSr_2Cu_2FeO_{7+\delta}$ stoichiometric oxides: (a) $YSr_2Cu_2FeO_8$ (S.G. *P4/mmm*) and (b) $YSr_2Cu_2FeO_7$ (S.G. *Ima2*). Color code: Fe in brown, Cu in blue, Sr in green, Y in grey and O in red.

oxide with a superconducting transition at a T_c of 70 K.[17] Lowering the oxygen content creates vacancies in the O3 positions of the $FeO_{1+\delta}$ layer, which leads to a tetrahedral coordination for all Fe atoms in the idealized $YSr_2Cu_2FeO_7$ (δ = 0) compound (Fig. 1b). The synthetized compounds with $\delta \sim 0$ are insulators with mainly Fe^{3+} and Cu^{2+} ions.[8,16,18,19]

The combination of Cu and Fe ions in different oxidations states, and the evolution of the electronic properties of the $YSr_2Cu_2FeO_{7+\delta}$ series, provides an excellent framework to examine the applicability of the SCAN+*U* approach in the DFT investigation of complex oxides. This study delves into the effects of U_{Cu} and U_{Fe} correction terms on the crystallographic, magnetic and electronic structures of the idealized end-members of $YSr_2Cu_2FeO_{7+\delta}$ (δ = 0 and 1). By conducting calculations with individual *U* terms ranging from 0 to 4 eV, we determine and discuss the appropriate set of *U* values for accurately describing the system. A relevant question arises regarding the transferability of U_{TM} parameters from simple oxides to their combinations in complex TM oxides. We will demonstrate that such transferability cannot be guaranteed.

Methodology

Calculations for the ideal stoichiometric end-members of the $YSr_2Cu_2FeO_{7+\delta}$ family, $YSr_2Cu_2FeO_8$ and $YSr_2Cu_2FeO_7$, have been performed using the *ab initio* total energy and molecular dynamics program VASP (Vienna Ab initio Simulation Package) developed at the Universität Wien.[20,21] The interaction of core electrons with the nuclei is described using the projector augmented wave (PAW) method[22] with $2s^22p^4$ of O, $3s^23p^63d^74s^1$ of Fe, $3p^63d^{10}4p^1$ of Cu, $4s^24p^65s^2$ of Sr, and $4s^24p^64d^15s^2$ of Y being treated as valence electrons. The energy cut-off for the plane wave basis set was fixed at a constant value of 600 eV throughout the calculations. The integration in the Brillouin zone was done on appropriate *k*-point sets determined by the Monkhorst–Pack scheme. The *k*-point meshes were set at 2 × 8 × 8 for $YSr_2Cu_2FeO_7$ and 10 × 10 × 4 for $YSr_2Cu_2FeO_8$, using a Gaussian smearing parameter of 0.05 eV. For the density of states (DOS) calculations, the tetrahedron method with Bloch corrections[23] was used. Self-consistency was achieved with a tolerance in total energy of 1×10^{-4} eV for geometry optimization and 1×10^{-6} eV for DOS calculations.

A local Hubbard-*U* (SCAN+*U*) was added to Fe and Cu atoms, following the simplified rotationally invariant framework developed by Dudarev *et al.*[24] Typically, *U* is formulated as $U_{eff} = U - J$, where *U* is the onsite Coulomb term and *J* is the exchange term. In this work, this effective parameter is simply referred as *U*. The *J* value was fixed to 1 eV. Effective *U* values between 0 and 4 eV were used for the 3d orbitals of Cu and Fe. It should be noted that a value of 4 eV for Fe and Cu was found appropriate in GGA + *U* investigations.[25–27] The local magnetic moments were taken from the difference between the projected electron density of up and down spins onto a 1 Å ionic radius sphere. Bader charge analysis[28] was performed on the charge density files[29] using the pymatgen package.[30]

The crystallographic models of $YSr_2Cu_2FeO_8$ and $YSr_2Cu_2FeO_7$ were, respectively, constructed taking the initial positions from $YSr_2Cu_2FeO_{7.86}$ (ICSD file 11514)[17] and $YSr_2Cu_2GaO_7$ (ICSD file 71263).[31] For the metallic $YSr_2Cu_2FeO_{7.86}$, López *et al.*[17] found a magnetic structure consisting of in-plane FM coupling within the $FeO_{1+\delta}$ layers and a weak AFM coupling between layers along the *c*-axis (A-type AFM ordering). Due to the soft character of the inter-plane magnetic interactions ($T_N \sim 20$ K[32]), subsequent DFT calculations utilized a ferromagnetic (FM) structure to model the idealized $YSr_2Cu_2FeO_8$,[8] which is also employed in the present study. Investigation of the idealized $YSr_2Cu_2FeO_7$ is carried out in the antiferromagnetic ground state (C-type AFM) and the metastable ferromagnetic structure (FM). Additional SCAN+*U* calculations have been conducted with the maximum *U* values tested ($U_{Cu} = U_{Fe}$ = 4 eV) using the A-type AFM magnetic ordering for $YSr_2Cu_2FeO_{7+\delta}$ with δ = 0 and 1. More details of magnetic structures are given in ref. 8.

Results

The experimental lattice parameters and bond distances of $YSr_2Cu_2FeO_{7+\delta}$ (δ = 0,1) crystal structures are reproduced well using both SCAN and SCAN+*U* methods, with errors below 3%. For conciseness, Table 1 lists only the values for SCAN+*U* with the highest *U* values tested, 4 eV for Fe and Cu. Noteworthily, introducing the *U* correction term reduces the discrepancies between the theory and experimental structural data. For instance, within the SCAN+*U* approach, the calculated unit cell volumes (errors of 0.9% and 0.7% for $YSr_2Cu_2FeO_8$ and $YSr_2Cu_2FeO_7$, respectively) are closer to the experimental values than those within the SCAN approach (errors of 2% and 1.2% for $YSr_2Cu_2FeO_8$ and $YSr_2Cu_2FeO_7$, respectively). Since the

Table 1 Calculated unit cell parameters (Å), unit cell volumes (Å^3), volume per atom (Å^3) and selected bond lengths (Å) for the $YSr_2Cu_2FeO_7$ and $YSr_2Cu_2FeO_8$ idealized oxides. The experimental data of $YSr_2Cu_2FeO_{7.86}$ (ICSD-11514[17]) and $YSr_2Cu_2FeO_{7.12}$ (ICSD-151654[19]) are included for comparison. Within the SCAN+U method U = 4 eV is used for Cu and Fe

$YSr_2FeCu_2O_8$	Experimental	SCAN	SCAN+U	$YSr_2FeCu_2O_7$	Experimental	SCAN AFM-C	SCAN+U AFM-C	SCAN FM	SCAN+U FM
a	3.8145(3)	3.7861	3.7989	a	22.9241(8)	22.8529	22.8568	22.9157	22.8640
c	11.327(7)	11.2755	11.3116	b	5.4584(2)	5.4411	5.4536	5.4365	5.4646
V	164.81(1)	161.62	163.26	c	5.4080(2)	5.3744	5.3893	5.3608	5.3956
V per atom	11.77	11.54	11.66	V	676.70	668.22	671.79	675.96	674.14
d Fe–O3	1.9072(2)	1.8930	1.8994	V per atom	12.89	12.85	12.91	13.00	12.96
d Fe–O1	1.8434(4)	1.8417	1.8591	Mean d Fe–O	1.8757	1.8732	1.8888	1.8880	1.8987
d Fe–O1/d Fe–O3	0.9663	0.9729	0.9788	Fe–O3–Fe	125.5°	124.5°	123.2°	120.1°	121.0°
d Cu–O2	1.9244(4)	1.9147	1.9232	Mean d Cu–O2	1.9335	1.9237	1.9368	1.9207	1.9366
d Cu–O1	2.117(4)	2.0812	2.0738	d Cu–O1	2.312(4)	2.3449	2.3210	2.3600	2.3071
d Cu–O1/d Cu–O2	1.1000	1.0870	1.0783	d Cu–O1/d Cu–O2	1.1958	1.2148	1.2019	1.2288	1.1913
d Cu–Cu	3.407(4)	3.4297	3.4459	d Cu–Cu	3.338(0)	3.3095	3.3379	3.3119	3.3676
d Cu–Fe	3.960(3)	3.9229	3.9329	d Cu–Fe	4.085(8)	4.0815	4.0681	4.0946	4.0543

Cu-3d states play a critical role in the metal-to-insulating transition in high-Tc cuprate superconductors,[33] the Cu–O distances are analyzed in detail. Fig. 2 shows the calculated Cu–O1 (apical oxygen) and Cu–O2 (equatorial oxygen) distances as a function of the U_{Cu} and U_{Fe} values. The results show that, for both $YSr_2Cu_2FeO_8$ and $YSr_2Cu_2FeO_7$, increasing U_{Cu} results in a better agreement with the experimental available values. It can be seen in Fig. 2a that, for the metallic phase $YSr_2Cu_2FeO_8$, at a fixed U_{Cu}, applying U_{Fe} produces a decrease in d Cu-O1 (a maximum variation of 4% for U_{Cu} = 0) and a subtle increase in d Cu–O2 (a maximum variation of 0.7% at U_{Cu} = 0). On the other hand, for the C-type AFM-$YSr_2Cu_2FeO_7$, the Cu–O distance depends mostly on U_{Cu}. Hence, at a fixed U_{Cu}, changing U_{Fe} has little to no effect on the Cu–O bonding distances.

For the sake of completeness, Fig. 2 incorporates data from a preceding PBE and PBE+U (U_{Cu} = U_{Fe} = 4 eV) investigation.[8] As previously discussed, the PBE functional tends to yield larger bonding lengths than the SCAN functional. Specifically, the Cu–O1 distance in the $YSr_2Cu_2FeO_7$ oxide exhibits the most significant deviation from experimental values (5.7%). Introducing the U parameter to the PBE method results in changes in the Cu–O bond distances, with d Cu–O1 for δ = 0 decreasing and the others increasing, following the same trends observed with SCAN+U.

Regarding the electronic properties of $YSr_2Cu_2FeO_8$, the SCAN functional correctly reproduces the itinerant electron character and metallic behavior of the oxide (calculated DOS in Fig. 3a). Applying the Hubbard correction (SCAN+U) produces a downshift of the occupied Fe/Cu-3d states, keeping the 3d orbitals atomic-like and diminishing their hybridization with the 2p-oxygen (less covalent TM–O bonding). This is clearly observed in Fig. 3a for the case with U_{Cu} and U_{Fe} = 4 eV. Moreover, since U penalizes the fractional occupation on metal ions, the electrons tend to localize in the majority spin in Cu-3d and Fe-3d orbitals and a band gap opens in the minority spin channel, resulting in a half-metal compound. Fig. 3b shows the dependence of the down-spin band gap with the U_{Cu} and U_{Fe} values employed in the SCAN+U calculations. Half-metallicity is largely influenced by the U value used for the Cu-3d states. When U_{Cu} < 1.0 eV, independent of the U_{Fe} tested

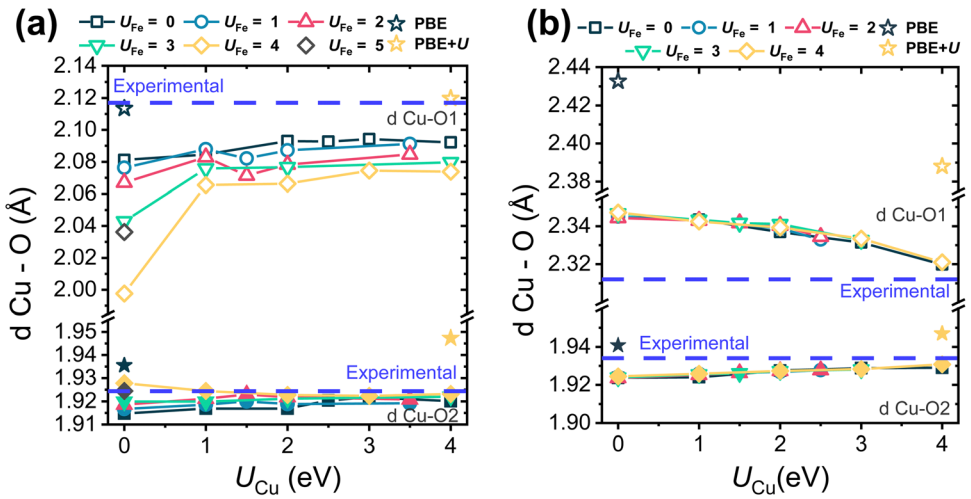

Fig. 2 Calculated Cu–O bond lengths (Å) within the SCAN+U approach as a function of U_{Cu} and U_{Fe} values for (a) $YSr_2Cu_2FeO_8$ and (b) $YSr_2Cu_2FeO_7$ idealized oxides. The experimental bond lengths are depicted as dashed blue lines. The PBE (U_{Fe} and U_{Cu} = 0 eV) and PBE+U (U_{Fe} and U_{Cu} = 4 eV) results from a previous investigation[8] are denoted by blue and yellow asterisks, respectively.

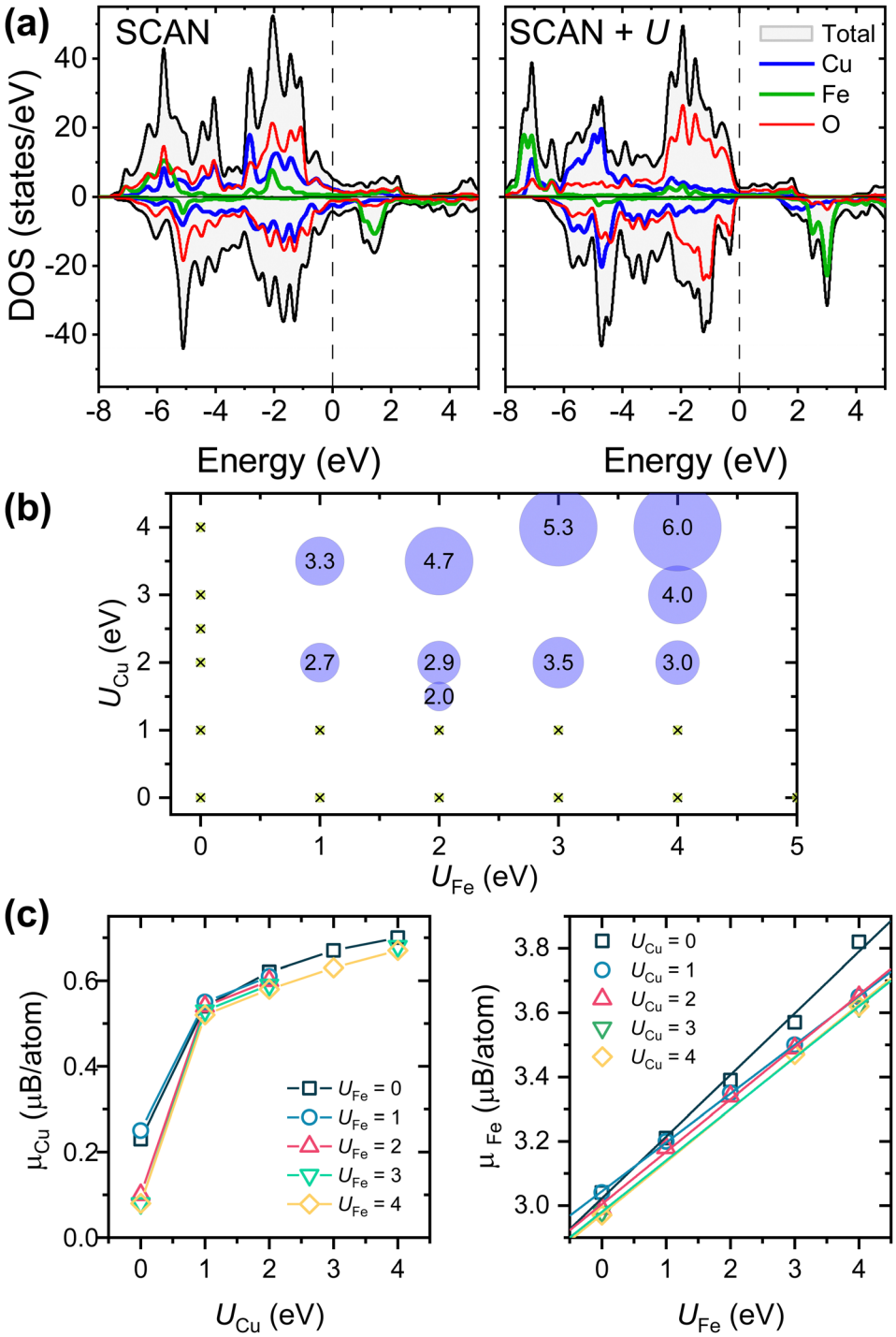

Fig. 3 (a) Calculated total and atom-projected density of states (DOS) for $YSr_2Cu_2FeO_8$ within the SCAN and SCAN+U approximation (U_{eff} = 4 eV for Cu and Fe). The Fermi level is set as the zero of energy. DOS units refer to the calculated cell. Up spin (or majority) and down spin (or minority) contributions are shown. Color code: total black, Cu blue, Fe green, and O red. (b) Effect of the on-site Coulomb repulsion parameters U_{Fe} *and* U_{Cu} within the SCAN+U approximation on the electronic properties of the $YSr_2Cu_2FeO_8$ idealized model. A metal (green dots) to half-metal (purple circles) transition occurs at $U_{Cu} \sim 2$ eV. For half-metallicity, the magnitude of the band gap in the down-spin channel is shown inside the purple circles. (c) Calculated local magnetic moments on Cu and Fe ions as a function of the U_{Fe} and U_{Cu} values employed in the SCAN+U method.

(maximum 5 eV), the DOS corresponds to a metallic compound. For $U_{Cu} > 1.0$ eV and $U_{Fe} > 0$, an energy gap opens in the down spin channel, whose energy increases with larger U_{Fe} (see the band gap values in the circles). In addition to half-metallicity, the introduction of the U parameter, and associated electron localization, produces increasing local magnetic moments (Fig. 3c) that deviate from the experimental observations, that is, μ_0(Fe) = 1.7–2 μB per ion and μ_0(Cu) = 0 μB.[17] In this

regard, the introduction of the U term does not benefit property prediction.

Interestingly, as depicted in Fig. 3b and c, maintaining metallic characteristics in $YSr_2Cu_2FeO_8$ is possible with combinations such as U_{Cu} = 0 eV and U_{Fe} = 5 eV, as well as U_{Fe} = 0 and U_{Cu} = 4 eV. This is to say, electron localization does not occur when either U_{Cu} or U_{Fe} is set to zero. Fig. 4 reveals the impact of increasing only U_{Fe} or U_{Cu}, while keeping the other U-value equal to zero. It can be inferred that since both Cu-3d and Fe-3d states contribute to the Fermi level, electron localization only occurs when both U-terms are greater than zero. Furthermore, the predominant contribution of Cu 3d-states at the Fermi level, characterized by a higher number of states compared to Fe 3d-states, results in U_{Cu} exerting a greater influence on the magnetic and electronic properties as well as on the Cu–O distances.

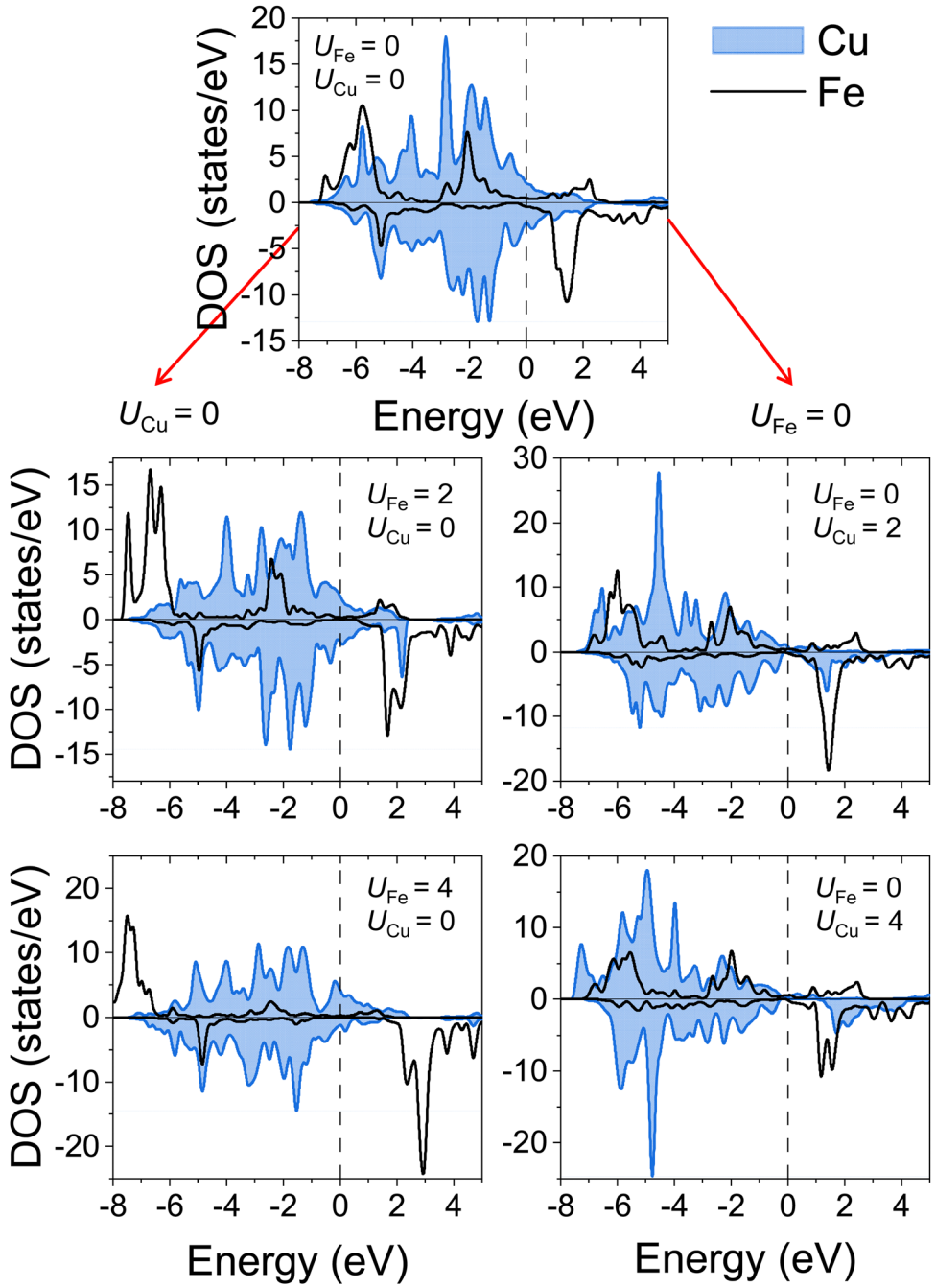

Fig. 4 Calculated atom-projected density of states for $YSr_2Cu_2FeO_8$ within the SCAN+U apporach. The evolution of the pDOS with U values for both TMs can be followed in columns. In the left column, U_{Cu} is set to zero and the metallic character is perserved independently of the U_{Fe} value. In the right column, U_{Fe} is set to zero, and increasing U_{Cu} drastically reduces the number of states at the Fermi level. The Fermi level is set as the zero of energy. Color code: Cu blue and Fe black.

Fig. 5a shows the calculated SCAN-DOS for the idealized model of C-type AFM-$YSr_2Cu_2FeO_7$. For this insulating oxide, the band gap extracted from diffuse reflectance spectroscopy (DRS) is in the range of 0.73–1.2 eV.[8] As previously reported, the PBE+U (U_{Cu} and U_{Fe} = 4 eV) predicts a band gap of 0.85 eV, while the bare PBE fails to reproduce the insulating character of $YSr_2Cu_2FeO_7$. The SCAN functional yields a band gap of 0.63 eV, which widens when the U term is applied (SCAN+U). With U = 4 eV for Fe and Cu (Fig. 5a), the band gap is as wide as 2.3 eV. Fig. 5b unveils how the band gap can be tuned by the choice of the U values. Noteworthily, the band gap depends linearly on U_{Cu}, but it is almost insensitive to the choice of U_{Fe}, similarly with the afore-mentioned trend in the calculated Cu–O distances in this oxide. The experimental band gap is reproduced for $0 < U_{Cu} < 1$ eV. For U_{Cu} = 0 eV, appropriate values of U_{Fe} range from 1 to the maximum value tested (4 eV), whereas for U_{Cu} = 1 eV, any U_{Fe} value (including U_{Fe} = 0) yields the same band gap. Fig. 6 depicts the specific effects of U_{Cu} and U_{Fe} in the calculated DOS. While both, Cu and Fe-3d states, are significant parts of the top of the valence band, the bottom of the conduction band is formed exclusively by Cu-3d states. As U_{Cu} increases, these empty states shift up in energy, thereby opening the band gap.

Investigation of the hypothetical FM-$YSr_2Cu_2FeO_7$ supports the minor impact of U_{Fe} in property prediction. The calculated DOSs for the FM configuration (shown in Fig. 7a), indicate that within the SCAN+U approach, the U term drives the oxide from a metallic state (as described by the SCAN) to an insulating state. Fig. 7b shows the band gap opening as a function of the U_{Cu} and U_{Fe} values used in the calculations. In the same way as in the C-type AFM-$YSr_2Cu_2FeO_7$, the U_{Cu} dominates the band

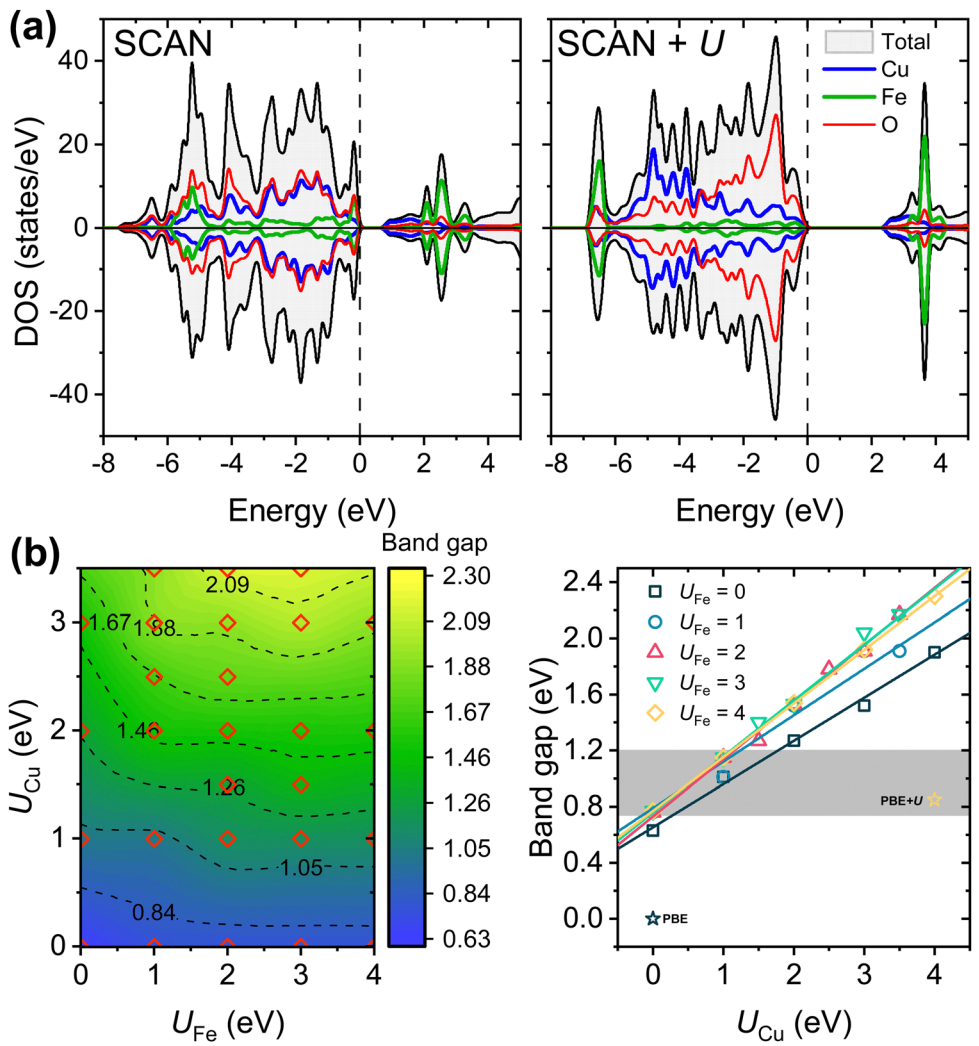

Fig. 5 (a) Calculated total and atom-projected density of states for $YSr_2Cu_2FeO_7$ in the C-type AFM configuration within the SCAN and SCAN+U approximation (U_{eff} = 4 eV for Cu and Fe). The Fermi level is set as the zero of energy. DOS units refer to the calculated cell. Up spin (or majority) and down spin (or minority) contributions are shown. Color code: total black, Cu blue, Fe green, and O red. (b) Dependence of the band gap for C-type AFM-$YSr_2Cu_2FeO_7$ with the U values on Fe and Cu utilized in the SCAN+U calculations. The experimental band gap range is denoted by a gray region. The PBE (U_{Fe} and U_{Cu} = 0 eV) and PBE+U values (U_{Fe} and U_{Cu} = 4 eV) from a previous investigation[8] are denoted by blue and yellow asterisks, respectively.

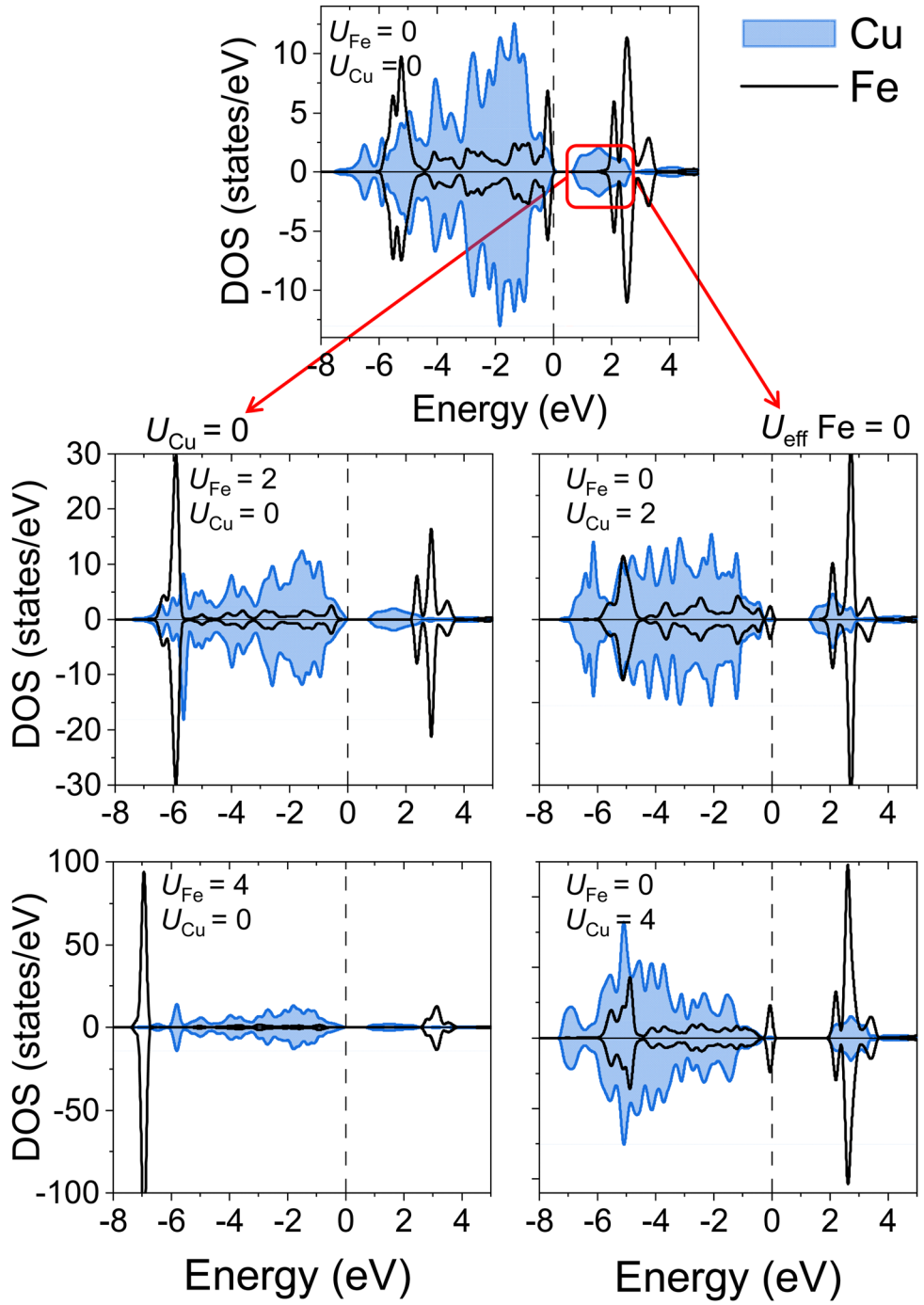

Fig. 6 Calculated atom-projected density of states for C-type AFM-$YSr_2Cu_2FeO_7$ within the SCAN+U methodology, showing the major impact of U_{Cu} on the electronic properties. The evolution of the pDOS with U values for both TMs can be followed in columns. In the left column, U_{Cu} is set to zero and the band gap value is perserved independently of the U_{Fe} value. In the right column, U_{Fe} is set to zero, and band gap widens with the increasing U_{Cu} values. Color code: Cu blue and Fe black.

gap opening, being the critical value U = 2 eV. In the insulating state, the magnitude of the band gap is nearly insensitive to U_{Fe}; for instance, a band gap of 0.8 eV is obtained when U_{Cu} = 4 eV and U_{Fe} ranging from 0 to 4 eV. It should be noted that due to the lack of experimental data for FM-$YSr_2Cu_2FeO_7$, it is not conceivable to extract an optimal U value to model its properties. FM-$YSr_2Cu_2FeO_7$ is metastable relative to C-type AFM under any DFT approximation, with energy differences per formula unit of 0.248 eV (PBE),[8] 0.414 eV (SCAN),[8] 0.424 eV (PBE+U, U_{Fe} = U_{Cu} = 4 eV),[8] and 0.330 eV (SCAN+U, U_{Fe} = U_{Cu} = 4 eV). It is therefore unlikely that such a phase could ever be prepared.

The stabilization of the C-type AFM magnetic structure in insulating $YSr_2Cu_2FeO_7$ is attributed to local antiferromagnetic

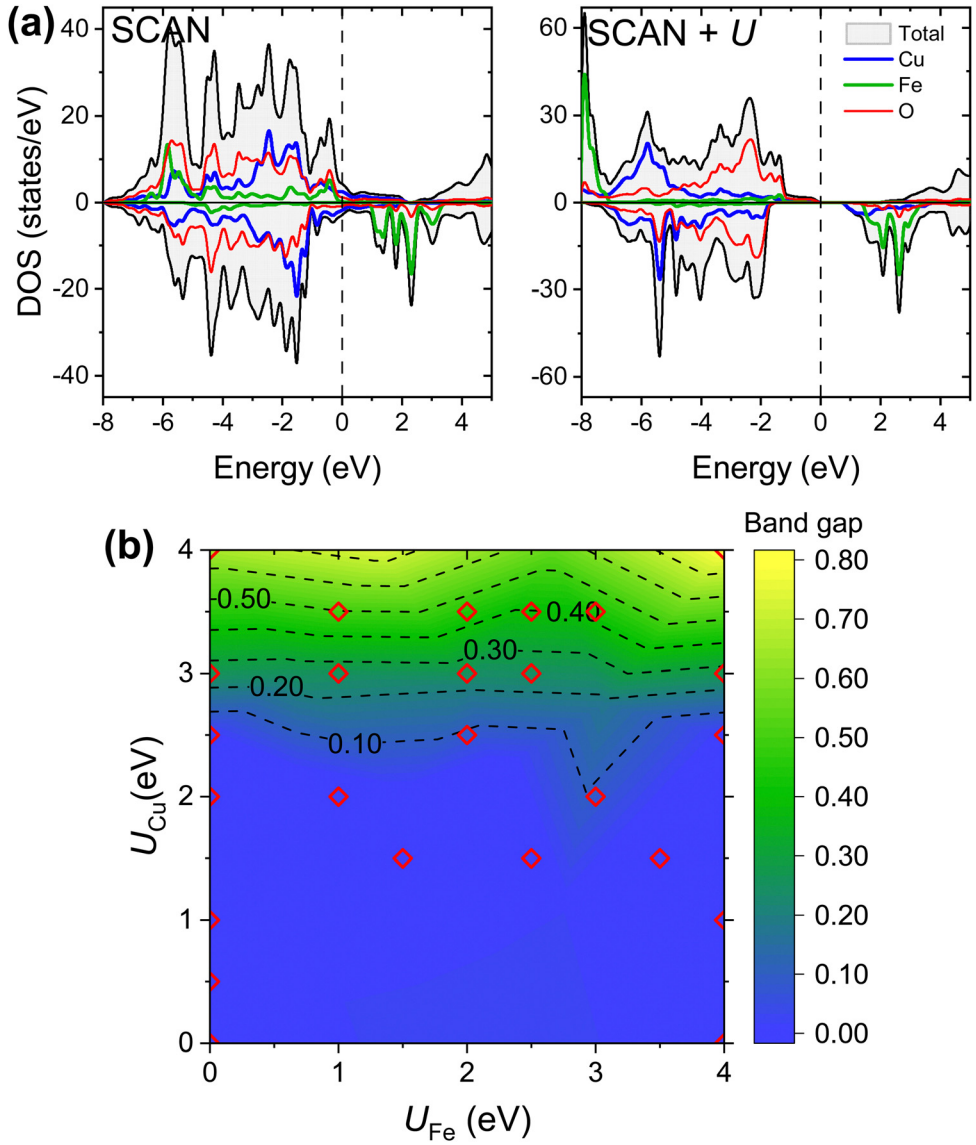

Fig. 7 (a) Calculated total and atom-projected density of states for $YSr_2Cu_2FeO_7$ in the FM configuration. The Fermi level is set as the zero of energy. DOS units refer to the calculated cell. Up spin (or majority) and down spin (or minority) contributions are shown. Color code: total black, Cu blue, Fe green, and O red. (b) FM-$YSr_2Cu_2FeO_7$ evolves from metallic (blue) to insulating behavior with increasing U_{Cu} values. The metal-to-insulator transition occurs at a critical U_{Cu} value of approximately 2.5 eV.

ordering within the Cu/Fe plane layer arising from superexchange interactions *via* oxygen bridges.[8,34] In contrast, in-plane AFM ordering is not observed in the metallic $YSr_2Cu_2FeO_8$, for which an A-type AFM magnetic structure is reported.[17] Noteworthily, the inter-plane magnetic interactions are weak throughout the $YSr_2Cu_2FeO_{7+\delta}$ system.[8,17,32,34] This is consistent with the small energy differences found between the inter-plane ferromagnetic and antiferromagnetic couplings in $YSr_2Cu_2FeO_7$ within the PBE, PBE+U and SCAN approximations.[8] For this oxide, the SCAN+U ($U_{Fe} = U_{Cu} = 4$ eV) yields a negligible energy ($E_{TotalFM} - E_{TotalA\text{-}AFM}$) difference of 0.004 eV per formula unit. Similarly, for the metallic $YSr_2Cu_2FeO_8$, the A-type AFM configuration is only 0.018 eV per formula unit more stable than the FM configuration within the SCAN +U ($U_{Fe} = U_{Cu} = 4$ eV).

Discussion

The principal drawback of the DFT+U schemes lies in the selection of the adjustable parameter, U. While U values can be derived from self-consistent calculations,[35] a common approach involves choosing these in order to match the experimental data, such as equilibrium volumes, formation energies, band gap values, transition pressures, intercalation voltages, and so on.[10,25,26,36–38] It is impossible to pinpoint an exact and universally applicable value for the U parameter to accurately reproduce all material properties.[37] In this study, suitable ranges of U values are determined through comparison with experimental data on crystalline, magnetic and electronic structures.

The appropriate Hubbard U parameter varies depending on the nature and oxidation state of the transition metal (TM) as well as the crystal structure.[25] $YSr_2Cu_2FeO_{7+\delta}$ (δ = 0,1) shares the same structural type, and for both compounds incorporating a U correction improves the reproduction of lattice parameters and Cu–O bond lengths. In the $YSr_2Cu_2FeO_{7+\delta}$ system, the oxygen content determines the oxidation states of Cu and Fe as well as the magnetic interactions. For the magnetic structures, the SCAN+U method performs equally well compared to the SCAN, PBE and PBE+U methods: they all capture the occurrence of in-plane AFM ordering for $\delta \sim 0$, and the soft character of the inter-plane interactions throughout the $YSr_2Cu_2FeO_{7+\delta}$ system. These DFT-trends, even when extracted from the idealized oxides with δ = 0 and 1, are in good agreement with the observed magnetic properties of $YSr_2Cu_2FeO_{7+\delta}$.[17,32,34]

The primary impact of U is observed in the electronic properties. In the metallic phase $YSr_2Cu_2FeO_8$, as expected, the U parameter penalizes electron delocalization, with $U_{Cu} > 1$ eV being detrimental for property prediction. On the other hand, for the insulating phase $YSr_2Cu_2FeO_7$, the electron correlation is better captured with $0 < U_{Cu} < 1$ eV and U_{Fe} =1–4 eV. Considering these findings, the $YSr_2Cu_2FeO_{7+\delta}$ system is better described with U_{Cu} = 1 eV, which improves the accuracy of the band gap for the insulating C-type AFM-$YSr_2Cu_2FeO_7$, while maintaining the metallic behavior of $YSr_2Cu_2FeO_8$. Importantly, once U_{Cu} is set to 1 eV, varying U_{Fe} between 0 and 4 eV has a minor impact on the calculated metal/insulating behavior of $YSr_2Cu_2FeO_8$/$YSr_2Cu_2FeO_7$ (Fig. 3b and 5b). The predominant role of U_{Cu} is consistent with the specific contributions of Cu-3d and Fe-3d states on the valence and conduction bands of $YSr_2Cu_2FeO_{7+\delta}$.

In the DFT+U framework, there exists dependence of the appropriate U values on the XC-functional used. Despite the limited number of studies addressing the estimation of suitable U values within the SCAN+U approach, a widespread observation is that the optimal U values for electronic property prediction are notably lower than those within the PBE+U method.[9,12,27] This remark is supported by comparing the current SCAN+U results for $YSr_2Cu_2FeO_7$ with a previous investigation using PBE+U (Fig. 5b).[8] In the PBE+U approach, applying U_{eff} values of $\sim$4 eV for Cu and Fe ions, a calculated band gap of 0.85 eV is achieved, which falls in the experimental range. However, using the same U values in the SCAN+U method significantly overestimates the band gap, widening it to 2.3 eV. Fig. 2 and 5b suggest that the calculated bonding distances and band gaps exhibit a linear trend with the U value, displaying similar slopes for both SCAN+U and PBE+U methods. Since the bare PBE and SCAN produce different values (either for band gaps or bond-lengths), the optimal U values matching the experimental data definitely depend on the chosen XC functional.

Finally, within the SCAN+U method, the optimal U values for modelling the $YSr_2Cu_2FeO_{7+\delta}$ compounds can be compared to those previously reported for the simple Fe and Cu oxides. Previous studies have suggested that the optimal U_{Fe} value is around $\sim$3 eV for FeO/Fe_2O_3/Fe_3O_4[9] and $BiFeO_3$.[12] Carter *et al.* demonstrated that, while SCAN is sufficient to reproduce the crystal structure and formation energies of CuO and Cu_2O, the proper simulation of the electronic structure requires the introduction of U_{Cu} at around $\sim$2 eV.[10] However, applying the combination extracted from simple oxides (U_{Cu} = 2 eV and U_{Fe} = 3 eV), a poor description of the electronic properties of the $YSr_2Cu_2FeO_{7+\delta}$ system is given. This combination leads to a half-metallic behavior (and electron localization) for $YSr_2Cu_2FeO_8$, and band gaps that deviate from the experimental values for $YSr_2Cu_2FeO_7$. In short, the appropriate U parameters found for the simple Cu/Fe oxides are not suitable for reproducing the properties of the complex oxides $YSr_2Cu_2FeO_{7+\delta}$. The differences between the optimal U-values for simple and complex TM oxides are linked to the specific contributions of the TM-d states in the electronic structure.

Conclusions

The SCAN functional effectively models the crystal structure and basic electronic and magnetic properties of complex oxides $YSr_2Cu_2FeO_{7+\delta}$ ($0 < \delta < 1$). Although adding a U correction on top is not necessary, it is found that applying a U_{Cu} value of 1 eV leads to a more accurate description of properties. In this case study, the Cu-3d states dominate, respectively, the Fermi level of $YSr_2Cu_2FeO_8$ and the bottom of the conduction band of $YSr_2Cu_2FeO_7$. Consequently, U_{Cu} has a greater impact than U_{Fe} in the calculated electronic properties and magnetic moments. Indeed, for a fixed U_{Cu}, the results are almost insensitive to U_{Fe}.

This case study highlights the importance of analyzing the role of the individual U parameters for the reliable SCAN+U investigations of complex oxides containing several TM ions. The optimal U-values certainly depend on the material under investigation (chemical composition and crystal structure), and U-transferability among materials is particularly risky for such complex oxides. The appropriate combination of U_{TM} terms may differ from the optimal values in the respective simple oxides. Therefore, the convenience of using the SCAN+U approach in the study of oxides containing several TM ions should be assessed for each material, considering whether the benefits in property prediction (compared to the SCAN functional) outweigh the efforts made in determining the optimal combination of individual U_{TM} values.

Author contributions

Marianela Gómez-Toledo: investigation, methodology, software, data curation, validation, formal analysis, visualization, and writing – original draft. Elena M. Arroyo-de Dompablo: investigation, conceptualization, supervision, funding acquisition, project administration, and writing – original draft.

Conflicts of interest

There are no conflicts to declare.

Acknowledgements

This research is part of the project ECSAWE-PID2022-139501OB-C22 funded by the MCIN/AEI/10.13039/501100011033 and by the ''ERDF A way of making Europe''. The authors thank funding from the MCIN/AEI/10.13039/501100011033-''NextGenerationEU''/PRTR (project TED2021-130452B-C21) and from the Universidad Complutense de Madrid (FEI-EU-22-01-4129585). Computational resources from the MALTA–cluster (Universidad de Oviedo) and I2Basque are acknowledged. The authors are grateful to S.A. López-Paz and S.García-Martín for their valuable discussions and helpful insights into the experimental aspects of the $YSr_2Cu_2FeO_{7+\delta}$ system.

References

1 J. Sun, A. Ruzsinszky and J. P. Perdew, *Phys. Rev. Lett.*, 2015, **115**, 036402.
2 Y. Hinuma, H. Hayashi, Y. Kumagai, I. Tanaka and F. Oba, *Phys. Rev. B*, 2017, 96.
3 D. A. Kitchaev, H. Peng, Y. Liu, J. Sun, J. P. Perdew and G. Ceder, *Phys. Rev. B*, 2016, **93**, 045132.
4 J. W. Furness, Y. Zhang, C. Lane, I. G. Buda, B. Barbiellini, R. S. Markiewicz, A. Bansil and J. Sun, *Commun. Phys.*, 2018, 1.
5 J. Varignon, M. Bibes and A. Zunger, *Phys. Rev. B*, 2019, 100.
6 L. Iglesias, M. Bibes and J. Varignon, *Phys. Rev. B*, 2021, **104**, 035123.
7 J. Kaczkowski, M. Pugaczowa-Michalska and I. Płowaś-Korus, *J. Magn. Magn. Mater.*, 2022, **548**, 168984.
8 M. Gómez-Toledo, S. A. López-Paz, S. García-Martín and M. E. Arroyo-de Dompablo, *Inorg. Chem.*, 2023, **62**, 3445–3456.
9 G. S. Gautam and E. A. Carter, *Phys. Rev. Mater.*, 2018, **2**, 095401.
10 O. Y. Long, G. S. Gautam and E. A. Carter, *Phys. Rev. Mater.*, 2020, **4**, 045401.
11 R. B. Wexler, G. S. Gautam, E. B. Stechel and E. A. Carter, *J. Am. Chem. Soc.*, 2021, **143**, 13212–13227.
12 J. Kaczkowski, M. Pugaczowa-Michalska and I. Plowas-Korus, *Phys. Chem. Chem. Phys.*, 2021, **23**, 8571–8584.
13 M. Verma and R. Pentcheva, *Phys. Rev. Res.*, 2022, 4.
14 Y. Zeng, Q. Hu, M. Pan, K. Zhang, S. Grasso, C. Hu and Q. Feng, *Adv. Powder Mater.*, 2022, **1**, 100019.
15 J. Shimoyama, K. Otzschi, T. Hinouchi and K. Kishio, *Physica C*, 2000, **341**, 563–564.
16 T. Mochiku, Y. Nakano, A. Hoshikawa, S. Sato, K. Oikawa, T. Ishigaki, T. Kamiyama, K. Kadowaki and K. Hirata, *Phys. C*, 2004, **412**, 115–119.
17 S. A. Lopez-Paz, X. Martinez de Irujo-Labalde, J. Sanchez-Marcos, C. Ritter, E. Moran and M. A. Alario-Franco, *Inorg. Chem.*, 2019, **58**, 12809–12814.
18 J. E. H. Sansom, E. Kendrick, H. A. Rudge-Pickard, M. S. Islam, A. J. Wright and P. R. Slater, *J. Mater. Chem.*, 2005, **15**, 2321–2327.
19 T. Mochiku, Y. Nakano, K. Oikawa, T. Kamiyama, H. Fujii, Y. Hata, I. Suzuki, I. Kakeya, K. Kadowaki and K. Hirata, *Phys. C*, 2003, **400**, 43–52.
20 G. Kresse and J. Furthmuller, *Phys. Rev. B: Condens. Matter Mater. Phys.*, 1996, **54**, 11169.
21 G. Kresse and D. Joubert, *Phys. Rev. B: Condens. Matter Mater. Phys.*, 1999, **59**, 1758.
22 P. E. Bloch, *Phys. Rev. B: Condens. Matter Mater. Phys.*, 1994, **50**, 17953.
23 P. E. Blochl, O. Jepsen and O. K. Andersen, *Phys. Rev. B: Condens. Matter Mater. Phys.*, 1994, **49**, 16223–16233.
24 S. L. Dudarev, G. A. Botton, S. Y. Savrasov, Z. Szotek, W. M. Temmerman and A. P. Sutton, *Phys. Status Solidi A*, 1998, **166**, 429–443.
25 L. Wang, T. Maxisch and G. Ceder, *Phys. Rev. B: Condens. Matter Mater. Phys.*, 2006, **73**, 195107.
26 M. E. Arroyo y de Dompablo, Y.-L. Lee and D. Morgan, *Chem. Mater.*, 2010, **22**, 906–913.
27 A. M. Ritzmann, J. M. Dieterich and E. A. Carter, *Phys. Chem. Chem. Phys.*, 2016, **18**, 12260–12269.
28 R. F. W. Bader, *Atoms in Molecules: A Quantum Theory*, Oxford University Press, Oxford, UK, 1990.
29 G. Henkelman, A. Arnaldsson and H. Jónsson, *Comput. Mater. Sci.*, 2006, **36**, 354–360.
30 S. P. Ong, W. D. Richards, A. Jain, G. Hautier, M. Kocher, S. Cholia, D. Gunter, V. L. Chevrier, K. A. Persson and G. Ceder, *Comput. Mater. Sci.*, 2013, **68**, 314–319.
31 G. Roth, P. Adelmann, G. Heger, R. Knitter and T. Wolf, *J. Phys. I*, 1991, **1**, 721–741.
32 Y. Hata, Y. Mihara, T. Mochiku, J.-I. Suzuki, I. Kakeya, K. Kadowaki, E. Kita and H. Yasuoka, *Phys. C*, 2004, **417**, 17–24.
33 M. Imada, A. Fujimori and Y. Tokura, *Rev. Mod. Phys.*, 1998, **70**, 1039.
34 M. Pissas, G. Kallias, A. Simopoulos, D. Niarchos and R. Sonntag, *Physica B*, 1998, **253**, 1–9.
35 F. Zhou, M. Cococcioni, C. A. Marianetti, D. Morgan and G. Ceder, *Phys. Rev. B: Condens. Matter Mater. Phys.*, 2004, **15**, 235121.
36 K. W. Lee and W. E. Pickett, *Phys. Rev. B: Condens. Matter Mater. Phys.*, 2006, **73**, 174428.
37 M. E. Arroyo-de Dompablo, A. Morales-Garcia and M. Taravillo, *J. Chem. Phys.*, 2011, **135**, 054503.
38 M. E. Arroyo-de Dompablo, P. Rozier, M. Morcrette and J. M. Tarascon, *Chem. Mater.*, 2007, **19**, 2411–2422.

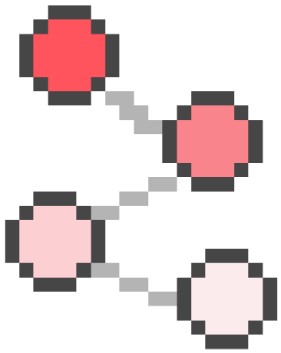

CAPÍTULO 6

***Ab Initio* Investigation of Oxygen Ion Diffusion in the Layered Perovskite System $YSr_2Cu_2FeO_{7+\delta}$ ($0 < \delta < 1$)**

applied sciences

MDPI

Article

Ab Initio Investigation of Oxygen Ion Diffusion in the Layered Perovskite System $YSr_2Cu_2FeO_{7+\delta}$ ($0 < \delta < 1$)

Marianela Gómez-Toledo * and Elena M. Arroyo-de Dompablo

Departamento de Química Inorgánica, Universidad Complutense de Madrid, 28040 Madrid, Spain; e.arroyo@quim.ucm.es

* Correspondence: mgom09@ucm.es

Abstract: Extensive research on transition metal perovskite oxides as electrodes in solid oxide cells (SOC) has highlighted the potential ability of Fe-based perovskite oxides to catalyze oxygen reduction/evolution reactions (ORR/OER). The layered perovskite-type system $YSr_2Cu_2FeO_{7+\delta}$ has been reported to possess attractive electrocatalytic properties. This work applies density functional theory (DFT) calculations to investigate oxygen ion diffusion in the $YSr_2Cu_2FeO_{7+\delta}$ system. For $\delta = 0.5$, it is found that in the most stable configuration, the oxygen vacancies in the $FeO_{1+\delta}$ plane are arranged to form Fe ions in tetrahedral, square pyramid, and octahedral coordination. *Ab initio* molecular dynamics (AIMD) simulations for $YSr_2Cu_2FeO_{7.5}$ ($\delta = 0.5$) yield an oxygen ion diffusion coefficient of 1.28×10^{-7} cm^2/s at 500 °C (Ea = 0.37 eV). Complementary results for $YSr_2Cu_2FeO_{7.2}$ ($\delta = 0.2$) and $YSr_2Cu_2FeO_{7.75}$ ($\delta = 0.75$) indicate that the oxygen diffusion occurs in the $FeO_{1+\delta}$ plane, and depends on the oxygen vacancies distribution around the Fe centers.

Keywords: perovskites; cuprates; DFT; SCAN; AIMD; SOFC; OER

Citation: Gómez-Toledo, M.; Arroyo-de Dompablo, E.M. *Ab Initio* Investigation of Oxygen Ion Diffusion in the Layered Perovskite System $YSr_2Cu_2FeO_{7+\delta}$ ($0 < \delta < 1$). *Appl. Sci.* **2024**, *14*, 6586. https://doi.org/10.3390/app14156586

Academic Editor: Leonarda Liotta

Received: 15 July 2024
Revised: 23 July 2024
Accepted: 24 July 2024
Published: 27 July 2024

1. Introduction

Hydrogen is considered the energy vector of the future. However, its sustainability depends on a broad range of technologies capable of producing clean hydrogen that is subsequently used to produce energy [1]. Technologies based on oxide ion transport (solid oxide cells, SOC) are expected to play a significant role: solid oxide electrolysis cells (SOEC) produce hydrogen from water electrolysis, while solid oxide fuel cells (SOFC) combine hydrogen and oxygen to form water [2]. The effective catalysis of the oxygen evolution reaction (OER) in SOEC and the oxygen reduction reaction (ORR) in SOFC have raised the necessity of designing and developing catalyst materials [3–6]. The electrocatalytic mechanisms of OER and ORR in SOC involve processes of oxide ion diffusion and electronic transfer. Therefore, a high mixed ionic-electronic conductivity (MIEC) is decisive for good performance. Transition metal oxides with a perovskite-type structure are attractive materials since they may present both ionic and electronic conductivity; the ionic through oxygen ion vacancies and the electronic through the corner-sharing octahedra frameworks [7]. In addition, perovskite oxides are structurally stable, possess flexible structure-compositions for easy tuning, and are cost effective. A large number of perovskite materials are known to catalyze the ORR in SOFC [8], whereas examples of the less mature SOEC technology have emerged in the last few years [6].

In addition to its MIEC properties, the ORR/OER catalyst must have chemical and mechanical stability and relatively low thermal expansion coefficients (TECs) that should be alike in the three cell components (electrolyte, anode, and cathode). Moreover, they should not react with each other at the working temperatures of the SOC. Fe-based perovskites are particularly appealing due to the high abundance of Fe oxides; their thermal expansion coefficient (TEC) values, which are closer to those of commonly used electrolytes; the energy of the Fe-O bonds in oxide-ion vacancy formation under the air and fuel operating conditions; and the remarkable variability of oxidations and spin states of Fe ions [9–14].

The $YSr_2Cu_2FeO_{7+\delta}$ ($0 \leq \delta \leq 1$) (YSCFO) system has recently been shown to display electrocatalytic activity and mixed ionic-electronic conductive (MIEC) properties, being therefore proposed as a potential air electrode for SOFCs [15]. According to the results obtained by López-Paz et al. [15], the area specific resistance (ASR) values measured in $YSr_2Cu_2FeO_{7+\delta}$: CGO|CGO| $YSr_2Cu_2FeO_{7+\delta}$: CGO symmetrical cells are 0.20 and 0.08 Ω cm^2 at 923 and 973 K, respectively; the activation energy is 1.40 ± 0.02 eV. The YSCFO shows an incremental increase of the TEC value from 18.02 × 10^{-6} K^{-1} in the RT-673 K range to 23.24 × 10^{-6} K^{-1} for 673–1173 K, associated with the oxygen loss above 673 K. Moreover, experimental measurements of DC resistance for $YSr_2Cu_2FeO_{7.08}$ and $YSr_2Cu_2FeO_{7.85}$ have shown, respectively, semiconducting and metallic behavior. The optical band gap for the insulating phase was reported to be between 0.73 and 1.2 eV [16]. In addition, the $YSr_2Cu_2FeO_{7.56}$ phase has been described as a p-type semiconductor from the analysis of the temperature dependence of the DC conductivity [15]. Previous works have demonstrated that the DFT methodology is suitable for reproducing the electronic and magnetic properties of the system [16,17].

The perovskite-related crystal structure of $YSr_2Cu_2FeO_{7+\delta}$ (Figure 1) presents an alternation of $FeO_{1+\delta}$/SrO/CuO_2/Y/CuO_2/SrO layers along the *c*-axis [18,19]. For $YSr_2Cu_2FeO_{7.85}$, the presence of only [FeO_6] octahedral units in the $FeO_{1+\delta}$ layers has been described [20]. It has also been reported that in the $YSr_2Cu_2FeO_{7.56}$ term, the oxygen non-stoichiometry accommodates the creation of vacancies in the $FeO_{1+\delta}$ planes in such a way that Fe adopts tetrahedral [FeO_4] and octahedral [FeO_6] coordination [21]. On the other hand, the low oxygen term $YSr_2Cu_2FeO_{7.08}$ consists of [FeO_4] tetrahedra. It is worth mentioning that the $YSr_2Cu_2FeO_{7+\delta}$ system has been demonstrated to exhibit partial occupancy of Cu sites with Fe [18,22]. Indeed, the synthesized compounds $YSr_2Cu_2FeO_{7.86}$ [20] and $YSr_2Cu_2FeO_{7.56}$ [21] present anti-site disorder, with a Cu/Fe mixing close to 15%.

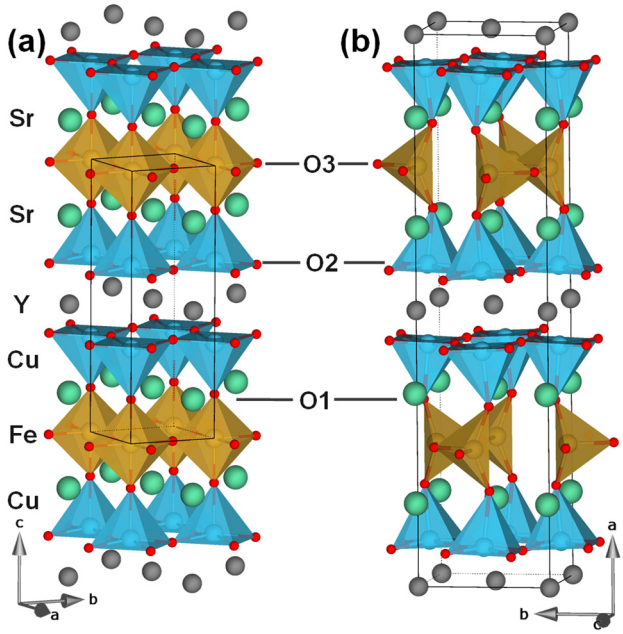

Figure 1. (**a**) Crystal structure of the ideal stoichiometric oxide $YSr_2Cu_2FeO_8$ (S.G. P4/*mmm*, ICSD file 11514). The unit cell has dimensions of $a_p \times a_p \times 3\ a_p$, where a_p refers to the cubic perovskite lattice parameter. (**b**) Crystal structure of the ideal stoichiometric oxide $YSr_2Cu_2FeO_7$ (S.G. I*ma2*, Initial cell parameters and atomic positions were taken from ICSD record of $YSr_2Cu_2GaO_{7.46}$, ICSD file 71263). Color code: Fe in brown, Cu in blue, Sr in green, Y in grey, and O in red.

The focus of this work is to study the MIEC properties of $YSr_2Cu_2FeO_{7+\delta}$ oxides, which were reported to present electrocatalytic activity. Specifically, this work aims to investigate oxygen diffusion in these materials and gain insights into how vacancies/oxygen content influence the diffusion mechanism. To achieve this goal, crystallographic models

for the idealized $YSr_2Cu_2FeO_{7+\delta}$ terms with δ = 0.5, 0.25, and 0.75 are proposed, and the ionic mobility is inferred from *Ab initio* molecular dynamics (AIMD). The ultimate goal of this work in the long term is to favor advancements in catalytic materials that will help overcome limitations in the development of efficient hydrogen production and utilization technologies.

2. Methodology

The calculations were performed using the Vienna Ab Initio Simulation Package (VASP) developed at the Universität Wien [23,24]. Our previous research showed that the strongly constrained and appropriately normed (SCAN) functional [25] correctly reproduces the electrical and magnetic properties of the $YSr_2Cu_2FeO_7$ and $YSr_2Cu_2FeO_8$ end members. Therefore, it was employed to study the intermediate compositions of the $YSr_2Cu_2FeO_{7+\delta}$ system. The interaction of core electrons with the nuclei is described by the projector augmented wave (PAW) method [26], with 2*s*2*p* of O, 3*d*4*s* of Fe, 3*d*4*p* of Cu, 4*s*4*p*5*s* of Sr, and 4*s*4*p*5*s*4*d* of Y treated as valence electrons. The energy cutoff for the plane wave basis set was fixed at a constant value of 600 eV throughout the calculations. The integration in the Brillouin zone is performed on appropriate sets of k-points, determined by the Monkhorst–Pack scheme. The k-point meshes were set at 10 × 10 × 4 using a Gaussian smearing parameter of 0.05 eV. For the density of states (DOS) calculations, the tetrahedron method with Bloch corrections was used [27]. Self-consistency was achieved with a tolerance in total energy of 1×10^{-4} eV for geometry optimization and 1×10^{-6} eV for DOS calculations.

To replicate the oxygen non-stoichiometry, the end-term $YSr_2Cu_2FeO_8$ (S.G. P*4/mmm*) is considered as the non-defective phase. Following our previous work, the starting positions for $YSr_2Cu_2FeO_8$ are taken from (ICSD file 11514, see Figure 1), considering a 2 × 2 × 1 superstructure [20]. Hence, the lattice parameters of the idealized model of $YSr_2Cu_2FeO_8$ are $2a_p \times 2a_p \times 3a_p$. To model the intermediate oxygen contents (δ = 0.2, 0.5, and 0.75), oxygen vacancies are accommodated in the O3 position of the $FeO_{1+\delta}$ layers. The construction of oxygen/vacancies configurations was carried out using the Pymatgen Python library (v.2023.9.10) [28]. All the models are considered in a ferromagnetic configuration. The Ewald summation method [29] was employed to choose, out of those generated, the most stable configurations for DFT calculations. The local magnetic moments and charges of each atom were obtained from the Bader charge analysis [30], which was performed on the charge density files [31] using the Pymatgen Python library [28].

For the ab initio molecular dynamics (AIMD) calculations, the generalized gradient approximation exchange and correlation functional developed by Perdew, Burke, and Ernzerhof (PBE) [32] was used. Sampling of the electronic structure was made at the gamma point only. Calculations at 1000, 1200, 1400, 1600, and 2000 K in the NVT ensemble were performed for $YSr_2Cu_2FeO_{7.5}$. First, the temperature was increased during 2000 steps, and it was then held constant for 12,000 successive steps, employing the Nóse–Hover thermostat [33]. A cutoff energy of 400 eV was used, along with a time step of 2 fs for all calculations. The data analysis was performed using the Pymatgen-diffusion [34] add-on for the Pymatgen [28] package. Ionic transport was monitored through mean square displacement (MSD). Studying the MSD variation of ions as a function of time, the diffusivity D can be extracted from the slopes for each simulated temperature, according to:

$$\langle |r_i(t) - r_i(0)| \rangle = 6Dt + B \quad (1)$$

The activation energy (E_a) of the process can be calculated from the linear fitting of the obtained data to the Arrhenius plot:

$$D = D_0 \exp\left(-\frac{E_a}{kT}\right) \quad (2)$$

where D_0 is the oxygen diffusivity at $T \rightarrow \infty$, that is to say, the maximum oxygen diffusivity. The AIMD calculated diffusivity can be compared to the experimentally determined tracer diffusivity (D*) [35].

3. Results and Discussion

To model the $YSr_2FeCu_2O_{7.5}$ phase, the four possible configurations in the $2a_p \times 2a_p \times 3a_p$ supercell were generated (Figure 2a). Note that, despite the experimental suggestions from the neutron powder diffraction (NPD) results for the $YSr_2Cu_2FeO_{7.56}$ phase [21], none of the four modelled configurations have Fe in solely tetrahedral [FeO_4] and octahedral [FeO_6] environments. The configuration where Fe forms tetrahedra (Th) [FeO_4], octahedra (Oh) [FeO_6], and square pyramids (SQP) [FeO_5] (Figure 2a) is the most stable, with a maximum energy difference obtained from geometrical optimization with the SCAN functional of 300 meV/f.u. with respect to the less stable configuration (all Fe ions in SQP).

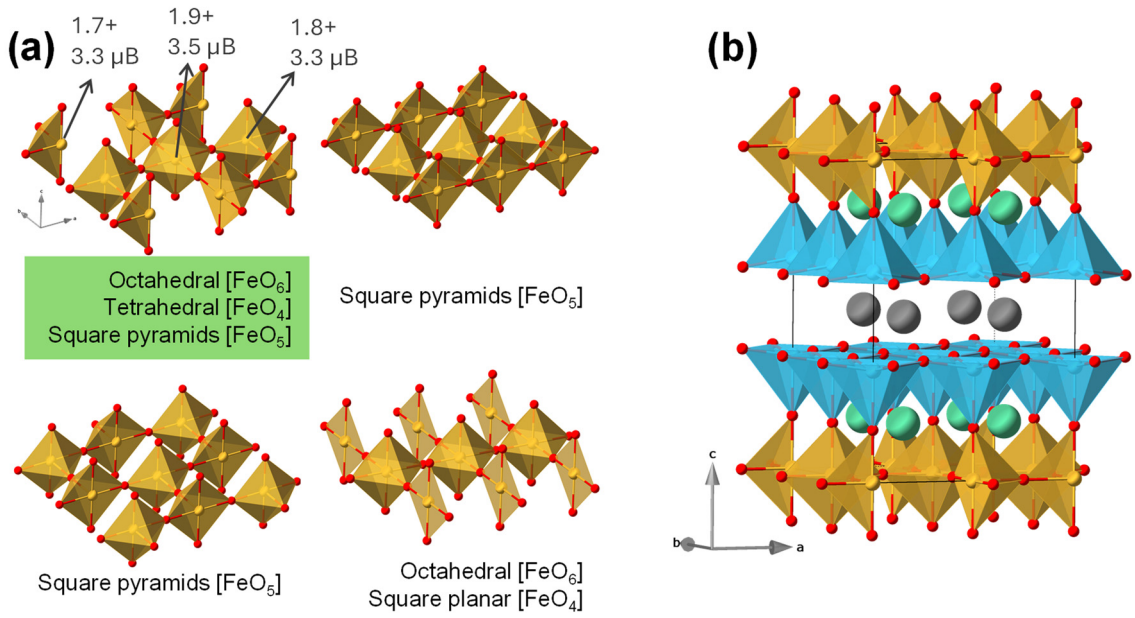

Figure 2. (**a**) Schematic representation of $FeO_{1+\delta}$ planes in the four possible configurations for $YSr_2Cu_2FeO_{7.5}$ considering the $2a_p \times 2a_p \times 3a_p$ supercell. Bader charges and magnetic moments are shown for the most stable configuration. (**b**) View of the crystal structure of the most stable model for $YSr_2Cu_2FeO_{7.5}$ ($2a_p \times 2a_p \times 3a_p$ supercell). Color code: Fe in brown, Cu in blue, Sr in green, Y in grey, and O in red.

For a $YSr_2FeCu_2O_{7.5}$ composition, the $2a_p \times 2a_p \times 3a_p$ cell is not compatible with Fe ions occupying exclusively Th and Oh. Hence, a $2a_p \times 4a_p \times 3a_p$ supercell was used to generate additional $YSr_2Cu_2FeO_{7.5}$ configurations. In this case, 91 configurations were generated using the Pymatgen package, some of them presenting Fe in solely tetrahedral [FeO_4] and octahedral [FeO_6] coordination. Among those configurations, the Ewald method allows the selection of the most stable. The SCAN geometry optimization shows that this configuration in the $2a_p \times 4a_p \times 3a_p$ supercell is 194 meV/f.u. less stable (more positive) than the most stable configuration in the $2a_p \times 2a_p \times 3a_p$ supercell (Fe in Oh, Th, and SQP). These findings advocate for detailed structural characterizations to precisely identify the local ordering of vacancies in the synthetized $YSr_2Cu_2FeO_{7+\delta}$ materials with $\delta \sim 0.5$.

Interestingly, from the calculated total energies, it can be inferred that the most stable configuration for $YSr_2Cu_2FeO_{7.5}$ (in the $2a_p \times 2a_p \times 3a_p$ unit cell, where Fe is found in Th, Oh, and SQP) is energetically favored respective to the end terms in 157 meV/f.u., according to the reaction ½ $YSr_2Cu_2FeO_8$ + ½ $YSr_2Cu_2FeO_7$ → $YSr_2Cu_2FeO_{7.5}$. This is in line with the feasibility of synthesizing YSCFO terms with $\delta \sim 0.5$, as was previously reported [15,21].

For this configuration of $YSr_2FeCu_2O_{7.5}$, AIMD calculations were performed at 1000, 1200, 1400, 1600, and 2000 K. The MSD slopes can be used to calculate the self-diffusion coefficient at each simulated temperature; for instance, Figure 3a shows the results at 1400 K that yield a diffusivity of 3.67×10^{-6} cm^2/s. An activation energy of 0.37 eV is extracted from the Arrhenius plot (Figure 3b). It is found that a high oxygen ion mobility occurs in the $FeO_{1+\delta}$ plane (Figure 3c), with a predicted diffusivity of 1.28×10^{-7} cm^2/s at 500 °C. Calculated AIMD oxygen diffusivity values of 3.1×10^{-9} cm^2/s (E_a = 0.50 eV) were previously reported for $GdBaCo_2O_{5.5}$ (GBCO) [36], whose diffusion mechanism has been extensively studied from AIMD simulations [37,38]. The $Na_{0.5}Bi_{0.5}Ti_{0.96}Mg_{0.04}O_{2.96}$ fast oxide ion conductor presents a calculated diffusivity from AIMD of 2.1×10^{-8} cm^2/s and E_a = 0.61 eV [39]. Therefore, considering the diffusivity showed by other perovskite oxides, the results herein suggest that the $YSr_2Cu_2FeO_{7.5}$ is a fast oxide ion conductor.

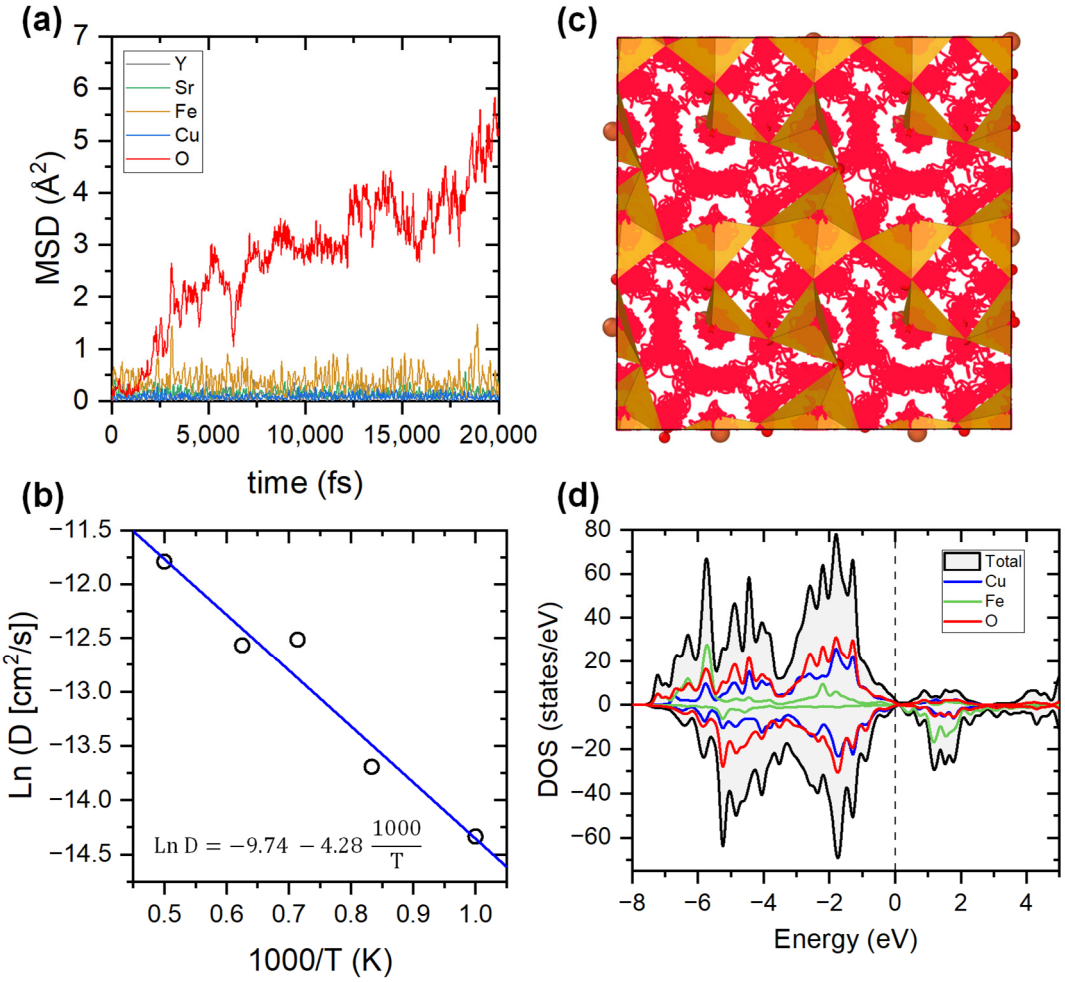

Figure 3. (**a**) MSD at 1400 K for the $YSr_2FeCu_2O_{7.5}$ (**b**) Arrhenius plot of diffusion coefficients obtained at each simulated temperature for $YSr_2FeCu_2O_{7.5}$. (**c**) Calculated trajectories for oxide ions in the $FeO_{1.5}$ plane of $YSr_2FeCu_2O_{7.5}$. Note that the diffusivity of oxygen (O3) takes place only in this plane. (**d**) Calculated atom projected DOS for the $YSr_2FeCu_2O_{7.5}$.

As for the electronic conductivity, the calculated DOS (Figure 3d) corroborates that the electronic charge density remains delocalized throughout the system. According to the calculated DOS, $YSr_2Cu_2FeO_{7.5}$ is a semi-metallic compound (0 eV band gap). These results agree with the MIEC characteristics found in $YSr_2Cu_2FeO_{7.56}$ by López et al. [21].

Several authors have previously reported an oxygen loss of around 5% when $YSr_2Cu_2FeO_{7.56}$ is heated above 673 K in air [15,22]. The oxygen loss, which leads to an oxygen composition around $YSr_2Cu_2FeO_{7.17}$, is fully reversible, and the $YSr_2Cu_2FeO_{7.56}$ phase is recovered

on cooling. In an attempt to achieve an oxygen concentration as close as possible to that experimentally observed on heating ($\delta \sim 0.17$), models of $YSr_2Cu_2FeO_{7.2}$ have also been studied by DFT. Since the $\delta = 0.2$ term is not compatible with a $2a_p \times 2a_p \times 3a_p$ supercell, the crystallographic models are constructed taking a $2a_p \times 5a_p \times 3a_p$ supercell. Among the models consisting of Fe exclusively in tetrahedra [FeO_4] and octahedra [FeO_6] coordination, the most stable configuration according to the Ewald summation method is selected (Figure 4a). For this configuration, AIMD calculations are performed at 800, 1000, 1200, 1600, and 1800K (up to 14 ps). The MSD (Figure 4b) indicates that oxygen ions do not diffuse in this material. Indeed, the oxygen anions appear to jump around their equilibrium position as any other ion in the structure. This proves the influence of transition metal coordination and points towards the beneficial effect of anion disorder on the oxygen ion diffusivity in the YSCFO system. More work is needed to confirm this hypothesis.

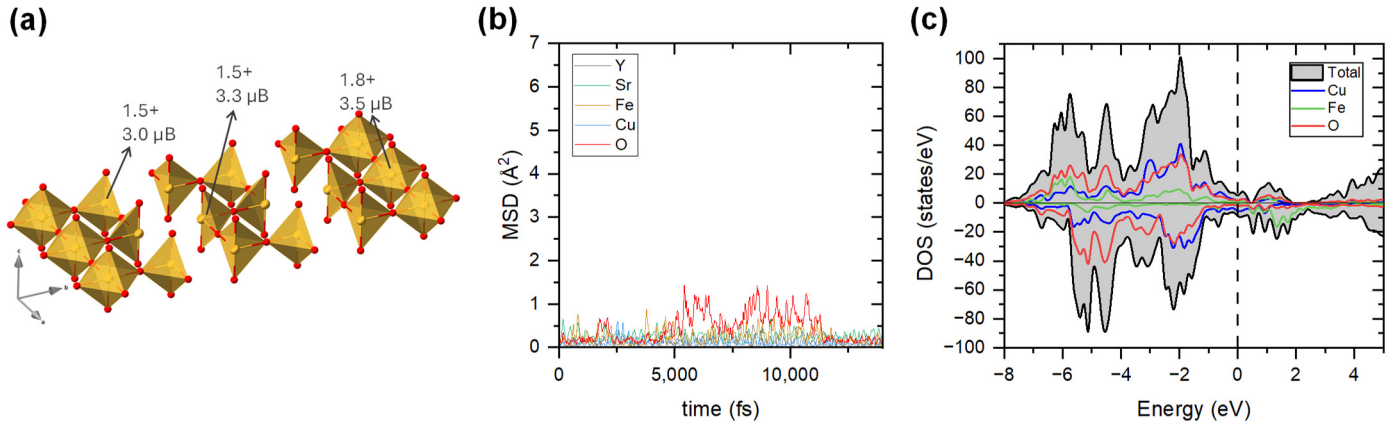

Figure 4. (**a**) Schematic representation of $FeO_{1+\delta}$ planes in the most stable configuration found for $YSr_2Cu_2FeO_{7.2}$ ($2a_p \times 5a_p \times 3a_p$ supercell). Color code: Fe in brown, and O in red. (**b**) MSD at 1600 K for the $YSr_2FeCu_2O_{7.2}$. (**c**) Calculated atom projected DOS for the $YSr_2FeCu_2O_{7.2}$.

The calculated DOS of the most stable configuration (Figure 4c) reveals that $YSr_2Cu_2FeO_{7.2}$ is a metallic phase in which the electronic charge density is delocalized in the bands formed by Cu and Fe 3*d*-orbitals. The itinerant character of electrons in the metallic phases of the YSCFO system has been previously discussed for end-term $YSr_2Cu_2FeO_8$ [16].

To verify that oxygen vacancies in the $FeO_{1+\delta}$ plane are responsible for oxygen diffusion, a $YSr_2FeCu_2O_{7.75}$ phase was investigated in which there is excess oxygen in the yttrium plane (Figure 5a). Note that the extra oxygen drives the coordination around some Cu ions from square pyramidal to octahedral. Although this configuration has not been experimentally observed in the YSFCO system, it is present in layered perovskite oxides $GdBa(Mn, Co)_2O_{5-x}$ [40,41]. AIMD simulation performed at 1400 K reveals high oxygen mobility (calculated D (1400 K) = 7.62×10^{-6} cm^2/s), similar to the AIMD value found for $YSr_2Cu_2FeO_{7.5}$ (see Figure 3a). Notably, oxygen diffusion is anisotropic, occurring only in the $FeO_{1+\delta}$ plane, while the oxygen added in the Y plane does not diffuse (Figure 5b). The calculated DOS for the $YSr_2FeCu_2O_{7.75}$ phase indicates a metallic behavior, similarly to the $\delta = 0.2$ and $\delta = 1$ terms. These results endorse a good electronic conductivity in the YSCFO system.

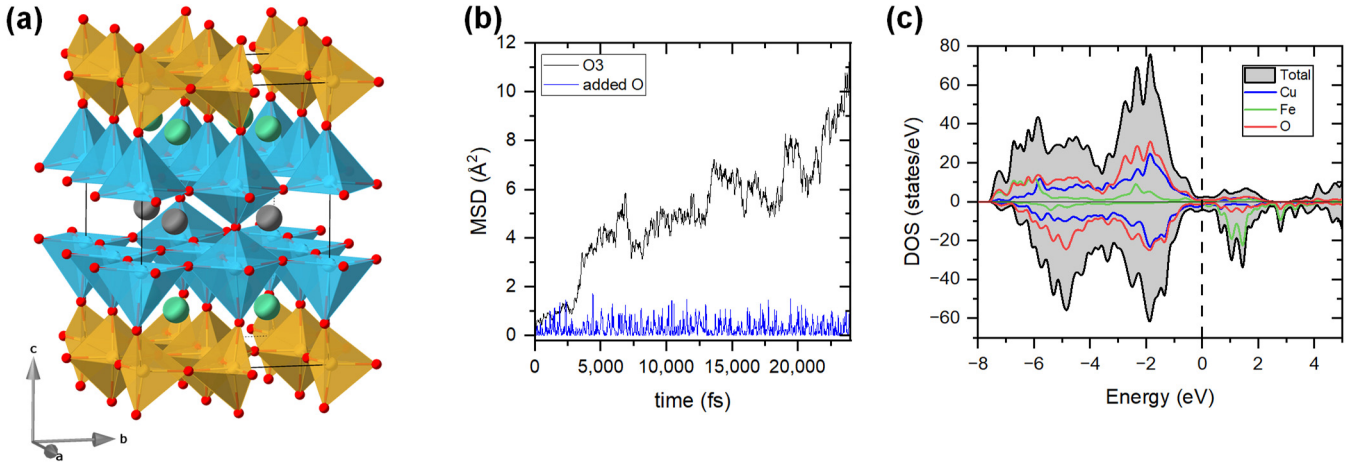

Figure 5. (**a**) Crystal structure of the most stable model found for $YSr_2Cu_2FeO_{7.75}$ ($2a_p \times 2a_p \times 3a_p$ supercell). Color code: Fe in brown, Cu in blue, Sr in green, Y in grey, and O in red. (**b**) MSD at 1400 K for the $YSr_2FeCu_2O_{7.75}$. The MSD of the added O in the Y plane is depicted as a blue line, and the MSD for the O3 ($FeO_{1.75}$ plane) in the structure is shown in black. (**c**) Calculated atom projected DOS for the $YSr_2FeCu_2O_{7.75}$.

4. Conclusions

The hydrogen economy comprises a broad spectrum of technologies, including solid oxide cells (SOC), which rely on oxygen ion transport in ceramic materials. Catalytic materials with fast kinetics for the involved reactions (ORR/OER) must possess high ionic and electronic conductivity. Such MIEC properties were recently discovered in $YSr_2Cu_2FeO_{7.56}$, which led to the present DFT investigation. The computational results herein have shown that the idealized $YSr_2Cu_2FeO_{7.5}$ compound presents a remarkable oxygen diffusion coefficient (predicted 1.28×10^{-7} cm^2/s at 500 °C) and attractive activation energy (Ea = 0.37 eV), which buttress the low ASR value (0.08 Ω cm^2 at 973 K) reported for the $YSr_2Cu_2FeO_{7.56}$ phase [15]. The AIMD calculations confirm that oxygen diffusion is anisotropic, taking place in the *ab* plane of the $FeO_{1+\delta}$ layers. In addition, the DFT results support a good electronic conductivity in the YFSCO materials, in line with previous experimental and computational findings. Although the MIEC properties can be anticipated from the DFT calculations, other requirements for OER/ORR catalysis (such as chemical and mechanical stability over cycling) must be experimentally examined.

It is worth remarking that, depending on the annealing history/oxygen content, anti-site disorder can exist, which is to say, Cu/Fe mixing can take place in the YSCFO system [19,20,42,43]. It is therefore foreseeable that anti-site defects could influence the diffusion mechanism that, in the idealized oxides, takes place exclusively in the $FeO_{1+\delta}$ layer. Further computational investigations will address the influence of anti-site defects in the MIEC properties of the $YSr_2Cu_2FeO_{7+\delta}$ ($0 < \delta < 1$) system.

Author Contributions: Conceptualization, E.M.A.-d.D.; methodology, M.G.-T.; software, M.G.-T.; validation, M.G.-T.; formal analysis, M.G.-T.; investigation, E.M.A.-d.D. and M.G.-T.; data curation, M.G.-T.; writing—original draft preparation, E.M.A.-d.D. and M.G.-T.; visualization, M.G.-T.; supervision, E.M.A.-d.D.; project administration, E.M.A.-d.D.; funding acquisition, E.M.A.-d.D. All authors have read and agreed to the published version of the manuscript.

Funding: This research was funded by the MCIN/AEI/10.13039/501100011033—"ERDF A way of making Europe" across the project ECSAWE-PID2022-139501OB-C22. Authors are also thankful for funding from MCIN/AEI/10.13039/501100011033-"NextGenerationEU"/PRTR (project TED2021-130452B-C21) and the Universidad Complutense de Madrid (FEI-EU-22-01-4129585).

Institutional Review Board Statement: Not applicable.

Informed Consent Statement: Not applicable.

Data Availability Statement: The raw data supporting the conclusions of this article will be made available by the authors on request.

Acknowledgments: Computational resources from the MALTA–cluster (Universidad de Oviedo) and I2Basque are acknowledged. The authors thank the contributions of L.M Barrajón-Acedo to the study of the $YSr_2Cu_2FeO_{7.5}$ phase.

Conflicts of Interest: The authors declare no conflicts of interest.

References

1. Megía, P.J.; Vizcaíno, A.J.; Calles, J.A.; Carrero, A. Hydrogen Production Technologies: From Fossil Fuels toward Renewable Sources. A Mini Review. *Energy Fuels* **2021**, *35*, 16403–16415. [CrossRef]
2. Jolaoso, L.A.; Bello, I.T.; Ojelade, O.A.; Yousuf, A.; Duan, C.; Kazempoor, P. Operational and scaling-up barriers of SOEC and mitigation strategies to boost H_2 production- a comprehensive review. *Int. J. Hydrogen Energy* **2023**, *48*, 33017–33041. [CrossRef]
3. Nechache, A.; Hody, S. Alternative and innovative solid oxide electrolysis cell materials: A short review. *Renew. Sustain. Energy Rev.* **2021**, *149*, 111322. [CrossRef]
4. Tarutin, A.P.; Filonova, E.A.; Ricote, S.; Medvedev, D.A.; Shao, Z. Chemical design of oxygen electrodes for solid oxide electrochemical cells: A guide. *Sustain. Energy Technol. Assess.* **2023**, *57*, 103185. [CrossRef]
5. Hu, S.; Li, J.; Zeng, Y.; Pu, J.; Chi, B. A mini review of the recent progress of electrode materials for low-temperature solid oxide fuel cells. *Phys. Chem. Chem. Phys.* **2023**, *25*, 5926–5941. [CrossRef] [PubMed]
6. Zheng, Y.; Chen, Z.; Zhang, J. Solid Oxide Electrolysis of H_2O and CO_2 to Produce Hydrogen and Low-Carbon Fuels. *Electrochem. Energy Rev.* **2021**, *4*, 508–517. [CrossRef]
7. Monama, G.R.; Ramohlola, K.E.; Iwuoha, E.I.; Modibane, K.D. Progress on perovskite materials for energy application. *Results Chem.* **2022**, *4*, 100321. [CrossRef]
8. Ji, Q.; Bi, L.; Zhang, J.; Cao, H.; Zhao, X.S. The role of oxygen vacancies of ABO_3 perovskite oxides in the oxygen reduction reaction. *Energy Environ. Sci.* **2020**, *13*, 1408–1428. [CrossRef]
9. Wang, C.; Miao, H.; Zhang, X.; Huang, J.; Yuan, J. On Fe-based perovskite electrodes for symmetrical reversible solid oxide cells—A review. *J. Power Sources* **2024**, *596*, 234112. [CrossRef]
10. Li, G.; Gou, Y.; Cheng, X.; Bai, Z.; Ren, R.; Xu, C.; Qiao, J.; Sun, W.; Wang, Z.; Sun, K. Enhanced Electrochemical Performance of the Fe-Based Layered Perovskite Oxygen Electrode for Reversible Solid Oxide Cells. *ACS Appl. Mater. Interfaces* **2021**, *13*, 34282–34291. [CrossRef]
11. Sayers, R.; Schiffmann, F.; Fearn, S.; Kilner, J.A.; Slater, B.; Romani, S.; Tatham, D.J.; Claridge, J.B.; Corà, F.; Rosseinsky, M.J. Internal Activation Strain and Oxygen Mobility in a Thermally Stable Layered Fe^{3+} Oxide. *Chem. Mater.* **2013**, *25*, 3441–3457. [CrossRef]
12. Chen, C.; Ciucci, F. Designing Fe-Based Oxygen Catalysts by Density Functional Theory Calculations. *Chem. Mater.* **2016**, *28*, 7058–7065. [CrossRef]
13. Ren, R.; Wang, Z.; Meng, X.; Xu, C.; Qiao, J.; Sun, W.; Sun, K. Boosting the Electrochemical Performance of Fe-Based Layered Double Perovskite Cathodes by Zn^{2+} Doping for Solid Oxide Fuel Cells. *ACS Appl. Mater. Interfaces* **2020**, *12*, 23959–23967. [CrossRef] [PubMed]
14. Moazzam, M.; Li, C.; Cordaro, G.; Dezanneau, G. Effect of A-site cation ordering on oxygen diffusion in $NdBa_2Fe_3O_8$ through molecular dynamics. *J. Solid State Chem.* **2023**, *325*, 124148. [CrossRef]
15. López-Paz, S.A.; Marín-Gamero, R.; Martínez de Irujo-Labalde, X.; Sánchez-Marcos, J.; Perez-Coll, D.; Alario y Franco, M.Á.; García-Martín, S. YBaCuO-type perovskites as potential air electrodes for SOFCs. The case of $YSr_2Cu_2FeO_{7+\delta}$. *J. Mater. Chem. A* **2021**, *9*, 8554–8560. [CrossRef]
16. Gómez-Toledo, M.; López-Paz, S.A.; García-Martín, S.; Arroyo-de Dompablo, M.E. Metal-to-Insulating Transition in the Perovskite System $YSr_2Cu_2FeO_{8-\delta}$ ($0 < \delta < 1$) Modeled by DFT Methods. *Inorg. Chem.* **2023**, *62*, 3445–3456. [CrossRef] [PubMed]
17. Gómez-Toledo, M.; Arroyo-de Dompablo, E.M. The SCAN+*U* method in the investigation of complex transition metal oxides: A case study on $YSr_2Cu_2FeO_{7+\delta}$ ($\delta = 0, 1$). *Phys. Chem. Chem. Phys.* **2024**, *26*, 17255–17264. [CrossRef]
18. Shimoyama, J.; Otzschi, K.; Hinouchi, T.; Kishio, K. Discovery of superconductivity in Fe-based cuprates. *Phys. C* **2000**, *341*, 563–564. [CrossRef]
19. Mochiku, T.; Nakano, Y.; Hoshikawa, A.; Sato, S.; Oikawa, K.; Ishigaki, T.; Kamiyama, T.; Kadowaki, K.; Hirata, K. Superstructure in $Sr_2YCu_2FeO_{6+d}$. *Phys. C-Supercond. Its Appl.* **2004**, *412*, 115–119. [CrossRef]
20. López-Paz, S.A.; Martinez de Irujo-Labalde, X.; Sanchez-Marcos, J.; Ritter, C.; Moran, E.; Alario-Franco, M.A. Soft Magnetic Switching in a $YSr_2Cu_2FeO_{7.85}$ Superconductor with Unusually High Iron Valence. *Inorg. Chem.* **2019**, *58*, 12809–12814. [CrossRef]
21. López-Paz, S.A.; Sari, D.P.; Hillier, A.D.; Alario-Franco, M.A. Coexistence of magnetism and superconductivity in the iron containing $YSr_2Cu_2FeO_{7.57}$ cuprate as studied by μSR. *AIP Adv.* **2021**, *11*, 015011. [CrossRef]
22. Sansom, J.E.H.; Kendrick, E.; Rudge-Pickard, H.A.; Islam, M.S.; Wright, A.J.; Slater, P.R. Synthesis and characterisation of the perovskite-related cuprate phases $YSr_2Cu_2MO_{7+y}$ (M = Co, Fe) for potential use as solid oxide fuel cell cathode materials. *J. Mater. Chem.* **2005**, *15*, 2321–2327. [CrossRef]

23. Kresse, G.; Furthmuller, J. Efficient iterative schemes for ab initio total-energy calculations using a plane-wave basis set. *Phys. Rev. B* **1996**, *54*, 11169. [CrossRef]
24. Kresse, G.; Joubert, D. From ultrasoft pseudopotentials to the projector augmented-wave method. *Phys. Rev. B* **1999**, *59*, 1758. [CrossRef]
25. Sun, J.; Ruzsinszky, A.; Perdew, J.P. Strongly Constrained and Appropriately Normed Semilocal Density Functional. *Phys. Rev. Lett.* **2015**, *115*, 036402. [CrossRef] [PubMed]
26. Bloch, P.E. Projector augmented-wave method. *Phys. Rev. B* **1994**, *50*, 17953. [CrossRef] [PubMed]
27. Blochl, P.E.; Jepsen, O.; Andersen, O.K. Improved Tetrahedron Method for Brillouin-Zone Integrations. *Phys. Rev. B* **1994**, *49*, 16223–16233. [CrossRef] [PubMed]
28. Ong, S.P.; Richards, W.D.; Jain, A.; Hautier, G.; Kocher, M.; Cholia, S.; Gunter, D.; Chevrier, V.L.; Persson, K.A.; Ceder, G. Python Materials Genomics (pymatgen): A robust, open-source python library for materials analysis. *Comput. Mater. Sci.* **2013**, *68*, 314–319. [CrossRef]
29. Toukmaji, A.Y.; Board, J.A., Jr. Ewald summation techniques in perspective: A survey. *Comput. Phys. Commun.* **1996**, *95*, 73–92. [CrossRef]
30. Bader, R.F.W. *Atoms in Molecules: A Quantum Theory*; Oxford University Press: Oxford, UK, 1990.
31. Henkelman, G.; Arnaldsson, A.; Jónsson, H. A fast and robust algorithm for Bader decomposition of charge density. *Comput. Mater. Sci.* **2006**, *36*, 354–360. [CrossRef]
32. Perdew, J.P.; Chevary, J.A.; Vosko, S.H.; Jackson, K.A.; Pederson, M.R.; Singh, D.J.; Fiolhais, C. Atoms, molecules, solids, and surfaces: Applications of the generalized gradient approximation for exchange and correlation. *Phys. Rev. B Condens. Matter* **1992**, *46*, 6671–6687. [CrossRef] [PubMed]
33. Nosé, S. A molecular dynamics method for simulations in the canonical ensemble. *Mol. Phys.* **1984**, *52*, 255–268. [CrossRef]
34. Deng, Z.; Zhu, Z.; Chu, I.-H.; Ong, S.P. Data-Driven First-Principles Methods for the Study and Design of Alkali Superionic Conductors. *Chem. Mater.* **2016**, *29*, 281–288. [CrossRef]
35. Zhu, Z.; Deng, Z.; Chu, I.-H.; Radhakrishnan, B.; Ping Ong, S. Ab Initio Molecular Dynamics Studies of Fast Ion Conductors. In *Computational Materials System Design*; Springer: Cham, Switzerland, 2018; pp. 147–168.
36. Chroneos, A.; Yildiz, B.; Tarancón, A.; Parfitt, D.; Kilner, J.A. Oxygen diffusion in solid oxide fuel cell cathode and electrolyte materials: Mechanistic insights from atomistic simulations. *Energy Environ. Sci.* **2011**, *4*, 2774–2789. [CrossRef]
37. Parfitt, D.; Chroneos, A.; Tarancón, A.; Kilner, J.A. Oxygen ion diffusion in cation ordered/disordered $GdBaCo_2O_{5+\delta}$. *J. Mater. Chem.* **2011**, *21*, 2183–2186. [CrossRef]
38. Hermet, J.; Geneste, G.; Dezanneau, G. Molecular dynamics simulations of oxygen diffusion in $GdBaCo_2O_{5.5}$. *Appl. Phys. Lett.* **2010**, *97*, 174102. [CrossRef]
39. He, X.; Mo, Y. Accelerated materials design of $Na_{0.5}Bi_{0.5}TiO_3$ oxygen ionic conductors based on first principles calculations. *Phys. Chem. Chem. Phys.* **2015**, *17*, 18035–18044. [CrossRef] [PubMed]
40. Taskin, A.A.; Lavrov, A.N.; Ando, Y. Achieving fast oxygen diffusion in perovskites by cation ordering. *Appl. Phys. Lett.* **2005**, *86*, 091910. [CrossRef]
41. Taskin, A.A.; Lavrov, A.N.; Ando, Y. Fast oxygen diffusion in A-site ordered perovskites. *Prog. Solid State Chem.* **2007**, *35*, 481–490. [CrossRef]
42. Fujii, H.; Mihara, Y.; Mochiku, T.; Hata, Y.; Kadowaki, K. Order, disorder and superconductivity in $FeSr_2YCu_2O_{6+d}$. *Phys. C-Supercond. Its Appl.* **2004**, *415*, 85–93. [CrossRef]
43. Hata, Y.; Mihara, Y.; Mochiku, T.; Suzuki, J.-i.; Kakeya, I.; Kadowaki, K.; Kita, E.; Yasuoka, H. Redistribution of Fe ion and superconductivity of $FeSr_2YCu_2O_{6+y}$ system. *Phys. C Supercond.* **2004**, *417*, 17–24. [CrossRef]

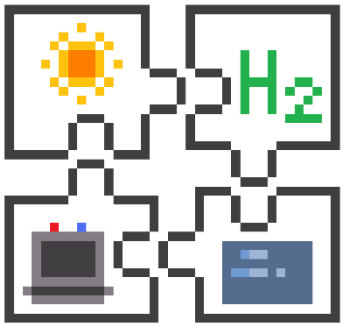

CAPÍTULO 7

Discusión

En este capítulo se presenta una discusión integradora de los resultados obtenidos en los capítulos 3 a 6 de esta tesis doctoral. Esta discusión está compuesta por tres secciones. En primer lugar, se comparan los dos materiales estudiados, $Sr_{2-x}Ba_xTa_2O_7$ ($0 \leq x \leq 1$) y $YSr_2FeCu_2O_{7+\delta}$ ($0 < \delta < 1$), destacando el papel fundamental que desempeña la naturaleza del metal de transición en la elección y aplicación de la metodología de cálculo. A continuación, se abordan las limitaciones computacionales inherentes a la modelización de los sistemas reales estudiados, retomando los desafíos expuestos en los Capítulos 4-6. Por último, se amplía el estudio computacional del sistema $YSr_2FeCu_2O_{7+\delta}$ mediante el análisis de descriptores electrónicos, concretamente el centro de banda 2*p* del oxígeno, con el objetivo de evaluar la utilidad de estos materiales para catalizar la ORR.

7.1. Influencia del metal de transición y su configuración electrónica

La investigación desarrollada en esta tesis doctoral se ha centrado en el estudio de perovskitas en capas con aplicaciones en el campo de la energía. En primer lugar, se ha avanzado en el diseño de perovskitas para la generación de H_2 verde. Concretamente, se ha estudiado la familia $Sr_{2-x}Ba_xTa_2O_7$ ($0 \leq x \leq 1$) (Capítulo 3) y su potencial aplicación como fotocatalizador de la reacción de electrolisis de agua. Por otro lado, se ha analizado el sistema $YSr_2FeCu_2O_{7+\delta}$ (Capítulos 4-6) para su aplicación en SOFC. Ambos compuestos representan ejemplos sobre la aplicabilidad de materiales con estructura derivada de la perovskita en la economía del hidrógeno. Sin embargo, aunque tengan una relación estructural, las notables diferencias entre las estructuras electrónicas de $Sr_{2-x}Ba_xTa_2O_7$ ($0 \leq x \leq 1$) y $YSr_2FeCu_2O_{7+\delta}$ ($0 < \delta < 1$) son, precisamente, las que dan lugar a sus propiedades y potenciales aplicaciones.

Los materiales propuestos para la producción de H_2 verde a través de fotoelectrocatálisis de agua suelen presentar metales de transición con configuraciones electrónicas d^0 o d^{10}. En el caso de la familia $Sr_{2-x}Ba_xTa_2O_7$, la configuración electrónica Ta-d^0 confiere al material un comportamiento semiconductor, lo cual es condición indispensable para fotocatalizar la reacción de electrolisis del agua. Generalmente, las propiedades electrónicas y magnéticas de compuestos con metales de transición d^0 pueden explicarse a través de modelos relativamente simples, aunque esto no quiere decir que su estudio computacional sea trivial. Como se ha discutido en el capítulo 3, en estos materiales, la BV está

compuesta por estados 2*p* del oxígeno, mientras que la BC la forman los estados n*d* vacíos del metal (véase **figura S3** en capítulo 3). El estudio de óxidos de metales de transición d^0 o d^{10} mediante DFT resulta relativamente sencillo e, incluso, aproximaciones como el funcional PBE han demostrado reproducir el comportamiento semiconductor de fotocatalizadores ampliamente utilizados. Este es el caso de TiO_2,[1] y también de los compuestos semiconductores estudiados en esta tesis, Sr_2Ta_2O y $BaSrTa_2O_7$. Como ya se ha comentado, a pesar de la imprecisión que presenta la metodología DFT para determinar el band gap de materiales aislantes o semiconductores,[2] se ha demostrado que la metodología es apropiada para extraer tendencias generales.

Para los materiales fotocatalizadores estudiados en esta tesis, se ha puesto de manifiesto que el funcional SCAN mejora los resultados de PBE, permitiendo una descripción adecuada de la estructura cristalina y electrónica. Este funcional ha permitido un estudio cualitativo y comparativo del impacto de las variaciones composicionales en las propiedades de la familia $Sr_{2-x}Ba_xTa_2O_7$ ($0 \leq x \leq 1$). Además, se ha podido llevar a cabo un estudio detallado de la fase Dion-Jacobson $BaSrTa_2O_7$, que presenta una mayor producción de hidrógeno que la perovskita $Sr_2Ta_2O_7$, aportando a partir de los resultados computaciones una posible explicación a este hecho experimental.

Sin embargo, tal y como se ha discutido en los capítulos 4, 5 y 6, el estudio de óxidos de metales de transición a través de cálculos DFT se complica cuando los orbitales *d* de la capa de valencia del metal están parcialmente ocupados. Para este tipo de materiales, las propiedades eléctricas y magnéticas son complejas, y requieren tener en cuenta las interacciones electrón-electrón. Por lo tanto, para comprender estos óxidos de metales de transición es necesario utilizar modelos más complejos que los empleados en la descripción de materiales con metales d^0. Uno de estos modelos es el modelo de Hubbard,[3] en el cual se asume que las únicas repulsiones interelectrónicas relevantes son aquellas que se producen entre los electrones de valencia del mismo átomo.[4] Las repulsiones se incluyen a través del parámetro *U*, lo que permite cuantificar energéticamente dicha repulsión interelectrónica. De acuerdo con el modelo de Hubbard, existe un equilibrio entre la anchura de las bandas *d* del metal (A) y la repulsión interelectrónica (*U*). Estos factores están determinados, entre otros, por la electronegatividad del metal de transición, el número de electrones 3*d*, el estado de oxidación y la estructura cristalina del material. De esta forma, si la anchura de las bandas 3*d* del metal

es menor que la repulsión interelectrónica (A < *U*), el material será un aislante de Mott. Por otra parte, si A > *U*, el material presentará un comportamiento metálico. Además, existen ciertos casos en los que A ≈ *U*.

El sistema $YSr_2FeCu_2O_{7+\delta}$ ($0 < \delta < 1$), estudiado en esta tesis doctoral, presenta una transición aislante–metal. Experimentalmente, en este sistema se observa un cambio en las propiedades electrónicas al pasar de la fase reducida $YSr_2FeCu_2O_{7.08}$ (medidas en esta tesis doctoral), donde los metales de transición presentan estados de oxidación formales Fe^{+3} y Cu^{+2}, a la fase oxidada, $YSr_2FeCu_2O_{7.85}$ (medidas con anterioridad a esta tesis doctoral), en la que los estados de oxidación formales son Fe^{+4} y Cu^{+3}/Cu^{+2}. Computacionalmente, de acuerdo con lo observado en la DOS calculada (SCAN/DFT+*U*), los electrones están localizados en la fase ideal $YSr_2FeCu_2O_7$ (aislante de Mott-Hubbard), presentando el material un comportamiento semiconductor. Por el contrario, en la fase $YSr_2FeCu_2O_8$, la DOS calculada indica que los electrones tienen un carácter itinerante que da lugar a un comportamiento metálico. Las propiedades electrónicas observadas y los resultados del cálculo computacional son, por lo tanto, consistentes. La visión global del sistema YSFCO es compatible con el modelo de Hubbard; podría decirse que, al introducir oxígeno en la fase $YSr_2FeCu_2O_7$, aumenta el estado de oxidación de Cu y Fe, la covalencia del enlace metal–oxígeno y, con ello, la anchura de la banda formada por la hibridación de los estados M 3*d* y O 2*p*, que supera a la repulsión interelectrónica.

En los capítulos 4 y 5 se ha enfatizado que el estudio computacional de este sistema requiere un funcional adecuado, que logre describir a la vez el comportamiento metálico de la fase ideal $YSr_2FeCu_2O_8$ y el comportamiento semiconductor de la fase ideal $YSr_2FeCu_2O_7$. En las últimas décadas, la metodología DFT+*U* se ha utilizado ampliamente para el estudio de óxidos de metales de transición. Aunque ofrece buenos resultados en el estudio de materiales con electrones localizados (A < U), la metodología DFT+*U* puede presentar problemas para predecir comportamientos metálicos. Los resultados presentados en esta tesis evidencian que este es el caso de $YSr_2FeCu_2O_8$, para el que el empleo del funcional PBE+*U* (capítulo 4) induce una excesiva localización electrónica, lo que da lugar a una sobreestimación de los momentos magnéticos experimentales. En otras palabras, el uso de DFT+*U* puede resultar inadecuado para materiales donde A > U. Por ello, la metodología DFT+*U*, sólo puede aplicarse con garantías **cuando se sabe de antemano** que se trata de sistemas

con electrones localizados. Hay que recalcar que, por el contrario, el funcional SCAN reproduce satisfactoriamente las propiedades magnéticas y electrónicas de todo el sistema YSCFO.

Adicionalmente, debe tenerse en cuenta que la inclusión de la repulsión interectrónica mediante la metodología DFT+*U* implica la determinación de parámetros *U* específicos para cada uno de los metales de transición, y que los valores apropiados dependen, además, del funcional utilizado. En el capítulo 5, dedicado a la metodología SCAN+*U*, se evidencia que, en el sistema YFSCO, el parámetro *U* asociado al Cu tiene una influencia más significativa que el asociado al Fe sobre los parámetros cristalinos, los momentos magnéticos y el comportamiento electrónico de las fases ideales $YSr_2FeCu_2O_7$ y $YSr_2FeCu_2O_8$. Asimismo, el hecho de que el valor de *U* adecuado para un material no sea necesariamente transferible a otros materiales, redunda en beneficio de la utilización del funcional SCAN frente a la metodología DFT+*U*.

En términos generales, podría plantearse que los avances en la metodología DFT (y el desarrollo de nuevos funcionales) han hecho posible el estudio de «cualquier» óxido de metales de transición. En este sentido, en esta tesis se ha demostrado que el funcional SCAN proporciona resultados fiables tanto en óxidos de metales de transición relativamente sencillos, como la familia $Sr_{2-x}Ba_xTa_2O_7$ ($0 \leq x \leq 1$) — compuesta por un único metal de transición que además es d^0 —, como para sistemas altamente complejos como $YSr_2FeCu_2O_{7+\delta}$ ($0 < \delta < 1$), que presenta dos metales de transición y una transición aislante-metal modulada por el contenido en oxígeno. No obstante, el estudio de óxidos de metales de transición mediante DFT todavía debe enfrentarse al desafío de «traducir» los sólidos reales a modelos cristalográficos asumibles, cuestión que se aborda en la siguiente sección.

7.2. Retos computacionales en el estudio de sistemas reales

Los cálculos DFT hacen posible evaluar, de forma independiente, el efecto de la composición y de la estructura cristalina en la estructura electrónica de un material, ya sea existente o virtual. De esta forma, es posible analizar la influencia de estos parámetros en las propiedades de interés para una aplicación concreta. Sin embargo, los sólidos reales suelen presentar estructuras cristalinas y composiciones químicas complejas, lo que dificulta su estudio mediante cálculos mecano-cuánticos.

La investigación computacional llevada a cabo en los capítulos 4, 5 y 6 de esta tesis doctoral sobre el sistema $YSr_2FeCu_2O_{7+\delta}$ ($0 < \delta < 1$) es un claro ejemplo de las aproximaciones, o simplificaciones, que deben realizarse para poder simular algunos materiales reales mediante DFT. Como se ha resaltado en estos capítulos, se han utilizado modelos idealizados para las composiciones $YSr_2FeCu_2O_7$ y $YSr_2FeCu_2O_8$. En primer lugar, no se ha tenido en cuenta la presencia del desorden catiónico (*antisite*), que se ha observado en estudios experimentales para varias fases del sistema.[5-9] En segundo lugar, se han estudiado las composiciones perfectamente estequiométricas $YSr_2FeCu_2O_7$ y $YSr_2FeCu_2O_8$, a pesar de que estas no se han obtenido experimentalmente, dado que siempre existe una desviación del contenido ideal en oxígeno.

Incorporar defectos *antisite* y ajustar el contenido en oxígeno a los valores determinados experimentalmente requeriría emplear grandes superceldas, cuyo cálculo demanda recursos computacionales considerablemente mayores. Adicionalmente, una vez generadas las superceldas, sería necesario generar diversas configuraciones, ordenando tanto las vacantes y los átomos de oxígeno, como los cationes Cu/Fe. El estudio de sistemas desordenados puede abordarse utilizando herramientas computacionales avanzadas, como el método SQS (Special Quasi-random Structures). No obstante, estas herramientas han quedado fuera del enfoque principal de la presente tesis doctoral, aunque podrían ser objeto de futuras investigaciones.

Al igual que ocurre con los extremos del sistema YSCFO, un estudio riguroso de las fases intermedias debería considerar los fenómenos estructurales comentados anteriormente, como son el *antisite* y la distribución de vacantes/oxígeno a 0 K. En este caso, en el capítulo 6 se han considerado algunas configuraciones, centradas principalmente en definir el orden de vacantes en la fase correspondiente a $\delta = 0.5$, así como los poliedros de coordinación del Fe.

Por otro lado, deben mencionarse las limitaciones asociadas a la metodología AIMD, que se ha empleado para estudiar de la difusión del ion óxido dentro de la estructura. Una de las desventajas que presenta la dinámica molecular *ab initio* es la imposibilidad de llegar a los tiempos de simulación accesibles a través de dinámica molecular clásica (del orden de 10^{-9} a 10^{-7} s), así como la necesidad de trabajar con sistemas de menor tamaño, debido al elevado coste computacional que implica calcular las fuerzas a partir de primeros principios. La simulación del

sistema $YSr_2FeCu_2O_{7+\delta}$, utilizando los recursos computacionales disponibles, ha requerido hasta 16 días de tiempo de CPU y hasta 4 semanas de tiempo real para cada temperatura simulada (compárese con 5 días de tiempo real para la resolución de la estructura electrónica de la fase ideal $YSr_2FeCu_2O_7$, utilizando el funcional SCAN). Esta problemática puede atenuarse empleando *Machine Learning* para obtener campos de fuerza específicos que describan las interacciones del material estudiado (*Machine Learning Force Fields*, MLFF). La metodología *Machine Learning*,[10] desarrollada recientemente, se ha empleado en el estudio de perovskitas de haluros[11] y de calcogenuro.[12] Los datos utilizados para entrenar el modelo de *Machine Learning* provienen de cálculos DFT, siendo necesarios entre 500 y 1000 cálculos *ab initio* para desarrollar el modelo.[13]

Con respecto a la familia $Sr_{2-x}Ba_xTa_2O_7$ ($0 \leq x \leq 1$), los modelos cristalográficos utilizados concuerdan con los materiales reales. Se trata en este caso de óxidos estequiométricos con un orden definido de Sr y Ba en la estructura cristalina. La utilización de estos modelos ha permitido obtener la estructura electrónica, a partir de la cual se han discutido las propiedades fotocatalíticas. Como se ha señalado con anterioridad, en esta tesis doctoral se han tratado aspectos electrónicos fundamentales para que se produzca la fotocatálisis, como son el band gap, la energía de las bandas de valencia y de conducción y, en definitiva, la composición y la estructura cristalina del fotocatalizador. No obstante, cabe destacar que el proceso de fotocatálisis es complejo y no depende únicamente de la estructura electrónica del material.[14] Para llevar a cabo una descripción detallada del proceso fotocatalítico es necesario tener en cuenta la localización de los pares electrón-hueco, además del tiempo de vida de las especies fotogeneradas. Por otra parte, deben emplearse también metodologías que permitan explorar estados excitados de las especies involucradas.[15] Considerando todo lo anterior, aunque no se hayan abordado todos los aspectos mencionados, los resultados aquí expuestos han arrojado algo de luz sobre la actividad catalítica de las fases $Sr_{2-x}Ba_xTa_2O_7$ ($0 \leq x \leq 1$) y, además, sirven como punto de partida para continuar con el estudio de $BaSrTa_2O_7$ como fotocatalizador.

A lo largo de la tesis se ha hecho un esfuerzo importante por contrastar los resultados DFT (óxidos ideales) con los datos experimentales (óxidos reales). En el caso de la familia $Sr_{2-x}Ba_xTa_2O_7$ ($0 \leq x \leq 1$), se ha logrado sintetizar y caracterizar las fases principales analizadas en el estudio DFT. Esto ha posibilitado comprobar la validez de las predicciones computacionales, pudiendo

comparar los valores obtenidos para los parámetros de red o del band gap con los resultados experimentales. Por otra parte, para $YSr_2FeCu_2O_{7+\delta}$, se ha logrado abordar en cierta medida algunos aspectos sobre la transición aislante–metal. Conocer el valor del band gap para la fase $YSr_2FeCu_2O_{7.08}$ ha sido crucial para evaluar el método SCAN+*U* (capítulo 5). Sin embargo, lamentablemente, no ha sido posible ampliar el estudio experimental de este sistema para explorar parámetros clave —como son la microestructura de las fases intermedias—, o realizar medidas de ASR o de difusión. Esta falta de datos experimentales limita la posibilidad de verificar las predicciones sobre la potencial aplicación de estos compuestos, que se discute en la siguiente sección.

7.3. Aplicaciones del sistema $YSr_2FeCu_2O_{7+\delta}$: Descriptores electrónicos a partir de cálculos DFT

Los cálculos DFT desempeñan un papel muy activo en el diseño de materiales con actividad catalítica en procesos de almacenamiento y conversión de energía. Algunos ejemplos relevantes incluyen los procesos tratados en esta tesis doctoral, es decir, la disociación del agua en hidrógeno (*Hydrogen Evolution Reaction*, HER) y oxígeno (*Oxygen Evolution Reaction*, OER), o la combinación de oxígeno e hidrógeno para producir agua (*Hydrogen Oxidation Reaction*, HOR y *Oxygen Reduction Reaction*, ORR).[16-19] Como se ha comentado en el capítulo 1, el diseño y desarrollo de materiales catalizadores para estas reacciones puede mejorarse mediante el uso de descriptores electrónicos.[20] Norskov y colaboradores demostraron que la energía del centro de banda *d* —referida al nivel de Fermi— de metales de transición y de sus aleaciones, se correlaciona con la energía de enlace superficial de los adsorbatos en procesos catalíticos como la HER.[16] Más recientemente, se ha demostrado que el centro de banda 2*p* del oxígeno —relativo al nivel de Fermi— está fuertemente correlacionado con la resistencia específica de superficie (ASR) medida experimentalmente, los coeficientes de intercambio superficial de oxígeno o la energía de formación de vacantes de oxígeno en perovskitas utilizadas como catalizadores de la ORR.[21, 22]

El objetivo final de los descriptores electrónicos es predecir propiedades catalíticas. En términos de aplicaciones, los resultados en perovskitas simples revelan que aproximar el centro de banda O 2*p* al nivel de Fermi influye positivamente en las propiedades catalíticas para ORR.[20, 23] Así, se ha demostrado que valores calculados con PBE+*U* para el centro de banda O 2*p* entre -1 y -1,8

eV corresponden a materiales con una alta actividad catalítica para la ORR (véase **figura 1.13**).[21] Los estudios existentes se han centrado, principalmente, en perovskitas simples ABO_3,[21-24] y pocos trabajos abordan óxidos de metales de transición con alta complejidad química y estructural. El sistema $YSr_2FeCu_2O_{7+\delta}$ ($0 < \delta < 1$), estudiado en esta tesis doctoral, constituye un candidato ideal para poner a prueba la capacidad predictiva del centro de banda O 2*p*, dado que presenta una complejidad que ha sido poco explorada hasta la fecha.

A partir de las densidades de estados calculadas para las fases del sistema YSCFO en los Capítulos 4-6, el centro de banda O 2*p* se ha calculado como el centroide de la densidad de estados proyectada del oxígeno, incluyendo estados ocupados y desocupados, según la **ecuación 7.1.** El centro de banda se refiere al nivel de Fermi, que se ha fijado en el mínimo de la banda de conducción.[23]

$$\text{Centro O } 2p = \frac{\int_{-\infty}^{\infty} \text{E O2}p\ (\text{E})\ \text{dE}}{\int_{-\infty}^{\infty} \text{O2}p\ (\text{E})\ \text{dE}} - E_{Fermi} \qquad (7.1)$$

El estudio realizado se ha limitado a considerar modelos con orden ferromagnético y cálculos usando el funcional SCAN, puesto que este reproduce correctamente las propiedades estructurales, magnéticas y electrónicas de los extremos $YSr_2Cu_2FeO_7$ ($\delta = 0$) y $YSr_2Cu_2FeO_8$ ($\delta = 1$). Además, existen trabajos previos que ponen de manifiesto que el funcional SCAN produce errores menores al comparar los valores predichos del centro de banda O 2*p* con los valores obtenidos mediante espectroscopía de emisión de rayos X (XES).[24] Por otro lado, para facilitar la comparación con los valores reportados para otras perovskitas, se han realizado cálculos adicionales utilizando el método PBE+*U* con un valor de U_{eff} de 4 eV para Cu y Fe.

En la **figura 7.1** se muestran los valores del centro de banda O 2*p* calculados para el sistema $YSr_2FeCu_2O_{7+\delta}$ ($0 < \delta < 1$), junto con un esquema de los planos $FeO_{1+\delta}$ para las configuraciones más estables con $\delta = 0{,}2$; 0,25 y 0,5 (señaladas como 1, 2 y 3, respectivamente). El área sombreada en gris indica el rango de valores del centro de banda O 2*p* (PBE+*U*) que la bibliografía existente considera de interés para el diseño de materiales catalíticos para procesos ORR.[23] Como se observa en la **figura 7.1a**, los valores obtenidos para el sistema YSCFO se encuentran dentro de esta región. Esta observación concuerda con los bajos

valores de ASR reportados por López-Paz *et al.*[6] (0,20 y 0,08 Ω cm² a 923 y 973 K, respectivamente), así como con los resultados obtenidos en el capítulo 6 de esta tesis doctoral, es decir, una elevada difusividad de oxígeno (1,28 × 10^{-7} cm²/s a 500 °C) y una baja energía de activación (0,37 eV).

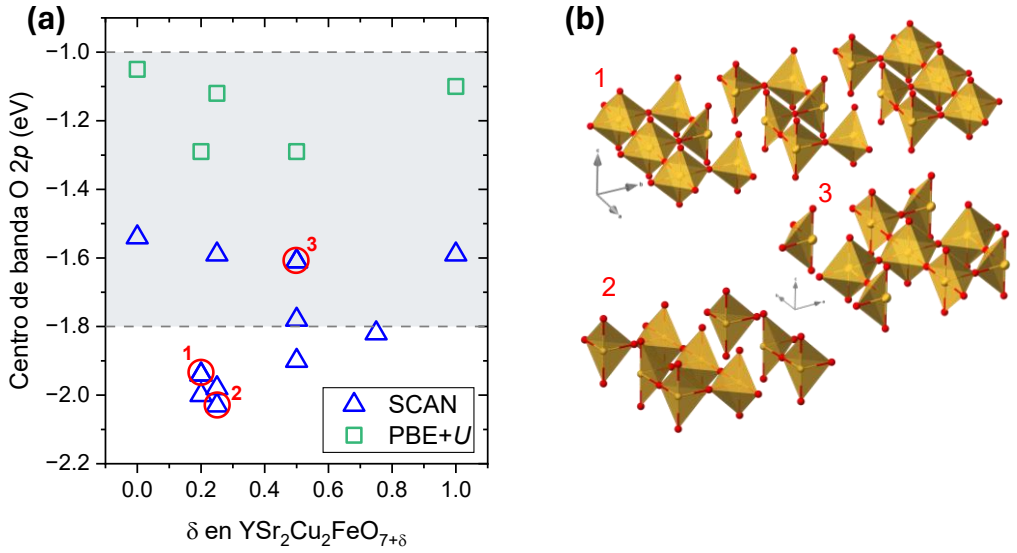

Figura 7.1. Valores calculados del centro de banda O 2p para el sistema $YSr_2Cu_2FeO_{7+\delta}$ ($0 < \delta < 1$) utilizando el funcional SCAN (triángulos azules). Para δ = 0,2; 0,25 y 0,5, los círculos rojos indican las configuraciones más estables. Para estas configuraciones, los resultados de cálculos adicionales con PBE+*U* aparecen como cuadrados verdes. La región sombreada en gris indica los valores prometedores del centro de banda O 2*p* para la actividad catalítica.[21] (b) Representación de los planos $FeO_{1+\delta}$ para las configuraciones ordenadas más estables encontradas para δ = 0,2 (etiquetada como 1); 0,25 (etiquetada como 2) y 0,5 (etiquetada como 3).

Sin embargo, aunque un material presente valores prometedores del centro de banda O 2*p* y valores de ASR favorables para catálisis, esto no asegura que su estabilidad no se vea comprometida bajo condiciones operativas de SOFC.[22, 25, 26] Un claro ejemplo es el BSCF ($Ba_{0.5}Sr_{0.5}Co_{0.8}Fe_{0.2}O_{3-\delta}$), un material con alta actividad — con un centro O 2*p* de -1,54 eV y valores ASR de 0,055–0,071 Ω cm² a 600 °C[27]— que presenta problemas de estabilidad.[28] Precisamente, la importancia de lograr un equilibrio entre la actividad catalítica y la estabilidad ha sido tratada con anterioridad por diferentes autores.[21] En este sentido, se ha visto que, para catalizar la OER, centros de banda muy cercanos al nivel de Fermi (valores demasiado cercanos a 0) pueden ser indicativos de inestabilidad del material. Concretamente, se ha observado la amorfización en materiales utilizados en electrolizadores alcalinos (AEL),[25] y una facilidad excesiva para formar vacantes de oxígeno en materiales catalíticos derivados de $BaFeO_3$.[29] En

el caso del sistema YSCFO , los valores del centro de banda O 2*p* están demasiado cerca del nivel de Fermi, lo que sugiere que la estabilidad de $YSr_2Cu_2FeO_{7+\delta}$ ($0 < \delta < 1$) bajo condiciones operativas de SOFC podría verse comprometida. En particular, Slater y colaboradores enfatizaron que los cambios estructurales asociados a la pérdida de oxígeno al calentar en aire la fase $YSr_2Cu_2FeO_{7.56}$ pueden ser un inconveniente para la utilización de este material.[9]

En resumen, en cuanto a las potenciales aplicaciones del sistema $YSr_2Cu_2FeO_{7+\delta}$ ($0 < \delta < 1$), los valores del centro de banda O 2*p* sugieren que este sistema podría exhibir una actividad catalítica significativa para los procesos ORR/OER, si bien estos centros de banda también son indicativos de una posible inestabilidad del material.

7.4. Referencias

(1) Zavatski, S.; Neilande, E.; Bandarenka, H.; Popov, A.; Piskunov, S.; Bocharov, D. Density functional theory for doped TiO_2: current research strategies and advancements. *Nanotechnology* **2024**, *35* (19). DOI: 10.1088/1361-6528/ad272e.

(2) Perdew, J. P.; Yang, W.; Burke, K.; Yang, Z.; Gross, E. K.; Scheffler, M.; Scuseria, G. E.; Henderson, T. M.; Zhang, I. Y.; Ruzsinszky, A.; et al. Understanding band gaps of solids in generalized Kohn-Sham theory. *Proc Natl Acad Sci U S A* **2017**, *114* (11), 2801-2806. DOI: 10.1073/pnas.1621352114.

(3) Hubbard, J. Electron correlations in narrow energy bands. *Proceedings of the Royal Society of London. Series A. Mathematical and Physical Sciences* **1997**, *276* (1365), 238-257. DOI: 10.1098/rspa.1963.0204.

(4) Woodward, P. M.; Karen, P.; Evans, J. S. O.; Vogt, T. *Solid State Materials Chemistry*; Cambridge University Press, 2021. DOI: 10.1017/9781139025348.

(5) Kumar, S.; Dogra, A.; Husain, M.; Kishan, H.; Awana, V. P. S. Comparative study of $MSr_2RECu_2O_{7+\delta}$ compounds with M=Al, Nb, Fe, Ru, Ga and Co and RE=Eu, Y. *Journal of Alloys and Compounds* **2010**, *493* (1-2), 352-357. DOI: 10.1016/j.jallcom.2009.12.101.

(6) López-Paz, S. A.; Marín-Gamero, R.; Martínez de Irujo-Labalde, X.; Sánchez-Marcos, J.; Perez-Coll, D.; Alario y Franco, M. Á.; García-Martín, S. YBaCuO-type perovskites as potential air electrodes for SOFCs. The case of $YSr_2Cu_2FeO_{7+\delta}$. *Journal of Materials Chemistry A* **2021**, *9* (13), 8554-8560. DOI: 10.1039/d1ta00111f.

(7) Mochiku, T.; Nakano, Y.; Oikawa, K.; Kamiyama, T.; Fujii, H.; Hata, Y.; Suzuki, J.; Kakeya, I.; Kadowaki, K.; Hirata, K. Atomic ordering in $FeSr_2LnCu_2O_{6+\delta}$ system (Ln=Nd, Y and Er). *Physica C: Superconductivity* **2003**, *400* (1-2), 43-52. DOI: 10.1016/s0921-4534(03)01322-4.

(8) Pissas, M.; Kallias, G.; Simopoulos, A.; Niarchos, D.; Kostikas, A. Mossbauer and crystal-structure study of $YSr_2Cu_2FeO_y$ isomorphic with $YBa_2(Cu_{1-x}Fe_x)_3O_y$. *Phys Rev B Condens Matter* **1992**, *46* (21), 14119-14125. DOI: 10.1103/physrevb.46.14119.

(9) Sansom, J. E. H.; Kendrick, E.; Rudge-Pickard, H. A.; Islam, M. S.; Wright, A. J.; Slater, P. R. Synthesis and characterisation of the perovskite-related cuprate phases $YSr_2Cu_2MO_{7+y}$(M = Co, Fe) for potential use as solid oxide fuel cell cathode materials. *Journal of Materials Chemistry* **2005**, *15* (23). DOI: 10.1039/b502641e.

(10) Wu, S.; Yang, X.; Zhao, X.; Li, Z.; Lu, M.; Xie, X.; Yan, J. Applications and Advances in Machine Learning Force Fields. *J Chem Inf Model* **2023**, *63* (22), 6972-6985. DOI: 10.1021/acs.jcim.3c00889.

(11) Chandrasekaran Selvaraj, S.; Koverga, V.; Ngo, A. T. Exploring Li-ion transport properties of Li_3TiCl_6: A machine learning molecular dynamics study. *Journal of The Electrochemical Society* **2024**, *171*. DOI: 10.1149/1945-7111/ad4ac9.

(12) Jaykhedkar, N.; Bystricky, R.; Sykora, M.; Bucko, T. How the temperature and composition govern the structure and band gap of Zr-based chalcogenide perovskites: insights from ML accelerated AIMD. *Inorg Chem* **2023**, *62* (31), 12480-12492. DOI: 10.1021/acs.inorgchem.3c01696.

(13) Deringer, V. L.; Caro, M. A.; Csanyi, G. Machine learning interatomic potentials as emerging tools for materials science. *Adv Mater* **2019**, *31* (46), e1902765. DOI: 10.1002/adma.201902765.

(14) Gupta, N. M. Factors affecting the efficiency of a water splitting photocatalyst: A perspective. *Renewable and Sustainable Energy Reviews* **2017**, *71*, 585-601. DOI: 10.1016/j.rser.2016.12.086.

(15) Morales-Garcia, A.; Vines, F.; Sousa, C.; Illas, F. Toward a rigorous theoretical description of photocatalysis using realistic models. *J Phys Chem Lett* **2023**, *14* (15), 3712-3720. DOI: 10.1021/acs.jpclett.3c00359.

(16) Greeley, J.; Jaramillo, T. F.; Bonde, J.; Chorkendorff, I. B.; Norskov, J. K. Computational high-throughput screening of electrocatalytic materials for hydrogen evolution. *Nat Mater* **2006**, *5* (11), 909-913. DOI: 10.1038/nmat1752.

(17) Yang, H.; Han, X.; Douka, A. I.; Huang, L.; Gong, L.; Xia, C.; Park, H. S.; Xia, B. Y. Advanced oxygen electrocatalysis in energy conversion and storage. *Advanced Functional Materials* **2020**, *31* (12). DOI: 10.1002/adfm.202007602.

(18) Yao, Z. C.; Tang, T.; Jiang, Z.; Wang, L.; Hu, J. S.; Wan, L. J. Electrocatalytic hydrogen oxidation in alkaline media: from mechanistic insights to catalyst design. *ACS Nano* **2022**, *16* (4), 5153-5183. DOI: 10.1021/acsnano.2c00641.

(19) Li, J. Oxygen evolution reaction in energy conversion and storage: design strategies under and beyond the energy scaling relationship. *Nanomicro Lett* **2022**, *14* (1), 112. DOI: 10.1007/s40820-022-00857-x.

(20) Wang, H.; Zhang, K. H. L.; Hofmann, J. P.; de la Peña O'Shea, V. A.; Oropeza, F. E. The electronic structure of transition metal oxides for oxygen evolution reaction. *Journal of Materials Chemistry A* **2021**, *9* (35), 19465-19488. DOI: 10.1039/d1ta03732c.

(21) Jacobs, R.; Mayeshiba, T.; Booske, J.; Morgan, D. Material discovery and design principles for stable, high activity perovskite cathodes for solid oxide fuel cells. *Advanced Energy Materials* **2018**, *8* (11). DOI: 10.1002/aenm.201702708.

(22) Lee, Y.-L.; Kleis, J.; Rossmeisl, J.; Shao-Horn, Y.; Morgan, D. Prediction of solid oxide fuel cell cathode activity with first-principles descriptors. *Energy & Environmental Science* **2011**, *4* (10). DOI: 10.1039/c1ee02032c.

(23) Giordano, L.; Akkiraju, K.; Jacobs, R.; Vivona, D.; Morgan, D.; Shao-Horn, Y. Electronic structure-based descriptors for oxide properties and functions. *Acc Chem Res* **2022**, *55* (3), 298-308. DOI: 10.1021/acs.accounts.1c00509.

(24) Jacobs, R.; Hwang, J.; Shao-Horn, Y.; Morgan, D. Assessing correlations of perovskite catalytic performance with electronic structure descriptors. *Chemistry of Materials* **2019**, *31* (3), 785-797. DOI: 10.1021/acs.chemmater.8b03840.

(25) Grimaud, A.; May, K. J.; Carlton, C. E.; Lee, Y. L.; Risch, M.; Hong, W. T.; Zhou, J.; Shao-Horn, Y. Double perovskites as a family of highly active catalysts for oxygen evolution in alkaline solution. *Nat Commun* **2013**, *4*, 2439. DOI: 10.1038/ncomms3439.

(26) Chen, C.; Baiyee, Z. M.; Ciucci, F. Unraveling the effect of La A-site substitution on oxygen ion diffusion and oxygen catalysis in perovskite $BaFeO_3$ by data-mining molecular dynamics and density functional theory. *Phys Chem Chem Phys* **2015**, *17* (37), 24011-24019. DOI: 10.1039/c5cp03973h.

(27) Shao, Z.; Haile, S. M. A high-performance cathode for the next generation of solid-oxide fuel cells. *Nature* **2004**, *431*, 170–173. DOI: 10.1038/nature02863.

(28) Sahini, M. G.; Mwankemwa, B. S.; Kanas, N. $Ba_xSr_{1-x}Co_yFe_{1-y}O_{3-\delta}$ (BSCF) mixed ionic-electronic conducting (MIEC) materials for oxygen separation membrane and SOFC applications: Insights into processing, stability, and functional properties. *Ceramics International* **2022**, *48* (3), 2948-2964. DOI: 10.1016/j.ceramint.2021.10.189.

(29) Chen, C.; Ciucci, F. Designing Fe-Based oxygen catalysts by density functional theory calculations. *Chemistry of Materials* **2016**, *28* (19), 7058-7065. DOI: 10.1021/acs.chemmater.6b02953.

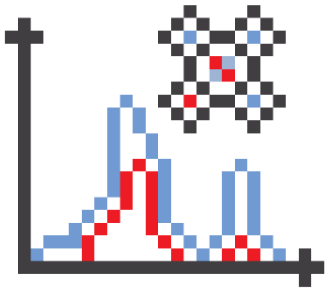

CAPÍTULO 8
Conclusiones

La presente tesis doctoral se ha centrado en el estudio computacional de óxidos de metales de transición con estructura basadas en capas perovskita, para aplicaciones en la producción y utilización de hidrógeno. Las conclusiones principales derivadas de esta tesis doctoral se resumen a continuación:

1) Se ha demostrado por primera vez la actividad fotocatalítica para la reacción de evolución de hidrógeno de la perovskita en capas $BaSrTa_2O_7$. La producción de hidrógeno utilizando $BaSrTa_2O_7$ como fotocatalizador es un 26% superior a la observada con $Sr2Ta_2O_7$. Los resultados de los cálculos DFT son consistentes con el comportamiento experimental. El estudio de la familia $Sr_{2-x}Ba_xTa_2O_7$ ($0 \leq x \leq 1$) ha permitido correlacionar la actividad fotocatalítica con la estructura cristalina y electrónica de estos óxidos. Se ha observado las diferencias en la estructura electrónica de $BaSrTa_2O_7$ respecto a $Sr_2Ta_2O_7$ tienen su origen en hay factores estructurales.

2) Los cálculos DFT llevados a cabo sobre estos materiales validan la utilización del funcional SCAN en el estudio de la estructura cristalina y electrónica de óxidos de metales de transición d^0. Aunque ambos materiales ($BaSrTa_2O_7$ y $Sr_2Ta_2O_7$) presentan una estructura en capas derivada de la perovskita y están compuestos por Ta, su band gap medido difiere en 0,6 eV. Dicha diferencia se reproduce adecuadamente utilizando el funcional SCAN. En cuanto a las propiedades catalíticas, los cálculos realizados no permiten profundizar en algunos aspectos específicos de la fotocatálisis. No obstante, estos resultados han permitido explorar tendencias generales dentro de la familia $Sr_{2-x}Ba_xTa_2O_7$ ($0 \leq x \leq 1$).

3) La capacidad del funcional SCAN queda confirmada con el estudio del sistema $YSr_2Cu_2FeO_{7+\delta}$ ($0< \delta <1$). Los cálculos realizados han permitido comparar diferentes metodologías DFT, como PBE, PBE+*U*, SCAN y SCAN+*U*, para modelar óxidos de alta complejidad estructural y electrónica. Se ha observado que las metodologías SCAN y GGA son válidas para simular las propiedades metálicas de la fase con mayor contenido en oxígeno $YSr_2Cu_2FeO_8$. Por el contrario, para la fase con menor contenido en oxígeno $YSr_2Cu_2FeO_7$, el carácter aislante se reproduce utilizando la metodología GGA+*U*, así como el funcional SCAN. Por lo tanto, estos resultados establecen que, entre los probados, el meta-GGA SCAN es el funcional más

adecuado para investigar las propiedades del sistema $YSr_2Cu_2FeO_{7+\delta}$ ($0 < \delta < 1$) en su conjunto.

4) Con respecto a la metodología SCAN+*U* en el estudio del sistema $YSr_2Cu_2FeO_{7+\delta}$ ($0 < \delta < 1$), los resultados obtenidos ponen de manifiesto que, aunque la introducción del parámetro *U* no resulta estrictamente necesaria, la aplicación de U_{Cu} = 1 eV da lugar a una descripción más exacta de las propiedades. La mayor contribución de los orbitales Cu-3*d* al nivel de Fermi de la fase oxidada ideal $YSr_2Cu_2FeO_8$ y al borde de la banda de conducción de la fase ideal reducida $YSr_2Cu_2FeO_7$, da como resultado a un mayor impacto del parámetro U_{Cu} sobre las propiedades electrónicas y los momentos magnéticos calculados, en comparación con el parámetro U_{Fe}.

5) Además, se ha comprobado que la introducción del término *U* utilizado en SCAN+*U* resulta en una excesiva localización electrónica y la obtención de momentos magnéticos elevados que se desvían de las observaciones experimentales. Los resultados obtenidos en el estudio SCAN+*U* de YSCFO subrayan la importancia de evaluar los parámetros *U* individuales para aquellos óxidos complejos con más de un metal de transición y demuestran que la transferibilidad del parámetro *U* entre distintos materiales y metodologías (utilizar el mismo valor de *U* para PBE y SCAN) es particularmente arriesgada para óxidos tan complejos como $YSr_2Cu_2FeO_{7+\delta}$ ($0< \delta <1$). Por último, se ha visto que la idoneidad de la metodología SCAN+*U* para el estudio de óxidos con múltiples metales de transición debe evaluarse para cada caso individual, sopesando si la mejora en la predicción de propiedades justifica el esfuerzo de optimizar los valores de *U*.

6) La combinación de cálculos DFT con Dinámica Molecular ha demostrado que en el sistema $YSr_2Cu_2FeO_{7+\delta}$ ($0< \delta <1$) se produce una difusión anisotrópica del oxígeno en el plano *ab* de las capas $FeO_{1-\delta}$. Los valores de energía de activación (Ea = 0.37 eV) y coeficiente de difusión de oxígeno (1.28×10^{-7} cm²/s a 500 °C) sugieren una posible aplicación del material como cátodo en SOFC. Sin embargo, otros factores clave para la catálisis ORR/OER, como la estabilidad química y mecánica, deben ser evaluados experimentalmente. Por lo tanto, es necesario continuar con investigaciones experimentales que

confirmen la utilidad de YSCFO. Dicho estudio es prioritario antes de embarcarse en estudios computacionales más complejos.

7) Se ha comprobado que las perovskitas en capas estudiadas ($Sr_{2-x}Ba_xTa_2O_7$ y $YSr_2Cu_2FeO_{7+\delta}$) presentan potencial para su aplicación en el campo de la energía. En particular, los resultados obtenidos en esta tesis doctoral indican que estos materiales podrían ser efectivos para llevar a cabo la evolución fotocatalítica de hidrógeno ($Sr_{2-x}Ba_xTa_2O_7$) y para actuar como cátodo en celdas de combustible de óxido sólido ($YSr_2Cu_2FeO_{7+\delta}$). A pesar de los resultados prometedores obtenidos en esta tesis doctoral, se hace necesario continuar explorando estas perovskitas en capas, ya que, en general, el número de trabajos centrados en ellas sigue siendo menor en comparación con las ampliamente investigadas perovskitas

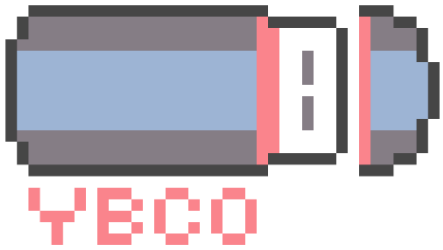

Anexo I

Esta tesis doctoral aborda el estudio del sistema $YSr_2Cu_2FeO_{7+\delta}$ ($0 < \delta < 1$), que pertenece a la familia de cupratos superconducotres, desde un punto de vista computacional. Por ello, en esta sección se dedican unas palabas a la estructura electrónica de cupratos como $YBa_2Cu_3O_{7-\delta}$, en los que las propiedades electrónicas dependen del contenido en oxígeno.

En los planos superconductores de los cupratos, es decir, aquellos formados por los cationes Cu(2) (véase la **figura 1.6**), existe la capa CuO_2^{2-}, ilustrada en la **figura Ia**, que forma las bases de las pirámides en YBCO. La presencia de la capa CuO_2^{2-} (con o sin oxígenos apicales) es esencial, ya que es donde se encuentran los portadores de carga.[1] La disposición de los átomos de Cu y O en estos planos influye directamente en las propiedades electrónicas del material. En la fase no dopada ($YBa_2Cu_3O_6$), el Cu de estos planos presentaría un estado de oxidación formal +2, de forma que su configuración electrónica sería $3d^9$. De acuerdo con el desdoblamiento de los orbitales *d* del Cu en una geometría plano-cuadrada representado en la **figura Ib**, el electrón desapareado ocuparía el orbital de mayor energía $3dx^2\text{-}y^2$. Teniendo en cuenta la densidad de estados de la capa CuO_2^{2-} representada de manera esquemática en la **figura Ic**, el electrón desapareado se encontraría en el estado resultante de la hibridación entre Cu $3d_{x^2\text{-}y^2}$ y O $2p_x$, $2p_y$, que presenta una mayor participación del Cu.

De esta forma, en la fase $YBa_2Cu_3O_6$ existiría una banda formada por estados Cu 3*d* y O 2*p* parcialmente ocupada. Según la teoría de bandas, en esta situación se espera un material con comportamiento metálico. Sin embargo, debido a la alta correlación electrónica existente entre los electrones *d* del Cu, el material $YBa_2Cu_3O_6$ es un aislante de Mott, cuya estructura electrónica puede describirse a través del modelo de Mott-Hubbard. De acuerdo con este modelo, se formarán dos bandas de Hubbard separadas por un band gap del orden del parámetro *U*, que permite tener en cuenta la repulsión interelectrónica, según aparece esquematizado en la **figura Id**.

Por lo tanto, las propiedades electrónicas de los cupratos superconductores pueden modularse a través del dopaje con huecos (*hole doping*). En estos compuestos la conductividad electrónica es de tipo p, es decir, está provocada por los huecos que se introduzcan en la banda formada por estados O 2*p* y Cu 3*d* (**figura Ic, d**). Este dopaje con huecos va ligado a la introducción de oxígeno en los bloques de reserva de carga (planos Cu(1)). Además, la existencia de la

superconductividad está ligada a este dopaje. En la mayoría de estos cupratos el papel de los bloques de reserva de carga es introducir huecos en la estructura electrónica al pasar de la fase aislante (fase no dopada, $YBa_2Cu_3O_6$) a la fase metálica superconductora (fase dopada con huecos, $YBa_2Cu_3O_7$).

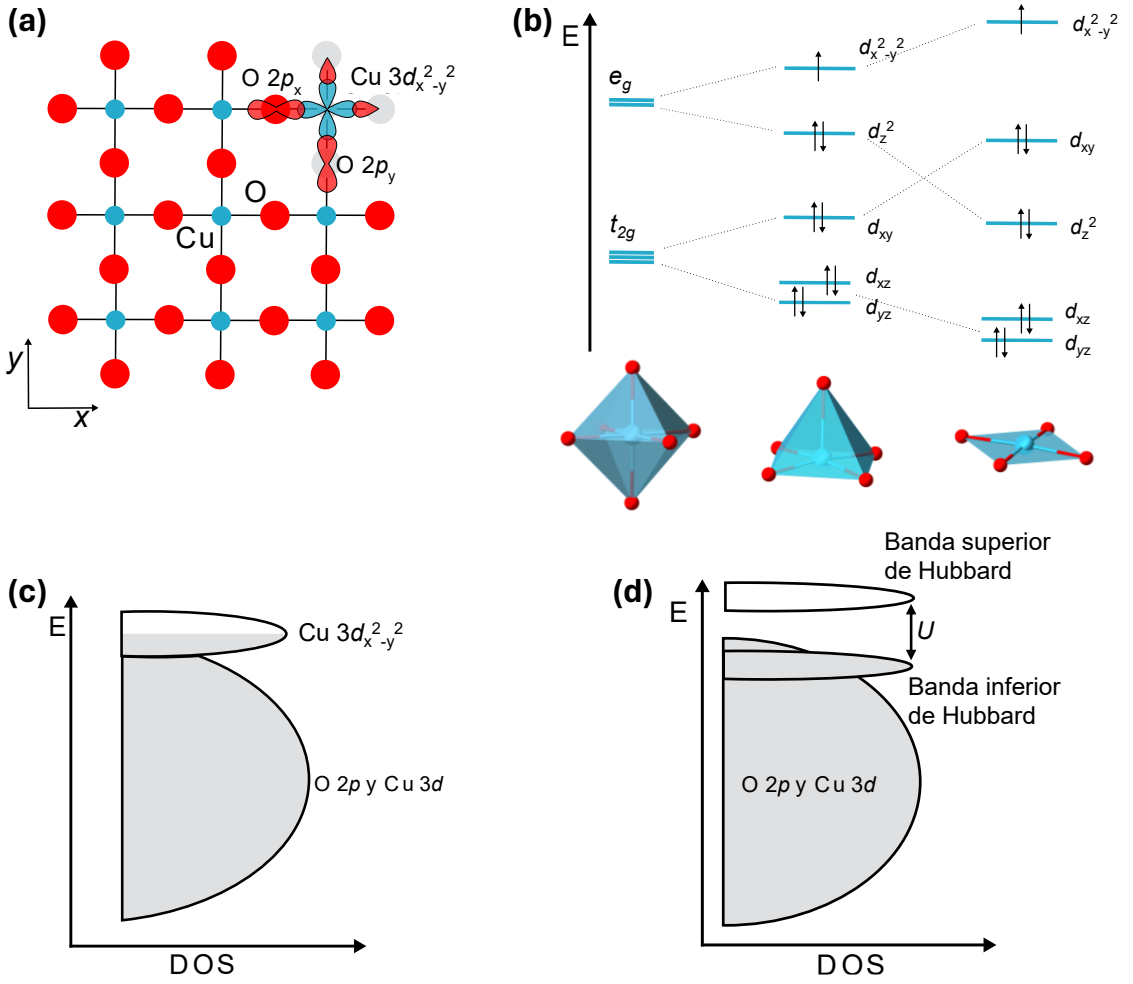

Figura I. (a) Estructura 2D de la capa $CuO2^{2-}$ presente en los cupratos superconductores de fórmula $YBa_2Cu_3O_{7-\delta}$. Color: Cu en azul y O en rojo (b) Esquema del desdoblamiento de los orbitales *d* del Cu en geometrías octaédrica, tetraédrica y plano-cuadrada de acuerdo con la Teoría del Campo de Cristal. (c) Representación esquemática de la densidad de estados de los planos CuO_2^{2-} en cupratos superconductores. (d) Esquema de la densidad de estados de los planos CuO_2^{2-} modificado de acuerdo con el modelo de Mott-Hubbard. (Adaptada de[1, 2])

Referencias

(1) Rao, C. N. R.; Gopalakrishnan, J. *New Directions in Solid State Chemistry*; Cambridge University Press, 1997. DOI: 10.1017/CBO9780511623141.

(2) Woodward, P. M.; Karen, P.; Evans, J. S. O.; Vogt, T. *Solid State Materials Chemistry*; Cambridge University Press, 2021. DOI: 10.1017/9781139025348.

(3) Cox, P. A. *Transition Metal Oxides: An Introduction to Their Electronic Structure and Properties*; Oxford University Press, 2010.